Orbital and Dynamical Investigation of the Galactic Center S-cluster

INAUGURAL-DISSERTATION

zur

Erlangung des Doktorgrades

der Mathematish-Naturwissenschaftlichen Fakultät

der Universität zu Köln

vorgelegt von

Basel Ali

aus Aleppo, Syrien

October 31, 2023

This dissertation has been accepted by the Faculty of Mathematics and Natural Sciences of the University of Cologne.

Berichterstatter:	Prof. Dr. Andreas Eckart
(Gutachter)	Prof. Dr. Peter Schilke

Tag der mündlichen Prüfung: 14.07.2023

Abstract

In close proximity to the bright radio source Sgr A* at the center of the Milky Way resides the so-called S-cluster. Based on the highly elliptical motion of these B-type stars, scientists were able to affirm that Sgr A* is the counterpart of a supermassive black hole. The latter affirmation opened a new door of challenges, such as how they arrived to the close vicinity of the SMBH, were they locally formed, and how to explain their observed dynamical features. These questions make the Galactic center environment an active area of research in current astrophysics and astronomy.

In total there are 108 stars, earlier studies were able to derive 37 orbits, while 71 still have no orbital solutions. In this thesis, I analyse data obtained from the Very Large Telescope in Chile to investigate the orbital and dynamical state of the S-cluster. The thesis is divided into three papers that encompass Bayesian methodology, machine learning clustering, three-dimensional structural analysis, image processing, and stellar dynamics.

In the first paper, I analyse the three-dimensional structure by means of visual inspection of 32 orbits of the S-stars and find that these stars are organized in two perpendicular highly inclined disks. The analysis shows that these stellar orbits are seen mostly edge-on and exhibit a thermalized eccentricity distribution. The structure can also be recovered in the distribution of the position angles of the projected semi-major axes. Furthermore, each disk contains clockwise and anti-clockwise moving stars, which could be explained using Kozai-Lidov cycles.

In the second paper, I explore different Bayesian methods in deriving multimodal posteriors that are expected in the orbital fitting problem in the absence of radial velocity measurements. The main motivation of this paper is obtaining orbital solution for the 71 stars, which have no radial velocity data. In total, I apply 8 different approaches that belong to Markov chain Monte Carlo, approximate Bayesian computations and nested sampling. In conclusion, I find that nested sampling is considered the best choice in terms of computation speed, uncertainty estimation and the ability to clearly detect multimodal posteriors. Furthermore, Ultranest, which is the optimal choice between the three nested sampling approaches, is then applied on the well-constraint orbit of S2.

In the third paper, I use Ultranest to obtain orbits for the 71 stars of the cluster. Due to the large number of stars and time limit of this thesis submission, I present the solutions of 20 orbits that were acquired till the current time. This is then followed by applying the machine learning clustering algorithm HDBSCAN on the specific angular momentum vectors of the 32 determined orbits from the first paper and of the newly determined orbits. The findings show the majority of the 57 orbits are arranged in a system of three highly inclined disks with a signature of a thermalized eccentricity distribution. In addition, I use three-body simulations to show that Kozai-Lidov cycles could be the cause of having two directions of motion in each of the observed disks. Nevertheless, future detailed N-body simulations are essential for certain conclusions on the formation of the cluster and the features of the structure.

Zusammenfassung

In unmittelbarer Nähe zur hellen Radioquelle Sgr A* im Zentrum der Milchstraße befindet sich der sogenannte S-Cluster. Basierend auf der stark elliptischen Bewegung dieser Sterne vom Typ B konnten Wissenschaftler bestätigen, dass Sgr A* das Gegenstück zu einem supermassereichen Schwarzen Loch ist. Die letztgenannte Behauptung öffnete eine neue Tür für Herausforderungen, z. B. wie sie in die unmittelbare Nähe des SMBH gelangten, wo sie lokal gebildet wurden und wie ihre beobachteten dynamischen Merkmale zu erklären sind. Diese Fragen machen die Umgebung des Galaktischen Zentrums zu einem aktiven Forschungsgebiet in der aktuellen Astrophysik und Astronomie.

Insgesamt gibt es 108 Sterne, frühere Studien konnten 37 Umlaufbahnen ableiten, während 71 noch keine Umlaufbahnlösungen haben. In dieser Arbeit analysiere ich Daten des Very Large Telescope in Chile, um den orbitalen und dynamischen Zustand des S-Clusters zu untersuchen. Die Dissertation ist in drei Artikel unterteilt, die die Bayes'sche Methodik, maschinelles Lernen, Clustering, dreidimensionale Strukturanalyse, Bildverarbeitung und Sterndynamik umfassen.

Im ersten Artikel analysiere ich die dreidimensionale Struktur mittels visueller Inspektion von 32 Umlaufbahnen der S-Sterne und finde heraus, dass diese Sterne in zwei senkrechten, stark geneigten Scheiben organisiert sind. Die Analyse zeigt, dass diese Sternbahnen meist von der Seite gesehen werden und eine thermalisierte Exzentrizitätsverteilung aufweisen. Die Struktur lässt sich auch in der Verteilung der Positionswinkel der projizierten großen Halbachsen wiederfinden.

Darüber hinaus enthält jede Scheibe sich im Uhrzeigersinn und gegen den Uhrzeigersinn bewegende Sterne, was mit Kozai-Lidov-Zyklen erklärt werden könnte.

Im zweiten Artikel untersuche ich verschiedene Bayes'sche Methoden zur Ableitung multimodaler Seitenzähne, die beim Orbitalanpassungsproblem ohne Radialgeschwindigkeitsmessungen erwartet werden. Die Hauptmotivation dieses Papiers ist das Erhalten einer orbitalen Lösung für die 71 Sterne, die keine Radialgeschwindigkeitsdaten haben. Insgesamt wende ich 8 verschiedene Ansätze an, die zur Markov-Kette Monte Carlo, approximative Bayes'sche Berechnungen und verschachteltes Sampling gehören. Zusammenfassend finde ich, dass verschachteltes Sampling in Bezug auf Rechengeschwindigkeit, Unsicherheitsschätzung und die Fähigkeit, multimodale Posterioren eindeutig zu erkennen, als die beste Wahl angesehen wird. Darüber hinaus wird Ultranest, das die optimale Wahl zwischen den drei verschachtelten Probenahmeansätzen darstellt, dann auf der gut eingeschränkten Umlaufbahn von S2 angewendet.

Im dritten Artikel verwende ich Ultranest, um Umlaufbahnen für die 71 Sterne des Haufens zu erhalten. Aufgrund der großen Anzahl von Sternen und der zeitlichen Begrenzung dieser Diplomarbeit präsentiere ich die Lösungen von 20 Orbits, die bis zum jetzigen Zeitpunkt erworben wurden. Anschließend erfolgt die Anwendung des Machine-Learning-Clustering-Algorithmus HDBSCAN auf die spezifischen Drehimpulsvektoren der 32 ermittelten Orbits aus dem ersten Paper und der neu ermittelten Orbits. Die Ergebnisse zeigen, dass die Mehrheit der 57 Umlaufbahnen in einem System aus drei stark geneigten Scheiben mit einer Signatur einer thermalisierten Exzentrizitätsverteilung angeordnet sind. Darüber hinaus verwende ich Drei-Körper-Simulationen, um zu zeigen, dass Kozai-Lidov-Zyklen die Ursache dafür sein könnten, dass in jeder der beobachteten Scheiben zwei Bewegungsrichtungen vorhanden sind. Dennoch sind zukünftige detaillierte N-Körper-Simulationen für bestimmte Schlussfolgerungen über die Bildung des Clusters und die Merkmale der Struktur unerlässlich.

Contents

Chapter 1

Introduction

1.1 The Galactic Center

The Galactic center in our Milky Way is considered to be one of the most peculiar environments in current Astrophysics and Astronomy. Not only because it contains the $\sim 4 \times 10^6\, M_\odot$ supermassive black hole Sgr A* at its core but also due to the unique dynamical features that are exhibited by the orbiting nuclear stellar cluster (Krabbe et al. (1995); Genzel et al. (2010); Eckart et al. (2017); Parsa et al. (2017); Gravity Collaboration et al. (2018); Do et al. (2019); Karas et al. (2021)) . To observe our area of interest, the telescope has to capture light traveling from a distance of around 8 kpc towards our home planet. More specifically, infrared telescopes are strongly preferred, since dust obscuration prevents us from spotting most of the structural details of the region in the optical window of the spectrum (see Figure 1.1). Once the infrared images are accessible, we identify a star-forming region in the inner 100-200 pc, which is most likely sustained by the neighbouring Central Nuclear Zone Figer (2004). Approaching closer to the center, one observes a few 10^8 giant molecular clouds and young binaries in the range between 10 and 100 pc (Perets et al. (2007)). This is followed by a ring of dense molecular cloud steamers, the so-called circum nuclear disk (CND) within the inner 1.5 - 4 pc (Guesten et al. (1987)). The CND and the mini-spiral arms of ionized gas are surrounded by supernova remnants, Sgr A west and some giant molecular clouds (Mezger et al. (1989)). As we reach the inner 0.5 pc, we spot a population of mostly low-mass red giants, massive blue giants and low-mass main sequence stars (Bartko et al. (2010)).

The spectroscopically determined young age of these stars gave rise to the for-

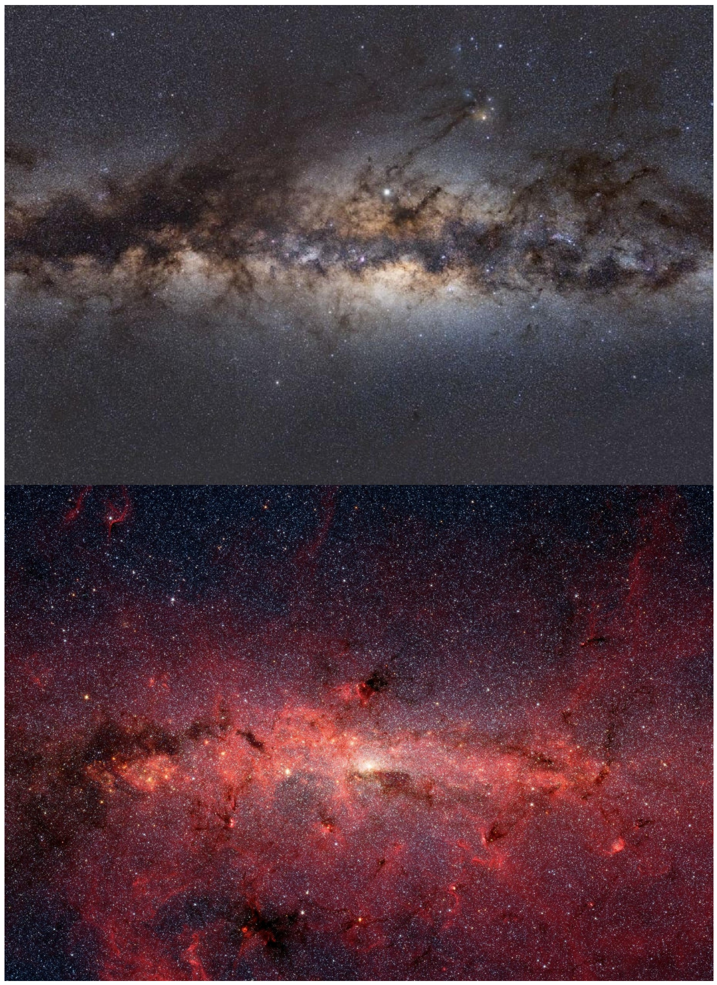

Figure 1.1: *The central region of the Milky Way as seen in optical (above) and in infrared (below) with image scale of about 273 pc $\times$ 196 pc. Optical image credit: Axel Mellinger/-Natasha Hurley-Walker. Infrared image credit: NASA,JPL-Caltech, Susan Stolovy (SS-C/Caltech) et al.*

mulation of the 'paradox of youth' (Ghez et al., 2003), since the formation of young stars in situ has been challenging to explain due to strong tidal forces, X-ray/UV irradiation, stellar winds, a large internal velocity dispersion of gas, strong poloidal magnetic field, and a general lack of dense molecular clouds in the vicinity of the SMBH (Morris, 1989, 1993).

1.2 The S-cluster

The central topic of this thesis is to study the orbital and dynamical features of the so-called S-cluster, which harbors the lighter 3.5-20 $M_\odot$ B-dwarfs with K_s-band magnitude of ≤ 18, orbiting the SMBH Sgr A*(Gravity Collaboration et al. (2018)). Located in the central arcseconds, the cluster contains 108 stars with most of them being early-type stars rather than late. More specifically, only S17, S21, S24, S38, S85, S89, S111 and S145 are identified as late type (Gillessen et al. (2017)). Among the properties of the S-stars are an effective temperature of 21,000-28,000 K, a rotational velocity of 60-170 km/s and a surface gravity of $\log g = 4.1 - 4.2$ (Ghez et al., 2003; Martins et al., 2008; Habibi et al., 2017). These latter properties fit well with the features of stars of spectral type B0-B3V with masses between 8 $M_\odot$ and 14 $M_\odot$. Concerning their age, Habibi et al. (2017) constrain it for the S2 star to be $6.6^{+3.4}_{-4.7}$ Myr based on 12 years of spectroscopic monitoring. For the other S stars, their age can spectroscopically be constrained within 15 Myr, while ages larger than 25 Myr can be excluded.

As for their orbits, Gillessen et al. (2017) determined the orbital elements for 32 stars, while Peißker et al. (2020d) presented 5 orbits for newly detected faint S-cluster members. On the other hand, deriving the orbital elements for the remaining stars was not possible so far, since they still show linear trajectories and hence the data represent a very small section of the orbit. This makes it tricky to have an initial guess that is required for the optimization algorithm. The exact extent of the cluster can be seen in Figure 1.2, marked by the square and surrounded by the so-called IRS stars. These infrared sources are a mixture of early and late type giants, except for IRS 7, which is of spectral type M supergiant (M2)(Genzel et al. (2000)).

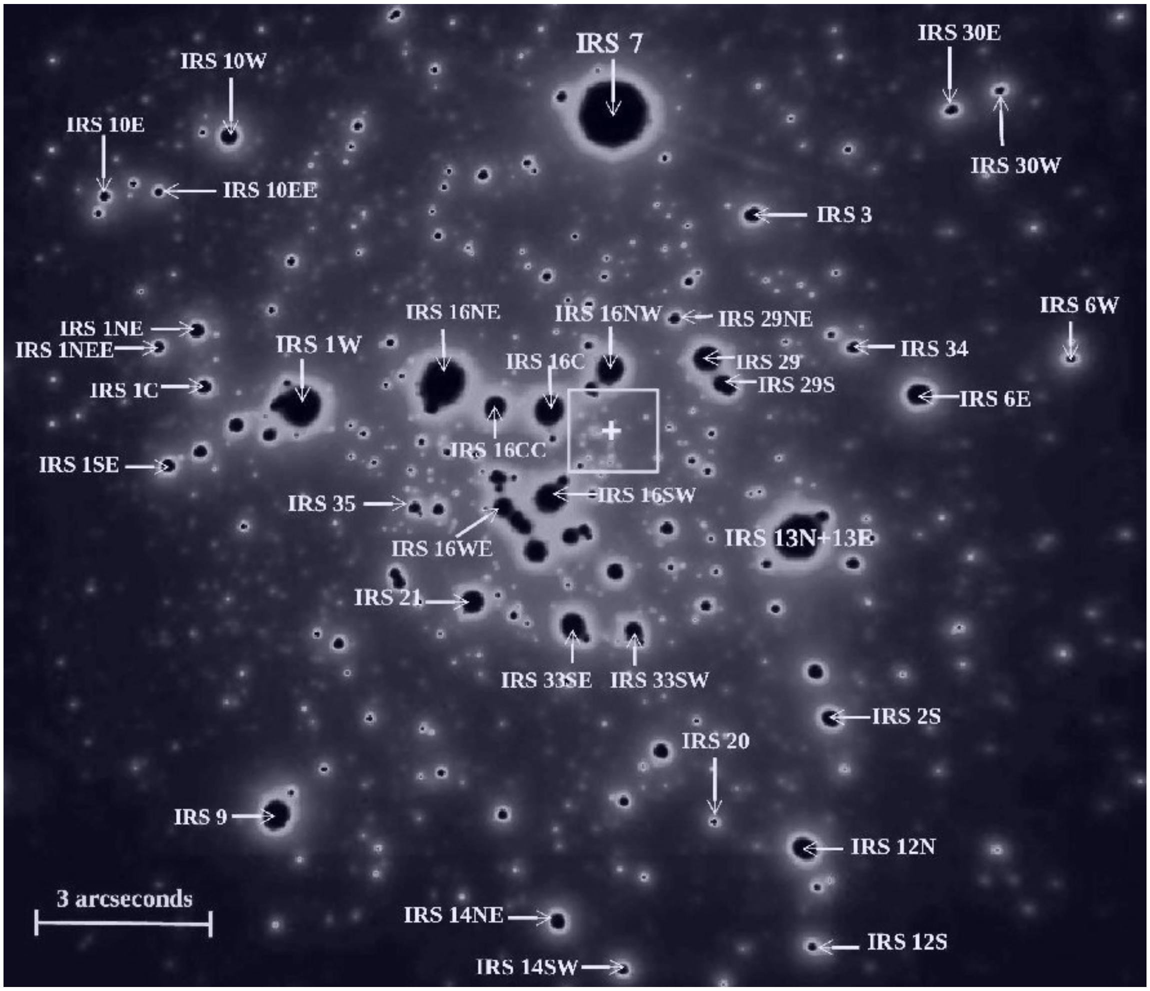

Figure 1.2: *A K_s-band (2.18 μm) image by the NACO instrument in the VLT observed in July 2005 with an image scale of 20″ × 20″. The nomenclatures of the IRS stars are included based on Viehmann, T. et al. (2005), as well as the location of the S-cluster (square) and the SMBH Sgr A* (cross). Regarding orientation, east is to the left and north is up.*

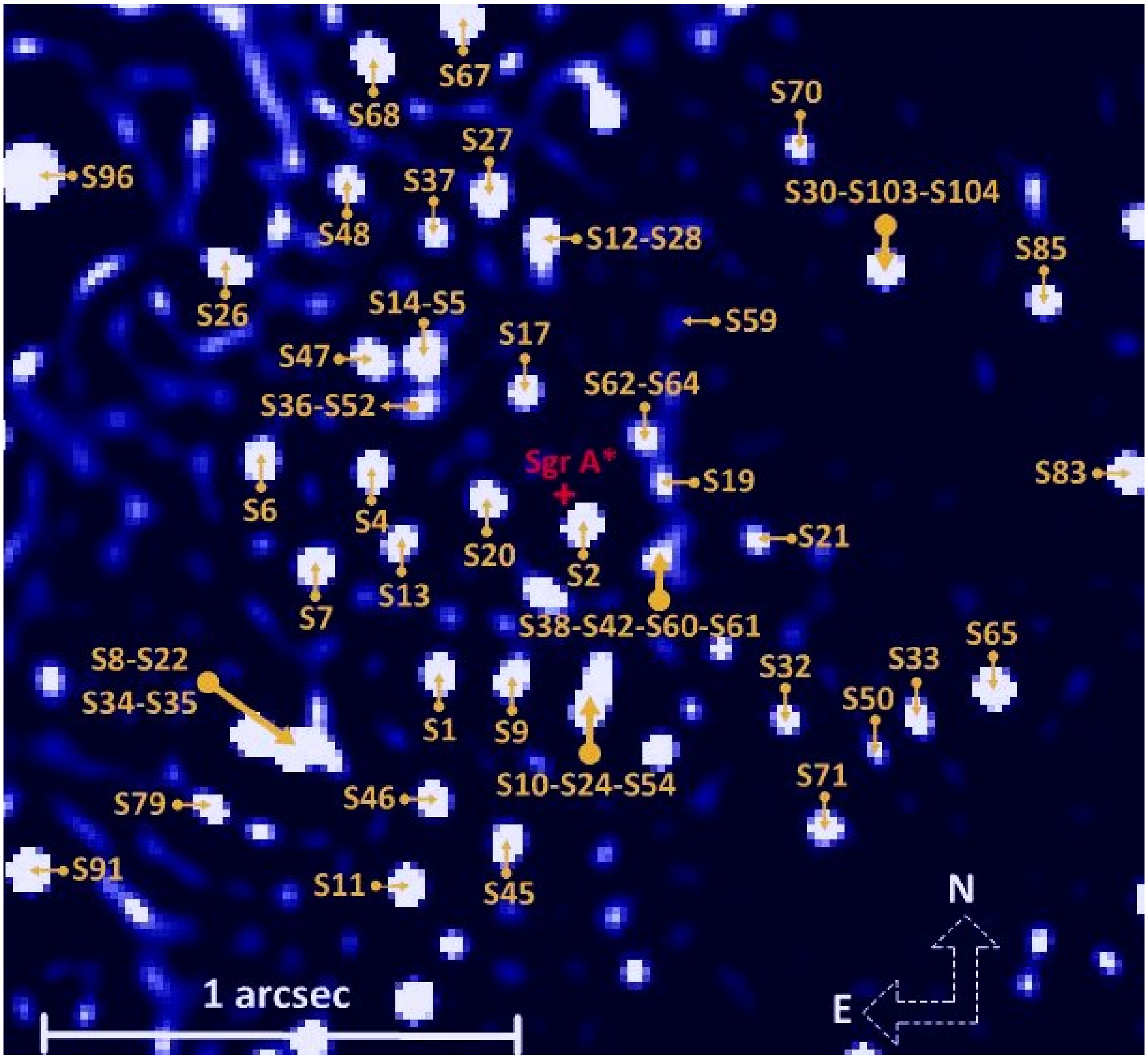

Figure 1.3: *A deconvolved K_s-band image showing the bulk region of the S-cluster (the square in Figure 1.2). Here, the bigger arrow heads refer to the presence of more than two stars at close distances. The image was taken by the NACO instrument in the VLT in early 2018.*

1.3 Keplerian Elements

The six orbital elements, first introduced by Johannes Kepler, are of great importance in predicting the motion of celestial objects and exploring their past and future dynamical features. To understand these elements, one needs to go through the Kepler problem. At first, we have the assumptions that:

1. The bodies are spherically symmetric and can be treated as point masses.

2. There are no external or internal forces acting upon the bodies other than their mutual gravitation.

The dynamical encounter between the two bodies occurs on the orbital plane, where the lighter body orbits the heavier one on a Keplerian orbit, which can be an ellipse, a parabola and a hyperbola.
The Keplerian Elements allow us to visualize the two-dimensional orbital plane in three dimensions with the help of a reference plane, which is in our case the celestial equator (see Figure 1.4). Starting with the shape of the orbit, we have two elements:

1. a: semi-major axis, which is half of the major axis that connects the pericenter (closest approach) with the apocenter (furthest approach).

2. e: eccentricity, which describes the deviation from a circle ($e = 0$), with an ellipse taking values between 0 and 1, a parabola when e=1 and hyperbola with e greater than 1.

The two elements which provide us with the orientation of the orbit in three dimensions w.r.t a reference plane are the following:

3. i: inclination, which is the angle between the orbital plane and the reference plane that the orbiting object makes when crossing the celestial equator from south to north with a range between $0\,^\circ$ and $180\,^\circ$.

4. Ω: right ascension of ascending node, which is measured on the reference plane and is the angle from a reference direction (NCP) to the ascending node, where the orbiting body crosses the celestial equator northwards with a range between 0 ° and 360 °.

The fifth element (ω) is the argument of the pericenter, which is defined as the angle between the ascending node and the direction of the pericenter. In simple words, it shows the orientation of the ellipse in the orbital plane. This angle also has the same range as Ω.
Finally, the sixth element can be chosen out of several parameters; such as the true anomaly (ν), which is the angle between the direction of the pericenter and the line pointing towards the current position of the orbiting body. The time of closest approach (t_p) can be an alternative to the true anomaly and is chosen as the sixth element throughout the analysis. Another alternative is the mean anomaly (M), which is the angle in an imaginary circular orbit corresponding to an object's eccentric anomaly (E).
With the introduction of the six orbital elements, one defines Kepler's equation as follows:

$$M = E - esinE \tag{1.1}$$

Where E is the eccentric anomaly, which is the angle that defines the position of a body on a Keplerian orbit, with M and e being introduced above.
The latter equation has no algebraic solution and therefore one needs to solve it numerically by finding the root of the following equation iteratively:

$$f(E) = E - esinE - M \tag{1.2}$$

To overcome this problem, we use the Newtonian method, which starts with $f(E)$, the derivative $f'(E)$ and an initial value E_0 as an approximate solution. Setting $e > 0.8$ and $E_0 = \pi$ as initial values, one obtains a better approximation by the following:

$$E_{n+1} = E_n - \frac{E_n - esinE_n - M}{1 - ecosE_n} \tag{1.3}$$

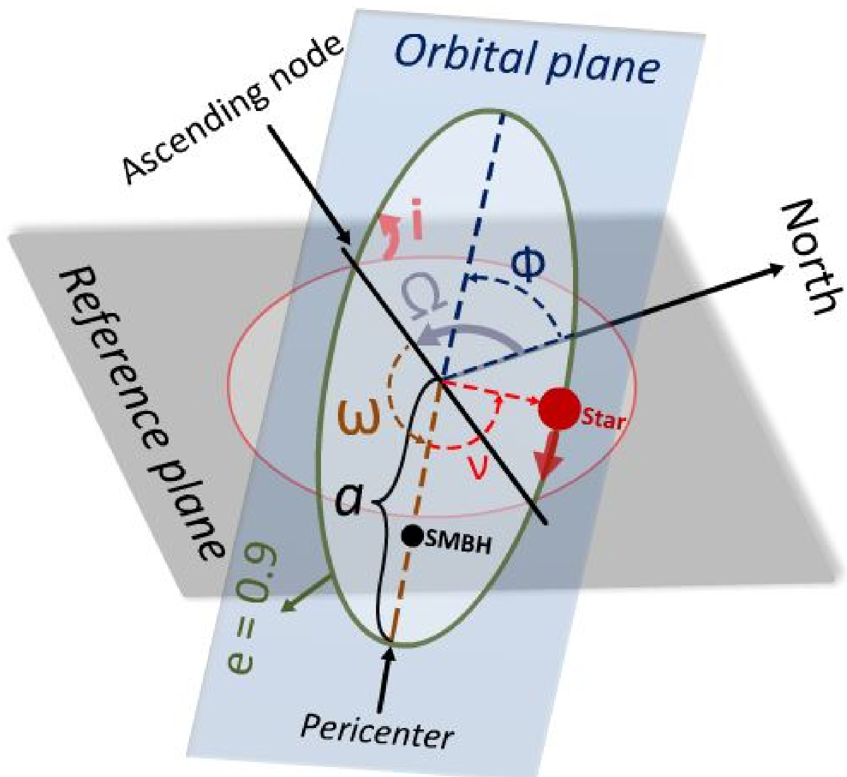

Figure 1.4: *An illustration of the Keplerian elements as defined above as well as of the position angle* Φ.

The iteration goes on until the initial guess is close enough to the solution and the derivative is obtained at these corresponding initial values. Consequently, the method will converge with the convergence being quadratic if the multiplicity of the root is 1. Alternatively, Mikkola (1987) presented a direct method as solution using approximations and the following cubic form of the equation:

$$E = M + e(3s - 4s^3) \tag{1.4}$$

with

$$s = z - \alpha / z \tag{1.5}$$

$$z = (\beta \pm \sqrt{\beta^2 + \alpha^3})^{1/3} \tag{1.6}$$

$$\alpha = (1 - e)/(4e + 0.5) \tag{1.7}$$

$$\beta = 0.5M/(4e + 0.5) \tag{1.8}$$

After solving Kepler's equation for the eccentric anomaly, one could proceed with Thiele-Innes elements that relate the orbital elements with the three spatial coordinates (Binnendijk (1960); Heintz (1978)):

$$A = cos(\Omega)cos(\omega) - sin(\Omega)sin(\omega)cos(i) \tag{1.9}$$

$$B = sin(\Omega)cos(\omega) + cos(\Omega)sin(\omega)cos(i) \tag{1.10}$$

$$C = sin(\omega)sin(i) \tag{1.11}$$

$$F = -cos(\Omega)sin(\omega) - sin(\Omega)cos(\omega)cos(i) \tag{1.12}$$

$$G = -sin(\Omega)sin(\omega) + cos(\Omega)cos(\omega)cos(i) \tag{1.13}$$

$$H = cos(\omega)sin(i) \tag{1.14}$$

$$\epsilon = a(cos(E) - e) \tag{1.15}$$

$$\eta = a\sqrt{(1 - e^2)}sin(E) \tag{1.16}$$

$$Y = B\epsilon + G\eta \tag{1.17}$$

$$X = A\epsilon + F\eta \tag{1.18}$$

$$Z = C\epsilon + H\eta \tag{1.19}$$

Where Y is the right ascension, X is the declination and Z is along the line of sight.

1.4 Statistical Methods

After being introduced to the relation between the state vectors and the orbital elements, one could now proceed with the proper modeling and methodology in order to find the optimal solution for a given dataset. Direct optimization models, which require an initial guess, are one possibility. For instance, one could create a mock ellipse from a given initial guess and then calculate the difference between the mock data points and the observed astrometric data using χ^2. The optimal solution would be the one with a minimum χ^2. Nevertheless, this direct method doesn't allow for degenerate solutions, such as the ones expected from stars with no radial velocity measurements. The lack of this information leads to two possible values for each of Ω and ω, since the ascending node is not certainly determined. Statistically, if better models are available that show this degeneracy, then they would be more accurate than direct models and present a proper solution.

A good point to start before continuing with the details of the methods is Bayes' Theorem. The Theorem is mathematically defined as follows:

$$P(A|B) = \frac{P(B|A)P(A)}{P(B)} \tag{1.20}$$

Where A and B are events, $P(A|B)$ is a conditional probability describing event A happening given B, $P(B|A)$ is the opposite of the latter, P(A) and P(B) are the probabilities of the occurrence of events A and B, respectively. In other words, the formula states that if we have prior knowledge or assessment of a certain outcome before adding any new experimental data, then one could obtain the posterior probability using Bayes' theorem by revising the prior probability after acquiring new information about the problem.

There have been several methods developed over the centuries to obtain the posterior probabilities. One famous example is the traditional Markov chain Monte Carlo algorithms (MCMCA), in which the so-called walkers explore the parameter space using proposal functions and exchange status until convergence is reached. Currently, there exist several updates to the original idea of MCMC, which is summarized in Metropolis et al. (1953). These updates usually differ in the proposal functions or as it is also called the 'move'. As an example, Goodman & Weare (2010) proposed an affine-invariant MCMC, in which the stretch move is applied on the walkers in the ensemble such that they satisfy detailed balance. In case the MCMC is not affine-invariant then the move is called a walk move. Other examples include differential evolution proposal, presented by Nelson et al. (2013), a clustered kernel-density-estimate proposal introduced by Farr & Farr (2015), or a proposal cycle that contains several functions, such as the one brought up by Ashton & Talbot (2021).

Another approach one could choose instead of MCMCA for posterior estimation is approximate Bayesian computations (ABC). Unlike MCMCA, ABC doesn't require the likelihood function to be specified, instead it is approximated by means of simulation using a distance measure and a threshold. The distance measure is used between the simulated data-set and the observed one, and along with a threshold, the algorithm either accepts or rejects the simulated set until the population size is a clear representative of the posterior distribution. This technique is called ABC-rejection sampling and its application can be seen in several publications such as Bertorelle et al. (2010) and Beaumont (2010). An enhancement to the latter concept was done by Toni & Stumpf (2009), who used ABC with sequential Monte Carlo (ABCSMC). The idea behind SMC is to assign likelihood weights to the simulated samples and repeat the sampling near the most probable sets. This allows the posterior estimation to be more accurate and precise. Concerning the distance measure, it could either be Euclidean, Manhattan, χ^2, or adaptive as demonstrated by Prangle (2017). The latter distance guarantees that each summary statistic has a similar influence by recalculating the weights and rescaling the impact. This is essentially helpful if the summary statistics vary largely in scale. Summary statistics are representatives of the raw output of the model and they're recommended to be used instead, since the probability of having a simulated sample with a small distance is inversely proportional to the dimensionality of the data.

Finally, instead of going with MCMC or ABC, one could proceed with the so-called Nested Sampling (NS). NS was recently presented by Skilling (2004) with the aim of calculating the evidence, also called the marginal likelihood, i.e., the integral over the prior and likelihood, with parallel estimation of the posterior samples. Initially, the algorithm starts by drawing N live points from the priors, or perform a prior transform, which is a transformation from a space where variables are independently and uniformly distributed between 0 and 1 to the parameter space of interest. This is then proceeded by calculating the likelihood of the N points while keeping track of the volume occupied by these points in the parameter space. This is followed by likelihood restrict prior sampling, in which the new sampled live point must have a likelihood higher than the minimum likelihood point that is removed before this step. This process is repeated until the remaining volume of the prior space is very small, i.e., the final live points share similar likelihoods.

The most recent improvements to NS usually vary in the way the new live point is sampled; for instance, it could either be by performing MCMC walk from the active points (Skilling (2004)), or bounding all live points with an ellipsoid and choosing the new point at random from within it after enlargement (Mukherjee et al. (2006)), or using clustered ellipsoidal nested sampling, which can form multiple ellipses around each individual peak in the likelihood space (Shaw et al. (2007)). The latter approach is proven to be of great importance in estimating multimodal posterior probabilities. Further enhancement to the algorithm was presented by Higson et al. (2018), the difference is that instead of choosing a fixed number of live points, the number is adapted with the purpose of sampling the posterior probability density more efficiently. Another development was introduced by Buchner (2021, 2019, 2016), implementing the parameter-free MLFriends algorithm, which creates ellipsoids around each live point and samples the new live point from them, with the shape of the ellipsoid determined by Mahalanobis distance and its size by cross-validation.

1.5 ML Clustering Algorithms

The benefits of machine learning algorithms are numerous in our current scientific community. For instance, clustering algorithms allow us to see the structural details of the data by classifying each data point into a certain group based on statistical measures such as the Euclidean distance to the neighbouring points. An example of such an algorithm is the K-Means (MacQueen (1967)), which requires the number of clusters to be specified. Then, each point is assigned to a cluster such that the variance is minimized and the cluster center is updated accordingly. One possibility to find the optimal number of clusters is to use the Elbow method (Satopaa et al. (2011)), which fits the model for different values of K with the elbow point being the one that fits the model best. Nevertheless, finding the number of clusters using this method can be challenging since one might not be certain which points exactly represents the elbow. In addition, the K-means algorithm doesn't detect outliers, which is also considered as a drawback.

A solution to this problem would be to use algorithms that don't require the number of clusters to be specified. An instance for such an algorithm is the so-called Density-Based Clustering Based on Hierarchical Density Estimates developed by Campello et al. (2013) and implemented in Python under the name HDBSCAN (McInnes et al. (2017)), which stands for Hierarchical Density-based Spatial Clustering of Applications with Noise. The algorithm starts by transforming the space to dense/sparse regions and building a minimum spanning tree via Prim's algorithm (Jarník (1930)). For transforming the space, the so-called mutual reachability distance is calculated for all points and given by the following:

$$d_{\mathrm{mreach}-k}(a,b) = \max\{\mathrm{core}_k(a), \mathrm{core}_k(b), d(a,b)\}$$

After obtaining the minimum spanning tree, it is then converted to a hierarchy of connected components, which is done by sorting the edges of the tree by distance in increasing order till obtaining a new merged cluster for each edge. This is then followed by cluster extraction, which starts by condensing down the large cluster hierarchy into a smaller tree with a little more data attached to each node. Here, the minimum cluster size is essential and used in evaluating the new clusters in such a way that the split has fewer points than the minimum cluster size. The next step is to calculate the cluster persistence scores and choose the clusters that persist and have a longer lifetime. For this purpose, the stability for each cluster is calculated as follows:

$$\sum_{p \in \text{cluster}} (\lambda_p - \lambda_{\text{birth}})$$

Now, if the sum of the stabilities of the child clusters is greater than the stability of the parent cluster, then we choose the cluster stability to be the sum of the child stabilities. On the other hand, if the parent cluster's stability is greater than the sum of its children, then we set the cluster to be a selected cluster and unselect all its descendants (see Figure 1.5).

As for outlier detection, the GLOSH algorithm is used, which stands for Global-Local Outlier Score from Hierarchies (Campello et al. (2015)). The algorithm can detect outliers if they're remarkably different from its local neighbourhood. In HDBSCAN, one obtains the persistence scores for each point along with their outlier scores, where higher values indicate a higher probability that the point is considered noise. At this point, all one needs to do is fine-tune the minimum cluster size and choose a suitable distance and proceed by assessing the clustering results with density-based clustering validation (DBCV), introduced by Moulavi et al. (2014) as follows:

$$DBCV(C) = \sum_{i=l}^{i=1} \frac{|C_i|}{|O|} V_C(C_i)$$

Where:

$$V_C(C_i) = \frac{min_{1 \leq j \leq l, j \neq i}(DSPC(C_i, C_j)) - DSC(C_i)}{max(min_{1 \leq j \leq l, j \neq i}(DSPC(C_i, C_j)), DSC(C_i))}$$

is the validity index of a cluster C_i, $DSPC(C_i)$ is the density separation of a pair of clusters, $DSC(C_i)$ is the density sparseness of a cluster, and $|O|$ and $|C_i|$ are

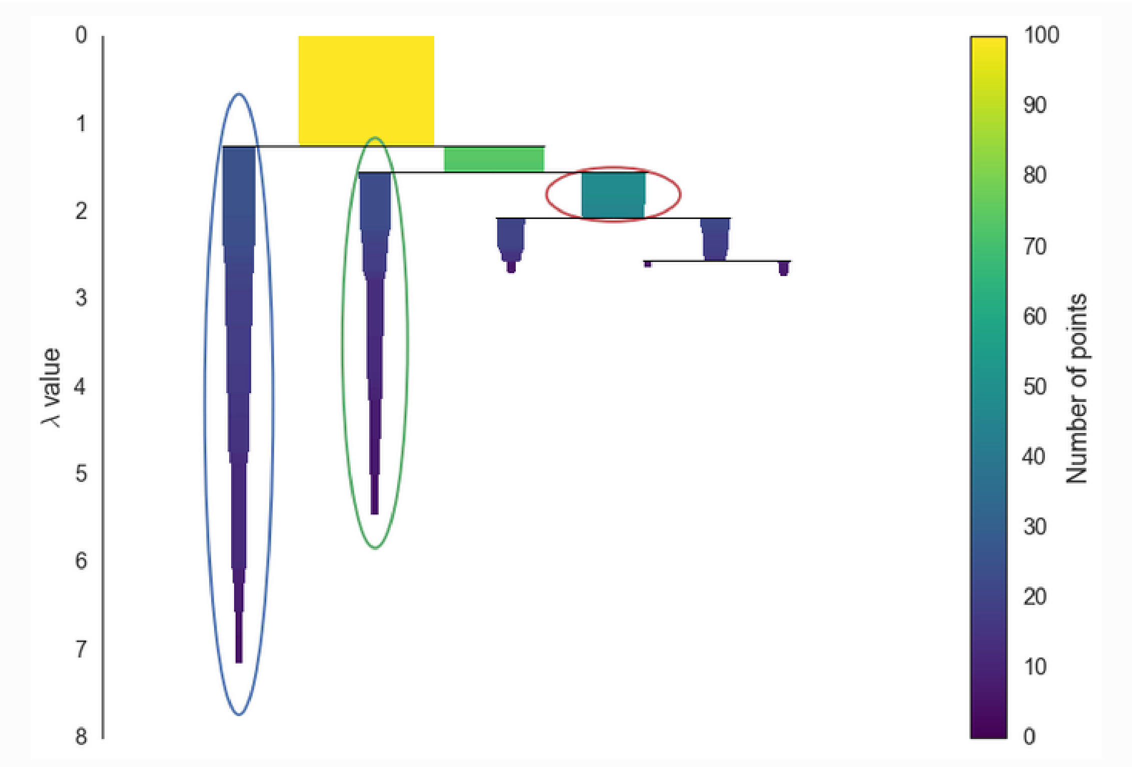

Figure 1.5: *An illustration of how cluster extraction is performed. Starting from the left, we find that the blue cluster is more persistent than the green and hence selected. Similarly, the second cluster is also chosen, while the cluster on the right has a stability greater than its children and hence they're unselected. Image credit:McInnes et al. (2017)*

the total number of objects under evaluation, including noise, and the size of the cluster, respectively. With this, one defines $DBCV(C)$ as the weighted average of the validity index of all clusters in C. As for the resulting value, it ranges from -1 to +1 with higher values indicating better solutions.

Chapter 2

Observations and Data Reduction

2.1 Observations

As mentioned earlier, the Galactic center is clearly distinguished using infrared radiation, which falls between the optical regime [400 nm – 700 nm] and the microwave regime [1 mm – 1 m]. More specifically, the motion of the S-stars can be traced at best with observations in near-infrared subcategory at a central wavelength of 2.18 mm and width of 0.35 mm (K_s-band) with dust extinction of less than 3 mag. In more detail, the most suitable environment to observe in this range should be very dry and located at high altitudes with atmospheric conditions containing as little water vapor as possible. For instance, the Very Large Telescope (VLT) in the Atacama desert in Chile, from which the data of this work is collected, is considered to be one of the best available options. The VLT is located 2635 m above sea level on Cerro Paranal in the driest desert on Earth; consisting of four Unit Telescopes (UT) with 8.2 m primary mirrors (see Figure 2.1). These UTs serve as an intereferometer, if they're operated together, achieving a very high angular resolution of up to 0.003 arcseconds. Furthermore, the telescopes are complemented by four movable Auxiliary Telescopes (ATs) with 1.8 m aperture. So far, the VLT provided us with many pioneer observations; such as the first direct image of an exoplanet and tracking the motion of stars around the SMBH at the center of the Milky Way.

For this work's analysis, the astrometric coordinates of the S-stars were acquired

Figure 2.1: *An image of the VLT during observations in the Atacama desert in Chile. Image credit: ESO/S. Brunier.*

from adaptive optics-assisted images taken by the NAOS-CONICA (NACO) instrument (see Figure 2.2), where NAOS is short for Nasmyth Adaptive Optic System and CONICA for Coude Near-Infrared Camera (Lenzen et al. (2003); Rousset et al. (2003)). Furthermore, the instrument was installed on the fourth unit telescope from 2001 to 2013 and then on the first unit from 2014 till 2019, and was decommissioned onward. More specifically, the images were obtained by the S13 camera with 13.24 mas/pix scale and the S27 camera with 27.0 mas/pix. In further detail, the NAOS is equipped with both visual and infrared wavefront sensors and 5 dichroic mirrors, where the latter split the light from the telescope between CONICA and NAOS wavefront sensors. In addition, a deformable mirror, which is controlled by a real-time computer, is used to reduce the distortion of the wavefront, which is caused by atmospheric turbulence, instrumental effects and image degradation produced by deviation in the telescope's structure that is triggered by heat, gravity and wind (see Figure 2.3).

The first required step to operate the instrument is to choose an appropriate AO guide source with a magnitude limit of K = 12 mag and a maximum separation of 55″. For the purpose of this work, IRS 7 was chosen as a guide star, located 5.5″ north of Sgr A* with K_s = 6.5 - 7.0 mag. Another possibility for a guide star would be to use laser guide star technique, where an artificial guide source is produced by exciting the Sodium atoms in the mesosphere using a Sodium laser. Another point worth mentioning is that the quality of the image is determined by the so-called Strehl ratio (SR), which is the ratio between the intensity peak of the corrected image and the theoretical point spread function, which represents the observed spread of a point source. Here, better quality images are the ones with higher SR and vice versa for low quality ones. After obtaining the AO-assisted images, further data reduction steps are needed, which are introduced in the following section.

Figure 2.2: *The NAOS-CONICA (NACO) at the VLT in operation in November 2001. Image credit: ESO*

2.2 Data Reduction

Data reduction refers to the required corrections in order to acquire a mosaic image suitable for further analysis. For the images taken by NACO, the data reduc-

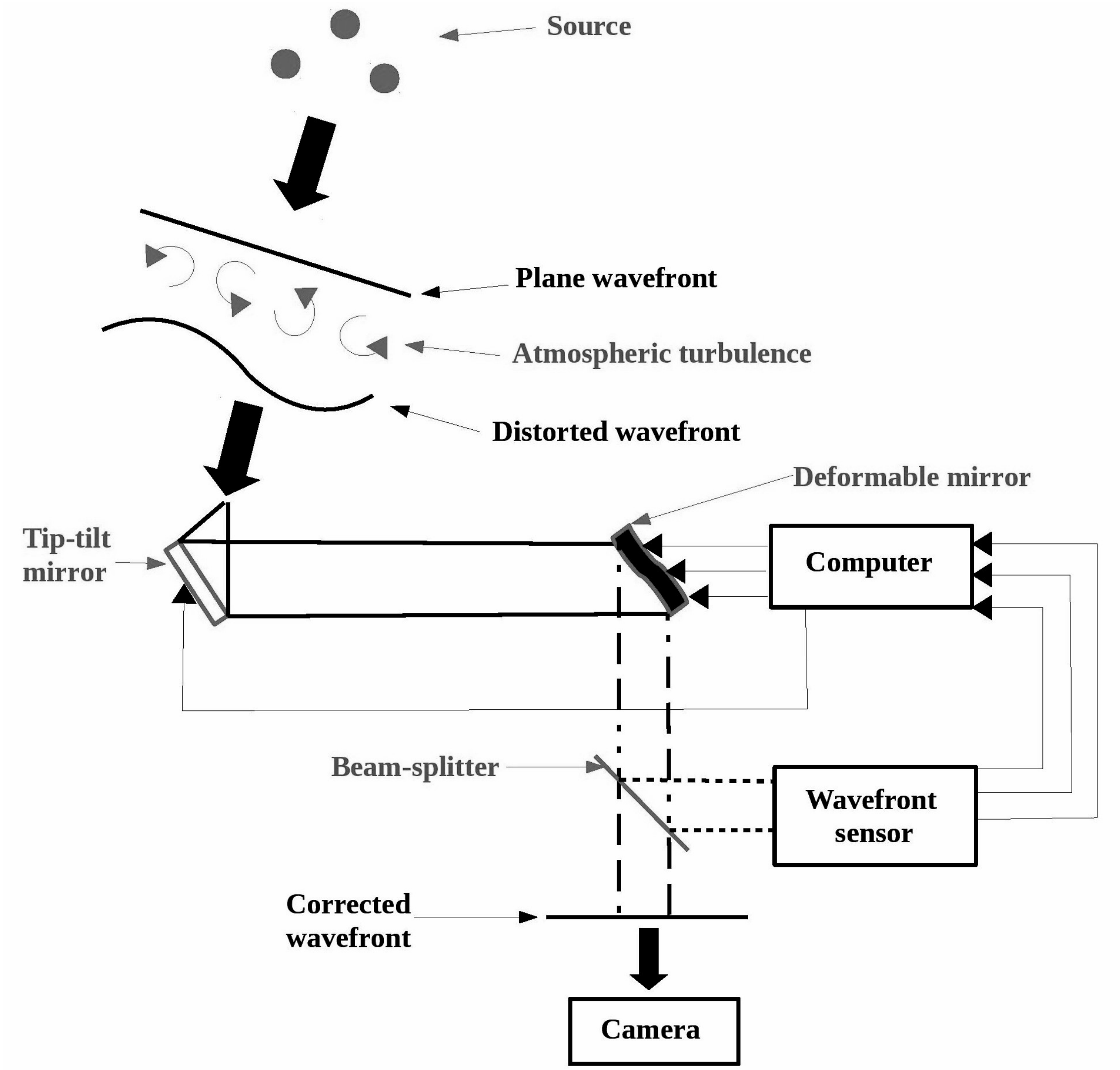

Figure 2.3: *A schematic set up of the adaptive optics system as operated in the NACO instrument.*

tion steps are the following:

2.2.1 Flat-fielding:

Flat-fielding is defined as the correction procedure for anomalies in the optical path, the large scale vignetting profile of the camera, and the small scale quantum efficiency variations in the detector. This step starts by producing images of uniform illuminated field such as the twilight sky of a lamp (on-off). The images are then averaged in case of using the twilight sky or subtracted and averaged when using a lamp. The latter step provides us with a pixel response map, by which the object frame is divided. Consequently, the object frame is flat-fielded and therefore corrected.

2.2.2 Bad and dead pixels' correction:

Bad and dead pixels can be distinguished by zero or relatively higher response value. These pixels heavily degrade the quality of the images and are caused by the manufacturing process. The required correction can be then performed by replacing these pixels with interpolations from neighbouring pixels.

2.2.3 Sky-subtraction:

The final step of data reduction is essential to remove the OH emission of the sky at λ = 2.18 μm. This is done by subtracting the sky frame from the object frame. Since the OH emission is variable, the sky frame has to be taken every 2 hours of on-source observations. In the case of Galactic center observations, which is considered to be a crowded field, the sky frame is obtained by observing a nearby field containing few sources. Reasonably, a dark cloud located at $400''$ north and $713''$ west of the region is chosen for subtraction.
Finally, the reduced images are shifted and stacked in a cube with a mean average to acquire a mosaic image for further analysis.

2.3 Deconvolution

An important post data reduction process is the so-called deconvolution, which helps restore the true point spread function (PSF) of the object. In greater detail, the PSF is the response of our instrument to a point source, which is ideally of an airy pattern. However, due to atmospheric turbulence and other telescope related-issues, the PSF deviates from the optimal pattern. Therefore, deconvolution is essential to remove the effects of convolution in the images. A comparison of several deconvolution methods can be found in Eckart et al. (2005). As for this work's analysis, the Lucy - Richardson (LR) deconvolution is performed on the mosaic images (Lucy (1974); Richardson (1972)). The first step of this procedure is to estimate the PSF by averaging the PSFs of bright and isolated sources such as the nearby IRS stars. This can be done using image processing programs such as StarFinder (Diolaiti et al. (2000)) or QFitsView (Thomas Ott, MPI Garching). Following the estimation of the PSF, the LR iterative algorithm can be run to remove the blurring effect and separate the flux contribution of nearby sources. The details of the algorithm are summarized as follows: Consider an image with intensity distribution I(x,y), which corresponds to observing a real image O(x,y). If one assumes a Poissonian nose, then the likelihood that I(x,y) occurs, given that O(x,y) is true, is defined as follows:

$$P(I/O)(x,y) = \prod_{x,y} \frac{(O(x,y) \circledast PSF(x,y))^{I(x,y)} exp(-O(x,y) \circledast PSF(x,y))}{I(x,y)!}$$

In order to maximize this likelihood, we set the derivative of $ln(P(I/O)(x,y))$ w.r.t $O(x,y)$ to zero, i.e.:

$$\frac{\partial ln(P(I/O)(x,y))}{\partial O(x,y)} = 0$$

Provided that the PSF is normalized, further computation leads to:

$$\frac{I(x,y)}{(O(x,y) \circledast PSF(x,y)} \circledast (PSF(x,y))^* = 1$$

With $(PSF(x,y))^*$ being the transpose of the PSF. Multiplying both sides of the latter equation with $O(x,y)$ gives:

$$O(x,y) = [\frac{I(x,y)}{(O(x,y) \circledast PSF(x,y)} \circledast (PSF(x,y))^*]O(x,y)$$

Using Picard iteration provides the following:

$$O_{n+1}(x,y) = [\frac{I(x,y)}{(O_n(x,y) \circledast PSF(x,y)} \circledast (PSF(x,y))^*]O_n(x,y)$$

Which is the RL equation or expectation maximization with n iterations. The convergence of the algorithm is reached when the maximum likelihood is achieved, which is accomplished with a large number of iterations (n = 10^4). The advantage of this method is that the flux is preserved and the noise amplification effects are reduced by suppressing the high spatial frequencies. On the other hand, a disadvantage can arise when the background resolves into point sources, which can be prevented by knowing the exact positional predictions of the studied sources.

2.4 Positions Extraction

After running the LR algorithm on the S13 camera images, one needs to perform a cross-correlation algorithm to align the dithered exposures. For this purpose, the S27 camera images were used to measure the positions of the SiO maser stars IRS 9, IRS 10EE, IRS 12N, IRS 15NE, IRS 17, IRS 19NW, IRS 28 and SiO-15 (Menten et al. (1997); Reid et al. (2003, 2007)). The latter step is essential to connect the NACO NIR data with the radio reference frame, as they appear in the S27 images but not in the S13 images, which has a narrower field of view. For each epoch, all $K_s - band$ frames of the cluster that showed Sgr A* flaring were included. Furthermore, the reduced data by Witzel et al. (2012) Table 2, Table 1 from Eckart et al. (2013) for the years between 2003 to mid 2010, and Table 1 from Shahzamanian et al. (2015) for the years between 2002 and 2012. In addition, the published data for S2 and S38 by Boehle et al. (2016) for the years 1995-2010 and 2004-2013 were used respectively. Regarding the uncertainty in positional measurements, Plewa et al. (2015) show that the infrared reference frame exhibit neither pumping nor rotation relative to the radio reference frame to within $7.0\ \mu$as $yr^{-1}\ arcsec^{-1}$. Over 20 years this amounts to an upper limit of about 0.14", i.e., 0.1-0.2 mas across the central 1". Therefore, verifying the positional measurements using stars with straight flight paths (S7, S10, S26, S30 and S65) leaves us with an uncertainty of less than 0.5 mas for the S13 camera images.

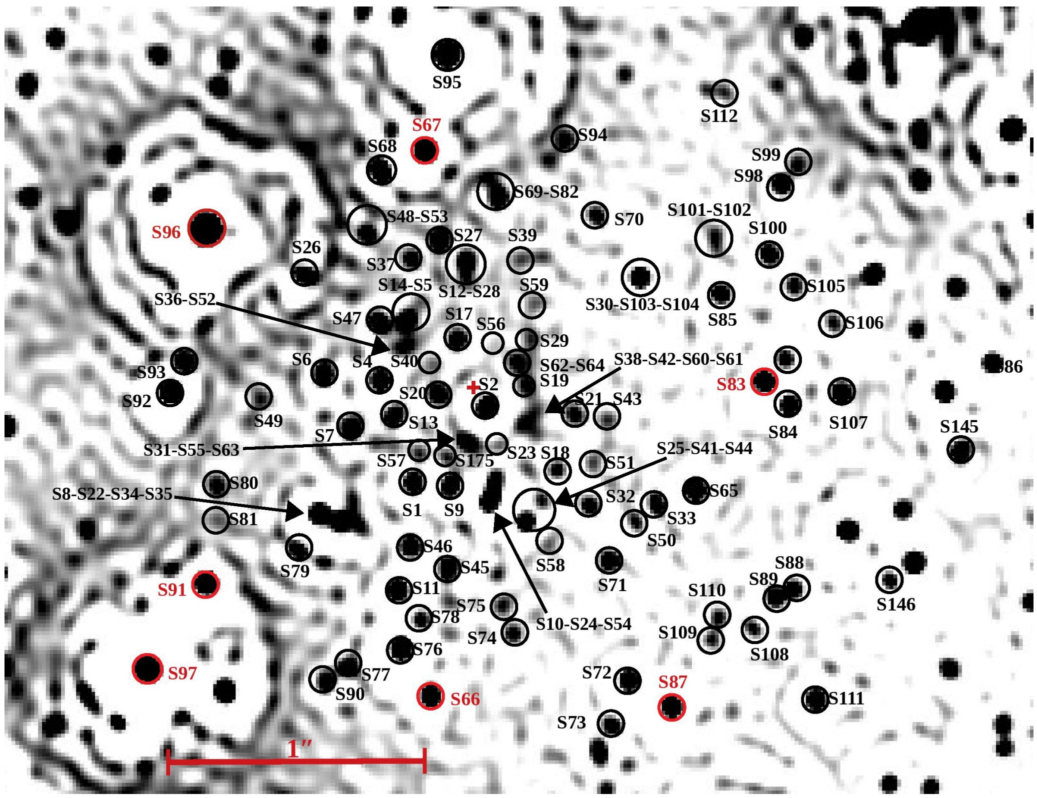

Figure 2.4: *A map of the inner 0.12 pc (3 arcseconds) region showing the S-cluster (black circles) and some neighboring CRD stars (red circles). The image was taken by the NACO instrument at the VLT in early 2018. The relatively wider circles refer to 2 or 3 stars being close together at the epoch of the image. In addition, the location of Sgr A* is located at the position of the red cross. In regard to orientation, east is to the left and north is up.*

Chapter 3

Paper I: Kinematic Structure of the Galactic Center S Cluster

Several studies have been aimed to the determination of the orbits of the S-cluster and studying their dynamics (Eckart et al. (2002); Schödel et al. (2002); Ghez et al. (2003, 2005); Eisenhauer et al. (2005); Gillessen et al. (2009, 2017)). In the current time, the orbits of 32 of these stars were successfully determined with the conclusion that they are moving on randomly oriented orbits based on the orientation of orbital angular momenta (Gillessen et al. (2017)).

In the following paper, I analyze the reduced data by the mentioned co-authors and study their three-dimensional structure. The analysis includes orbital fitting of 39 stars, deriving proper motions for the remaining stars, inspection of the position angles of the projected semi-major axes, and structure identification by means of visual inspection. The first finding in this work is that the both of the inclination angles and positions angles of the projected semi-major axis strongly depart from a uniform distribution. In other words, the distributions show a rather non-random organized state. More specifically, the distribution of the inclinations is concentrated around 90°, revealing an edge-on orientation. Secondly and based on an iterative visual inspection of the orbits in 3D, I find that the 32 S-stars, including 7 stars from the clock-wise rotating disk (CRD), are arranged in two almost edge-on disks located at $\pm 45^\circ$ with respect to the Galactic plane. Each of the two disks contains clockwise and anti-clockwise moving stars. As for the eccentricities, we find that one of the disks shows thermal distribution, while the other peaks around 0.4. Furthermore, we speculate that one of the disks could possibly be an extension of the CRD.

In addition, a detailed dynamical discussion is also included with the main topics being Hills mechanism, resonant and non-resonant relaxation, and Kozai-Lidov cycles. The findings may be the result of all of the latter mentioned dynamical processes and detailed N-body simulations that account for all these dynamical interactions are required for a solid conclusion for the origin of this structure. Moreover, the current configurations imply that there were no major perturtbations in the region in the recent past, as this would cause randomization of the orbits. The paper also contains enhanced graphics that show the motion of the S-stars in 3D and their corresponding disks from several viewing angles. This contribution was done by Anna Luka Höfling, who was an intern in the infrared group at the I. Physikalisches Institut of the University of Cologne.

The Astrophysical Journal, 896:100 (19pp), 2020 June 20 https://doi.org/10.3847/1538-4357/ab93ae
© 2020. The American Astronomical Society. All rights reserved.

Kinematic Structure of the Galactic Center S Cluster

Basel Ali[1], Daria Paul[1], Andreas Eckart[1,2], Marzieh Parsa[1,2], Michal Zajacek[2,3], Florian Peißker[1], Matthias Subroweit[1], Monica Valencia-S.[1], Lauritz Thomkins[1], and Gunther Witzel[2]

[1] I. Physikalisches Institut der Universität zu Köln, Zülpicher Str. 77, D-50937 Köln, Germany; eckart@ph1.uni-koeln.de

[2] Max-Planck-Institut für Radioastronomie, Auf dem Hügel 69, D-53121 Bonn, Germany

[3] Center for Theoretical Physics, Polish Academy of Sciences, Al. Lotnikow 32/46, 02-668 Warsaw, Poland

Received 2019 December 30; revised 2020 March 31; accepted 2020 April 21; published 2020 June 17

Abstract

We present a detailed analysis of the kinematics of 112 stars that mostly comprise the high-velocity S cluster and orbit the supermassive black hole Sgr A* at the center of the Milky Way. For 39 of them, orbital elements are known; for the remainder, we know proper motions. The distribution of the inclinations and the proper motion flight directions deviate significantly from a uniform distribution, which one expects if the orientation of the orbits are random. Across the central arcseconds, the S-cluster stars are arranged in two almost edge-on disks that are located at a position angle approximately $\pm 45°$ with respect to the Galactic plane. The angular momentum vectors for stars in each disk point in both directions, i.e., the stars in a given disk rotate in opposite ways. The poles of this structure are located only about 25° from the line of sight. This structure may be the result of a resonance process that started with the formation of the young B-dwarf stars in the cluster about 6 Myr ago. Alternatively, it indicated the presence of a disturber at a distance from the center comparable to the distance of the compact stellar association IRS 13.

Unified Astronomy Thesaurus concepts: Galactic center (565); Black holes (162); Star clusters (1567); Stellar dynamics (1596)

Supporting material: animation, machine-readable tables

1. Introduction

The Galactic Center (GC) stellar cluster harbors a number of stellar associations with different ages and potentially different origins. The luminous 20–30$M_\odot$ O/WR stars appear to reside in at least one single disk-like structure most likely coupled to their formation process (Levin & Beloborodov 2003; Yelda et al. 2014). Their ages have been derived as 6 ± 2 Myr (Paumard et al. 2006). The S cluster, consisting of lighter 3.5–20 $M_\odot$ stars, contains the 4 million solar-mass supermassive black hole (SMBH, Sgr A*; Parsa et al. 2017; Gravity Collaboration et al. 2018) and appears to be somewhat decoupled from the stellar disk at larger radii. Of $K_s \leqslant 18$ stars that reside with separations of less than 1″ or those stars that have known semimajor axes of less than 1″, the predominant fraction are B stars. This is especially true for the brightest of the stars (Gillessen et al. 2017; Habibi et al. 2017).

Gillessen et al. (2009) also derive the volume density distribution of the the S-cluster B stars. They find for the 15 stars with a semimajor axes of less than 0.″5 in projection a three-dimensional power-law slope of -1.1 ± 0.3. This appears to be marginally larger than the slope derived for a more spread out cluster population of B stars, implying that the S stars form a distinct possibly cusp-like component.

A detailed near-infrared spectroscopic study of the S stars (Ghez et al. 2003; Martins et al. 2008; Habibi et al. 2017) shows that these stars are most likely high-surface-gravity (dwarf) stars The authors' analysis reveals an effective temperature of 21,000–28,500 K, a rotational velocity of 60–170 km s^{-1}, and a surface gravity of $\log g = 4.1$–4.2. These properties are characteristic for stars of spectral-type B0-B3V with masses between 8 $M_\odot$ and 14 $M_\odot$. Their age is estimated to be less than 15 Myr. For the early B-dwarf (B0–B2.5V) star S2 (Martins et al. 2008), the age is estimated to be $6.6^{+3.4}_{-4.7}$ Myr. This compares well with the age of the clockwise-rotating disk (CWD) of young stars in the GC. Habibi et al. (2017) conclude that the low ages for the high-velocity stars favor a scenario in which they formed in a local disk rather than in field binaries subjected to binary disruption and stellar scattering.

The stars in galactic bulges or central stellar clusters often show peculiar kinematic arrangements. From theory (e.g., Contopoulos 1988), observations of external galaxies, and the Milky Way (MW), it has become evident that boxy and peanut-shape stellar orbits have a significant influence on the appearance of galactic bulges. Perturbations in the vertical direction lead to orbits with a boxy appearance (Chaves-Velasquez et al. 2017). Hernquist & Weinberg (1992) also described boxy and disk-like appearances as possible structures in post-merger bulges. Quillen et al. (1997) discovered boxy and peanut-shape bulges in highly inclined galaxies. Quillen et al. (2014) present a simple resonant Hamiltonian model for the vertical response of a stellar disk to the growth of a bar perturbation. As the perturbation grows, the stars become trapped in vertical inner Lindblad resonances and are lifted into higher-amplitude orbits. The vertical structure of a boxy and peanut-shape bulge as a function of radius and azimuthal angle in the galaxy plane can be predicted from the strength and speed of the bar perturbation and the derivatives of the gravitational potential. This model predicts that stars on the outer side of the resonance are lifted higher than stars on the inner side, offering an explanation for the sharp outer edge of the box/peanut.

The MW is a barred galaxy whose central bulge has a box/peanut shape and consists of multiple stellar populations with different orbit distributions (e.g., Gerhard et al. 2016). Infrared observations revealed that the MW bulge shows a boxy/peanut or X-shaped bulge. Simulations indicate that about 20% of the mass of the MW bar is associated with the shape (Abbott et al. 2017).

While these structures are associated with resonances linked to a bar or central cluster potential, they can also be the result of a perturbation due to interacting mass. Gualandris & Merritt (2009) study the short- and long-term effects of an intermediate-mass black hole (IMBH) on the orbits of stars bound to the SMBH at the center of the MW. The authors consider 19 stars in the S-star cluster and an SMBH mass between 400 and 4000 $M_\odot$ and a distance from Sgr A* between 0.3 and 30 mpc. They find that for the more massive perturbers, the orbital elements of the S stars could experience changes at the level of about 1% in just a few years. On timescales of 1 Myr or longer, the IMBH efficiently randomizes the eccentricities and orbital inclinations of the S stars. These results support, on the one hand, that the relatively short-scale response of the S stars to a nearby perturbation can occur. On the other hand, the orbits are clearly not fully randomized, implying that a recent perturbation by massive IMBH within the S cluster can be excluded. Resonances could occur, however, if a perturber is located outside the S cluster.

In Section 2, we present the observations and data reduction. In the discussion in Section 3, we first show in Section 3.1 the histograms and visualizations that highlight our observational results. In Section 3.2, we discuss our findings in terms of stellar dynamical considerations. A summary and conclusions are given in Section 4. Finally, in Section 5, we describe the three enhanced graphics that show the projected orbital arrangements in motion.

2. Observations and Data Reduction

The positions of the S stars are calculated from the AO-assisted imaging data of the GC from 2002–2015 taken by the NAOS-CONICA (NACO) instrument installed at the fourth (from 2001–2013) and then the first (from 2014 on) unit telescope of the Very Large Telescope (VLT).[4] The K_s-band (2.18 μm) images obtained by the S13 camera (with a 13 mas pix^{-1} scale) and the S27 camera of NACO (with a 27 mas pix^{-1} scale) are used. The AO guide star is IRS 7 with $K_s = 6.5$–7.0 mag located at about 5.″5 north of Sgr A*. The data reduction consists of the standard steps like flat-fielding, sky subtraction, and bad-pixel correction. A cross-correlation algorithm is used to align the dithered exposures. We use the 27 mas pix^{-1} scale images to measure the position of the SiO maser stars IRS 9, IRS 10EE, IRS 12N, IRS 15NE, IRS 17, IRS 19NW, IRS 28, and SiO-15 (Menten et al. 1997; Reid et al. 2003, 2007), which were needed to find the connection of the NACO NIR data and the radio reference frame. In order to measure the position of the S stars, the Lucy–Richardson deconvolution algorithm is used to resolve the sources in the 13 mas pix^{-1} scale images. For each epoch, we included all available K_s-band frames of the GC stellar cluster that were taken with a close to diffraction-limited AO correction and showed Sgr A* flaring. We use the reduced data presented by Witzel et al. (2012), Table 2, 2003 to mid-2010, and Eckart et al. (2013), Table 1, and Shahzamanian et al. (2015), Table 1, 2002–2012. We supplemented additional imaging data for observing epochs in 2016, 2017, and 2018 for all sources and further 2019 data for the sources S62, S29, S19, S42, S38, S60. For the stars S2 and S38, we also used the positions published by Boehle et al. (2016) for the years 1995–2010 and 2004–2013, respectively. As described by Parsa et al. (2017; and following the approach by Gillessen et al. 2009), the data were added by applying a constant linear positional shift between the two data sets. In addition, we took into account the mean difference between the proper motions of the VLT and Keck coordinate systems. These differences become evident, e.g., in Table 1 in Gillessen et al. (2017; see also Boehle et al. 2016).

The selected objects comprise all stars brighter than $K_s = 18.0$ that are detectable at all epochs and show no signs of being severely confused with other stars of the cluster for most epochs (see also the discussion by Sabha et al. 2012; Eckart et al. 2013). An overview image is shown in Figure 1. The positional results were verified by using stars S7, S10, S26, S30, and S65 as references as these object have almost straight flight paths with no detectable curvature. For the stars with orbital sections that are short or show no curvature, we fitted a straight line to the flight path.

Plewa et al. (2015) find from the average velocity differences in radial and tangential directions that the infrared reference frame shows neither pumping nor rotation relative to the radio system to within $\sim$7.0 μas yr^{-1} arcsec^{-1}. Over 20 yr, this amounts to an upper limit of about 0.″14, i.e., typically to 0.1–0.2 mas across the central 1″ diameter cluster of high-velocity stars. Hence, verifying the positional measurements using stars with straight flight paths leaves us with an uncertainty of less than 0.5 mas for the 13 mas pix^{-1} scale images.

In addition to the positional measurements that substantially cover sections of the curved orbits as made use of the time variable radial velocities and their uncertainties as presented in Figure 8 by Gillessen et al. (2017).[5] This includes the radial velocity data for S2 from the AO-assisted field spectrometer SINFONI installed on the fourth unit telescope of the VLT and

Table 1
Parameters for the Disk Solutions

i_b	R'	R/R'	μ	ΔR
90	1	3.00	3.0	0.15
90	3.5	1.30	4.0	0.070
90	6.2	1.13	6.6	0.042
90	10.4	1.05	10.7	0.018
0	1	0.77	3.0	0.13
0	3.5	0.90	4.0	0.070
0	7.2	0.97	7.5	0.033
0	11.1	0.98	11.4	0.018

Note. Listed are i_b, the inclination of the stellar disks to the orbit of the perturber; R', the initial ratio of the semimajor axes of the stars in the disk and the perturber; R/R', the current ratio of the stellar disk in relation to the initial ratio; μ, the value of Tisserand's parameter that is expected to be preserved; and ΔR, half the variation width of the current ratio of semimajor axes.

4 Program IDs: 60.A-9026(A), 713-0078(A), 073.B-0775(A), 073.B-0085(E), 073.B-0085(F), 077.B-0552(A), 273.B.5023(C), 073-B-0085(I), 077.B-0014 (C), 077.B-0014(D), 077.B-0014(F), 078.B-0136(A), 179.B-0261(A), 179.B-0261(H), 179.B-0261(L), 179.B-0261(M), 179.B-0261(T), 179.B-0261(N), 179.B-0261(U), 178.B-0261(W), 183.B-0100(G), 183.B-0100(D), 183.B-0100 (I), 183.B-0100(J), 183.B-0100(T), 183.B-0100(U), 183.B-0100(V), 087.B-0017(A), 089.B-0145(A), 091.B-0183(A), 095.B-0003(A), 081.B-0648(A), 091.B-0172(A).

5 This covers S1, S2, S4, S8, S9, S12, S13, S14, S17, S18, S19, S21, S24, S31, S38, and S54.

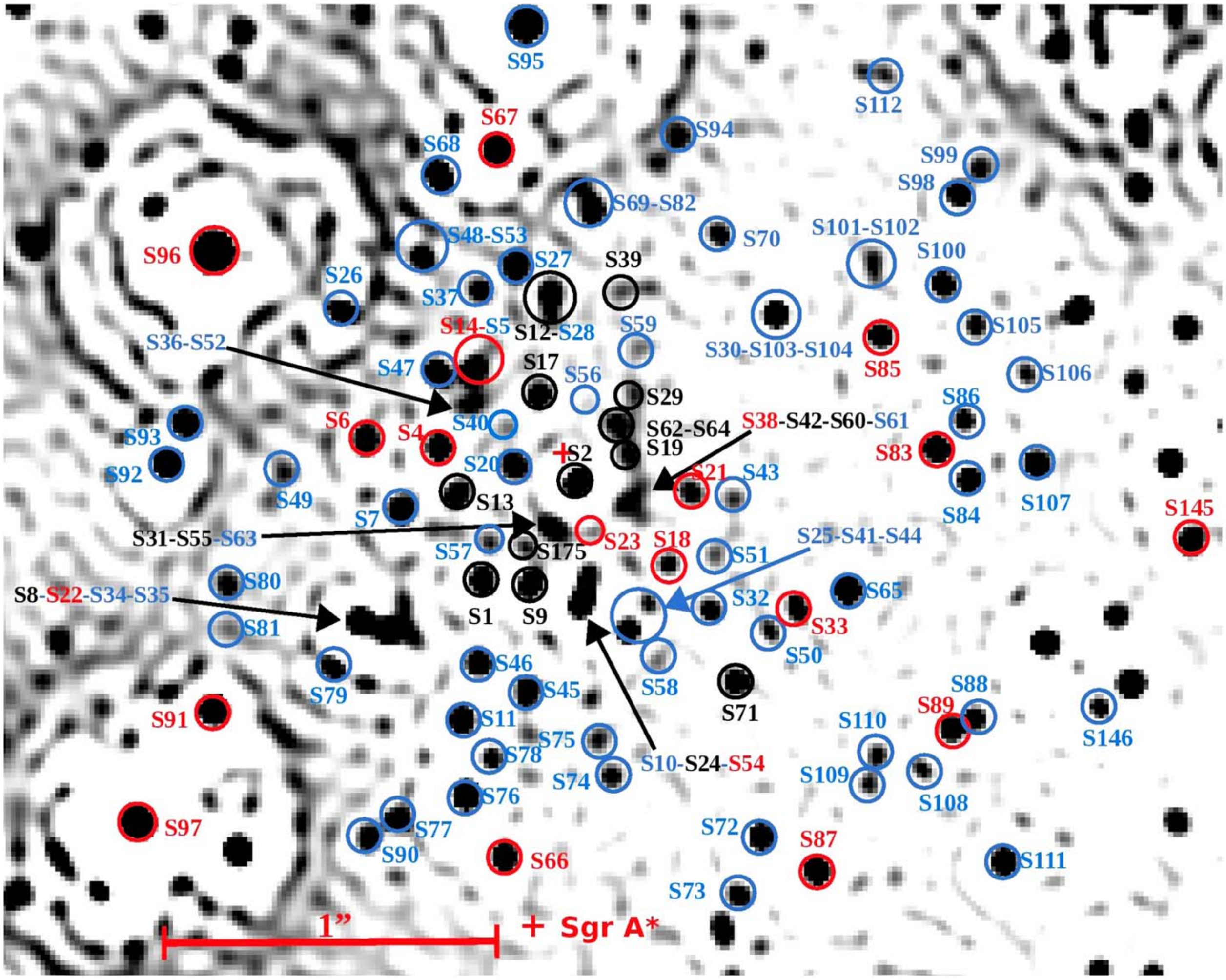

Figure 1. Map of the region showing the S cluster and some neighboring stars. East is to the left, north is up. We included their nomenclature and encircled two or three stars if they happen to be close together at the epoch of the image. The image was obtained by NACO at the VLT in early 2018. Sgr A*, the counterpart of the supermassive black hole, is located at the position of the red cross. Stars encircled by red and black lines belong to the corresponding disk systems described in Section 3. For all of these stars, orbital elements are known. Blue circles mark the stars for which we only have short linear sections of their orbits.

taken from Gillessen et al. (2009). The radial velocity measurements used for S38 are from Boehle et al. (2016).

For the central stars that have larger orbital sections measured, we modeled the Newtonian stellar orbits by integrating the equation of motion using the fourth-order Runge–Kutta method with 12 or 6 initial parameters, respectively (i.e., the positions and velocities in three dimensions). To determine the six orbital elements, a corresponding number of observables must be provided. These are the projected positions α, δ; the proper motions v_α, v_δ; the radial velocity v_z; and the projected orbital acceleration. However, higher order moments of the latter two quantities can also be used as replacements or in support. The results compare favorably with those of the fitting routine starting by solving Kepler's equation, which can be done using the iterative Newtonian method. This optimization method is implemented in Python in the Scipy package under the name Sequential Least Squares Programming. The optimized results along with boundaries on each of the elements are then used for bootstrap resampling to get error estimations. We used a fixed central black hole mass of $4.3 \times 10^6\, M_\odot$ at a distance of 8.3 kpc (Gillessen et al. 2017; Parsa et al. 2017). The results are listed in the appended Tables 2 and 3.

However, we point out that ambiguities in the inclinations of the orbits due to missing radial velocity information do not affect our prime observables as used in Section 3.1.3. These are the directions of the semimajor axes of the sky-projected orbits and the projected true (i.e., three -dimensional) semimajor axes of the orbits. These quantities are listed in Tables 4 and 5. In total, we analyzed 105 S-cluster members and seven sources (S66, S67, S83, S87, S91, S96, S97) that belong to the the clockwise-rotating stellar disk (CWD) of He stars (Levin & Beloborodov 2003; Paumard et al. 2006). This results in our case in 39 stars with orbital elements; for the remaining stars, we fitted straight trajectories. These compare well within the uncertainties with the parameters derived for 40 stars by 29
Gillessen et al. (2017). For a discussion of the organization of S-cluster sources, see also Yelda et al. (2014). For the remaining stars, we just fit a straight line to obtain their proper

Table 2
Orbital Elements for Stars in the Black Disk

Star	a (mpc)	Δa (mpc)	e	Δe	i (deg)	Δi (deg)	ω (deg)	$\Delta\omega$ (deg)	Ω (deg)	$\Delta\Omega$ (deg)	$t_{\rm clos}$ (yr)	$\Delta t_{\rm clos}$ (yr)
1.	2.	3.	4.	5.	6.	7.	8.	9.	10.	11.	12.	13.
S1	22.675	0.257	0.665	0.003	121.066	0.401	109.893	0.458	352.484	0.286	2000.261	0.001
S2	5.034	0.001	0.887	0.002	137.514	0.401	73.416	0.745	235.634	1.031	2002.390	0.020
S8	16.637	0.182	0.768	0.022	75.057	0.573	337.931	2.120	317.075	0.630	1979.216	0.037
S9	11.125	0.030	0.791	0.036	81.876	0.458	137.854	0.573	158.079	0.229	1972.924	0.023
S12	11.962	0.105	0.906	0.003	33.060	0.516	311.173	0.802	236.173	1.146	1995.881	0.001
S13	9.580	1.264	0.415	0.030	24.694	7.219	256.513	11.459	47.842	15.126	2004.015	0.507
S17	13.037	0.794	0.421	0.020	95.799	0.172	319.481	3.495	194.118	1.432	1991.906	0.067
S19	11.122	3.130	0.626	0.090	72.021	2.807	131.093	12.261	337.415	4.469	2004.275	0.004
S24	45.115	7.475	0.682	0.061	95.226	4.240	244.596	3.151	14.381	1.604	2023.963	0.311
S29	34.694	3.803	0.335	0.078	100.955	0.688	331.341	11.975	171.257	1.432	2054.568	4.322
S31	16.582	4.514	0.521	0.151	108.919	10.256	321.487	24.603	145.990	19.882	2019.201	1.132
S39	13.919	2.068	0.831	0.042	86.058	13.002	36.784	9.339	159.282	0.688	1999.108	0.338
S42	38.562	4.057	0.644	0.043	67.666	0.802	37.930	2.578	206.379	1.031	2011.876	0.716
S55	4.360	0.002	0.740	0.010	141.692	1.604	133.499	3.896	129.890	4.183	2009.310	0.030
S60	20.369	1.799	0.832	0.033	130.806	2.979	42.743	11.688	193.774	17.189	2021.883	1.103
S62	3.603	0.002	0.980	0.000	61.765	0.057	45.034	0.057	112.414	0.057	2003.441	0.009
S64	15.952	3.947	0.347	0.161	113.789	2.406	154.985	31.883	165.699	7.047	2005.906	6.192
S71	39.052	1.266	0.916	0.043	67.151	4.354	336.842	2.120	35.466	2.578	1689.433	18.447
S175	29.808	0.001	0.999	0.001	93.793	0.001	65.260	0.001	349.733	0.001	2009.976	0.001

Note. Following the stellar designation in column (1), we list consecutively the following quantities with their uncertainties: semimajor axis, ellipticity, inclination, argument of periapse, longitude of ascending node, and the time of closest approach.

(This table is available in machine-readable form.)

Table 3
Orbital Elements for Stars in the Red Disk

Star	a (mpc)	Δa (mpc)	e	Δe	i (deg)	Δi (deg)	ω (deg)	$\Delta\omega$ (deg)	Ω (deg)	$\Delta\Omega$ (deg)	$t_{\rm clos}$ (yr)	$\Delta t_{\rm clos}$ (yr)
1.	2.	3.	4.	5.	6.	7.	8.	9.	10.	11.	12.	13.
S4	14.555	0.034	0.443	0.014	80.386	0.229	286.823	0.229	259.092	0.229	1954.476	0.011
S6	25.229	0.574	0.891	0.021	86.459	1.490	119.175	0.974	86.116	3.782	1932.803	5.140
S14	9.037	2.426	0.798	0.287	107.716	21.944	378.668	28.904	231.532	19.194	2000.453	3.942
S18	9.253	0.212	0.461	0.017	111.727	4.011	374.084	3.724	54.202	1.833	1997.061	0.006
S21	8.662	0.162	0.772	0.016	59.530	1.891	161.173	3.266	262.930	0.917	2027.290	0.017
S22	52.357	2.553	0.489	0.062	106.914	0.859	94.366	15.756	289.859	3.953	1996.959	5.234
S23	10.389	1.945	0.462	0.205	47.326	6.303	30.882	13.980	249.638	26.986	2024.577	8.064
S33	31.326	4.263	0.664	0.059	64.057	1.891	304.183	2.464	107.086	4.412	1923.847	11.286
S38	5.598	0.205	0.812	0.050	157.774	15.011	11.001	9.626	96.375	8.308	2003.406	0.339
S54	48.225	10.890	0.897	0.018	58.384	2.120	151.891	4.641	254.164	5.672	2002.326	0.042
S66	61.777	2.985	0.160	0.028	126.738	1.432	144.271	7.850	87.892	2.292	1794.519	13.396
S67	47.708	1.938	0.082	0.045	131.895	2.292	226.548	4.469	79.756	5.042	1740.000	15.852
S83	58.717	4.729	0.377	0.048	125.592	1.261	207.697	7.391	87.433	7.506	2049.789	14.833
S85	184.115	3.611	0.773	0.006	85.084	1.089	157.907	4.183	107.544	0.974	1930.384	8.658
S87	109.645	1.066	0.163	0.060	117.514	1.662	334.779	3.610	105.367	2.578	627.690	12.927
S89	42.801	2.027	0.651	0.224	91.731	1.490	123.644	1.089	234.282	1.547	1777.211	21.179
S91	78.892	1.958	0.322	0.034	113.560	2.005	366.120	4.870	101.643	2.636	1086.879	21.025
S96	54.529	1.070	0.289	0.078	127.712	2.865	238.179	5.730	121.582	4.927	1688.413	22.780
S97	92.859	2.783	0.382	0.033	112.300	1.891	38.503	4.354	109.148	2.177	2161.556	14.970
S145	42.278	0.501	0.550	0.016	83.136	7.506	177.388	2.406	263.904	0.229	1808.606	4.260

Note. Following the stellar designation in column (1), we list consecutively the following quantities with their uncertainties: semimajor axis, ellipticity, inclination, argument of periapse, longitude of ascending node, and the time of closest approach.

(This table is available in machine-readable form.)

30

Table 4
Position Angles of the Black Disk

Star	$m1(t$, R.A.) (mas yr^{-1})	$\Delta m1$ (mas yr^{-1})	$m2(t$, decl.) (mas yr^{-1})	$\Delta m2$ (mas yr^{-1})	Φ (deg)	$\Delta\Phi$ (deg)
1.	2.	3.	4.	5.	6.	7.
S1	0.767	0.086	8.710	0.086	5.035	0.562
S2	1.608	0.951	−21.019	0.951	175.624	2.584
S8	−14.616	0.233	14.989	0.233	−44.278	0.637
S9	−10.771	0.472	22.951	0.472	−25.141	1.066
S12	4.253	0.292	17.785	0.292	13.450	0.914
S13	0.678	0.334	−17.274	0.334	177.751	1.108
S17	−5.771	0.319	−22.271	0.319	−165.473	0.795
S19	−5.404	0.241	12.290	0.241	−23.735	1.030
S24	2.820	0.068	13.475	0.068	11.820	0.284
S29	−1.500	0.054	10.578	0.054	−8.070	0.289
S31	−6.491	0.159	12.484	0.159	−27.471	0.646
S39	4.367	0.195	−12.792	0.195	161.153	0.826
S42	7.952	0.076	13.161	0.076	31.141	0.282
S55	−4.814	1.328	28.810	1.328	−9.487	2.605
S60	−2.209	0.163	16.687	0.163	−7.542	0.556
S62	15.992	1.793	−20.849	1.793	142.511	3.910
S64	3.155	0.173	−15.407	0.173	168.428	0.630
S71	−5.393	0.049	−9.191	0.049	−149.594	0.264
S175	1.688	0.079	−5.430	0.079	162.729	0.7912

Note. Following the stellar designation in column (1), we list consecutively the following quantities with their uncertainties: slopes of the R.A. and decl. data as a function of time and the corresponding position angles ϕ.

(This table is available in machine-readable form.)

Table 5
Position Angles of the Red Disk

Star	$m1(t$, R.A.) (mas yr^{-1})	$\Delta m1$ (mas yr^{-1})	$m2(t$, decl.) (mas yr^{-1})	$\Delta m2$ (mas yr^{-1})	Φ (deg)	$\Delta\Phi$ (deg)
1.	2.	3.	4.	5.	6.	7.
S4	−22.725	0.305	−4.321	0.305	−100.766	0.755
S6	−14.624	0.161	−1.734	0.161	−96.761	0.628
S14	−17.048	0.510	−15.601	0.510	−132.461	1.265
S18	18.905	0.443	13.206	0.443	55.064	1.101
S21	26.326	0 .557	5.246	0.557	78.730	1.189
S22	−5.898	0.024	1.998	0.024	−71.287	0.219
S23	22.507	0.392	2.768	0.392	82.990	0.990
S33	15.026	0.100	−1.445	0.100	95.493	0.378
S38	29.086	0.919	1.432	0.919	87.182	1.809
S54	11.014	0.048	5.224	0.048	64.624	0.228
S66	−9.965	0.028	−0.174	0.028	−91.001	0.161
S67	10.856	0.044	0.054	0.044	89.715	0.232
S83	9.884	0.029	2.013	0.029	78.486	0.166
S85	4.688	0.005	−1.380	0.005	106.407	0.058
S87	−5.897	0.010	2.186	0.010	−69.664	0.094
S89	11.564	0.067	8.097	0.067	55.001	0.274
S91	−7.563	0.017	0.848	0.027	−83.604	0.128
S96	8.376	0.026	−2.054	0.026	103.781	0.174
S97	−7.486	0.013	1.026	0.013	−82.195	0.101
S145	11.179	0.046	1.170	0.046	84.023	0.235

Note. Following the stellar designation in column (1), we list consecutively the following quantities with their uncertainties: slopes of the R.A. and decl. data as a function of time and the corresponding position angles ϕ.

(This table is available in machine-readable form.)

31

Table 6
Position Angles of the Linear Stellar Trajectories

Star 1.	$m1(t, \text{R.A.})$ (mas yr^{-1}) 2.	$\Delta m1$ (mas yr^{-1}) 3.	$m2(t, \text{decl.})$ (mas yr^{-1}) 4.	$\Delta m2$ (mas yr^{-1}) 5.	Φ (deg) 6.	$\Delta\Phi$ (deg) 7.
S5	−6.121	0.207	7.610	0.318	−38.813	1.502
S7	−3.768	0.063	−1.826	0.117	−115.849	1.494
S10	−4.823	0.090	3.667	0.059	−52.752	0.677
S11	8.486	0.152	−4.849	0.241	119.743	1.303
S20	−4.661	0.203	−5.363	0.214	−139.005	1.675
S25	−2.441	0.105	1.724	0.181	−54.768	3.063
S26	5.700	0.131	1.930	0.157	71.292	1.475
S27	0.215	0.143	3.609	0.173	3.416	2.261
S28	4.381	0.412	5.065	0.392	40.860	3.452
S30	0.318	0.102	3.296	0.098	5.504	1.757
S32	−3.609	0.125	−0.199	0.238	−93.150	3.774
S34	9.899	0.209	4.441	0.156	65.837	0.876
S35	1.834	0.097	3.727	0.187	26.197	1.656
S36	0.268	0.246	−1.360	0.431	168.848	10.561
S37	−6.324	0.351	9.605	0.283	−33.359	1.653
S40	4.172	0.585	5.165	0.935	38.929	6.414
S41	1.331	0.130	−3.197	0.182	157.405	2.302
S43	5.119	0.177	6.135	0.430	39.839	2.201
S44	−6.662	0.559	−8.450	0.589	−141.746	3.038
S45	−5.688	0.162	−4.037	0.117	−125.363	1.100
S46	0.966	0.186	4.566	0.161	11.950	2.268
S47	−3.058	0.448	2.789	0.186	−47.633	4.594
S48	−1.626	0.212	10.040	0.418	−9.198	1.238
S49	15.222	0.268	−0.760	0.664	92.859	2.494
S50	−1.370	0.362	10.459	0.327	−7.462	1.963
S51	8.422	0.509	7.655	0.397	47.730	2.273
S52	4.627	0.501	−5.721	0.298	141.033	3.369
S53	7.096	0.366	9.465	0.504	36.860	2.039
S56	−18.748	0.685	−1.319	0.411	−94.026	1.259
S57	−9.770	0.521	−0.312	0.360	−91.828	2.112
S58	7.686	0.356	5.449	0.202	54.667	1.603
S59	7.458	0.375	−1.606	0.342	102.154	2.579
S61	−4.487	0.561	−6.718	1.017	−146.258	5.195
S63	−13.15	0.847	4.335	0.549	−71.755	2.419
S65	2.401	0.097	−1.616	0.124	123.940	2.305
S68	3.971	0.236	3.108	0.148	51.946	2.119
S69	−1.786	0.207	2.052	0.558	−41.037	8.384
S70	−4.141	0.235	−3.600	0.263	−131.006	2.626
S72	9.101	0.200	−5.645	0.133	121.811	0.825
S73	−9.223	0.245	−7.771	0.156	−130.115	0.941
S74	−0.170	0.209	5.026	0.242	−1.941	2.380
S75	7.138	0.249	2.330	0.321	71.921	2.404
S76	−3.329	0.182	4.898	0.161	−34.201	1.700
S77	9.536	0.439	−6.606	0.524	124.711	2.460
S78	−16.728	0.429	−5.989	0.360	−109.697	1.190
S79	0.040	0.218	4.269	0.449	0.536	2.932
S80	−4.640	0.221	6.325	0.435	−36.261	2.288
S81	5.072	1.908	6.529	0.739	37.842	10.906
S82	−8.689	0.329	−14.942	0.373	−149.821	1.128
S84	3.926	0.084	1.282	0.218	71.916	2.903
S86	−0.892	0.308	−4.872	0.392	−169.627	3.601
S88	−3.941	0.265	−7.715	0.227	−152.939	1.702
S90	1.713	0.349	1.266	0.228	53.536	7.452
S92	5.530	0.095	2.238	0.303	67.966	2.718
S93	−2.972	0.349	−1.755	0.374	−120.553	6.099
S94	−13.564	0.513	2.089	0.735	−81.243	3.052
S95	5.273	0.295	0.987	0.101	79.402	1.208
S98	−7.985	0.186	1.922	0.284	−76.465	1.947
S99	−10.093	0.459	0.240	0.336	−88.638	1.906
S100	−1.392	0.202	−2.557	0.200	−151.432	3.969
S101	2.168	0.422	5.836	0.400	20.376	3.864
S102	−5.376	0.594	8.018	0.512	−33.842	3.380

Table 6
(Continued)

Star 1.	$m1(t$, R.A.) (mas yr^{-1}) 2.	$\Delta m1$ (mas yr^{-1}) 3.	$m2(t$, decl.) (mas yr^{-1}) 4.	$\Delta m2$ (mas yr^{-1}) 5.	Φ (deg) 6.	$\Delta\Phi$ (deg) 7.
S103	11.849	0.405	−3.727	0.736	107.463	3.288
S104	10.255	0.344	−2.270	0.507	102.481	2.733
S105	3.908	0.336	−7.620	0.482	152.849	2.484
S106	1.135	0.275	−0.981	0.570	130.845	17.841
S107	−0.580	0.112	4.581	0.228	−7.217	1.426
S108	3.868	0.420	0.449	0.422	83.377	6.208
S109	7.021	0.374	−4.926	0.278	125.050	2.089
S110	−2.956	0.267	−1.221	0.251	−112.442	4.534
S111	−2.490	0.245	−7.337	0.255	−161.253	1.819
S112	3.062	0.439	10.822	0.341	15.797	2.205
S146	−3.465	0.905	−0.189	0.986	−93.118	16.281

Note. Following the stellar designation in column (1), we list consecutively the following quantities with their uncertainties: slopes of the R.A. and decl. data as a function of time and the corresponding position angles ϕ.

(This table is available in machine-readable form.)

motion speed and direction. Their inclusion in the presented discussion awaits the determination of orbital elements. For completeness, we list the kinematic properties of these stars in the appended table (appended Table 6).

3. Discussion

A close inspection of the orbital parameters showed that the stars in the central arcseconds are arranged in two orthogonal disks. There are three observational facts that support this finding:

1. The distribution of inclinations clustering around 90°. This shows that stellar orbits are seen preferentially edge on.
2. The distribution of semimajor axes of the projected ellipses in the sky shows that the stars populating the disks can indeed be separated into two groups.
3. The observation of accumulation of orbits that appear face on or edge on from certain directions shows the presence of two orthogonal stellar disks.

In the following, we describe these findings in more detail and then highlight present stellar dynamical concepts that may explain the phenomenon.

3.1. Histograms and Visualizations

3.1.1. Orbital Inclinations

In Figure 2, we show that the inclinations derived by us and those provided by Gillessen et al. (2017) are in very good agreement. The same can be said for all of the other orbital elements shown in Figure 2. In Figure 3, we show the distribution of all 39 stars with orbital fits in comparison to a sin i distribution as one might have expected for a fully uniformly randomized scenario. Here, sin i refers to the expected shape of the uniformly distributed inclination angles and not the trigonometric sine function of the angle. This ideal shape is also referred to as the Gilbert-sine distribution (Gilbert 1895). In Figure 3, both distributions are normalized to an integral value of unity. Compared to the sin i distribution, the measured distribution shows a deficit of stars with inclinations in the intervals 0°–20° and 160°–180°. It also has a full width at half-power of around only 80°, although one would expect a width of about 100° for a sin i distribution. In addition, the measured distribution shows an excess of stars around inclinations of 80°–140°. The preference for high inclinations can also not be due to a field-of-view effect due to the small size of the S cluster within the large GC stellar cluster (see Appendix A). Also, biases for the orbital elements due to incomplete orbital coverage are not important for the analysis of our problem (see Appendix B). Hence, this comparison shows that in the set of 39 S-cluster stars, edge-on orbits are preferred.

3.1.2. Distribution of Orbits in Space

In Figure 4, we show the three-dimensional distribution of the orbits. In all projections, the two organization of two orthogonal disks (black and red) of the stars is apparent. The coloring is based on visual inspection of perpendicularity in three dimensions. In Figures 4(a)–(d), we show the orbits using the complete set of orbital elements. In Figures 4(e)–(h), we show the circularized orbits after the eccentricity had been set to zero and the long orbital axes had been set to a constant value. In this version, only the orbital angles are preserved and the bunching into orbital families becomes most apparent. In Figures 4(a) and (e), the face-on view as seen from Earth is presented. In this case, the black orbital family is seen almost edge on. In Figures 4(b) and (f), the set of orbits has been rotated by 25° from elevations −90° to −115°. Here, the two orbital families are both seen edge on. In Figure 5, we show a smoothed version of the pole vision for the circularized orbits in Figure 4(f). Here, the X-shape structure of the two disks can be seen more clearly. In Figures 4(c) and (g), the set of orbits has been rotated by −100° in azimuth (keeping the elevation at 0). In this case, the black orbital family is seen face on while the red orbital family is edge on. In Figures 4(d) and (h), we rotated to elevation −25° (and azimuth at 0°) such that the red system is then seen face on and the black system is edge on.

The two orbital disk systems are well separable (see above) but rather thick. Furthermore, the orthogonal X-shaped disk structure becomes apparent only in alternating zones in the position angle histogram (see Figure 8) and in Ω diagrams as well (see Figure 6). This leads to the fact that they cannot easily

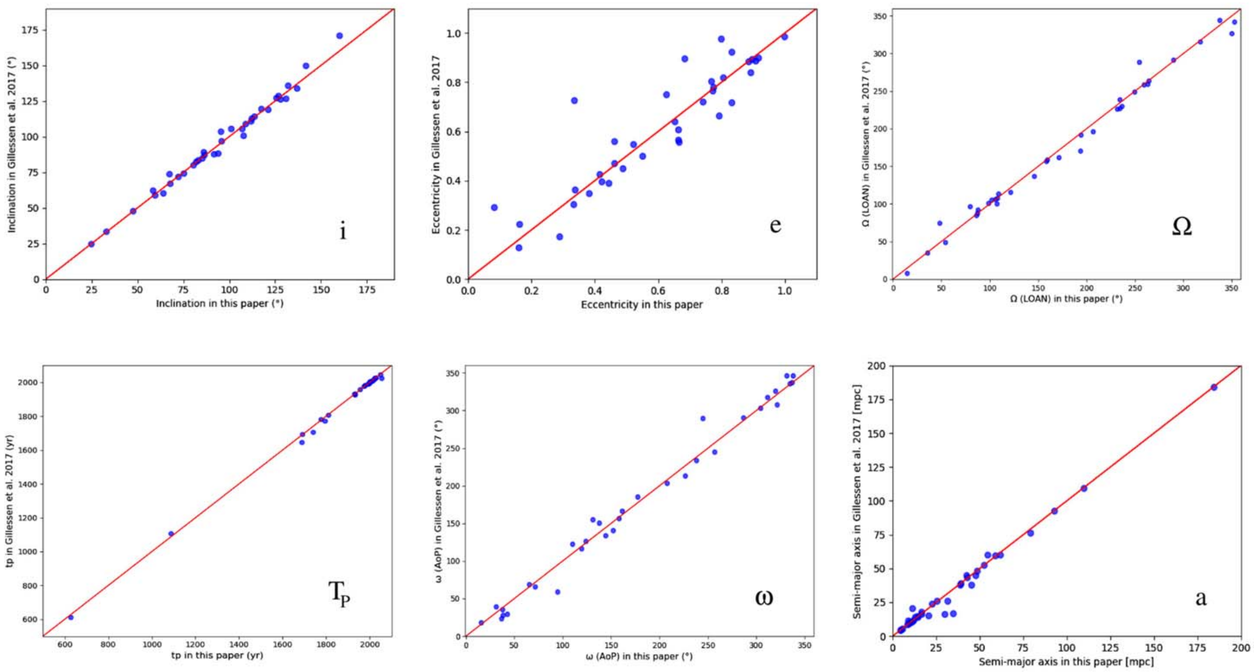

Figure 2. A comparison between the orbital elements listed by Gillessen et al. (2017) and in this paper.

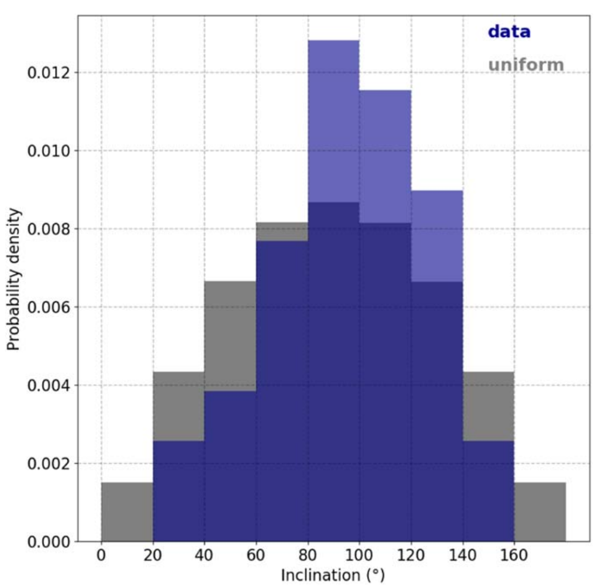

Figure 3. A comparison between the measured distribution of orbital inclinations and the expected sin i distribution.

be recognized in polar diagrams as used by, e.g., Gillessen et al. (2017) in their Figure 12 or Yelda et al. (2014) in their Figure 21. In Figure 6, we show the inclination of the stars as a function of the longitude of the ascending node Ω. The color indicates their membership in either the red or the black disk. It becomes clear that the two disks cannot easily be identified as the angular momentum vectors of the disk members point in opposite directions. Comparing Figure 8 and Figure 6, one can also see that the two disks can be better separated by evaluation in the position angle histogram instead of evaluating the longitude of the ascending node Ω.

However, compared to Figure 6, the inclined and face-on representations of the disk members as shown in Figure 4 are better grouped together, because the direction of the angular momentum vector is not relevant in this representation.

Here, looking at circularized orbits as described above is more successful in searching for face-on orbits that bunch close to the circumference of the sky-projected distributions as in Figures 4(g) or (h).

In Figures 7(a) and (b), we show the inclinations of the two stellar systems. On the right-hand side of Figure 7, we show the distribution of inclinations for all stars within the central acrseconds for which we can provide Newtonian orbital fits. In particular, the distributions for the two disks do not follow a sin i distribution as one might have expected for a fully randomized scenario. There is a clear clustering of inclinations around a mean value of $\sim 90°$ with the bulk of the higher inclined stellar orbits contained within an interval width of 50° (red disk with bulk between 80° and 130°) or even a width of only 40° (black disk with bulk between 70° and 110°). In comparison to the expected width of about 100° for a sin i distribution, this implies that the two separate disk are highly biased toward high inclinations. There are also no stars with inclinations in the intervals 0°–20° and 160°–180°.

It follows that the S-cluster stars for which we obtained orbits are organized in two highly inclined disk systems that are arranged in an X shape.

3.1.3. Distribution of Orbits in the Sky 34

As most stars have high inclinations, the relative orientation of their orbits in the sky can be investigated by comparing the

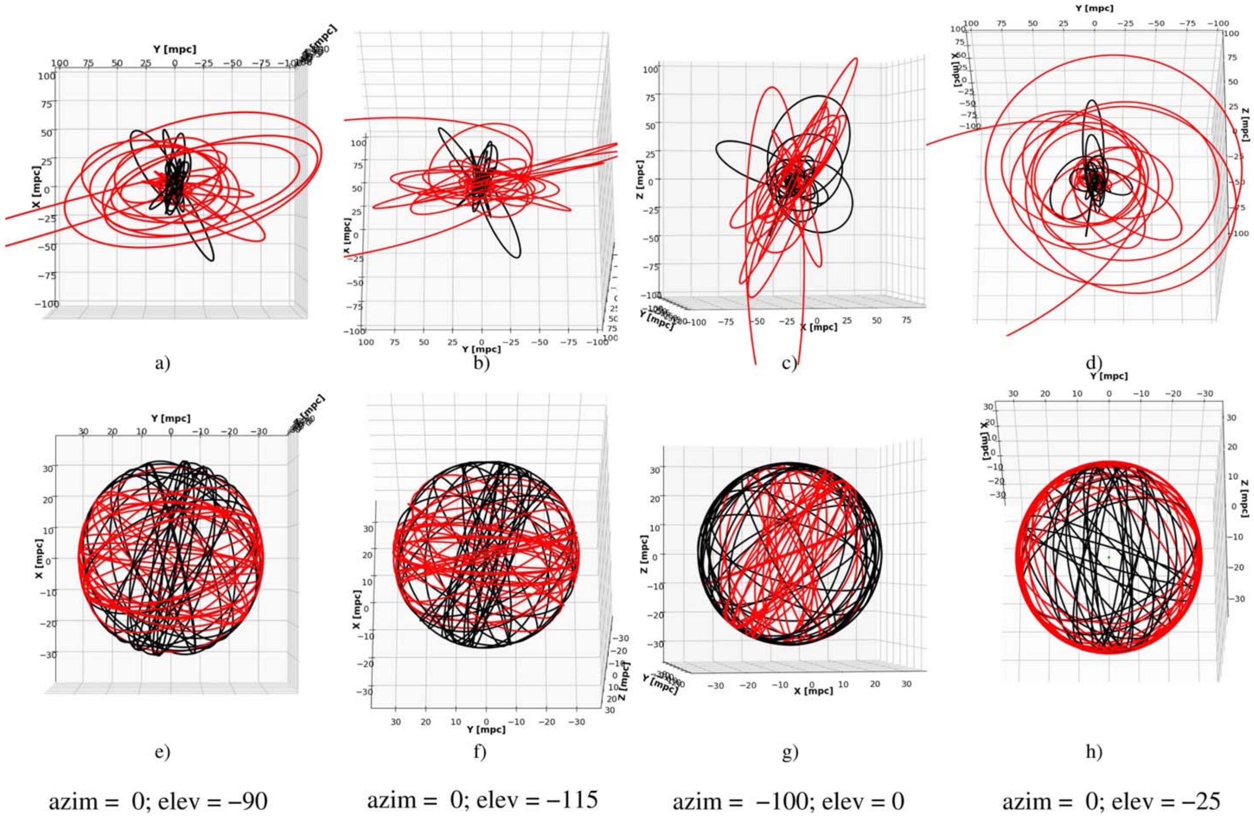

Figure 4. Visualizations of the distribution of all 39 orbits of the S-cluster stars. In the top row, the orbital elements as derived from the observational data are used. In the bottom row, the ellipticities have been set to zero and the semimajor axes have been set to a constant value. Hence, only the orientation angles of the orbits are relevant for the visualization. The azimuthal and elevation angles for the corresponding projections are given. Panels (a) and (e) show the line-of-sight view as observed. Panels (b) and (f) show both disk systems seen edge on. In (c) and (g), the orbits of the black system are face on, and those of the red system are edge on. Finally, panels (d) and (h) show the red system face on, the black system edge on. We refer also to the animation that shows the projected orbital arrangements in motion in Figure 17.

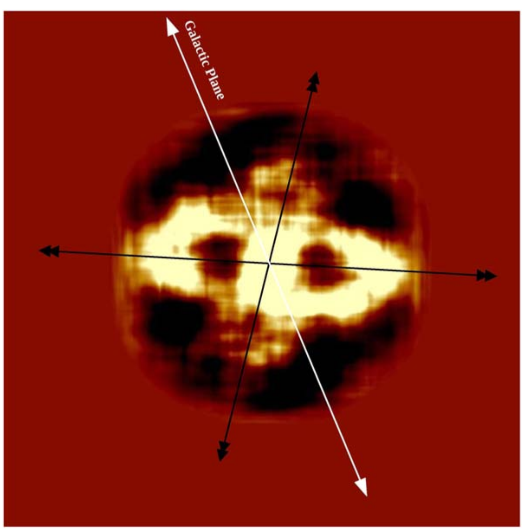

Figure 5. Smoothed representation of the pole vision image of the circularized orbit distribution shown in Figure 4(f). We subtracted the distribution expected from 39 randomly oriented orbits. Here the 39 orbits are generated, assuming a sin i uniform distribution for the inclinations, and a circular uniform distribution of the longitude of ascending node after setting $e = 0$ and $a = \text{const}$. As in Figure 4(f), the black lines indicate the directions of the disks and the white line the direction of the Galactic plane.

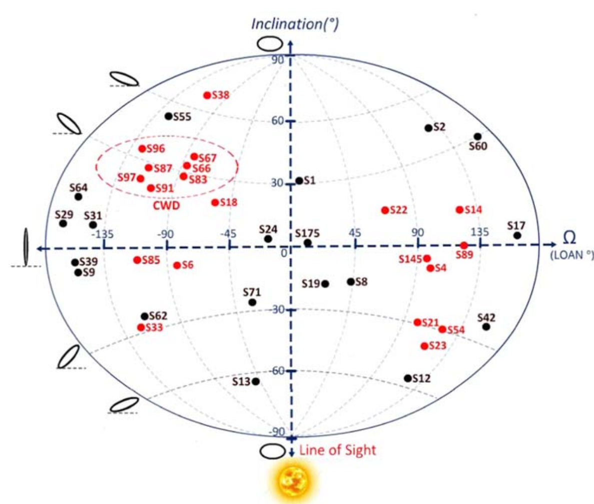

Figure 6. The inclination as a function of the (LOAN) longitude of the ascending node Ω.

35

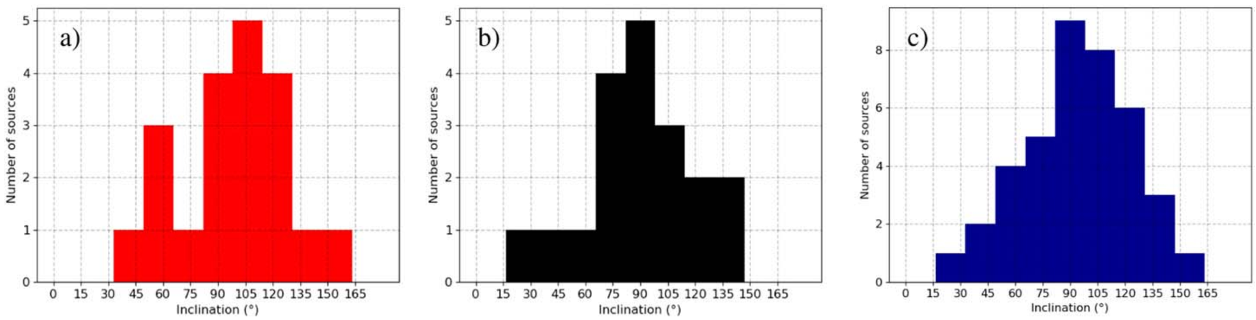

Figure 7. Inclination angles of all 39 stars with known orbits. We find that most of the orbits are highly inclined and seen almost edge on. (a) Red disk: inclination angles of all 20 stars, which orbit in the east–west disk. (b) Black disk: inclination angles of all 19 stars, which orbit in the north–south disk. (c) All stars in a combined histogram.

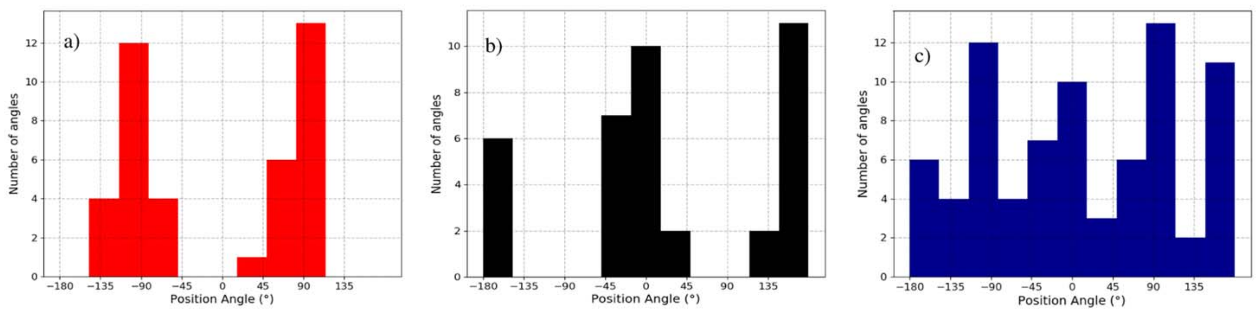

Figure 8. The distributions of the position angles of the semimajor axes of the sky-projected orbits show that the orbits of the stars in the red and black systems are orthogonal to each other. (a) Position angles of the 19 stars, which orbit in the black north–south disk. (b) Position angles of the 20 stars, which orbit in the red east–west disk. (c) Position angles of all 39 stars with known orbits.

position angles of the semimajor axes of their sky-projected orbits.

In Figure 9(a), we show the position angles of the sky-projected orbital ellipses in a circular histogram. The orthogonal red and black orbital families are apparent. In Figure 9(b), we show the same diagram consisting of lines indicating the same position angles but now smoothed with a circular Gaussian with a width corresponding to about one-fifth of the line length. Here, the representation of the line density is enhanced. Both stellar disks have an angle of about 45° with respect to the Galactic plane.

The stars can clearly be separated into two groups (black and red) that form two stellar disks oriented almost perpendicular to each other. In Figure 8, we show how the position angles of the projected orbits are distributed for the two disks and for all of the 39 stars. Each of the position angles is supplemented by a second angle separated by 180°. Through this we account for the fact that the stars will ascend and descend on their highly elliptical orbits. The total number of angles considered in Figure 8 is 78.

The red disk clusters around $\pm 90°$, while the black disk is concentrated around the angles 0° and $\pm 180°$. In order to investigate the statistical significance of this arrangement, we need to apply methods that have been developed for directional statistical analysis. Starting with the multimodal distribution of position angles, we can apply Rao's spacing test (Jammalamadaka & SenGupta 2001). The test is based on the idea that if the underlying distribution is uniform, then the observation of N successive directions should be approximately evenly spaced. They should show an angular separation of about $360°/N$. Large deviations from this distribution, resulting from unusually large spaces or unusually short spaces between the observed directions, are evidence for directionality. The test is more powerful than the Rayleigh test (Durand & Arthur 1958) when it comes to multimodal distributions. After placing all 78 position angles on a circle, we performed the test and the resulting p-value is 0.01 with a test statistic of 154.12 and a critical statistic of 152.46, allowing us to reject the hypothesis that the distribution is uniform. In addition, we performed the Hodges–Ajne test (Ajne 1968; Bhattacharayya & Johnson 1969) for uniformity of a circular distribution. The test is based on the idea that if the number of points in an arc exceeds the expected number for a uniform distribution, then the hypothesis is rejected. The implemented Hodges–Ajne test in Python returns either 1 or 0 as a p-value. Applying it to our position angle distribution, we obtained a p-value of 0.

Hence, they can be separated very well. Thanks to the high inclination of the orbits, the pole of this distribution (i.e., the region where most orbits cross each other) is close to the line of sight and the two stellar systems can be separated even in their direct projected appearance in the sky. The same can be done with the projection of the semimajor axes of the three-dimensional orbits, as shown in Figure 9(c). To get a clear view, we rotate the orbital arrangement close to the pole vision

36

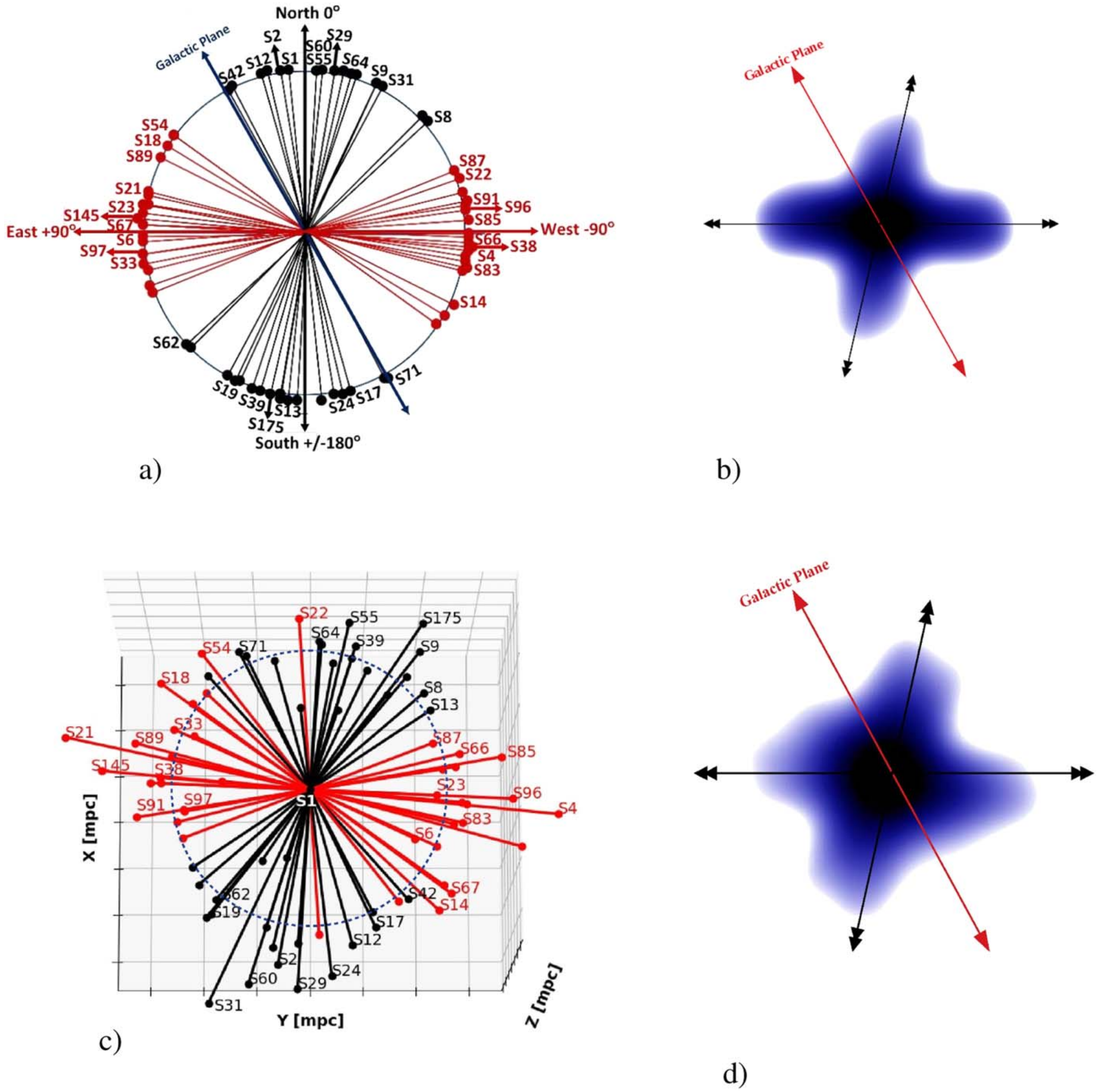

Figure 9. Angular arrangement of the disks for all 39 stars for which we have orbital solutions. We labeled the lines for all stars. (a) Here we show for all stars the position angles of the semimajor axes of their sky-projected orbits. The shape of the two disks is remarkably clear. (c) The position angles of the projected semimajor axes of the three-dimensional orbits of all stars after rotation close to the pole vision of the system. The X shape is observed in the range between elevation $-90°$ and $-115°$ but most clearly close to elevation $-100°$. The two disks are well separable. (b) and (d) are the same as in (a) and (c), but smoothed with a circular Gaussian of a width corresponding to about one-fifth of the line length in figure section (a) and (c). For (d), only the position angle line in (c) inside the dashed circle has been used for the convolution.

and use the projected semimajor axes of the orbits. The smoothed version of the distribution is shown in Figure 9(d).

We note that the trend of having two orthogonal disks is probably also continued toward stars with separations to Sgr A* smaller than those of the star S2. The recently found high-velocity star S62 (Peißker et al. 2020) lies to within 30° close to the black disk. This star has separation from Sgr A* ranging between 17.8–740 au, compared to S2 with 120–970 au. We expect to find stars close to the red disk with similarly short periods and small distances to Sgr A*.

This shows that the highly inclined stellar orbits can indeed be separated into two groups that represent two orthogonal disks.

3.1.4. Orbital Eccentricities

Gillessen et al. (2017) find that the distribution of
eccentricities of the S-star cluster is thermal, which is in 37
agreement with Figure 10(c). However, this obviously does not necessarily imply that the orbits are randomly oriented. The two disk systems show that the S-star cluster is highly

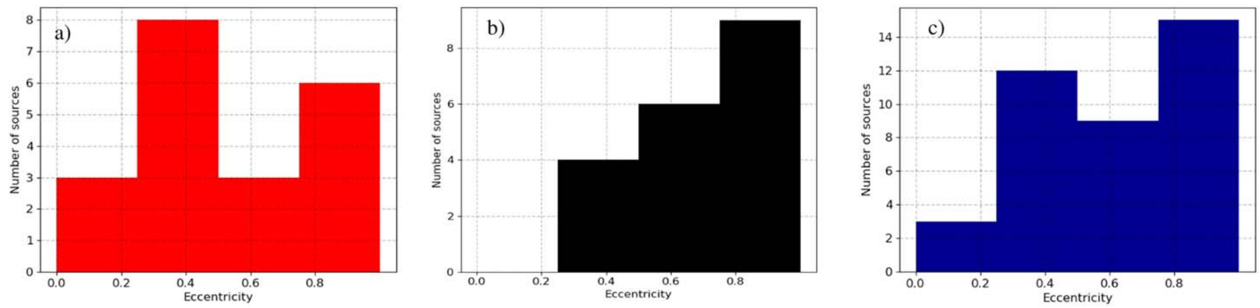

Figure 10. (a) Eccentricities of the 20 stars, which orbit in the red east–west disk. (b) Eccentricities of the 19 stars, which orbit in the black north–south disk. (c) Eccentricities of all 39 stars with known orbits (including the seven exmembers).

organized. In Figures 10(a) and (b), we show the histogram of eccentricities for the two disk systems. There are only about half the number of sources in the individual histograms; however, within the uncertainties, we find at least for the black disk a distribution that is consistent with a thermal distribution. The distribution of the red disk is much flatter and is even biased toward the low-ellipticity side of the diagram, i.e., toward the less thermal side. This would imply a more thermal, relaxed distribution as expected from the Hills mechanism (Hills 1988) for the black disk. For the red disk, the implication is that it is more influenced by a disk-migration scenario as it approaches the less-than-thermal side of the graph. This is consistent with the fact that the black disk is more compact—it is confined to within a radius of about 1″—and the red disk is significantly larger, with stars confined to within a 2.″3 radius. However, while at first glance it may be coupled to the CWD of He stars (Levin & Beloborodov 2003; Paumard et al. 2006), it is likely to have a different origin or history because the angular momentum vectors for individual stars in each disk point in opposite directions. Here, the scattering of resonance mechanisms may be more important than at larger distances from Sgr A* (see discussion in Section 3.2.1).

It is not clear if and how the more compact black disk is coupled to the counterclockwise disk claimed to be perpendicular to the CWD (Paumard et al. 2006). How the two stellar disks are arranged in projection against the sky and the GC stellar cluster is shown in Figure 11.

3.2. Stellar Dynamical Considerations

Stars bound to an SMBH interact gravitationally. The reason for the nonisotropic distribution of S-cluster members may be inferred by comparing the characteristic timescales of different dynamical processes (nonresonant two-body relaxation, resonant relaxation) with the estimated age of S stars. For the S2 star, Habibi et al. (2017) derive an age of $6.6^{+3.4}_{-4.7}$ based on 12 years of spectroscopic monitoring, with the cumulative signal-to-noise ratio of $S/N > 200$, with an upper limit on the formation time of S stars of <15 Myr. This is consistent within uncertainties with the formation time of the clockwise (CW) disk of young, massive OB/WR stars, 5 ± 1 Myr, which occupies the region beyond the S cluster at the deprojected distance between ∼0.04 and 0.5 pc (Genzel et al. 2010). This suggests a common origin of massive OB stars in the CW disk and those of lighter S stars of spectral-type B.

Recently, a group of NIR-excess compact sources was identified (Eckart et al. 2013), whose spectral properties, in particular for the intensively monitored DSO/G2 object (Gillessen et al. 2012; Witzel et al. 2014; Valencia-S. et al. 2015), suggest that these could be pre-main-sequence stars of Class I source with an even younger age of ∼0.1–1 Myr (Zajaček et al. 2017). If DSO/G2, G1 object and other NIR-excess sources are pre-main-sequence stars of class I (with the age of ∼0.1–1 Myr), then their orbits should also keep dynamical imprints of the initial formation process, e.g., most likely an infall of the molecular clump and a subsequent in situ star formation (Jalali et al. 2014). In that case, NIR-excess sources could form a dynamically related group of objects, e.g., their inclinations would be comparable, which can be tested observationally in the future when orbital elements for more objects will be inferred. In case additional gas infall occurred after the stellar disk formation, its effect is “superimposed’ on the dynamical effect any residual disk gas could have had. The evidence for the inspiral of fresh gas is supported by Yusef-Zadeh et al. (2013, 2017), who identified traces (SiO outflows, bipolar outflows) of recent star formation (10^4–10^5 yr ago) in the inner parsec. In addition, the discovery of the population of compact NIR-excess sources (DSO, G1 etc.) supports the theory of recent and ongoing star formation and molecular gas replenishment in the inner parsec.

3.2.1. Basic Dynamical Timescales

The population of S stars consisting of two disks is not relaxed, hence any current configuration is subject to resonant and nonresonant relaxation processes in the nuclear star cluster. The configuration of two perpendicular stellar disks can be stable over a timescale of 10^8 yr as demonstrated in the simulations by Mastrobuono-Battisti et al. (2019) that we refer to later. In the current section, we mention key dynamical processes that might have contributed to the X structure and so far could have influenced it. In particular, the resonant relaxation process can lead to the spread in orbital inclinations in each disk. An important quantity to understand the dynamics of a stellar system is the relaxation timescale within which a system reaches a statistical equilibrium through stellar interactions. Persistent torques acting between the orbits of the S stars will lead to the rapid resonant relaxation of the orbital orientation vectors (vector resonant relaxation) and the slower 38
relaxation of the eccentricities (scalar resonant relaxation). These mechanisms both act at rates much faster than two-body

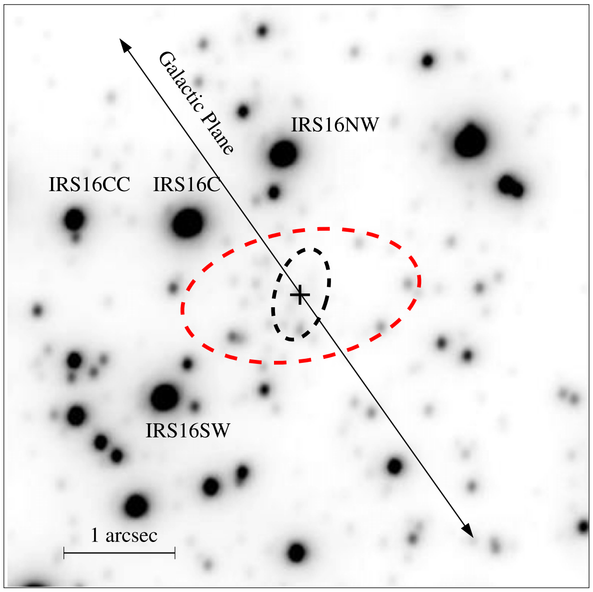

Figure 11. Location and extent of the red and black stellar disks with respect to the GC stellar cluster and the Galactic plane. Sgr A* is located at the center of the open cross close to S2. East is to the left, north is up. The semimajor axis of the black (red) dashed ellipse is about twice the median of 0.″4 or 16 mpc (1.″18 or 47 mpc), the semimajor axes of all orbits attributed to the black (red) disk system. The minor axes of the ellipses have been chosen such that they include the central half of the corresponding disk system orbits. The red dashed line comprises the bulk of the S-cluster stars. The epoch of the underlying image is early 2018.

or nonresonant relaxation. Possible physical sources of orbit perturbations are discussed in Section 3.2.2.

(a) Resonant relaxation timescales

To calculate typical timescales, we adopt the relations presented by Hopman & Alexander (2006). The nonresonant relaxation timescale dominated by two-body interactions can be expressed as follows:

$$T_{\rm NR} = A_\Lambda \left(\frac{M_\bullet}{M_\star}\right)^2 \frac{P(a)}{N(<a)}, \tag{1}$$

where $P(a) = 2\pi[a^3/(GM_\bullet)]^{1/2}$ is the Keplerian orbital period and A_Λ is a dimensionless factor that contains the Coulomb logarithm. $N(<a)$ is the number of stars with semimajor axes smaller than a given semimajor axis a. For stellar mass $M_\star$, we take $M_\star = 10\,M_\odot$, which is the order of magnitude estimated for several S stars (Genzel et al. 2010; Habibi et al. 2017).

For *scalar resonant relaxation*, which changes the value of the angular momentum $|\boldsymbol{J}|$, we consider the typical timescale in the following form:

$$T_{\rm RR,s} = \frac{A_{\rm RR,s}}{N(<a)} \left(\frac{M_\bullet}{M_\star}\right)^2 P^2(a)|1/t_{\rm M} - 1/t_{\rm GR}|, \tag{2}$$

where the factor $A_{\rm RR,s} = 3.56$ is inferred from N-body simulations of Rauch & Tremaine (1996). The timescales $t_{\rm M}$ and $t_{\rm GR}$ correspond to the mass precession and to the general relativity (GR) timescale, respectively. The mass precession takes place due to the potential of an extended stellar cluster and may be expressed as

$$t_{\rm M} = A_{\rm M} \frac{M_\bullet}{N(<a) M_\star} P(a), \tag{3}$$

where the factor $A_{\rm M}$ is of the order of unity. Closer to the black hole associated with Sgr A*, the GR precession is the dominant effect, which takes place on the timescale of $t_{\rm GR}$,

$$t_{\rm GR} = \frac{8}{3}\left(\frac{J}{J_{\rm LSO}}\right)^2 P(a), \tag{4}$$

where $J_{\rm LSO} \equiv 4GM_\bullet/c$ is the angular momentum of the last stable orbit.

Vector resonant relaxation keeps the magnitude but changes the direction of the angular momentum $\boldsymbol{J}$. The timescale of the vector resonant relaxation can be estimated as

$$T_{\rm RR,v} \simeq 2A_{\rm RR,v}\left(\frac{M_\bullet}{M_\star}\right)\frac{P(a)}{N^{1/2}(<a)}, \tag{5}$$

where the factor $A_{\rm RR,v} = 0.31$ (Rauch & Tremaine 1996).

Another process that induces the eccentricity–inclination oscillations is the Kozai–Lidov mechanism, which involves three bodies, i.e., the inner binary system (black hole–star) perturbed by a stellar or a gaseous disk (Šubr & Karas 2005) or an inner binary (star–star) perturbed by the black hole (Stephan et al. 2016). The timescale of Kozai–Lidov oscillations induced by a self-gravitating disk having the mass of M_r at the distance of r from the Galactic center is (Šubr & Karas 2005; Hopman & Alexander 2006)

$$T_{\rm KL} = 2\pi\left(\frac{M_\bullet}{M_r}\right)\left(\frac{r}{a}\right)^3 P(a). \tag{6}$$

For quantitative estimates, we used a specific mass density profile of stars $\rho_\star(r)$ to calculate timescales expressed by Equations (1)–(6). We adopted a broken power-law profile according to (Schödel et al. 2009; Antonini et al. 2012)

$$\rho_\star = \rho_0\left(\frac{r}{r_{\rm b}}\right)^{-\gamma_{\rm s}}\left[1+\left(\frac{r}{r_{\rm b}}\right)^2\right]^{(\gamma_{\rm s}-1.8)/2}, \tag{7}$$

where $\gamma_{\rm s}$ is the inner slope, and $r_{\rm b}$ is the break radius, for which we take $r_{\rm b} = 0.5$ pc. Setting $\rho_0 = 5.2 \times 10^5\,M_\odot\,{\rm pc}^{-3}$ gives the integrated, extended mass in accordance with Schödel et al. (2009), within their inferred range of $\sim(0.5\text{–}1.5)\times 10^6\,M_\odot$ (with the black hole mass subtracted). We consider two cases for the inner slope:

1. $\gamma_{\rm s} = 1.0$, which is consistent with the volume density of the S cluster, $\rho_{\rm S} \propto r^{-1.1\pm0.3}$, based on the orbits of 15 stars with the semimajor axis of $a \lesssim 0.''5$ (Genzel et al. 2010),
2. $\gamma_{\rm s} = 0.5$, which represents the overall observed stellar distribution in the central parsec (Buchholz et al. 2009).

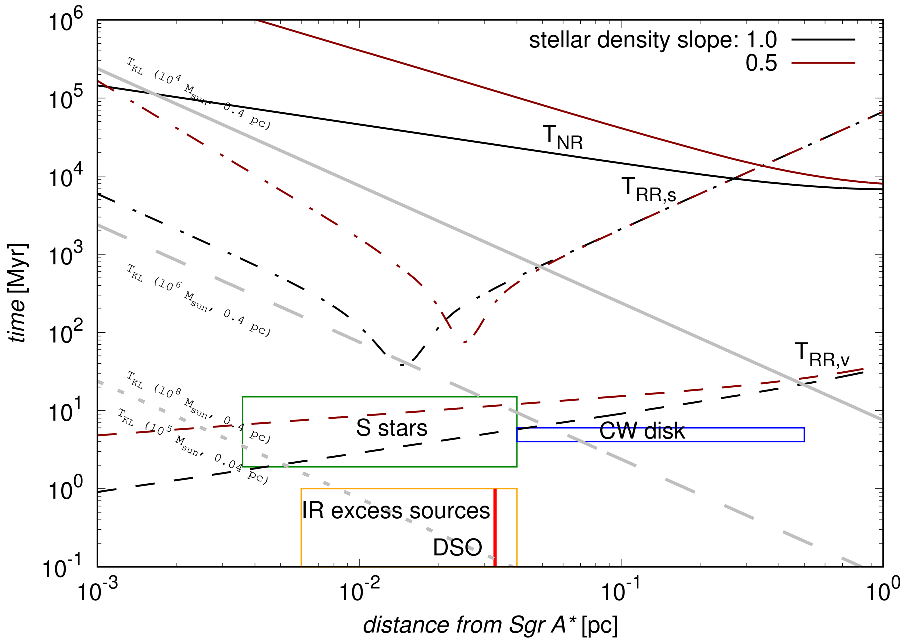

Figure 12. The time in millions of years (Myr) vs. the semimajor axis in parsecs (pc) for the inner slope of the stellar-density distribution equal to $\gamma_s = 0.5$ and $\gamma_s = 1.0$, which are depicted by different colors, dark red and black, respectively. Different lines correspond to the estimates of typical timescales of dynamical processes operating in the central parsec: T_{NR} corresponds to nonresonant relaxation (solid black and dark-red lines), $T_{RR,s}$ stands for scalar resonant relaxation (dotted–dashed black and dark-red lines) , $T_{RR,v}$ for vector resonant relaxation (dashed black and dark-red lines), and T_{KL} for Kozai–Lidov timescales (gray solid, long-dashed, and short-dashed lines, depending on the mass and the distance of the stellar disk). All timescales are calculated according to relations given in Equations (1)–(6) for the individual stellar mass of $M_\star = 10\,M_\odot$ when relevant. The distinct minimum time for scalar resonant relaxation corresponds to the semimajor axis, where GR precession takes over the extended Newtonian-mass precession. The values in parentheses next to the Kozai timescale, e.g., $T_{KL}(10^4\,M_\odot, 0.4\text{ pc})$, represent the parameters of the massive gaseous or stellar disk, in particular $M_r = 10^4 M_\odot$, which is at the distance of $r = 0.4$ pc; see also Equation (6). The rectangles stand for the distance as well as the determined age of different stellar populations, namely S stars, CW-disk stars, and NIR-excess sources; specifically, the DSO is represented by the thick solid red line. The inner radius of the S-cluster box is now represented by the S62 semimajor axis (Peißker et al. 2020).

Using the two stellar distributions, we show the timescale estimates alongside the characteristic stellar structures (S stars, CW disk, DSO, and other NIR-excess sources) in the time–semimajor axis plot, see Figure 12.

We adopt the age constraints of S stars from the recent spectroscopic study of Habibi et al. (2017), where they show that S stars are young and comparable in terms of age to OB stars from the CW disk. However, it is premature to claim that these two populations are identical in terms of age. They could have formed in two separate star formation events, with a different dynamical configuration.

The findings in this work, in particular the comparisons in Figure 12, suggest that the S cluster has not yet completely relaxed in either a resonant or nonresonant way. Short-period S-cluster members could have been influenced by vector resonant relaxation, which changed their orbital inclination, especially for more peaked stellar-density distributions with $\gamma_s \sim 1.0$; see Figure 12. However, because of the young age of S stars comparable to CW-disk stars, vector resonant relaxation is not expected to lead to the complete randomization of stellar inclinations for S stars with larger semimajor axes (longer periods) as has been previously argued to explain the apparent nearly isotropic S-cluster distribution (Genzel et al. 2010), which is not confirmed in this work. Scalar resonant relaxation, which influences orbital eccentricities and semimajor axes of stars, takes place on timescales at least one order of magnitude longer than the age of S stars.

Hence, the S cluster can in principle keep the nonisotropic structure, consisting of two inclined disks embedded within the outer CW disk. This may be hypothesized to originate in the way the S cluster formed. In particular, the S stars were likely formed within the infalling cloud/streamer that formed the disk around Sgr A* upon its impact, as seems to be the case for OB stars that are a part of the CW disk farther out (Levin & Beloborodov 2003). Due to its age of several million years, the S cluster is expected to keep the imprints of the original formation mechanism within the gas/stellar disk, which potentially consisted of more inclined streamers. The coexistence of more inclined gaseous disks is also predicted by hydrodynamical simulations of star formation in the Galactic center within an infalling massive molecular cloud. The multiple inclined disks may result from an infall of a massive molecular cloud or from a cloud–cloud collision (Hobbs & Nayakshin 2009; Alig et al. 2013; Lucas et al. 2013).

(b) Kozai–Lidov oscillations due to a massive disk

In addition, the current S-cluster distribution can reflect the perturbation by an outer massive stellar or gas disk in the distance range of 0.04–0.5 pc, which led to Kozai–Lidov-type resonances, i.e., to the interchange between the orbital eccentricity and inclination because of the conservation of the z component of the angular momentum, $L_z = \sqrt{(1-e^2)}\cos i = \text{const}$. 40

The Kozai–Lidov process can be induced by a rather massive gaseous disk present in the past. Concerning the gas disk, in Figure 12 we can see that this would be the case for a

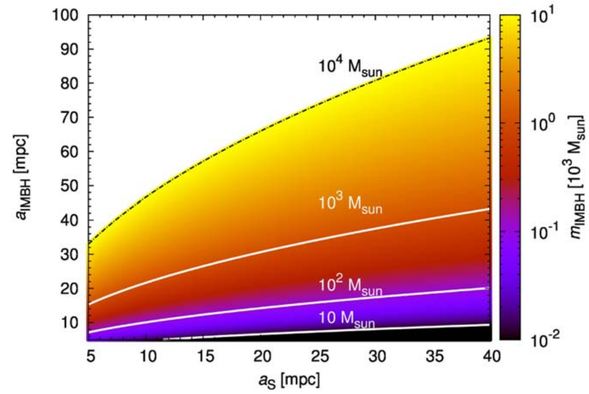

Figure 13. The color-coded mass of the IMBH as a function of its semimajor axis (circular orbit) and the semimajor axis of S stars for which the timescale of Kozai–Lidov oscillations is 1.9 Myr (lower limit on the age of S stars).

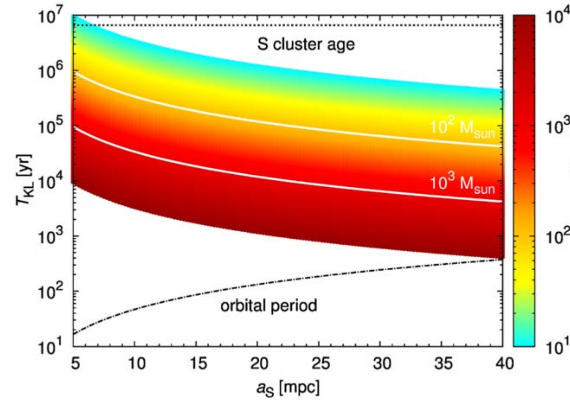

Figure 14. The color-coded mass of the IMBH as a function of the Kozai–Lidov timescale and of the semimajor axis of S stars. The IMBH is assumed to have a semimajor axis of 0.04 pc and its orbit is highly eccentric, $e = 0.99$.

very massive disk of $M_r = 10^8\,M_\odot$ positioned at $r = 0.4$ pc (outer boundary of the CW disk). The same Kozai timescale is obtained for a less massive disk of $M_r = 10^5\,M_\odot$ that is closer, at $r = 0.04$ pc (inner boundary of the CW disk), i.e., one order of magnitude closer to the black hole. Such a scenario with a massive gaseous disk that extended to smaller radii in the past than the current stellar disk was studied by Chen & Amaro-Seoane (2014). In their study, the Kozai–Lidov resonance induced by the disk could explain the current, thermalized distribution of mostly B-type S stars as well as the presence of more massive OB stars outside the S cluster. In their Figure 1, the estimate of the age of the DSO/G2 NIR-excess object is $\sim 10^5$–$10^{5.5}$ yr, consistent with the pre-main-sequence star as studied by Zajaček et al. (2017).

(c) Kozai–Lidov oscillations due to a massive perturber (IMBH)

Alternatively, the Kozai–Lidov oscillation on the timescale of the order of 1 Myr can develop due to the presence of a massive body–perturber in the inner parsec, in particular the IMBH of mass $M_{\rm IMBH}$ with the semimajor axis of $a_{\rm IMBH}$ and the eccentricity $e_{\rm IMBH}$. Any S-star then behaves as a test body that orbits Sgr A* and is perturbed by an IMBH farther out. The period of the oscillation is (Naoz 2016)

$$T_{\rm KL}^{\rm IMBH} = 2\pi \frac{\sqrt{GM_\bullet}}{Gm_{\rm IMBH}} \frac{a_{\rm IMBH}^3}{a_\star^{3/2}} (1 - e_{\rm IMBH}^2)^{3/2}. \quad (8)$$

To get the specific estimates of the mass of the IMBH and its location with respect to the S cluster, we assume the IMBH orbits Sgr A* on a circular orbit and hence $e_{\rm IMBH} = 0$. In Figure 13, we show how the location of the IMBH with respect to the S cluster depends on its mass (in the range 10–$10^4\,M_\odot$) in order to induce Kozai–Lidov oscillation in the inclination and the eccentricity during the lifetime of the S cluster. We assumed $T_{\rm KL} = 1.9$ Myr. We see that IMBHs with mass of $m_{\rm IMBH} = 10^3\,M_\odot$ and lower would essentially have to orbit Sgr A* within the S cluster on a circular orbit. Only those with $m_{\rm IMBH} = 10^4\,M_\odot$ and heavier could also be located outside the inner arcsecond to induce the Kozai–Lidov resonance in short enough time for S-cluster members.

From Equation (8), it is apparent that the Kozai–Lidov timescale can significantly shorten for perturbers–IMBHs that orbit Sgr A* on a highly eccentric orbit, which can originate due to dynamical scattering in the nuclear star cluster. Specifically, for the IMBH semimajor axis of $a = 0.04$ pc (approximately S cluster length-scale) and the eccentricity of $e_{\rm IMBH} = 0.99$, even stellar black holes of mass of the order of $m_{\rm IMBH} = 10\,M_\odot$ could induce Kozai–Lidov oscillation within the S-cluster lifetime; see Figure 14. For heavier IMBHs, the Kozai–Lidov timescale shortens as $T_{\rm KL} \propto m_{\rm IMBH}^{-1}$.

In conclusion, a massive perturber within or just outside the S cluster can induce the eccentricity–inclination Kozai–Lidov oscillations within the S-cluster lifetime, i.e., an initially disk-like stellar system can get misaligned or an initially spherical system can become nonisotropic with respect to the inclination distribution, especially due to Kozai–Lidov dependency on initial inclinations—it applies most significantly to highly inclined stellar orbits with respect to the perturber, $i \sim 40°$–$140°$. Once the system is perturbed due to the Kozai–Lidov resonance, it would take at least $T_{\rm RR,\,v} \approx 10^6$ yr for vector resonant relaxation to randomize orbits. Hence, the current S-cluster state can reflect a recent perturbation due to the presence of an IMBH. Although detailed dynamical modeling is beyond the scope of this paper, the analysis of Tisserand's parameter can give limited insight into the action of a massive perturber near the S cluster surrounding Sgr A*.

(d) Tisserand's parameter

Tisserand's parameter is a dynamical quantity that is used to describe restricted three-body problems in which the three objects all differ greatly in mass. Tisserand's parameter is calculated from several orbital elements (semimajor axis a, orbital eccentricity e, and inclination i_b) of a small object and a larger perturbing body, all of which are in orbit about a greater central mass. This parameter is a dynamically useful quantity as it is approximately conserved during an encounter of the two smaller bodies. It therefore allows us to connect the post-encounter dynamical properties with the pre-encounter properties (Merritt 2013). In the following, we see that the analysis of Tisserand's parameter for the S-cluster stars suggests that two perpendicular disks can be supported by a heavy mass just outside the S cluster, influencing its dynamics.

Tisserand's parameter can be written as

$$T = \frac{a_{\rm Pert}}{2a} + \left[\frac{a}{a_{\rm Pert}}(1 - e^2)\right]^{1/2} \cos(i_b). \quad (9)$$ 41

The ratio between the semimajor axes of a massive perturber and the stars is $R' = a_{\rm Pert}/a$. Assuming the stars are in a disk

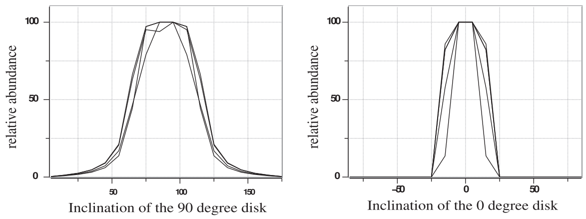

Figure 15. The peak normalized distributions of inclinations $i_{\rm obse}$ that can be derived from $i_b = 90°$ (left) and $i_b = 0°$ (right) via Tisserand's parameter using the observed distribution of eccentricities.

and had semimajor axes $a = a_{\rm Pert}/R'$ and an eccentricity e close to zero, then $T = R'/2 + R'^{-1/2}$. Then, T or $\mu = R' + 2R'^{-1/2}$, respectively, describe the initial setup. For $R' = 1$, one finds $T = 3/2$ and $\mu = 3$. For the current orbital elements (a, e, i_b) and the current ratio $R = a_{\rm Pert}/a$, one can write Tisserand's relation for each star as

$$R + 2[R^{-1}(1 - e^2)]^{1/2}\cos(i_b) \approx \mu. \tag{10}$$

Here, i_b is the inclination of the stars with respect to the plane in which the massive perturber orbits the central mass and $R = a_{\rm Pert}/a$ is the current ratio between the semimajor axes of a massive perturber and the stars. This expression can be rewritten as

$$\cos(i_b) = \pm\sqrt{\frac{R(\mu - R)^2}{4(1 - e^2)}}. \tag{11}$$

This relation has simple solutions for cases in which $\mu \sim R$ with μ now containing information on the initial conditions R'. For $R'/R > 1.0$, one can reproduce the $i_b = 90°$ disk and for $R'/R < 1.0$ one can reproduce the $i_b = 0°$ disk. If one allows the current ratio R to vary by a few percent and uses the distribution of observed eccentricities as an input, one can reproduce the distribution of observed stellar inclinations for the $i_b = 90°$ disk. Compared to the $i_b = 90°$ disk, the inclination distribution for the $i_b = 0°$ disk turns out to be narrower. Both distributions are shown in Figure 15. On the sky, we observe both disks such that their inclinations toward the observer are both close to the observed inclination $i_{\rm obs} = 90°$; hence, the two distributions are superimposed if derived from observations of the central arcsecond in total.

Solving Equation (11) for increasing values of R', one finds that the value for the current ratio R approximates that for initial ratio R'. In Figure 16, we plot the current ratio R in relation to R'. The top graph shows how R/R' approximates unity for the $i_b = 90°$ disk as listed in Table 1. The bottom graph shows the same for the $i_b = 0°$ disk. For values $R' \geqslant 6 .... 8$, the difference between the two ratios drops so that R/R' gets close to unity to within less than about three to five times the width by which we need to let R vary to explain the observed distributions of inclinations (see Figure 16). This means that for these cases, the initial conditions are very similar to the current conditions and the two orthogonal disks may be populated by objects with rather similar dynamical properties. Hence, we find as a result the analysis of Tisserand's parameter that two perpendicular disks can be supported by a heavy mass just outside the S cluster, influencing its dynamics. This fits well with IRS 13E being a possible disturber of the S-cluster star. A discussion is given in Section 3.2.2.

Under the influence of a massive perturber, the eccentricity and inclination of the stars may vary periodically with the stars'

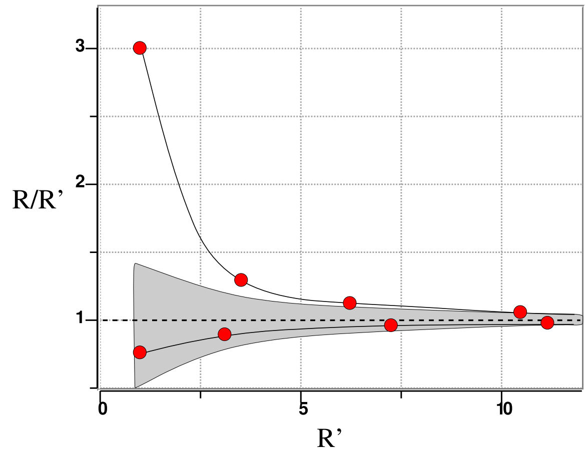

Figure 16. The current ratio R in relation to the initial ratio R/R' as a function of the initial ratio R'. The gray areas shows the range covered by three times the actual range by which the current ratio R is allowed to carry in order to explain the distribution of inclinations.

argument of periapsis ω under conservation of $(1 - e^2)\cos(i)$. The timescale for these "Kozai–Lidov cycles" is of the order of 10^6 yr for the S stars within the central 1″–3″ if the mass of the perturber is of the order of 10^3–$10^4 M_\odot$ (see text and Equation 8.175 in Merritt 2013). However, there is no specific timescale associated with Tisserand's parameter and the formation or conservation of the system. If at the time of the formation of the stellar disk the stars had the observed configuration, then they will all satisfy Equation (11) from the start and at all later times, until some other perturbation acts. Stars that are on orbits that do not satisfy the relation will be removed or associated with one of the disks on a few Lidov–Kozai timescales or the resonant relaxation timescales (see above). Two orthogonal disks will be supported by Tisserand's relation and the interrelation of stellar angular momenta as described by Equation (11).

3.2.2. Possible Sources of Perturbation

The strong vertical resonances expressing themselves via the X-shaped structure in the stellar distribution can be the result of a resonant relaxation process solely determined by the mean field of stars in the cluster. Furthermore, the growth of the Galactic bar could trigger inner Lindblad resonances, in which the stars are lifted into higher-amplitude orbits (Quillen 2002; Binney & Tremaine 2008). However, one may identify possible sources of perturbation that imposed these resonances or influenced the relaxation process.

Possibility 1: The B stars of the S cluster are estimated to have an age less than 15 Myr. However, star S2 has an age of about 7 Myr, which is compatible with the age of the CWD of young stars in the GC. It is quite likely that S stars formed almost simultaneously with the OB/WR stars that are part of the CW disk (Habibi et al. 2017). It is thought that the CW-disk stars formed in situ in a massive gaseous disk (Levin & Beloborodov 2003). The origin of this disk could have been a massive molecular cloud with the radius of ∼15 pc and the impact parameter of ∼26 pc, which was tidally disrupted, spiraled in, and subsequently formed an eccentric disk (Mapelli et al. 2012) where stars formed. It cannot be excluded that the stellar disk, which previously extended below 0.04 pc where the S cluster is located now, was perturbed by the infall of 42 another massive molecular cloud that formed a disk or a ring with an inclination of β with respect to the stellar disk (Mapelli et al. 2013; Trani et al. 2016). The influx of gas that led to their formation also induced the perturbances in the young S cluster, resulting in vertical resonances that relaxed to the structure seen today. According to the numerical simulations of Mapelli et al. (2013) and Trani et al. (2016), the precession driven by the gas disk in the inner 0.5 pc on the stellar disk can significantly increase the stellar inclinations within a few million years, which leads to the disk tilting and/or warping. As the precession is faster for outer disk parts, $T_{\rm prec} \propto a_\star^{-3/2}$, the S cluster could in principle represent a "primordial" disk part with two perpendicular streamers that have warped to form the CW disk at larger distances. Further warping at largest distances led to disk dismembering, which can account for $\sim$80% of OB stars that are not part of any disk (Yelda et al. 2014). Two innermost, nearly perpendicular stellar disks are in a dynamically very stable configuration, because the mutual disk precession $T_{\rm DISC} \propto \cos\beta^{-1}$ around each other goes to infinity for the inclination β that approaches 90°.

Possibility 2: As the orbits are clearly not fully randomized, a massive IMBH within the S cluster can probably be excluded (see comments in the introduction and see Gualandris & Merritt 2009). However, an IMBH as a massive perturber well outside the S cluster could provide a long-term influence on the orbits resulting in vertical resonances. The analysis of the Kozai–Lidov oscillations and Tisserand's parameter both suggests that a massive perturber may have influenced the stellar dynamics in the central arcsecond. For an initial ratio of the semimajor axes of the stars and the perturber of $R' \geqslant 6 \ldots 8$, the ratio between the initial and current ratio becomes unity. In this case, the dynamical situation may not have changed very much since the system was set up. Assuming that the semimajor axes a of the stars can be taken as a measure of the radius of the S-star cluster, i.e., $a = 0\farcs5$, then $R' \sim R \sim 3\farcs5$ (0.13 pc projected distance). This fits well with the separation of IRS 13E from Sgr A* and the S-cluster star. IRS 13E lies within $\sim$15° in one of the stellar disks. It may harbor an up to $10^4 M_\odot$ IMBH and a few hundred solar masses of stars (Krabbe et al. 1995; Maillard et al. 2004; Schödel et al. 2005; Tsuboi et al. 2017). The analysis of the Kozai–Lidov oscillations and Tisserand's parameter then indicate that the 0°–90° disk in Section 3.2.1(d) can to first order be identified as the red and black disk as discussed in Sections 3.1.3 and 3.1.2.

The possibility of different coexisting stellar disks in the GC has also been discussed theoretically by Mastrobuono-Battisti et al. (2019). Here, the authors simulate multiple stellar disks in the central stellar cluster. Each disk is added after 100 Myr. In particular, in the bottom panel of their Figure 1, one can see that even after 100 Myr two separate stellar disks can still be distinguished. The first one got thicker but is still well defined.

4. Summary and Conclusions

We present a detailed analysis of the kinematics of the stars in the innermost stellar cluster for which we have orbital elements. The high-velocity S-cluster stars orbit the SMBH Sgr A* at the center of the MW. The distribution of inclinations and position angles of the sky-projected orbits deviate significantly from a uniform distribution which one would have expected if the orientation of the orbits are random. The stars are arranged in two stellar disks that are perpendicular to each other and located within a position angle of about ±45° with respect to

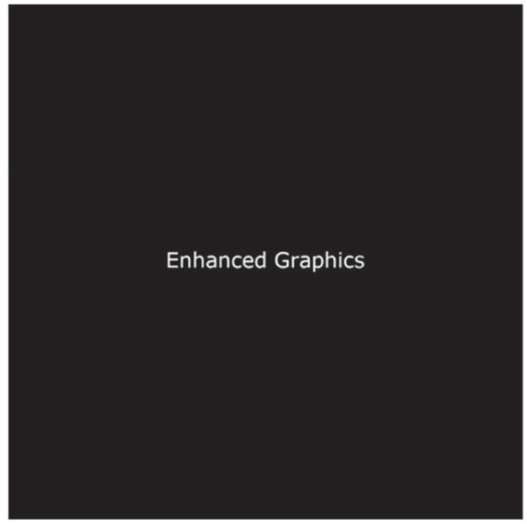

Figure 17. Animation of the projected orbital arrangements in motion. There are three sequences in the animation: the full three-dimensional orbits using all orbital elements, a sequence where the ellipticity has been set to zero, and a normalized sequence where the semimajor axes have been set to a constant and the ellipticity has been set to zero.

(An animation of this figure is available.)

the Galactic plane. The distribution of eccentricities of the inner (black) north–south disk system suggests that it is relaxed and thermal as it may be expected from the Hills mechanism. The east–west (red) disk system is more influenced by a disk-migration scenario as it approaches the less-than-thermal side in the distribution of the eccentricities.

While it cannot be excluded that the red disk is the inner part of the CWD of He stars (Levin & Beloborodov 2003; Paumard et al. 2006) or is connected to it, the black disk system is much more compact and possibly more thermally relaxed. It is uncertain if or how it is connected to the large central cluster.

Because the angular momentum vectors of the stars in each disk point in opposite directions, i.e., the stars in a given disk rotate both ways, it appears to be unlikely that the origin or history of these stars is the same as the one discussed for the massive young stellar disks containing the He stars (Levin & Beloborodov 2003; Paumard et al. 2006; Lu et al. 2009, 2013; Yelda et al. 2014). Most likely, the S-cluster structure is strongly influenced by the Kozai–Lidov resonances or vector resonant relaxations.

This prominent X-shaped arrangement is most likely a result of the interaction of stars with each other that can be described via the resonant relaxation process. An estimate of the resonant relaxation timescale indicates that the structure started to evolve into the current X shape in the same time interval during which most of the young stars in the central stellar cluster were formed. The presence of a highly ordered kinematic structure at the center of the nuclear stellar cluster and in the immediate vicinity of the SMBH Sgr A* also indicates that for a very long time, no major perturbation of the system occurred that could have led to a randomization of the stellar orbits in the central arcsecond.

5. Enhanced Graphics 43

Figure 17 provides three animations where the SMBH Sgr A* is located at the center of the three-dimensional arrangement.

The animations hold for a short while at the positions under which the orbital configuration can be seen in special projections: red system face on, line-of-sight view, pole vision, and red system edge on. Labels in units of milliparsecs are given at the edges. In each animation, we list the corresponding azimuth and elevation angle, with 0° and -90°, respectively, being the line-of-sight direction. In the first sequence, we show the full three-dimensional orbits using all orbital elements. The dots on the orbits indicate the position of the star. The corresponding time is given in a text line above. In the second sequence, the ellipticity has been set to zero. Finally, we show the ball of wool configuration. Here, semimajor axes have been set to a constant and the ellipticity has been set to zero.

We are grateful to Anna Luka Höfling, who prepared the enhanced graphics as an intern in the infrared group at the I. Physikalisches Institut of the University of Cologne. We received funding from the European Union Seventh Framework Program (FP7/2007-2013) under grant agreement No. 312789—Strong gravity: Probing Strong Gravity by Black Holes Across the Range of Masses. This work was supported in part by the Deutsche Forschungsgemeinschaft (DFG) via the Cologne Bonn Graduate School (BCGS), the Max Planck Society through the International Max Planck Research School (IMPRS) for Astronomy and Astrophysics, as well as special funds through the University of Cologne and CRC 956—Conditions and Impact of Star Formation under project A2. M. Z. acknowledges the financial support by the National Science Centre, Poland, grant No. 2017/26/A/ST9/00756 (Maestro 9). We thank the German Academic Exchange Service (DAAD) for support under COPRAG2015 (No.57147386) and the the Czech Science Foundation—DFG collaboration (EC 137/10-1).

Appendix A
Field-of-view Effects

By restricting the field of view toward a central section with radius $\Delta s \sim 0\farcs5$ covering the surface $4(\Delta s)^2$ in the sky, one introduces a bias toward higher inclinations. Sources with low inclinations with orbits outside the selected area and sources with large three-dimensional distances from the center pass through the selected area only if their orbits have high inclinations. We assume that the central volume is $16(\Delta s)^3$ and the volume attributed to the outer stars within the column $4(\Delta s)^2$ is $8(\Delta s)^2$. The central arcsecond is dominated by young stars. Early-type stars are abundant within the central $5''$ radius (i.e., $10\Delta s$) of the nuclear cluster with a surface (volume) density dropping with an exponent of -1.8 (-2.8; Buchholz et al. 2009). Taking the volume density at $3''$–$4''$ radius, i.e., at 6 to 8 times Δs, then the number ratio of stars between those that are within the volume of the central arcsecond and those that are only in projection in that region is

$$\left(\frac{\Delta s}{(6\,....\,8)\,\Delta s}\right)^{-2.8}\frac{16(\Delta s)^3}{8(\Delta s)^2 10\Delta\ s} = (30\,....\,67). \tag{A1}$$

Hence, the bias is only of the order of a few percent and the clustering toward 90° inclination can be fully attributed to the intrinsic properties of the stellar orbits.

In summary, these findings indicate that independent of the three-dimensional orientation, the determined stellar orbits in the S cluster are preferentially seen edge on.

Appendix B
Biases Due to Incomplete Orbital Coverage

O'Neil et al. (2019) discuss the influence of orbital elements resulting from fits to data that only cover the orbits in an incomplete way. They introduce an observable-based prior (OBP) paradigm and the corresponding bias factors with respect to uniform priors (UP). In our case, the orbital coverage of the fitted orbits indicates three groups.

The first group, which contains stars with 40%–100% orbital coverage, has no difference between the bias factor of uniform priors UP and the bias factor of the OBP for the black hole mass and the distance to the GC. The second group, which contains stars with 20%–35% orbital coverage, has a difference of 0.3σ between the bias factor of UP [0.5σ–0.8σ] and the bias factor of OBP [0.2σ–0.5σ] for the case of the SMBH mass and the distance to it. The last group, which contains stars with 5%–15% orbital coverage, has a difference of [0.51σ–0.6σ] between the bias factor of UP [0.98–1] and the bias factor of OBP [0.4σ–0.47σ] for the case of SMBH mass and the distance to it. The bias factor difference for the orbital elements (O'Neil et al. 2019) was only done for the case of 16% orbital coverage, i.e., valid only for the last group. Here, a value of 1 indicates high bias and a value of -1 is low bias (see O'Neil et al. 2019).

In summary, the inclination bias factor difference is extremely small. For 19 stars only, we find a 0.6σ difference. Hence, our finding that the stars are preferentially on highly inclined orbits is unaffected by this bias. Also, the orbital elements we derive for the stars are only affected in a minimal way.

ORCID iDs

Basel Ali https://orcid.org/0000-0002-5728-4054
Andreas Eckart https://orcid.org/0000-0001-6049-3132
Michal Zajacek https://orcid.org/0000-0001-6450-1187
Florian Peißker https://orcid.org/0000-0002-9850-2708
Gunther Witzel https://orcid.org/0000-0003-2618-797X

References

Abbott, C. G., Valluri, M., Shen, J., & Debattista, V. P. 2017, MNRAS, 470, 1526
Ajne, B. 1968, Biometrika, 55, 343
Alig, C., Schartmann, M., Burkert, A., & Dolag, K. 2013, ApJ, 771, 119
Antonini, F., Capuzzo-Dolcetta, R., Mastrobuono-Battisti, A., & Merritt, D. 2012, ApJ, 750, 111
Bhattacharayya, G., & Johnson, R. 1969, Biometrika, 56, 446
Binney, J., & Tremaine, S. 2008, in Galactic Dynamics, ed. J. Binney & S. Tremaine (2nd ed.; Princeton, NJ: Princeton Univ. Press), 539
Boehle, A., Ghez, A. M., Schödel, R., et al. 2016, ApJ, 830, 17
Buchholz, R. M., Schödel, R., & Eckart, A. 2009, A&A, 499, 483
Chaves-Velasquez, L., Patsis, P. A., Puerari, I., Skokos, C., & Manos, T. 2017, ApJ, 850, 145
Chen, X., & Amaro-Seoane, P. 2014, ApJL, 786, L14
Contopoulos, G. 1988, A&A, 201, 44
Durand, D., & Arthur, G. J. 1958, JG, 66, 229
Eckart, A., Mužić, K., Yazici, S., et al. 2013, A&A, 551, A18
Genzel, R., Eisenhauer, F., & Gillessen, S. 2010, RvMP, 82, 3121
Gerhard, O., Wegg, C., & Portail, M. 2016, in The Universe of Digital Sky Surveys, ed. N. R. Napolitano (Cham: Springer), 41
Ghez, A. M., Duchêne, G., Matthews, K., et al. 2003, ApJL, 586, L127
Gilbert, G. 1895, Bull. Phil. Soc. Washington, 12, 241
Gillessen, S., Eisenhauer, F., Trippe, S., et al. 2009, ApJ, 692, 1075
Gillessen, S., Genzel, R., Fritz, T. K., et al. 2012, Natur, 481, 51
Gillessen, S., Plewa, P. M., Eisenhauer, F., et al. 2017, ApJ, 837, 30 44
Gravity Collaboration, Abuter, R., Amorim, A., et al. 2018, A&A, 615, L15
Gualandris, A., & Merritt, D. 2009, ApJ, 705, 361
Habibi, M., Gillessen, S., Martins, F., et al. 2017, ApJ, 847, 120

Hernquist, L., & Weinberg, M. D. 1992, ApJ, 400, 80
Hills, J. G. 1988, Natur, 331, 687
Hobbs, A., & Nayakshin, S. 2009, MNRAS, 394, 191
Hopman, C., & Alexander, T. 2006, ApJ, 645, 1152
Jalali, B., Pelupessy, F. I., Eckart, A., et al. 2014, MNRAS, 444, 1205
Jammalamadaka, S. R., & SenGupta, A. 2001, Topics in Circular Statistics (Singapore: World Scientific)
Krabbe, A., Genzel, R., Eckart, A., et al. 1995, ApJL, 447, L95
Levin, Y., & Beloborodov, A. M. 2003, ApJL, 590, L33
Lu, J. R., Do, T., Ghez, A. M., et al. 2013, ApJ, 764, 155
Lu, J. R., Ghez, A. M., Hornstein, S. D., et al. 2009, ApJ, 690, 1463
Lucas, W. E., Bonnell, I. A., Davies, M. B., & Rice, W. K. M. 2013, MNRAS, 433, 353
Maillard, J. P., Paumard, T., Stolovy, S. R., & Rigaut, F. 2004, A&A, 423, 155
Mapelli, M., Gualandris, A., & Hayfield, T. 2013, MNRAS, 436, 3809
Mapelli, M., Hayfield, T., Mayer, L., & Wadsley, J. 2012, ApJ, 749, 168
Martins, F., Gillessen, S., Eisenhauer, F., et al. 2008, ApJL, 672, L119
Mastrobuono-Battisti, A., Perets, H. B., Gualand ris, A., Neumayer, N., & Sippel, A. C. 2019, MNRAS, 490, 5820
Menten, K. M., Reid, M. J., Eckart, A., & Genzel, R. 1997, ApJL, 475, L111
Merritt, D. 2013, Dynamics and Evolution of Galactic Nuclei (Princeton, NJ: Princeton Univ. Press)
Naoz, S. 2016, ARA&A, 54, 441
O'Neil, K. K., Martinez, G. D., Hees, A., et al. 2019, AJ, 158, 4
Parsa, M., Eckart, A., Shahzamanian, B., et al. 2017, ApJ, 845, 22
Paumard, T., Genzel, R., Martins, F., et al. 2006, ApJ, 643, 1011
Peißker, F., Eckart, A., & Parsa, M. 2020, ApJ, 889, 61
Plewa, P. M., Gillessen, S., Eisenhauer, F., et al. 2015, MNRAS, 453, 3234
Quillen, A. 2002, AJ, 124, 400
Quillen, A. C., Kuchinski, L. E., Frogel, J. A., & DePoy, D. L. 1997, ApJ, 481, 179
Quillen, A. C., Minchev, I., Sharma, S., Qin, Y.-J., & Di Matteo, P. 2014, MNRAS, 437, 1284
Rauch, K. P., & Tremaine, S. 1996, NewA, 1, 149
Reid, M. J., Menten, K. M., Genzel, R., et al. 2003, ApJ, 587, 208
Reid, M. J., Menten, K. M., Trippe, S., Ott, T., & Genzel, R. 2007, ApJ, 659, 378
Sabha, N., Eckart, A., Merritt, D., et al. 2012, A&A, 545, A70
Schödel, R., Eckart, A., Iserlohe, C., Genzel, R., & Ott, T. 2005, ApJL, 625, L111
Schödel, R., Merritt, D., & Eckart, A. 2009, A&A, 502, 91
Shahzamanian, B., Eckart, A., Valencia-S., M., et al. 2015, A&A, 576, A20
Stephan, A. P., Naoz, S., Ghez, A. M., et al. 2016, MNRAS, 460, 3494
Šubr, L., & Karas, V. 2005, A&A, 433, 405
Trani, A. A., Mapelli, M., Bressan, A., et al. 2016, ApJ, 818, 29
Tsuboi, M., Kitamura, Y., Tsutsumi, T., et al. 2017, ApJL, 850, L5
Valencia-S., M., Eckart, A., Zajaček, M., et al. 2015, ApJ, 800, 125
Witzel, G., Eckart, A., Bremer, M., et al. 2012, ApJS, 203, 18
Witzel, G., Ghez, A. M., Morris, M. R., et al. 2014, ApJL, 796, L8
Yelda, S., Ghez, A. M., Lu, J. R., et al. 2014, ApJ, 783, 131
Yusef-Zadeh, F., Royster, M., Wardle, M., et al. 2013, ApJL, 767, L32
Yusef-Zadeh, F., Wardle, M., Kunneriath, D., et al. 2017, ApJL, 850, L30
Zajaček, M., Britzen, S., Eckart, A., et al. 2017, A&A, 602, A121

Chapter 4

Paper II: Comparing Different Bayesian Methods in Deriving Multimodal Posteriors - Application on Orbital Fitting in the Absence of Radial Velocity Measurements

As mentioned in the previous paper, 71 stars of the cluster have no determined orbits. The challenge arises from the fact that these stars have swiped only a short section of their orbits and hence there exist many possible solutions. Furthermore, the lack of radial velocity measurement makes finding a solution even more difficult, as it leads to two possible solutions for each of the longitude of ascending node and argument of pericenter.

In the following paper, I explore different Bayesian methods to derive the orbital elements of these stars. Since all objects have no radial velocity measurements, the methods are required to find multimodal posteriors. In total, I try 8 different approaches that belong to Markov Chain Monte Carlo (MCMC) algorithms, approximate Bayesian computation (ABC) and nested sampling (NS). As a result, I find that NS outperforms both MCMC and ABC in terms of speed and uncertainty estimation. More specifically, the algorithm Ultranest, implemented by Buchner (2021, 2019, 2016), is the optimal choice among the 3 selected NS approaches for the 8th-dimensional orbital fitting problem. This is justified by a better uncertainty estimation strategy, computational features and naturally the ability to clearly detect multimodal posteriors.

On the one hand, I find that all MCMCA approaches fail in obtaining the required posteriors, which can be attributed to the walkers being stuck in local minima. On the other hand, ABC shows a good computational performance, however, the computation time is very long and hence not suitable for the orbital fitting problem.

Consequently, Ultranest is chosen for application on the well-constraint orbit of S2. As a result, I find that Ultranest is able to clearly detect the two expected solutions with great agreement with the literature. Therefore, I consider the method to be suitable for further application on the remaining S-stars.

Draft version April 28, 2023
Typeset using LaTeX **preprint** style in AASTeX631

Comparing Different Bayesian Methods in Deriving Multimodal Posteriors - Application on Orbital Fitting in the Absence of Radial Velocity Measurements

Basel Ali,[1] Matthias Subroweit,[1] Andreas Eckart,[1,2] and Christian Straubmeier[1]

[1] *I.Physikalisches Institut der Universität zu Köln, Zülpicher Str. 77, 50937 Köln, Germany*
[2] *Max-Plank-Institut für Radioastronomie, Auf dem Hügel 69, 53121 Bonn, Germany*

Submitted to ¿¿¿¿¿

ABSTRACT

We present a comparison between Markov chain Monte Carlo algorithms, approximate Bayesian computations and nested sampling in deriving multimodal posteriors. This is done by application on the orbital fitting problem in case no radial velocity measurements are obtainable. Our results show that all chosen approaches of MCMC fail to achieve the desired outcome, while both ABC and NS show similar behaviour with the former requiring a much longer computation time. In conclusion, we report that NS outperforms both MCMC and ABC. More specifically, we find that the approach implemeneted in the package Ultranest is considered to be the optimal choice for our problem in terms of computational features and uncertainty estimation strategy. Furthermore, we apply the chosen approach on the data of the star S2 and we find that it is able to clearly detect the two solutions with great agreement with the literature.

Keywords: Bayesian Statistics, Nested sampling, Markov chain Monte Carlo , Orbital fitting, Multimodal distributions

1. INTRODUCTION

Finding an orbit of a celestial object is not regarded as a trivial task. Things get more complicated if no radial velocity measurements are obtainable, which gives rise to multimodal distributions of the fitted parameters. Achieving multimodal posteriors is a current active research area in Bayesian computation, which is considered vital in almost all scientific research nowadays. The importance arises with the ability to achieve the most consistent and robust interpretation of the data. A good starting point to get a glimpse of the concept is to introduce the so-called Bayes theorem that takes the following form:

$$P(A|B) = \frac{P(B|A)P(A)}{P(B)} \tag{1}$$

Where A and B are events, $P(A|B)$ is a conditional probability describing event A happening given B, $P(B|A)$ is the opposite of the latter, P(A) and P(B) are the probabilities of the occurrence of events A and B, respectively. In simple words, the formula states that if we have prior knowledge or assessment of a certain outcome before adding any new experimental data, then one could obtain the posterior probability using Bayes' theorem by revising the prior probability after acquiring new information about the problem.

Currently, there exist several methods to derive to the posteriors probability. Firstly, one has the traditional Markov chain Monte Carlo algorithms (MCMCA), in which the so-called walkers explore the parameter space using proposal functions and exchange status until convergence is reached. This efficient method has been applied numerously in many fields and shown to give reliable outcomes. Another approach is Approximate Bayesian Computation (ABC), unlike MCMCA, which requires the likelikhood function to be specified, ABC approximates the likelihood function by simulating from the prior distribution and comparing the outcome to the observed data using a distance measure. Finally, the re-

Corresponding author: Basel Ali
ali@ph1.uni-koeln.de

cently proposed method called Nested Sampling (NS) is considered to be promising and very efficient.

Several studies have already been published in introducing and applying these methods on current scientific problems. These problems usually contain unimodal posteriors and exploring the parameter space is considered trivial compared to spotting two or three modes as the desired outcome. The search of multimodal distributions is considered an active area of research in Bayesian computations and the performance of different methods is still being investigated, specially in higher dimensional problems.

1.1. *Markov Chain Monte Carlo Algorithms*

The idea of Monte Carlo simulation has been present in the scientific community since the 17th century. Scientists as Stanislaw Ulam , Nicholas Metropolis and John von Neumann are considered pioneers in examining this methodology. In particular, the work by Metropolis et al. (1953) established the foundation of our current understanding of these algorithms. The initial step, as mentioned briefly above, the so called walkers contain random samples drawn from the prior distributions of the parameters. This is then followed by applying a proposal function in order to guide the walkers in the parameter space and hence deriving the required posteriors. In our present time, the most recent algorithms of MCMC differ usually in the proposal functions or as it is also called the 'move'. For instance, in Goodman & Weare (2010), which propose an affine-invariant MCMC, the stretch move is applied on the walkers in the ensemble such that they satisfy detailed balance. In case the MCMC is not affine-invariant then the move is called a walk move. Further examples include differential evolution proposal, introduced by Nelson et al. (2013), a clustered kernel-density-estimate proposal implemented by Farr & Farr (2015), or a proposal cycle that contain several functions, such as the one brought up by Ashton & Talbot (2021).

1.2. *Approximate Bayesian Computation*

This type of methodology, unlike MCMCA, doesn't require the likelihood function to be specified, instead it is be approximated by means of simulation using a distance measure and a threshold. The distance measure is used between the simulated data-set and the observed one, and along with a threshold, the algorithm either accepts or rejects the simulated set until the population size is a clear representative of the posterior distribution. This technique is called ABC-rejection sampling and its application can be seen in several publications such as Bertorelle et al. (2010) and Beaumont (2010). A significant improvement to ABC-rejection sampling was performed by Toni & Stumpf (2009), who used ABC with sequential Monte Carlo (ABCSMC). SMC states that one could assign likelihood weights to the simulated samples and repeat the sampling around the most probable samples. This allows the posterior estimation to be more accurate and precise. It is also recommended to use summary statistics of the output of the5865 model instead of the raw outcome, since the probability of having a simulated sample with a small distance is inversely proportional to the dimensionality of the data. As for the distance measure, it could be euclidean, Manhattan, or adaptive as demonstrated by Prangle (2017). The adaptive distance ensures that each summary statistic has similar influence by recalculating the weights and rescaling the impact. This is particularly helpful if the summary statistics vary largely in scale.

1.3. *Nested Sampling*

Nested sampling (NS) was recently developed by Skilling (2004) and is established to calculate the evidence, also called the marginal likelihood, i.e., the integral over the prior and likelihood, with parallel estimation of the posterior samples. In general, the algorithm starts by drawing N live points from the prior, or perform a prior transform, which is a transformation from a space where variables are independently and uniformly distributed between 0 and 1 to the parameter space of interest. The next step is to calculate the likelihood of the N points and keep track of the volume occupied by these points in the parameter space. This is followed by likelihood restrict prior sampling, in which the new sampled live point must have a likelihood higher than the minimum likelihood point that is removed before this step. This process is repeated until the remaining volume of the prior space is very small, i.e., the final live points share similar likelihoods. The most recent developments to NS usually differ in the way the new live point is sampled; for instance, it could either be by performing MCMC walk from the active points (Skilling (2004)), or bounding all live points with an ellipsoid and choosing the new point at random from within it after enlargement (Mukherjee et al. (2006)), or using clustered ellipsoidal nested sampling which can form multiple ellipses around each individual peak in the likelihood space (Shaw et al. (2007)). The latter approach is proven to be of great importance when encountering multimodal posteriors. Further enhancement to the algorithm was presented by Higson et al. (2018), the difference is that instead of choosing a fixed number of live points, the number is adapted with the purpose of sampling the posterior probability density more efficiently. Another development was introduced by Buchner (2021, 2019, 2016), implementing the parameter-free MLFriends algorithm, which creates ellipsoids around each live point and sample the new live point from them, with the shape of the ellipsoid determined by Mahalanobis distance and its size by cross-validation.

In this work, we apply 8 different approaches that belong to MCMCA, ABC and NS on the 8-dimensional orbital fitting problem in the absence of radial velocity data. The latter constraint gives rise to mostly two and in one case three modes of the posteriors of two of the fitted parameters.

In the following, we first present details of the problem, then proceed by the settings of each method. Secondly, we show the outcome of all approaches and choose the optimal one for further application on a real dataset.

2. IMPLEMENTATION

2.1. *Orbital Fitting*

In observational astronomy and astrophysics, if one has no access to radial velocity instruments, then the data contains only the projected motion of the celestial object, i.e., the right ascension and declination. This leads to difficulties in obtain the Keplerian elements (a, e, i, Ω,ω, T_p) (see Figure 1), in particular, the position of the ascending node, which is required for the calculation of Ω and ω is uncertain and could be at one of two possible positions. A possibility would be to use direct optimization models that require an initial guess and restrict the range of the angles to 180 degrees instead of 360. However, there is a significant probability that the corrected and true value is contained in the eliminated half. Furthermore, the latter technique doesn't explore the large parameter space and the computations heavily depend on the choice of the initial guess. Therefore, bias and uncertainty remain an issue. A better suited approach would be to completely explore the parameter space and hence eliminate bias in the solution and to have a methodology that is able to clearly detect multimodal posteriors. The number of possible modes depend on the true value of the angles, which in case of 0, 180 and 360 degrees, reaches three modes, due to the circular nature of the range of these angles. Otherwise, only two modes are observed. The other four orbital elements are computationally certain and show unimodal posteriors, unless the period is small, which then leads to two modes of T_p.

The fitting procedure starts with solving the following Kepler's equation:

$$E - esin(E) = M \tag{2}$$

Where E is the eccentric anomaly, e the eccentricity and M the mean anomaly. The equation is usually solved for E iteratively using the Newtonian method. To speed things up, Mikkola (1987) presented a direct method as solution using approximations and the following cubic form of the equation:

$$E = M + e(3s - 4s^3) \tag{3}$$

with

$$s = z - \alpha/z \tag{4}$$

$$z = (\beta \pm \sqrt{\beta^2 + \alpha^3})^{1/3} \tag{5}$$

$$\alpha = (1 - e)/(4e + 0.5) \tag{6}$$

$$\beta = 0.5M/(4e + 0.5) \tag{7}$$

After solving Kepler's equation for the eccentric anomaly, one could proceed with Thiele-Innes elements that relate the orbital elements with the three spatial coordinates (Binnendijk (1960); Heintz (1978)):

$$A = cos(\Omega)cos(\omega) - sin(\Omega)sin(\omega)cos(i) \tag{8}$$

$$B = sin(\Omega)cos(\omega) + cos(\Omega)sin(\omega)cos(i) \tag{9}$$

$$C = sin(\omega)sin(i) \tag{10}$$

$$F = -cos(\Omega)sin(\omega) - sin(\Omega)cos(\omega)cos(i) \tag{11}$$

$$G = -sin(\Omega)sin(\omega) + cos(\Omega)cos(\omega)cos(i) \tag{12}$$

$$H = cos(\omega)sin(i) \tag{13}$$

$$\epsilon = a(cos(E) - e) \tag{14}$$

$$\eta = a\sqrt{(1 - e^2)}sin(E) \tag{15}$$

$$Y = B\epsilon + G\eta \tag{16}$$

$$X = A\epsilon + F\eta \tag{17}$$

$$Z = C\epsilon + H\eta \tag{18}$$

Where Y is the right ascension, X is the declination and Z is along the line of sight.

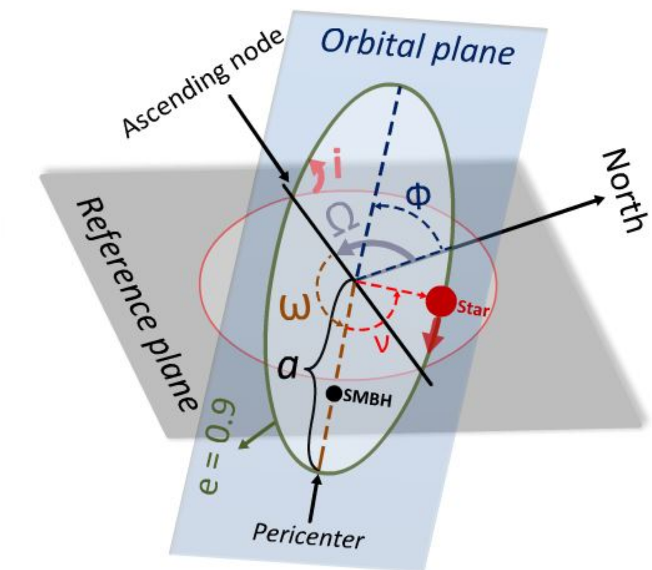

Figure 1. *An illustration of the Keplerian elements (a, e, i, Ω,ω, T_p)*

2.2. *Details of the Methods*

2.2.1. *Priors*

An important step before running the algorithms is to define the nature of the priors for the fitting. We choose the Galactic center (GC) environment with informative Gaussian priors for the central black hole mass and distance to the GC with $m_0 = 4.154 \pm 0.014\ 10^6 M_{solar}$ and $D_0 = 8178 \pm 35$ (The GRAVITY Collaboration et al. (2019)). As for the orbital elements, the prior of the semi-major axis is chosen to be uniform in log space, uniform priors for e^2 and $cos(i)$, and uniform priors for each of Ω,ω and T_p. Concerning the boundaries of each elements, the semi-major axis ranges from 1 mpc to 100 mpc, the eccentricity between 0.001 and 0.999, the inclination between 0 and π, Ω and ω between 0 and 2π, and T_p between 2000 and 2050.

2.2.2. *Model*

Having defined the priors, we can now proceed by creating a dataset within the same time-span as the real dataset using Thiele-Innes elements (Binnendijk (1960); Heintz (1978)), where Kepler's equation is solved using the approach of Mikkola (1987). More specifically, for MCMCA, one needs to define the log-likelihood function (LL) as follows:

$$LL = -0.5 \times \sum [((R.A. - Y)/raerr)^2 + ((Dec. - X)/decerr)^2] \tag{19}$$

Where Dec. and R.A. are coordinates of the real dataset with their corresponding uncertainties (raerr, decerr), and X,Y are the simulated dataset with the same time span. As for NS, a prior transform step is required before one defines the log-likelihood function. Unlike the latter two, ABC doesn't require the likelihood function to be defined, rather it is approximated using simulations. More precisely, one needs to set a threshold and a distance before running the algorithm. After setting up the requirements of each approach, one proceeds by running the sampler and storing the results for interpretation. The details of each sampler are summarized in Table 1.

3. RESULTS

3.1. *Mock data*

For comparing all 8 approaches, we generate mock datasets for short-period and long-period orbits with similar uncertainties to the observed dataset, which is around half a pixel (see Table 2). We then run the samplers and plot the results in a customized corner plot, which is able to detect multimodal posteriors and show the 95% confidence interval. The results can be summarized as follows:

1. MCMCA: We find that all three approaches of MCMCA fail in detecting the required multimodal posteriors. For the short-period orbit (SPO), we find that emcee (Goodman & Weare (2010)) gives two modes for each of a, e and i where they should have only one mode. The modes of ω are detected, however, only one mode is prominent. while only one mode was achieved for Ω. The situtation is similar for the long-period orbit (LPO) where also several false modes are detected for all parameters (see Figures 2, 3). As for kombine (Farr & Farr (2015)), we find that it fails in providing the correct solution for both the SPO and LPO (see Figures 4, 5). On the other hand, Bilby-MCMC (Ashton & Talbot (2021)) was able to find only one mode of each ω and Ω with correct values for each of a, e, i, m_0 and D_0 (see Figure 6). However, a drawback of this approach is the very long computation time. Due to the latter disadvantage, it was not possible to derive any solution to the LPO. In conclusion, we find that MCMCA are not recommended with the provided sampling parameters for the orbital fitting problem.

2. NS: All NS approaches were able to find the required solutions for the SPO with the derived uncertainties for Dynamical NS (Higson et al. (2018); Speagle (2020)) being much larger than Nestle (Barbary (2021)) and Ultranest (Buchner (2021, 2019, 2016)). As for the LPO, Nestle fails to

Sampler	Reference	Details
emcee - MCMC	Goodman & Weare (2010)	walkers = 500, iterations = 4000, burn-in fraction = 0.5
kombine - MCMC	Farr & Farr (2015)	walkers = 500, iterations = 4000, test steps = 16
Bilby-MCMC	Ashton & Talbot (2021)	number of samples = 1000, number of parallel-tempered chains = 16
Nestle - NS	Barbary (2021)	number of live points = 400, method = 'multi' (Shaw et al. (2007)), decline factor = 1.0
Dynesty - Dynamical NS	Speagle (2020), Higson et al. (2018)	number of initial live points = 5000, batch = 1000 live points, bounds = multi (Buchner (2016)), sampling = slice (Skilling (2006))
Ultranest - NS	Buchner (2021, 2019), Buchner (2016)	number of live points = 8000, sampling = slice sampler with mixture random direction and no region filter
ELFI - ABC	Lintusaari et al. (2018)	sampling = ABCSMC (Toni & Stumpf (2009)), distance = Euclidean threshold = a list from 0.7 to 0.01, N samples = 1000
ELFI - ABC	Lintusaari et al. (2018)	sampling = ABCSMC (Toni & Stumpf (2009)), distance = Manhattan threshold = a list from 0.7 to 0.01, N samples = 1000

Table 1. A list of the 8 approaches with their corresponding references and sampling parameters.

derive the correct value for the semi-major axis, while successfully estimating the remaining posteriors with greater uncertainties than the case of the SPO. This is expected, since the number of possible orbits is much higher than in the case of the SPO. On the other hand, both dynamical NS and Ultranest were able to derived the required posteriors with the uncertainties of Ultranest being more reasonable and smaller than the ones of dynamical NS. In conclusion, we find that Ultranest outperforms both Nestle and DNS (see Figures 7, 8, 9, 10, 11, 12).

3. ABC: Even though the algorithm is showing similar behaviour to the approaches of NS, the long required computation time makes this method less favourable. In greater detail, we find that using Manhattan distance the three modes of ω were detected, while using Euclidean distance gives only two modes for LPO. Nevertheless, the remaining posteriors are more or less the same. As for SPO, both distances show the same outcome (see Figures 13, 14, 16, 15).

Consequently, NS outperforms both MCMCA and ABC with Ultranest being the optimal recommended choice for the orbital fitting problem.

3.2. *Application on real dataset (S2)*

After comparing all approaches, we proceed with Ultranest and apply it on the S-cluster star S2. The data acquisition is described in detail in Ali et al. (2020) and the astrometric data with their corresponding uncertainties were used for the purpose of this work. We note that before running the algorithm, the range of both the semi-major axis and t_p were decreased to [1 - 30 mpc] and [2000 - 2030 yr] respectively. The latter step is helpful is decreasing the computation time and in restricting the large parameter space. In addition, the results were achieved after several runs in parallel on multiple cores with each having an initial live points of 10^4. Not obtaining the solution after one run could be to several reasons; one of which is the difference between the quality of the observed data points and the simulated one. Secondly, the range of likelihood of the initial live points might have not been close enough to the real solution and hence didn't lead to proper convergence or clearly detecting the second mode. The problem can be also solved by increasing N live points to 10^5, however, this requires a greater computation power and hence executing several 10^4 runs in parallel on several cores is more efficient. In Figure 17, we show the outcome of applying Ultranest on S2. As can be seen, the algorithm is able to clearly detect the two modes of ω and Ω and derive the remaining parameters with great agreement with the published orbital elements (see Table 3). In further de-

1.	2.	3.	4.	5.	6.	7.
Orbit	a [mpc]	e	i [deg]	Ω [deg]	ω [deg]	t_p [yr]
Short-period orbit	5	0.7	90	45	90	2005
Long-period orbit	50	0.7	45	0	135	2005

Table 2. A list of the orbital elements for the mock datasets of the short-orbit period and long-period orbit. The Keplerian elements start with the semi-major axis (a), eccentricity (e), inclination (i), argument at the pericenter (ω), longitude of ascending node (Ω) and time of closest approach (t_p).

tail, it took around 18 million likelihood evaluations for reaching convergence with an evidence estimate of -60.63 $\pm$ 0.04363 and an effective sample size (ESS) of 67375.6. In addition, the algorithm explored the parameter space until a log-likelihood of -23.66.

4. DISCUSSION AND CONCLUSION

We demonstrated that using NS as a methodology for deriving multimodal posteriors of the 8-dimensional orbital fitting problem is more efficient than both MCMCA and ABC. On the one hand, the failure of MCMCA with the given details in Table 1 may be attributed to the walkers being stuck in local minima and hence not being able to clearly detect the second mode of the posteriors. On the other hand, ABC performance is similar to NS, however, the long required computation time makes this approach unfavourable.

As mentioned above, Ultranest is chosen to be the optimal option for the current problem in regard to both computational speed and uncertainty estimation. This outcome is somehow expected since, as explained in detail in Buchner (2021, 2019, 2016), the algorithm implements a better uncertainty estimation strategy than the one in nestle (Barbary (2021)) or dynesty (Speagle (2020)). The strategy takes into account the scatter in both volume estimates and likelihood estimates, while the other two approaches include a static volume uncertainty estimate. In addition, Ultranest supports parallelization on multiple cores, which allows for a faster computational speed. As can be seen above, we find that Ultranest is able to clearly detect the two solution for the well-known orbit of S2 with great agreement with the literature. Finally, a detailed discussion of the theoretical background of all three methodologies is beyond the scope of this work.

Acknowledgments:

We received funding from the European Union Seventh Framework Program (FP7/2007-2013) under grant agreement No. 312789—Strong gravity: Probing Strong Gravity by Black Holes Across the Range of Masses. This work was supported in part by the Deutsche Forschungsgemeinschaft (DFG) via the Cologne Bonn Graduate School (BCGS), the Max Planck Society through the International Max Planck Research School (IMPRS) for Astronomy and Astrophysics, as well as special funds through the University of Cologne and CRC956— Conditions and Impact of Star Formation under project A2. We thank the German Academic Exchange Service (DAAD) for support under COPRAG2015 (No.57147386) and the the Czech Science Foundation—DFG collaboration (EC 137/10-1).

1.	2.	3.	4.	5.	6.	7.	8.	9.
Star	a ± Δa	e ± Δe	i ± Δi	Ω ±ΔΩ	ω ± Δω	t_p ± Δt_p	m_0 ± Δm_0	D_0 ± ΔD
	[mpc]		[deg]	[deg]	[deg]	[yr]	[$M_\odot$x10^6]	[pc]
S2	$5.09^{+0.27}_{-0.26}$	$0.88^{+0.02}_{-0.02}$	$135.22^{+2.33}_{-2.47}$	$55.10^{+18.36}_{-18.25}$ $235.26^{+17.90}_{-18.02}$	$71.06^{+15.62}_{-15.61}$ $251.02^{+15.83}_{-15.83}$	$2017.98^{+0.13}_{-0.15}$	$4.15^{+0.03}_{-0.02}$	$8175.63^{+72.47}_{-64.85}$

Table 3. The results of applying Ultranest on the Star S2. The Keplerian elements start with the semi-major axis (a), eccentricity (e), inclination (i), argument at the pericenter (ω), longitude of ascending node (Ω) and time of closest approach (t_p). The mass of Sgr A* is listed as m_0 and the distance to the Galactic center as D_0.

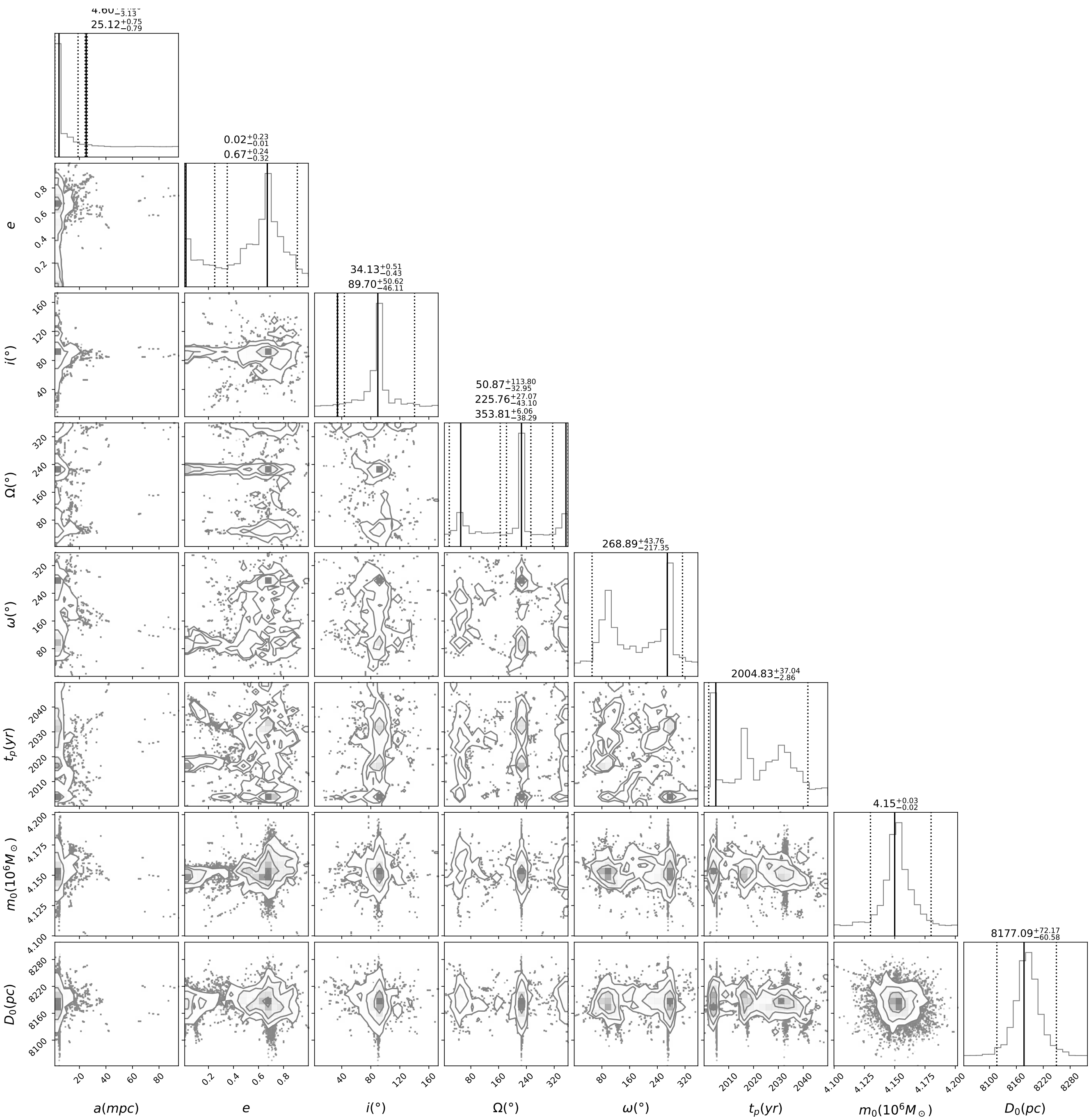

Figure 2. *A customized corner plot of the emcee-MCMC approach for SPO. The eight parameters are the semi-major axis (a), eccentricity (e), inclination (i), argument at the pericenter (ω), longitude of ascending node (Ω) and time of closest approach (t_p), mass of the SMBH (m_0) and distance to the GC (D_0). The uncertainties represent the 95% confidence interval.*

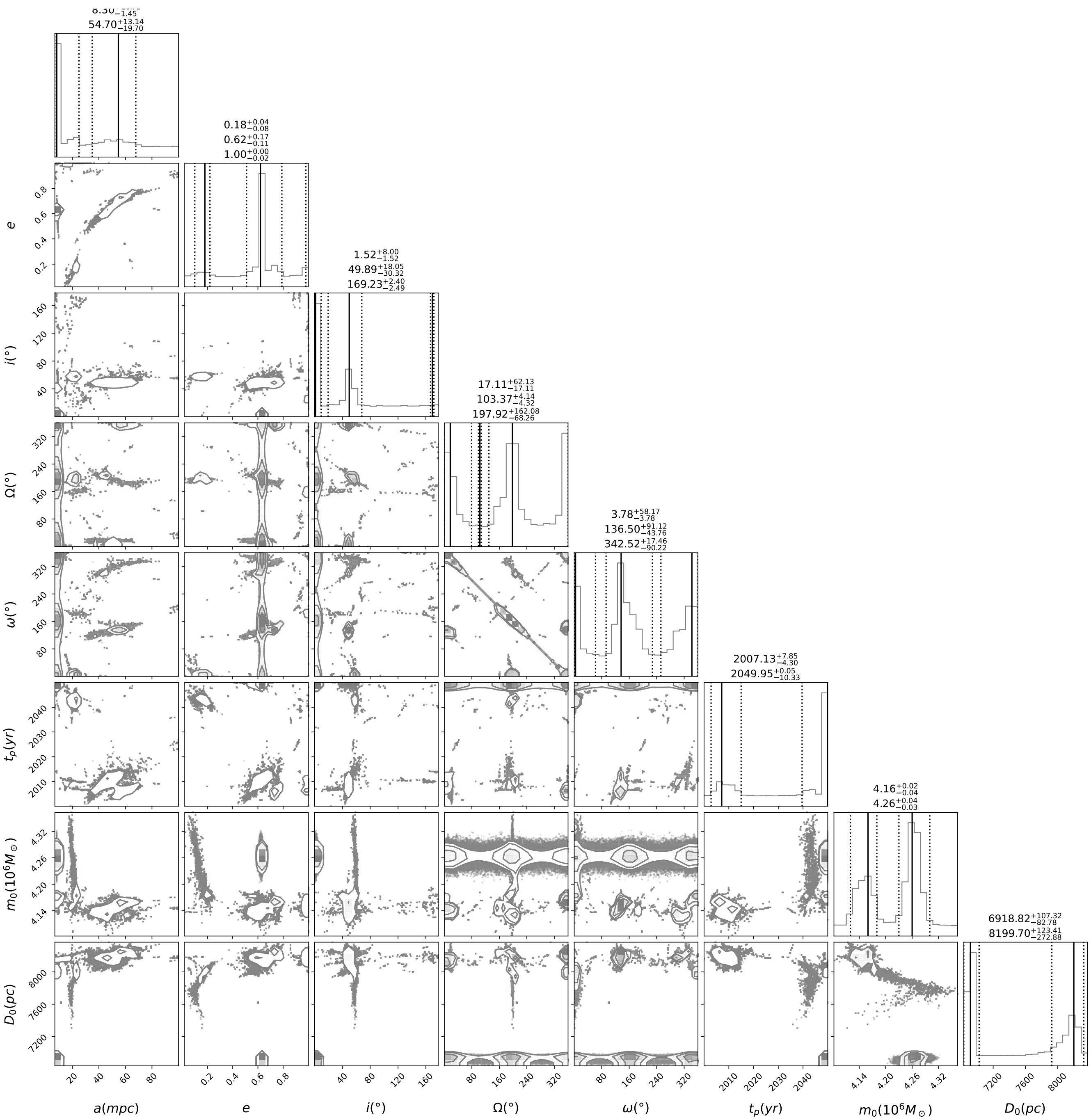

Figure 3. *A customized corner plot of the emcee-MCMC approach for LPO. The eight parameters are the semi-major axis (a), eccentricity (e), inclination (i), longitude of ascending node (Ω), argument at the pericenter (ω), time of closest approach (t_p), mass of the SMBH (m_0) and distance to the GC (D_0). The uncertainties represent the 95% confidence interval.*

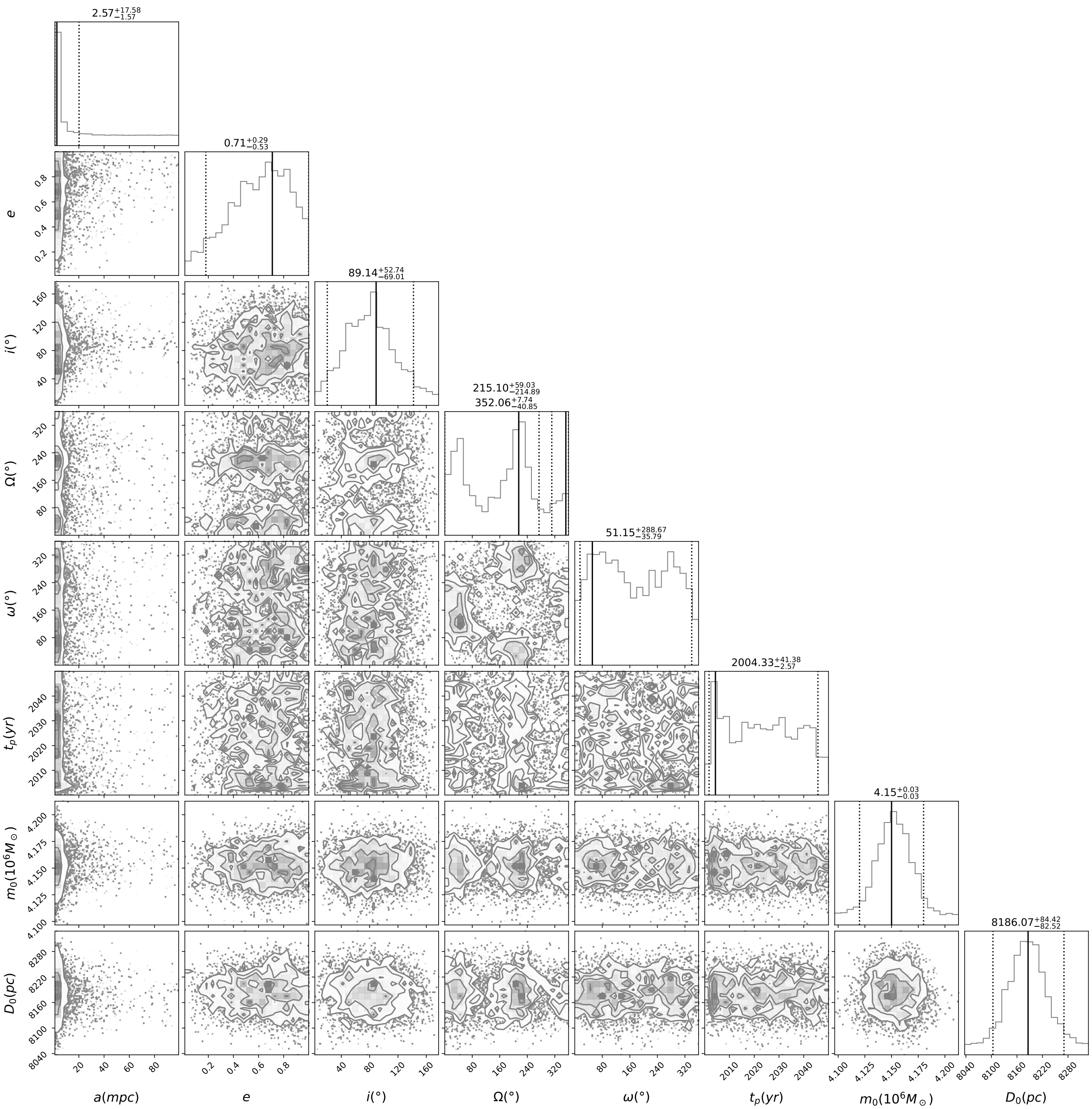

Figure 4. *A customized corner plot of the kombine-MCMC approach for SPO. The eight parameters are the semi-major axis (a), eccentricity (e), inclination (i), longitude of ascending node (Ω), argument at the pericenter (ω), time of closest approach (t_p), mass of the SMBH (m_0) and distance to the GC (D_0). The uncertainties represent the 95% confidence interval.*

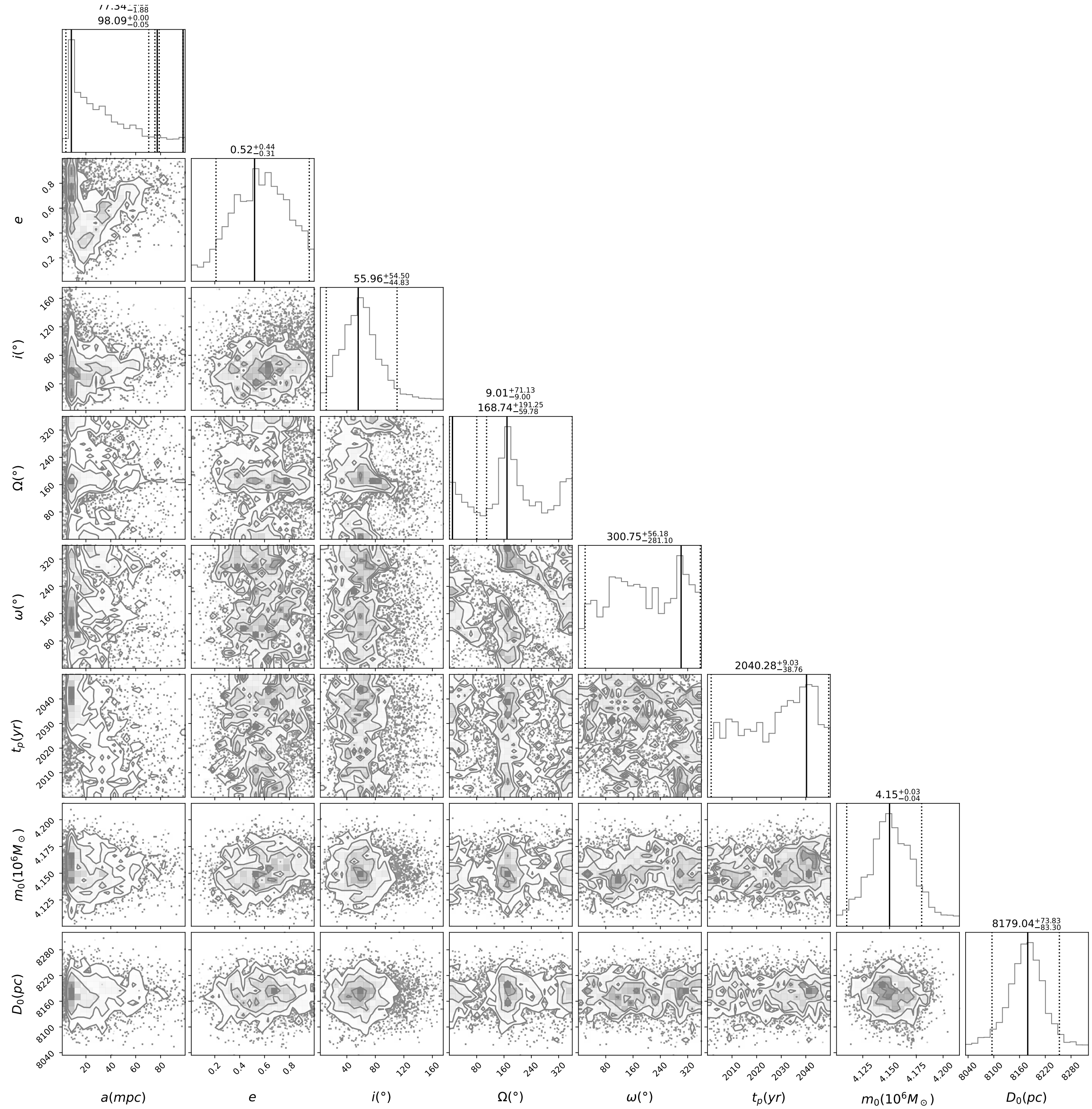

Figure 5. *A customized corner plot of the kombine-MCMC approach for LPO. The eight parameters are the semi-major axis (a), eccentricity (e), inclination (i), longitude of ascending node (Ω), argument at the pericenter (ω), time of closest approach (t_p), mass of the SMBH (m_0) and distance to the GC (D_0). The uncertainties represent the 95% confidence interval.*

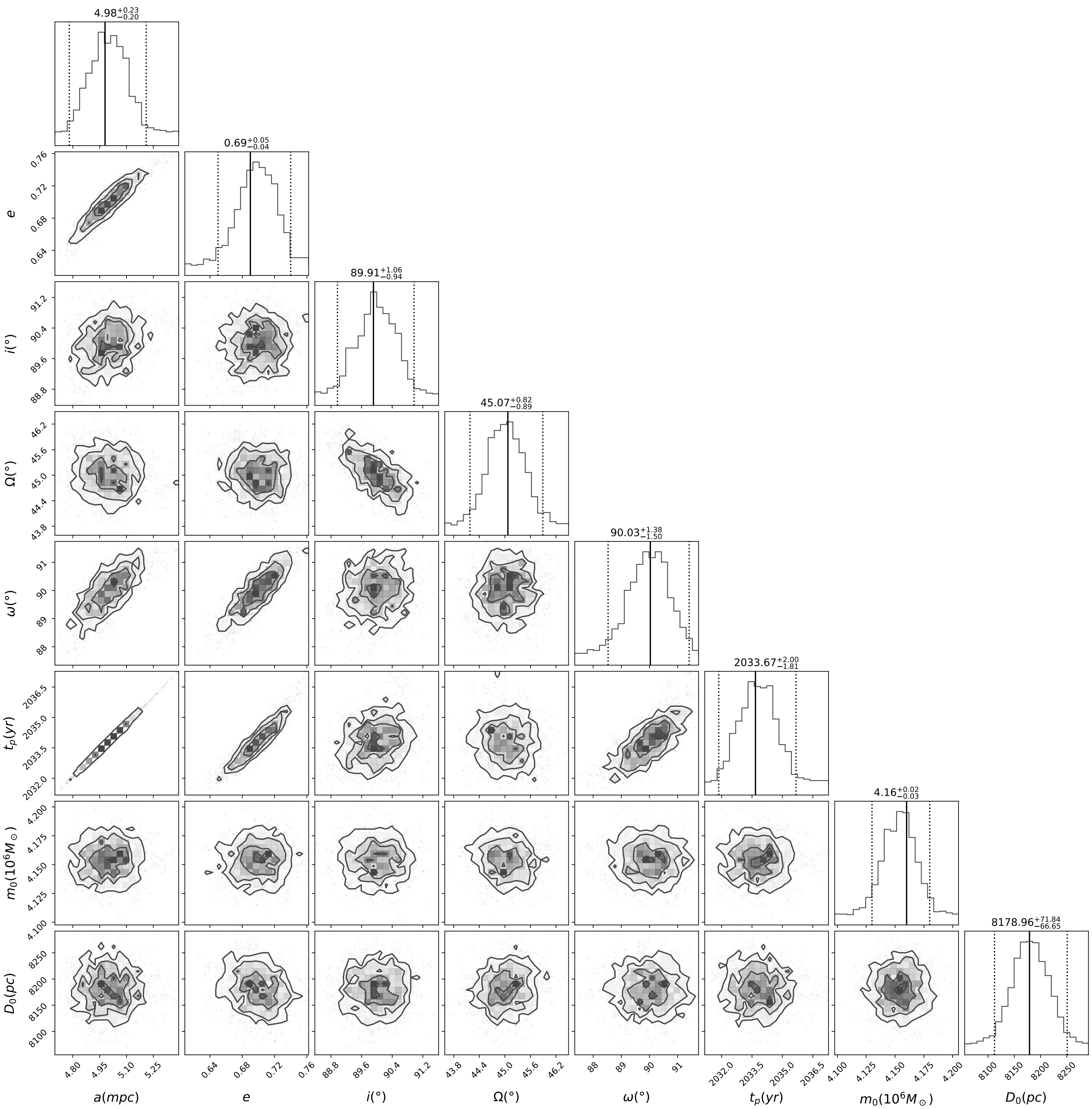

Figure 6. *A customized corner plot of the bilby-MCMC approach for SPO. The eight parameters are the semi-major axis (a), eccentricity (e), inclination (i), longitude of ascending node (Ω), argument at the pericenter (ω), time of closest approach (t_p), mass of the SMBH (m_0) and distance to the GC (D_0). The uncertainties represent the 95% confidence interval.*

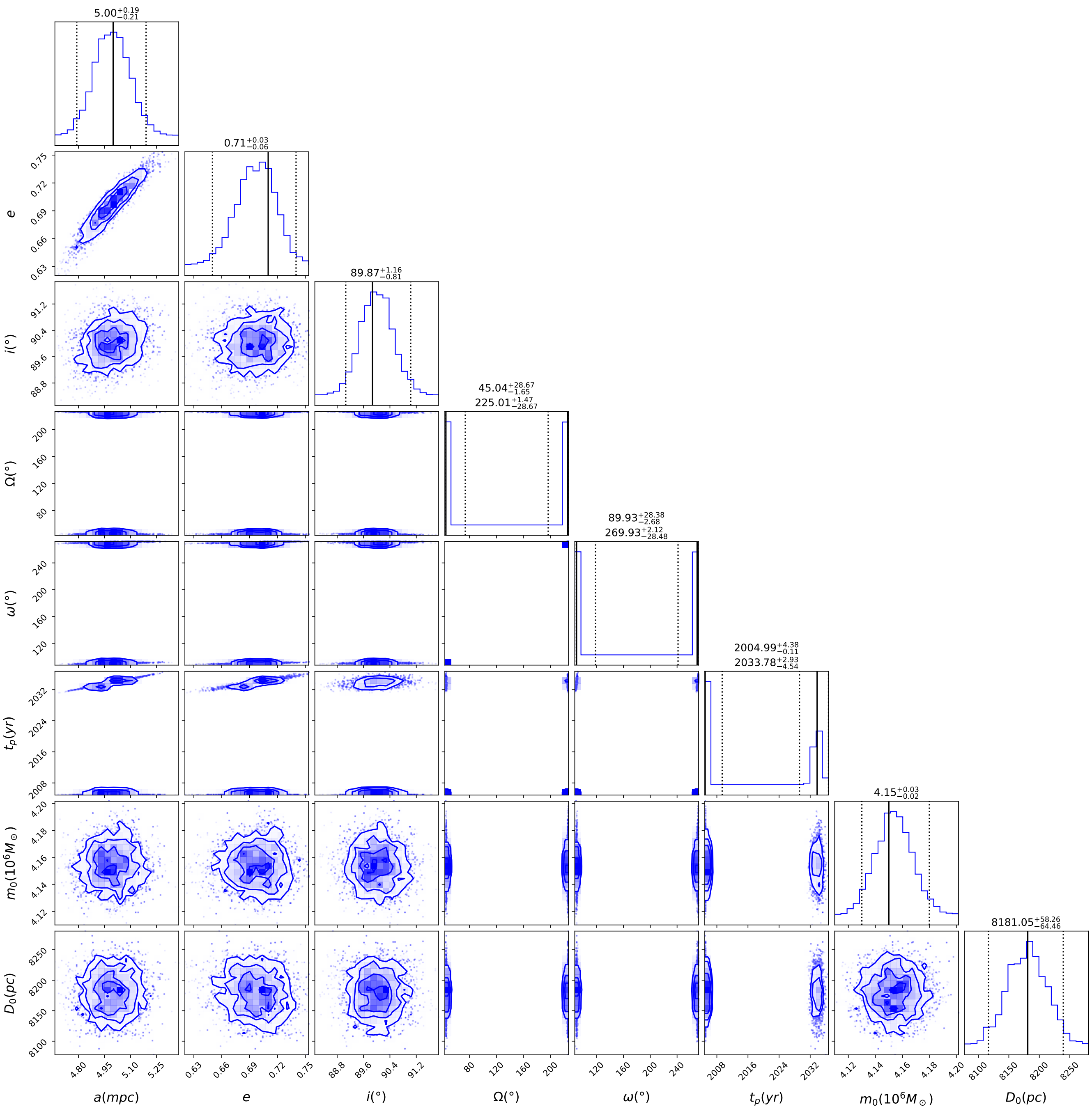

Figure 7. *A customized corner plot of the nestle-NS approach for SPO. The eight parameters are the semi-major axis (a), eccentricity (e), inclination (i), longitude of ascending node (Ω), argument at the pericenter (ω), time of closest approach (t_p), mass of the SMBH (m_0) and distance to the GC (D_0). The uncertainties represent the 95% confidence interval.*

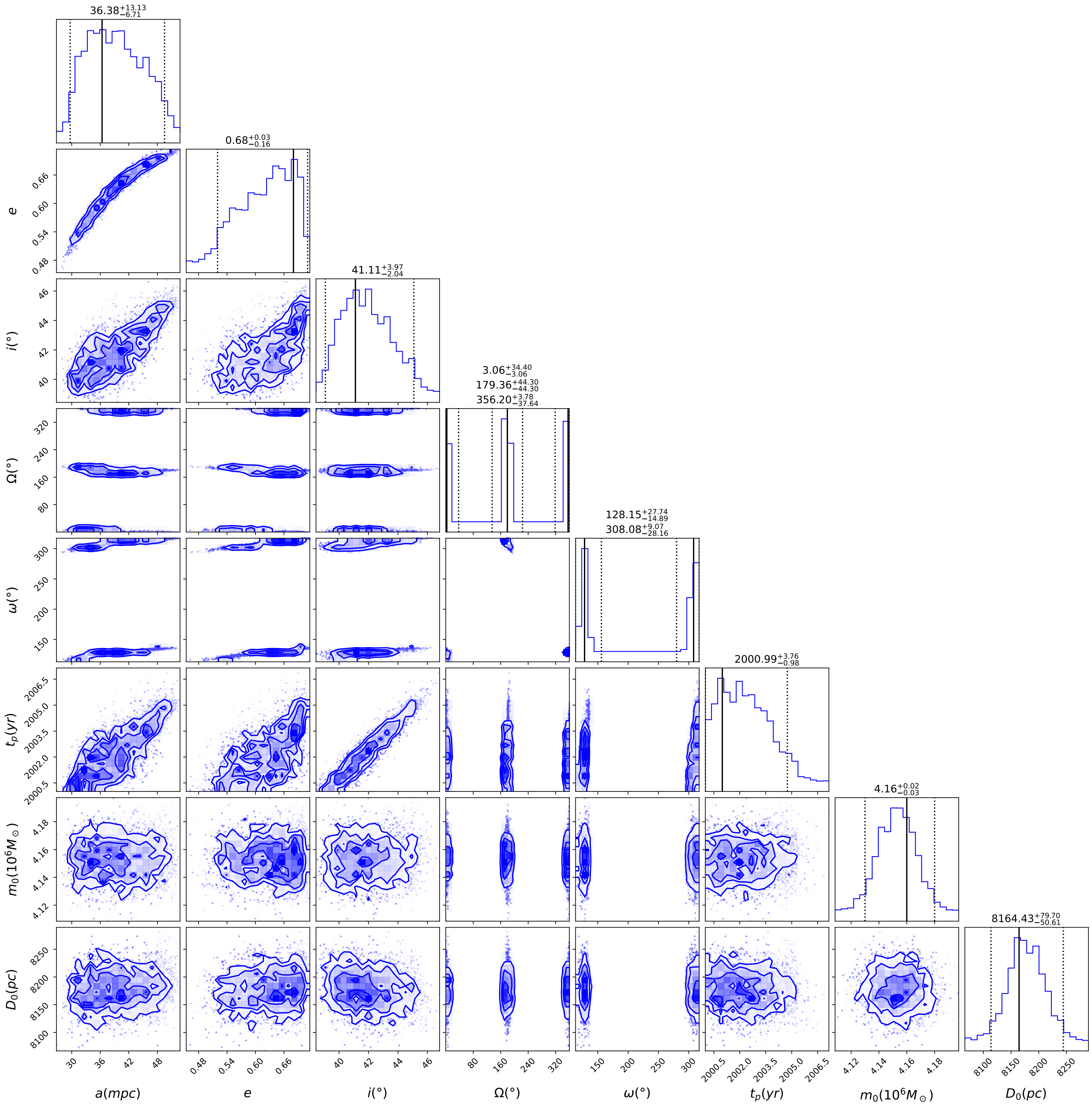

Figure 8. *A customized corner plot of the nestle-NS approach for LPO. The eight parameters are the semi-major axis (a), eccentricity (e), inclination (i), longitude of ascending node (Ω), argument at the pericenter (ω), time of closest approach (t_p), mass of the SMBH (m_0) and distance to the GC (D_0). The uncertainties represent the 95% confidence interval.*

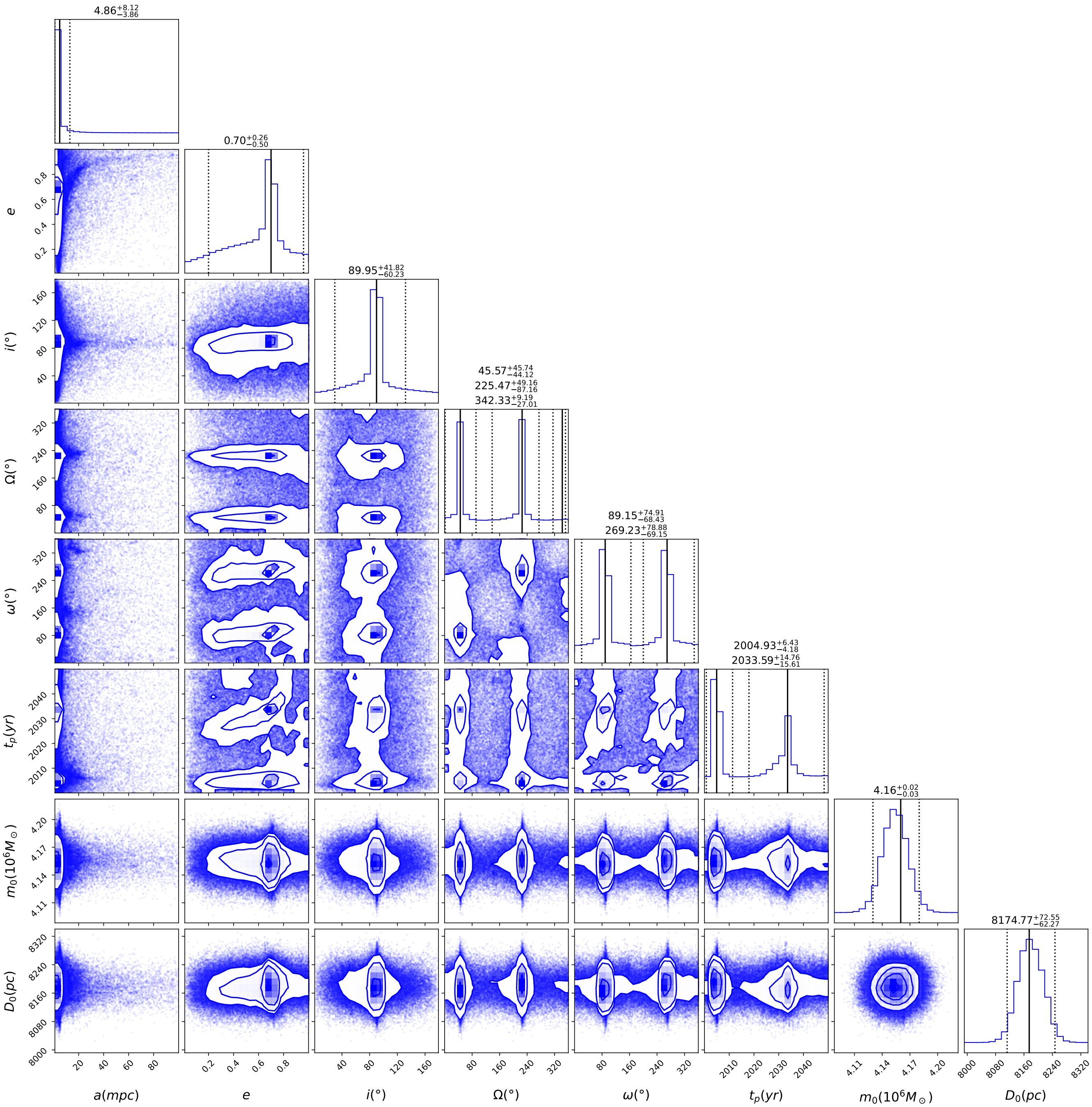

Figure 9. *A customized corner plot of the dynesty-Dynamical NS approach for SPO. The eight parameters are the semi-major axis (a), eccentricity (e), inclination (i), longitude of ascending node (Ω), argument at the pericenter (ω), time of closest approach (t_p), mass of the SMBH (m_0) and distance to the GC (D_0). The uncertainties represent the 95% confidence interval.*

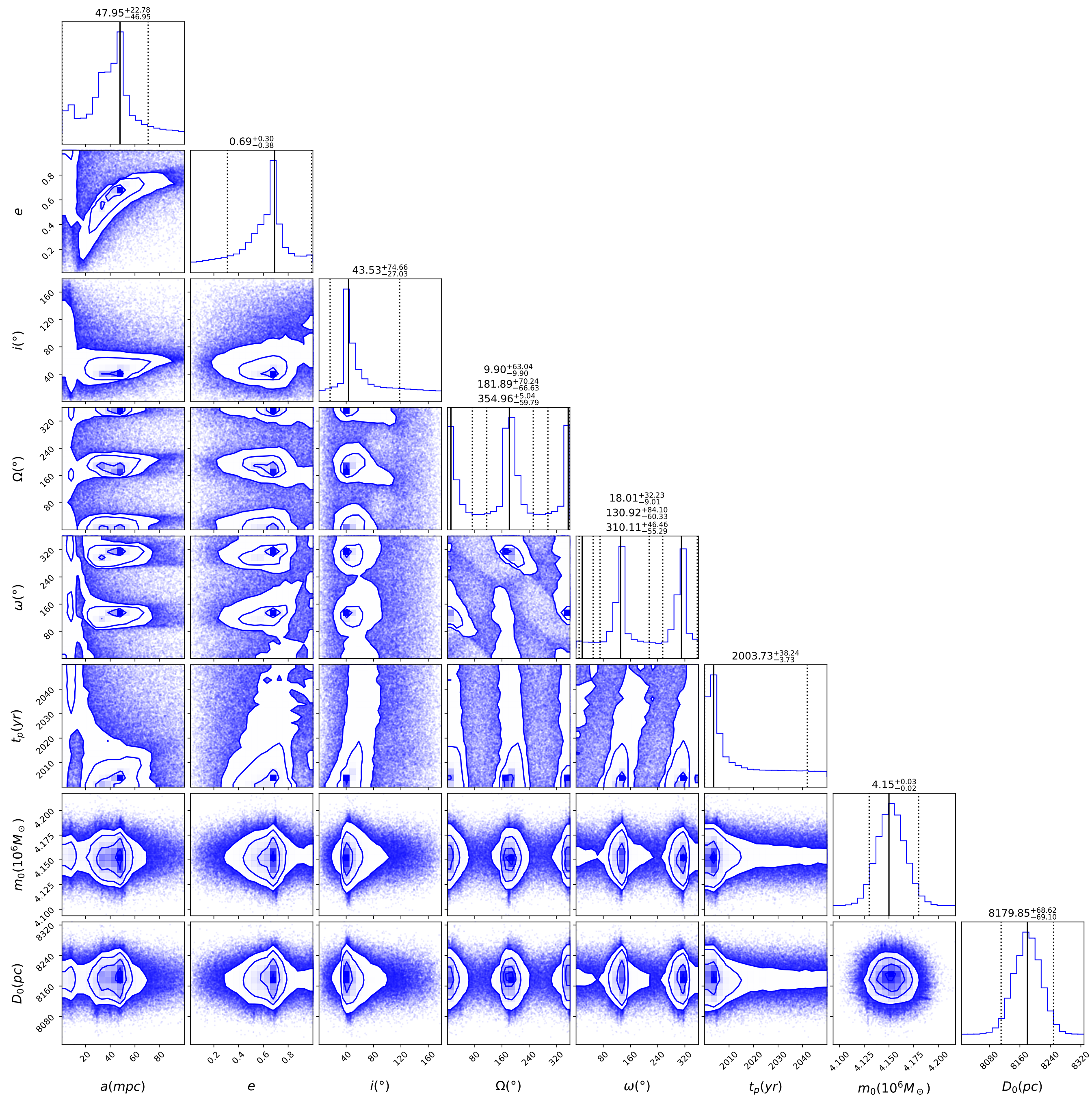

Figure 10. *A customized corner plot of the dynesty-Dynamical NS approach for LPO. The eight parameters are the semi-major axis (a), eccentricity (e), inclination (i), longitude of ascending node (Ω), argument at the pericenter (ω), time of closest approach (t_p), mass of the SMBH (m_0) and distance to the GC (D_0). The uncertainties represent the 95% confidence interval.*

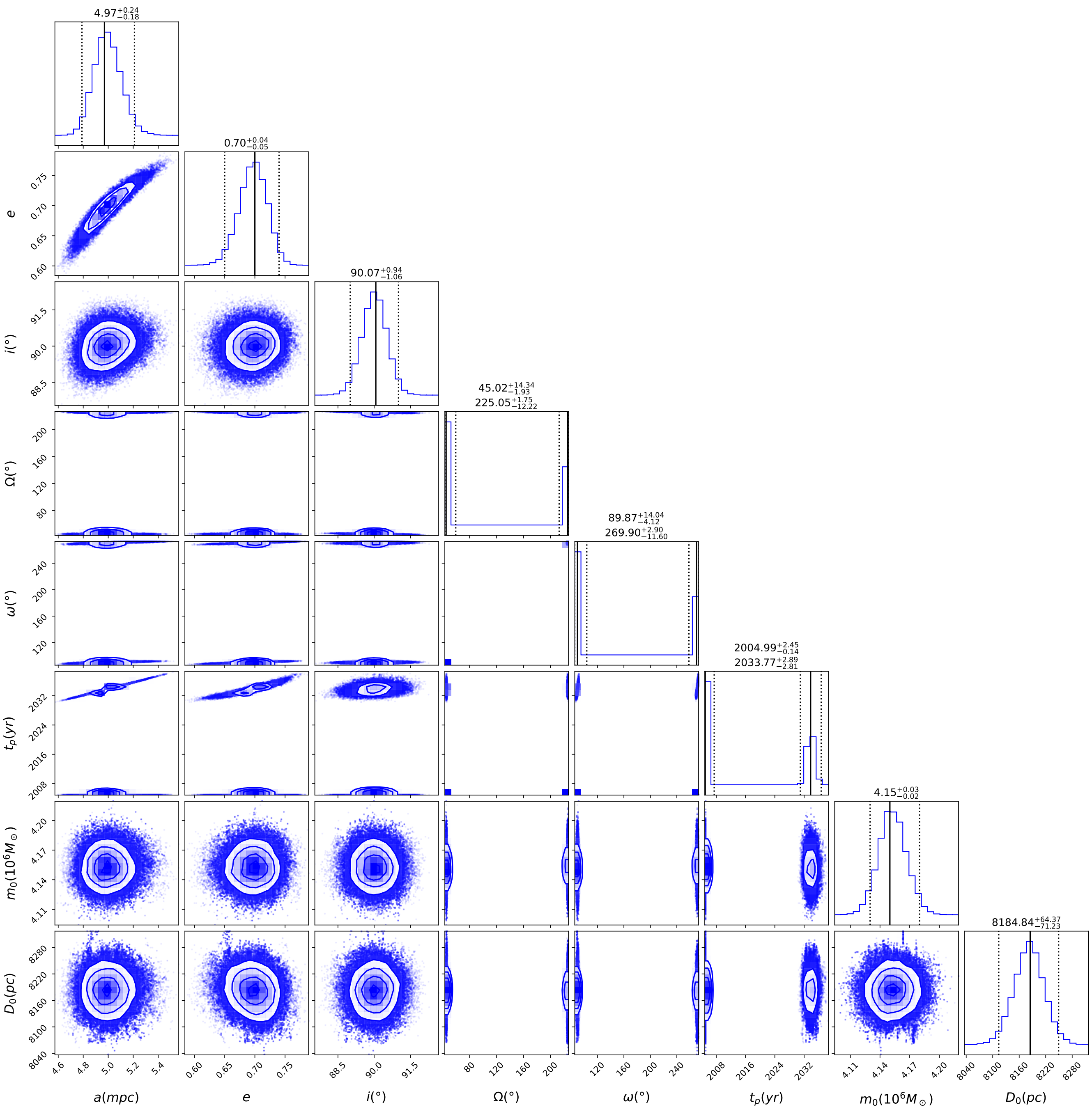

Figure 11. *A customized corner plot of the Ultranest-NS approach for SPO. The eight parameters are the semi-major axis (a), eccentricity (e), inclination (i), longitude of ascending node (Ω), argument at the pericenter (ω), time of closest approach (t_p), mass of the SMBH (m_0) and distance to the GC (D_0). The uncertainties represent the 95% confidence interval.*

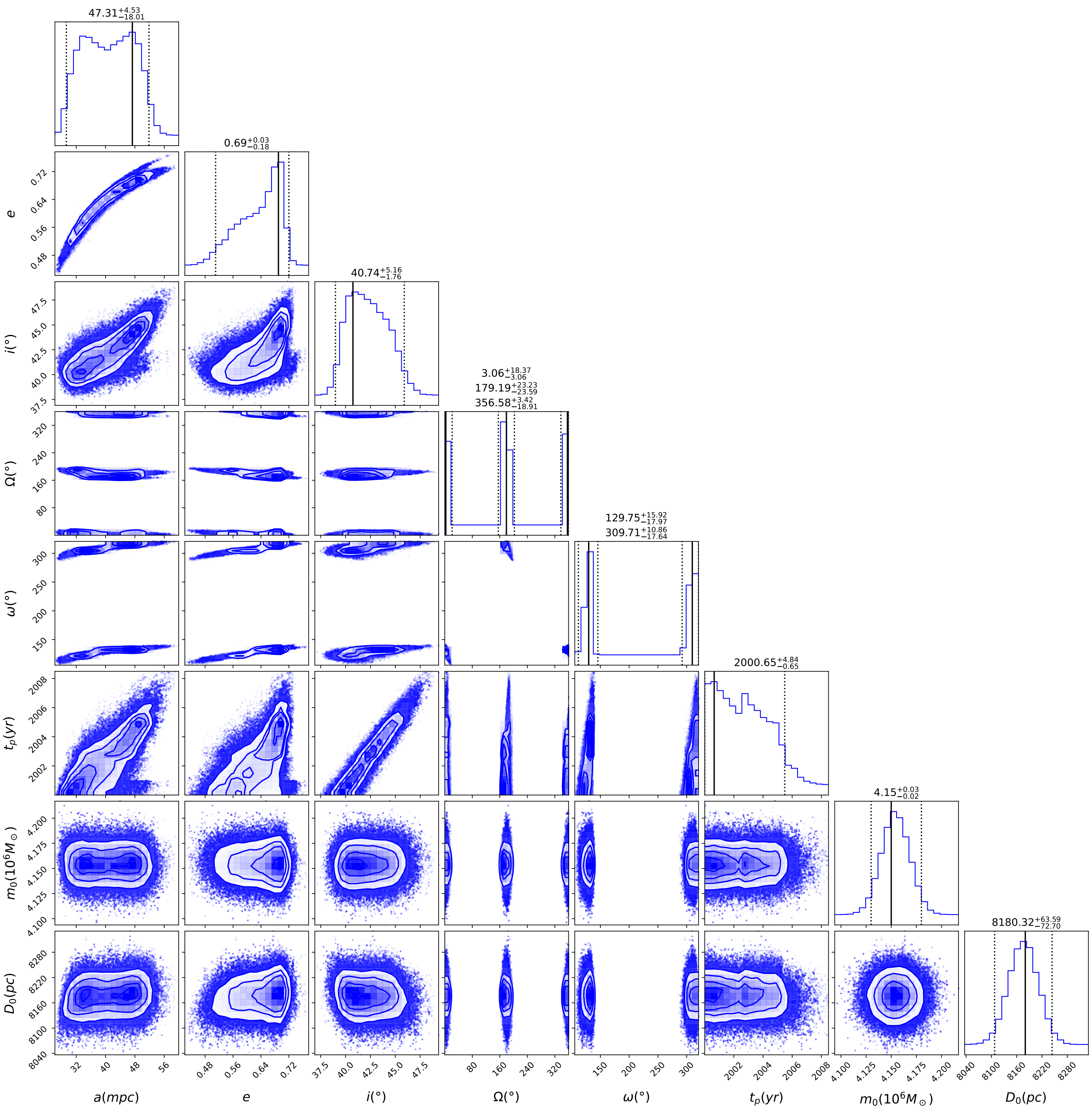

Figure 12. *A customized corner plot of the Ultranest-NS approach for LPO. The eight parameters are the semi-major axis (a), eccentricity (e), inclination (i), longitude of ascending node (Ω), argument at the pericenter (ω), time of closest approach (t_p), mass of the SMBH (m_0) and distance to the GC (D_0). The uncertainties represent the 95% confidence interval.*

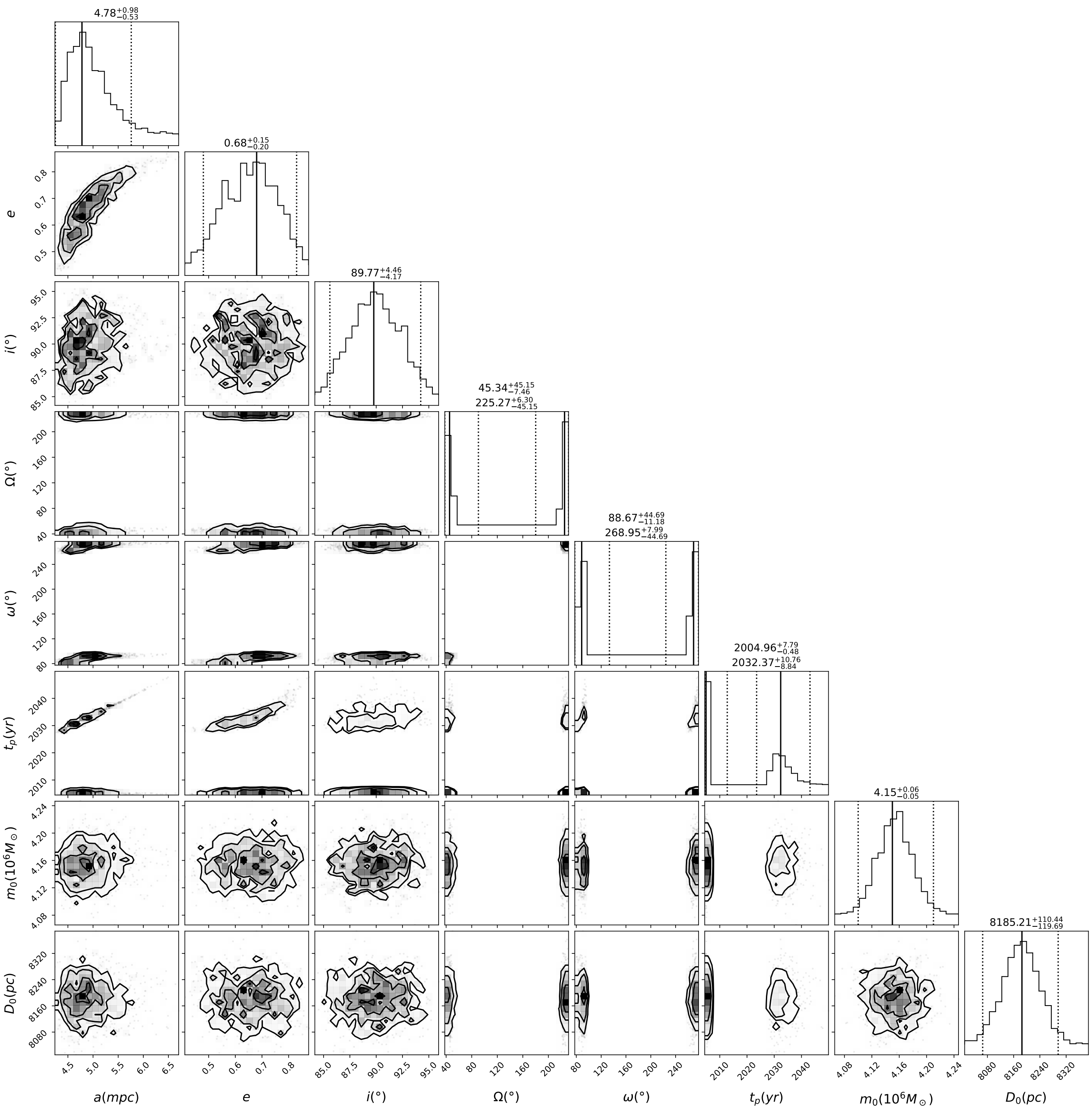

Figure 13. *A customized corner plot of the ELFI-ABC-Euclidean approach for SPO. The eight parameters are the semi-major axis (a), eccentricity (e), inclination (i), longitude of ascending node (Ω), argument at the pericenter (ω), time of closest approach (t_p), mass of the SMBH (m_0) and distance to the GC (D_0). The uncertainties represent the 95% confidence interval.*

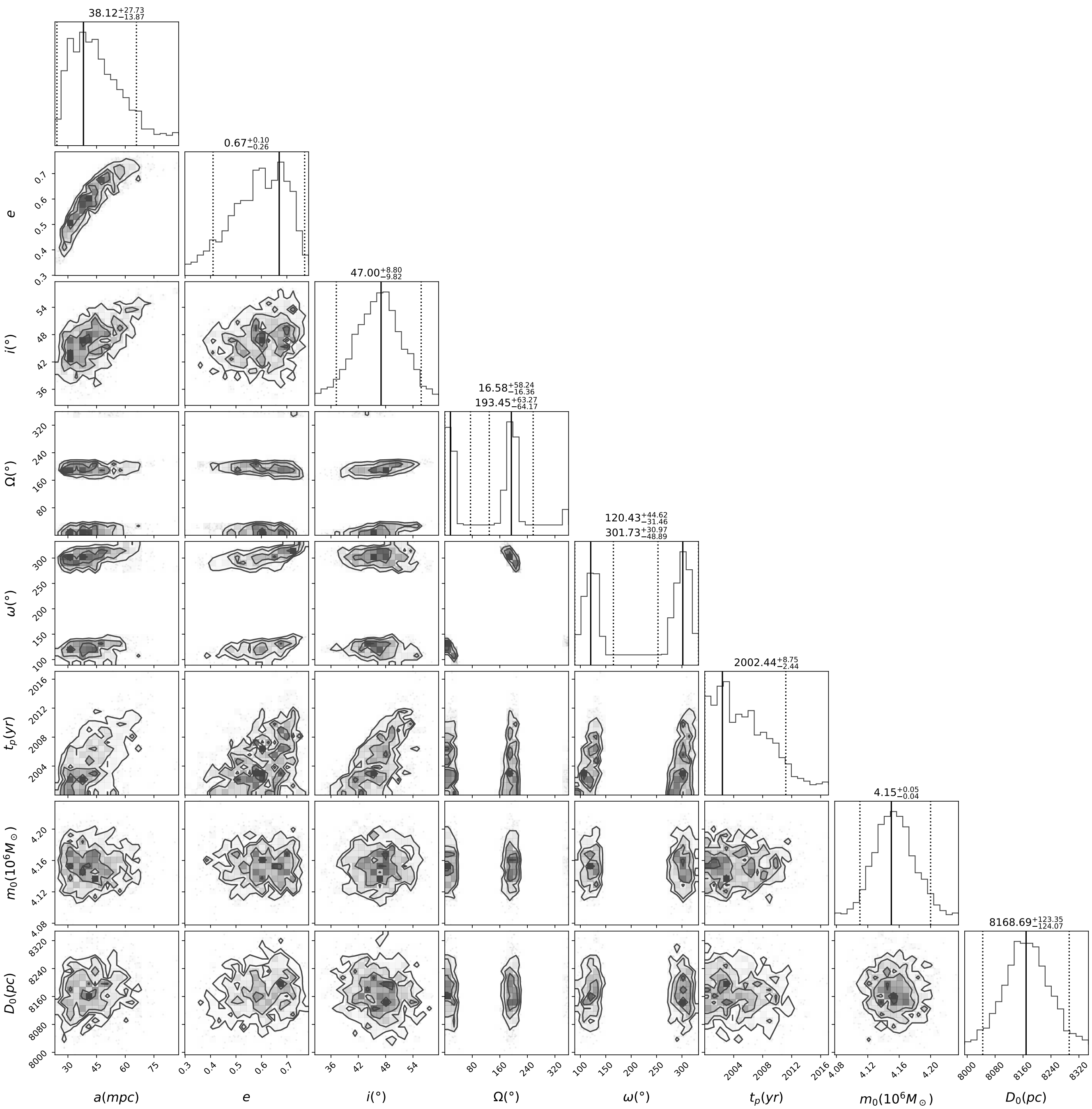

Figure 14. *A customized corner plot of the ELFI-ABC-Euclidean approach for LPO. The eight parameters are the semi-major axis (a), eccentricity (e), inclination (i), longitude of ascending node (Ω), argument at the pericenter (ω), time of closest approach (t_p), mass of the SMBH (m_0) and distance to the GC (D_0). The uncertainties represent the 95% confidence interval.*

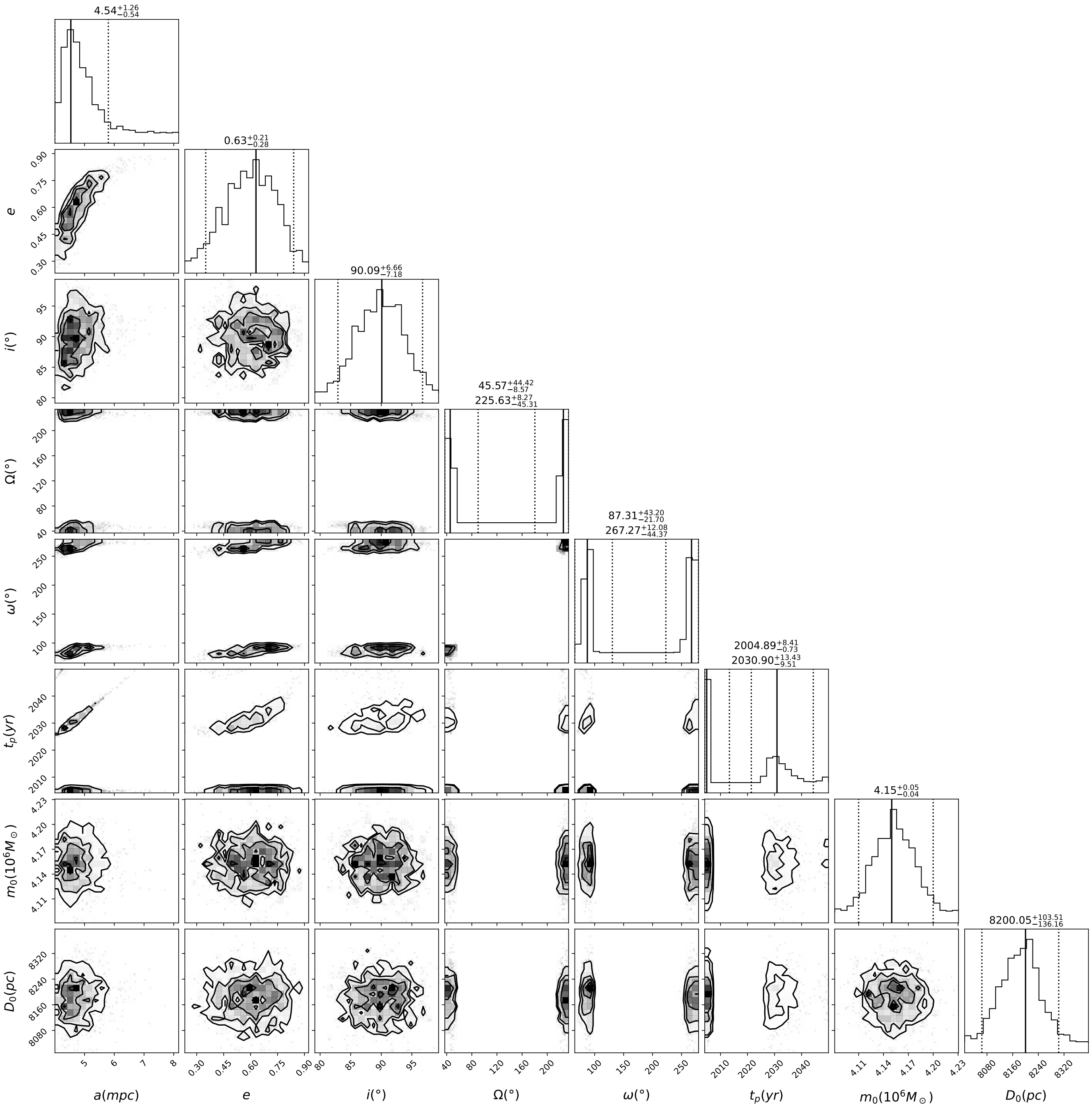

Figure 15. *A customized corner plot of the ELFI-ABC-Manhattan approach for SPO. The eight parameters are the semi-major axis (a), eccentricity (e), inclination (i), longitude of ascending node (Ω), argument at the pericenter (ω), time of closest approach (t_p), mass of the SMBH (m_0) and distance to the GC (D_0). The uncertainties represent the 95% confidence interval.*

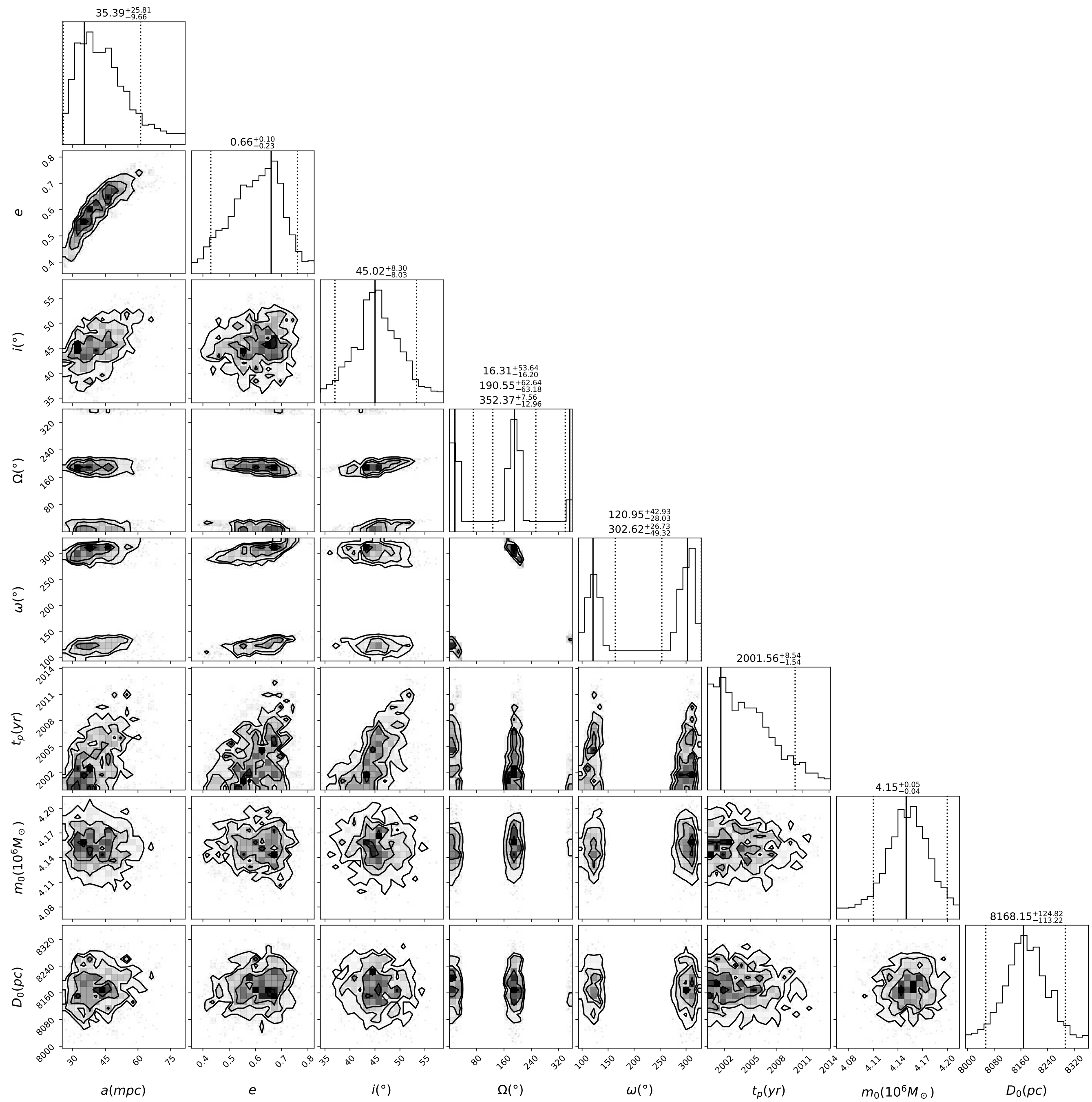

Figure 16. *A customized corner plot of the ELFI-ABC-Manhattan approach for LPO. The eight parameters are the semi-major axis (a), eccentricity (e), inclination (i), longitude of ascending node (Ω), argument at the pericenter (ω), time of closest approach (t_p), mass of the SMBH (m_0) and distance to the GC (D_0). The uncertainties represent the 95% confidence interval.*

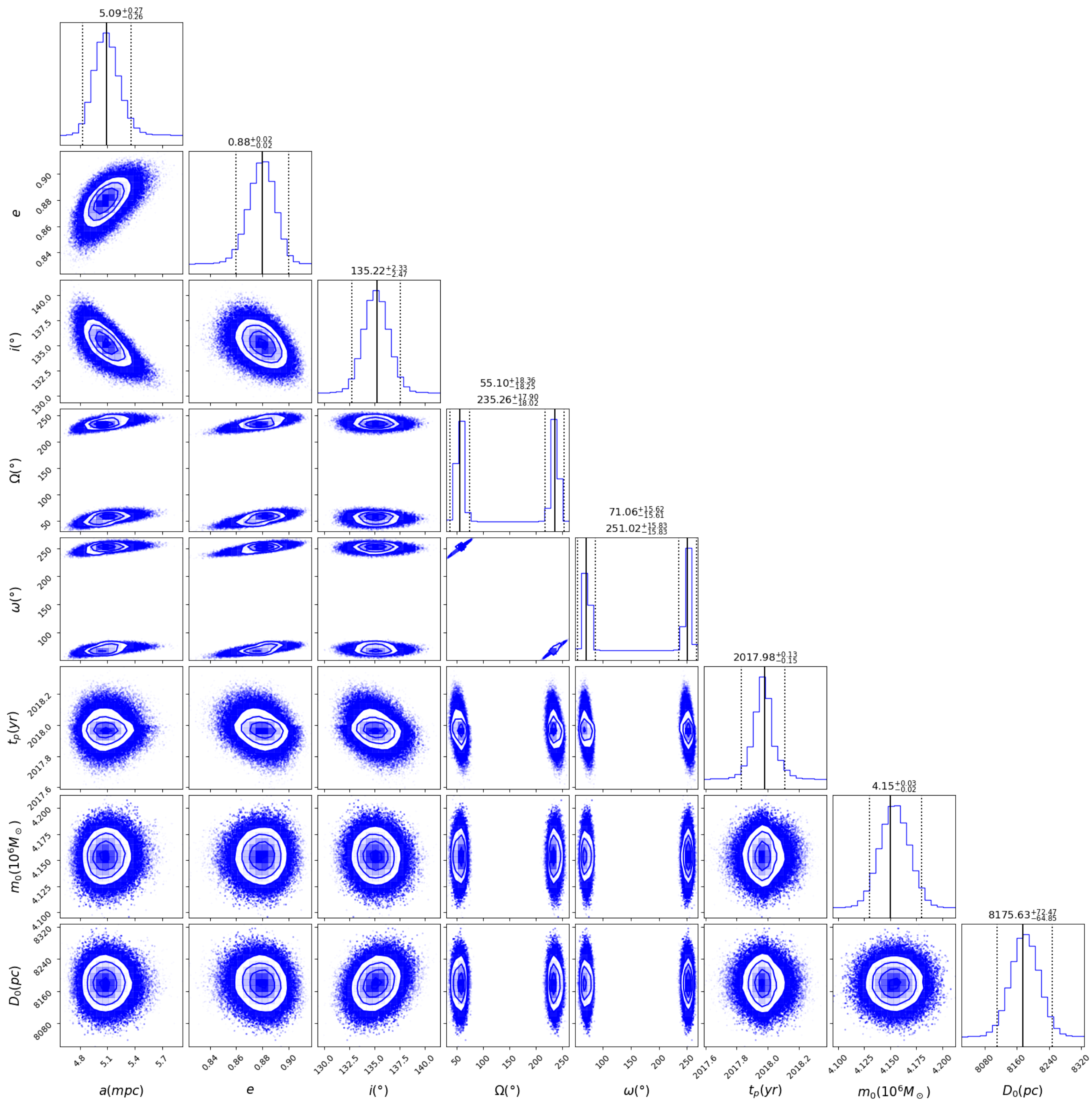

Figure 17. *A customized corner plot of the orbit of S2 using Ultranest. The eight parameters are the semi-major axis (a), eccentricity (e), inclination (i), longitude of ascending node (Ω), argument at the pericenter (ω), time of closest approach (t_p), mass of the SMBH (m_0) and distance to the GC (D_0). The uncertainties represent the 95% confidence interval.*

REFERENCES

Ali, B., Paul, D., Eckart, A., et al. 2020, The Astrophysical Journal, 896, 100, doi: 10.3847/1538-4357/ab93ae

Ashton, G., & Talbot, C. 2021, Monthly Notices of the Royal Astronomical Society, 507, 2037, doi: 10.1093/mnras/stab2236

Barbary, K. 2021, nestle: Nested sampling algorithms for evaluating Bayesian evidence, Astrophysics Source Code Library, record ascl:2103.022. http://ascl.net/2103.022

Beaumont, M. A. 2010, Annual Review of Ecology, Evolution, and Systematics, 41, 379, doi: 10.1146/annurev-ecolsys-102209-144621

Bertorelle, G., BENAZZO, A., & MONA, S. 2010, Molecular Ecology, 19, 2609, doi: https://doi.org/10.1111/j.1365-294X.2010.04690.x

Binnendijk, L. 1960, Properties of Double Stars: A Survey of Parallaxes and Orbits (University of Pennsylvania Press). http://www.jstor.org/stable/j.ctv4t7zpt

Buchner, J. 2016, Statistics and Computing, 26, 383, doi: 10.1007/s11222-014-9512-y

—. 2019, PASP, 131, 108005, doi: 10.1088/1538-3873/aae7fc

—. 2021, The Journal of Open Source Software, 6, 3001, doi: 10.21105/joss.03001

Farr, B., & Farr, W. M. 2015

Goodman, J., & Weare, J. 2010, Communications in Applied Mathematics and Computational Science, 5, 65, doi: 10.2140/camcos.2010.5.65

Heintz, W. D. 1978, Double stars / Wulff D. Heintz (D. Reidel Pub., Co Dordrecht, Holland ; Boston), ix, 174 p. :

Higson, E., Handley, W., Hobson, M., & Lasenby, A. 2018, Statistics and Computing, 29, 891, doi: 10.1007/s11222-018-9844-0

Lintusaari, J., Vuollekoski, H., Kangasrääsiö, A., et al. 2018, Journal of Machine Learning Research, 19, 1. http://jmlr.org/papers/v19/17-374.html

Metropolis, N., Rosenbluth, A. W., Rosenbluth, M. N., Teller, A. H., & Teller, E. 1953, The Journal of Chemical Physics, 21, 1087, doi: 10.1063/1.1699114

Mikkola, S. 1987, Celestial Mechanics and Dynamical Astronomy, 40, 329, doi: 10.1007/BF01235850

Mukherjee, P., Parkinson, D., & Liddle, A. R. 2006, ApJL, 638, L51, doi: 10.1086/501068

Nelson, B., Ford, E. B., & Payne, M. J. 2013, The Astrophysical Journal Supplement Series, 210, 11, doi: 10.1088/0067-0049/210/1/11

Prangle, D. 2017, Bayesian Analysis, 12, 289 , doi: 10.1214/16-BA1002

Shaw, J. R., Bridges, M., & Hobson, M. P. 2007, Monthly Notices of the Royal Astronomical Society, 378, 1365, doi: 10.1111/j.1365-2966.2007.11871.x

Skilling, J. 2004, in American Institute of Physics Conference Series, Vol. 735, Bayesian Inference and Maximum Entropy Methods in Science and Engineering: 24th International Workshop on Bayesian Inference and Maximum Entropy Methods in Science and Engineering, ed. R. Fischer, R. Preuss, & U. V. Toussaint, 395–405, doi: 10.1063/1.1835238

Skilling, J. 2006, Bayesian Analysis, 1, 833 , doi: 10.1214/06-BA127

Speagle, J. S. 2020, MNRAS, 493, 3132, doi: 10.1093/mnras/staa278

The GRAVITY Collaboration, Abuter, R., Amorim, A., et al. 2019, A&A, 625, L10, doi: 10.1051/0004-6361/201935656

Toni, T., & Stumpf, M. P. H. 2009, Bioinformatics, 26, 104, doi: 10.1093/bioinformatics/btp619

Chapter 5

Paper III: An Update on the Dynamics of the Galactic Center S Cluster

After selecting the best method for the orbital fitting problem, I proceed in this paper by applying it on the remaining 71 S-stars. The paper is still a work in progress and the presented 20 orbits are the ones obtained so far and few of them may still require further processing. As it can be seen, the orientation of the orbits is clearly determined, which is essential for the three dimensional structural analysis. I then proceed by applying machine-learning clustering algorithm (HDBSCAN) on the specific angular momentum vectors of the 32 orbits from Ali et al. (2020), the 5 orbits from Peißker et al. (2020a) and of the newly determined orbits.

The analysis shows that more than half of the 57 orbits are arranged in a system of three highly inclined disks. Two of these disks, namely, the black (7 stars) and the green (6 stars) are oriented with a separation of 45 °, while both being almost orthogonal to the thicker and more populated red disk (22 stars). The latter is possibly connected to the CRD, as they appear closly oriented in space.

Furthermore, the distribution of the inclination angle of each of the disk and of all 57 orbits peaks around 90 degrees, meaning an edge-on orientation. As for the eccentricity, I find that the cluster exhibits a thermalized distribution, which is concluded in earlier studies. The observed configurations can be the result of several dynamical processes that probably have started with the formation time of the cluster. In the paper, I demonstrate that having both clockwise and anti-clock wise moving stars in a single disk is probably the results of Kozai-Lidov cycles. In addition, both modes of the longitude of ascending node represent the same structure in 3D and the difference is only present in the direction of motion.

In conclusion, the findings hint to a local formation origin in the near vicinity of the current observed position of the cluster. Nevertheless, detailed N-body simulations that account for all mentioned dynamical processes are required for a proper interpretation and conclusion.

Finally, as the third paper is still currently under construction, since there are still 51 objects with no determined orbits, the conclusions reported above are still open to revision and modification. Despite the prevailing circumstances, it seems that stellar disk formation and persistence in time in the near vicinity of Sgr A* is apparently possible. However, how exactly these disks were formed and how they remained in structure are questions for a detailed theoretical research.

Draft version May 1, 2023
Typeset using LaTeX **preprint** style in AASTeX631

An Update on the Dynamics of the Galactic Center S-cluster - Identification of Four Stellar Disks Around Sgr A*

Basel Ali,[1] Andreas Eckart,[1,2] Florian Peißker,[1] Michal Zajaček,[3,4,1] Matthias Subroweit,[1] Nadeen B. Sabha,[5] Gunther Witzel,[2] and Daria Paul[1]

[1]*I.Physikalisches Institut der Universität zu Köln, Zülpicher Str. 77, 50937 Köln, Germany*
[2]*Max-Plank-Institut für Radioastronomie, Auf dem Hügel 69, 53121 Bonn, Germany*
[3]*Department of Theoretical Physics and Astrophysics, Faculty of Science, Masaryk University, Kotlářská 2, 611 37 Brno, Czech Republic*
[4]*Center for Theoretical Physics, Al. Lotników 32/46, 02-668 Warsaw, Poland*
[5]*Institut für Astro- und Teilchenphysik, Universität Innsbruck, Technikerstr. 25, 6020 Innsbruck, Austria*

ABSTRACT

We provide an update on the dynamics of the Galactic center S-cluster by proposing new orbital solutions for 20 stars, along with a detailed analysis of all determined orbits thus far. The newly derived orbits exhibit multimodal posteriors, as it is expected with the lack of radial velocity measurements. We find that almost all of the 20 orbits are highly inclined and highly elliptical, which are also features of the orbits in the region.The three-dimensional inspection of the orbits (57), which was performed using machine-learning clustering algorithms, reveals that the majority of these stars are organized in a system of three highly inclined disks. While the black disk (7 stars) and the green disk (6 stars) are oriented with around 45 degrees separation, both are observed to be almost perpendicular to the red disk (22 stars). Due to the presumed young age of the S-stars and the current observational findings, it is very likely that they were formed rather locally just outside the inner arcsecond, then migration via the two-body relaxation within each disc accompanied by the Hills mechanism probably took place. The dynamical configurations we observe today are most likely the result of several dynamical processes such as Kozai-Lidov cycles and resonant relaxation.

Keywords: Galactic center, Black holes, Stellar dynamics, Star clusters

1. INTRODUCTION

In recent decades, the infrared high-resolution studies of the Galactic center has provided the manifestation of puzzling yet unique dynamical features of a dense nuclear stellar cluster (Alexander 2005; Schödel et al. 2014; Alexander 2017). More specifically, we observe a population of young O/WR- and B-type stars orbiting the $\sim 4 \times 10^6\, M_\odot$ supermassive black hole in the innermost parsec (SMBH, Sgr A*; Krabbe et al. 1995; Genzel et al. 2010; Eckart et al. 2017; Parsa et al. 2017; Gravity Collaboration et al. 2018; Do et al. 2019; Karas et al. 2021). The spectroscopically determined young age of the stars gave rise to the formulation of the 'paradox of youth' (Ghez et al. 2003), since the formation of young stars in situ has been challenging to explain due to strong tidal forces, X-ray/UV irradiation, stellar winds, a large internal velocity dispersion of gas, strong poloidal magnetic field, and a general lack of dense molecular clouds in the vicinity of the SMBH (Morris 1989, 1993).

On the other hand, there are several indicators of the recent in-situ star-formation. First, historically, there was a clear detection of about two dozen early-type blue supergiants with HeI emission lines in their spectra. Seven most luminous HeI stars provide about half of the UV ionizing flux in the region (Blum et al. 1995; Krabbe et al. 1995; Najarro et al. 1997). These HeI stars must have formed only a few million years ago. Second, a significant fraction of O/WR stars seem to reside in one or two disks, one of which is distinctly spotted on the sky moving clockwise with projected boundaries between ~ 0.04 pc and ~ 0.5 pc. The other anticlockwise disk is less distinct, but the system of stars belonging to it exhibits large inclinations with

Corresponding author: Basel Ali
ali@ph1.uni-koeln.de

respect to the clockwise system (Bartko et al. 2009). Based especially on the steep drop in the surface density with radius, this clockwise rotating disk (hereafter CRD) implies a distinct formation process of these stars in situ, most likely via the fragmentation of an accretion disc that becomes self-gravitating at larger distances from the SMBH (Paczynski 1978; Shlosman & Begelman 1987; Collin & Zahn 1999; Levin & Beloborodov 2003; Milosavljević & Loeb 2004; Nayakshin & Cuadra 2005; Nayakshin 2006; Nayakshin et al. 2007; Wardle & Yusef-Zadeh 2008; Yelda et al. 2014). This event is estimated to have occurred 6 ± 2 Myr ago (Paumard et al. 2006), which is comparable in time to the energetic episode that created the large-scale Fermi bubbles (Su et al. 2010). Third, compact stellar associations of NIR-excess, extremely reddened stars on the length-scale of one arcsecond ($\sim$ 0.04 pc), presumably hosting young dust-embedded stellar objects, such as the IRS 13N association (0.5” north of IRS 13E complex; Eckart et al. 2004; Mužić et al. 2008), point towards the formation of these dust-enshrouded stars within an infalling fragmenting molecular cloud. The infrared-excess G sources or Dusty S-cluster Objects (DSOs) within the inner S cluster, including the most prominent G1 and G2/DSO sources, bear observational similarities to IRS 13N sources (Ciurlo et al. 2020; Peißker et al. 2020, 2021a), mainly in terms of the prominent near-infrared excess that is consistent with the origin in the dense dusty envelope of an accreting young stellar object of type I (Zajaček et al. 2017). Furthermore, water maser and SiO emission sources, bipolar outflow as well as proplyd-like bow-shock sources are another indicator supporting a very recent star-formation process in the inner parsec (Yusef-Zadeh et al. 2015b,a, 2017; Peißker et al. 2019, 2021b).

The B-type stars, the so-called S-stars, occupy the inner arcsecond moving on highly inclined and highly eccentric orbits. Earlier studies of 32 of these stars concluded that they are moving on randomly oriented orbits based on the orientation of orbital angular momenta (Gillessen et al. 2017). In contrast, Ali et al. (2020) found based on three-dimensional inspection of the orbits that the S-stars are rather organized in two almost edge-on perpendicular disks embedded within the CRD. The angular momentum vectors in a given disk point in two directions, i.e, almost half of the angular momentum vectors point towards the north and the other half towards the south or similarly in the other perpendicular stellar disk, they point towards the west and the east. Apparently, there are no indications after all that the orbits exhibit a random distribution based on the precise monitoring of the S-cluster (Peißker et al. 2020a; Peißker et al. 2020d; Ali et al. 2020; Peißker et al. 2021b). This finding has implications for both the formation as well as the current dynamical evolution of the S-cluster. Among the properties of the S-stars are an effective temperature of 21,000-28,000 K, a rotational velocity of 60-170 km/s and a surface gravity of $\log g = 4.1-4.2$ (Ghez et al. 2003; Martins et al. 2008; Habibi et al. 2017). These latter properties fit well with the features of stars of spectral type B0-B3V with masses between 8 $M_\odot$ and 14 $M_\odot$. Concerning their age, Habibi et al. (2017) constrain it for the S2 star to be $6.6^{+3.4}_{-4.7}$ Myr based on 12 years of spectroscopic monitoring. For the other S stars, their age can spectroscopically be constrained within 15 Myr, while ages larger than 25 Myr can be excluded. Overall, S stars were likely formed in situ in one or more closely spaced star-forming episodes induced by an infall of the colder dense gas. The total number of the S-stars is 108 including the 32 orbits determined by Gillessen et al. (2017) and Ali et al. (2020). Recently, Peißker et al. (2020d) reported the detection of five new faint S-cluster members, some of which approach Sgr A* with an even smaller pericenter distance than S2, with S62 and S4714 potentially reaching the pericenter distances of $\sim$ 450 and $\sim$ 320 gravitational radii, respectively. Additionally, we note, as concluded by Yelda et al. (2014), that the stars S66, S67, S83, S87, S96 and S97 are part of the clockwise rotating disk. Therefore, we do not consider them as members of the S-cluster.
In this research, we present precise orbital solutions for the 20 members of the S-cluster. We begin with the observations and data reduction in Section 2, which is followed by the results and findings in Sections 3. In Sections 4, stellar dynamical considerations are discussed. Finally, the summary and conclusions are provided in Section 5.

2. OBSERVATIONS AND DATA REDUCTION

The positional data were extracted from images taken by the NAOS-CONICA (NACO) instrument, which was mounted at the Very Large Telescope (VLT) at Paranal/Chile and recently has been decommissioned. These images are assisted with adaptive optics (AO) with IRS 7 (6.5-7 K_s-band magnitude) as a guide star located 5”.5 north of Sgr A*. In further detail, the K_s-band images were acquired by the S13 and S27 cameras of NACO with 13 and 27 mas/pix scale, respectively. The data collection was preceded by the usual data reduction steps such as flat-fielding, sky subtraction, and bad-pixel correction. In addition, the images of S27 camera were used to measure the positions of the SiO maser stars IRS 9, IRS 10EE, IRS 12N, IRS 15NE, IRS 17, IRS 19NW, IRS28 and SiO-15 (Menten et al.

1997; Reid et al. 2003, 2007; Borkar et al. 2020), which are then used to connect near-infrared (NIR) data and the radio-reference frame. Following the data reduction steps, we performed Lucy-Richardson deconvolution algorithm on the S13 camera images to resolve the sources. For each epoch, we included all available K_s-band frames of the GC stellar cluster that were taken with a close-to diffraction-limited AO correction and showed Sgr A* flaring. We made use of the reduced data presented by Witzel et al. (2012), Table 2, 2003 to mid-2010, Eckart et al. (2013), Table 1, and Shahzamanian et al. (2015), Table 1, 2002-2012. For verifying the extracted positions, we use the predicted position of the thoroughly analysed star S2 to pinpoint the location of Sgr A* and then calculate the offset to the selected star.

The extinction-corrected magnitude in the K_s-band of the S-stars ranges between 12.8 (S76; Gillessen et al. 2017) and 18.5 (S4713; Peißker et al. 2020d). The detection of all of the 108 sources was successful with no severe confusion with other stars at each year between 2002 and 2018 (Sabha et al. 2012; Eckart et al. 2013).

As for the determination of the orbits, we explain the methodology in great details in Ali et al (in prep.). In short, we conclude in Ali et al (in prep) that Ultranest, which is a nested sampling techniques deveoloped by Buchner (2021, 2019, 2016), is able to detect multimodal posteriors, which are expected in case no radial velocity measurements are obtainable. Since the majority of the S-stars lack these measurements, the ascending node is not certainly determined, which leads to two possible values for each of the longitude of the ascending node (Ω) and argument of the pericenter (ω). The algorithm is proven to be very efficient in exploring the parameter space and hence removing any bias in the derived elements. In addition, the boundaries of the semi-major axis is initially set to the range between 1 and 200 mpc, while increasing to higher values or decreasing to lower values in case convergence was not reached. Similarly, the time of closest approach was initially set between 2000 and 2200 years and increased/decreased with poor convergence. As for the remaining parameters, they were set as mentioned in Ali et al (in prep.). Furthermore, the initial number of live points for the algorithm Ultranest was 10^4.

Before analysing the structure in three-dimensions, an important point to consider is that the orientation of the structure is determined by only the inclination and the longitude of the ascending node. Furthermore, both the ascending node and the descending node represent the same plane in 3D and hence using only one of them is sufficient and will simplify the analysis. In other words, if we consider only the clockwise direction, i.e., values between 0 and 180 degrees, and shift the ones between 180 and 360 to the clockwise range, then no structural information is lost. After obtaining the orbits, we calculate the specific angular momentum vectors of the 32 stars in Ali et al. (2020), after updating their orbital elements for $m_0 = 4.15$ million solar masses and $D_0 = 8178$ pc (see Table 1). In addition, we include the orbits of the five faint sources from Peißker et al. (2020d). We then calculate the vectors of the newly derived orbits and use machine learning clustering algorithm HDBSCAN (McInnes et al. (2017), Campello et al. (2013)), which stands for Hierarchical Density-based Spatial Clustering of Applications with Noise, to find the structure in 3D. We note that the anti-clockwise vectors were multiplied by a minus sign to be converted to the clockwise direction. One could naturally use both directions, however, the algorithm might classify one point as an outlier, while structure-wise the point represents an orbit that falls within the plane of the clustered points on the opposite side. Therefore, using only the clockwise direction gives more certainty in the clustering results. We also note that the errors of the orbital elements are included as weights in the chosen distance metric, which is Minkowski with p=1, i.e., Manhattan distance. Furthermore, we choose a minimum cluster size between 3 and 12 and minimum samples between 3 and 8. The clustering results are then evaluated using the density-based clustering validation (DBCV) score of total determined clusters (Moulavi et al. (2014)) and of each individual cluster. In addition, the outlier scores for each vector are estimated using the GLOSH algorithm, which stands for Global-Local Outlier Score from Hierarchies (Campello et al. (2015)).

3. RESULTS

By inspecting the new orbital solutions, we find that for all stars the multimodal posteriors are clearly detected with reasonable uncertainties. Even though for some cases the uncertainty of the semi-major axis is large, however, the uncertainties represent 2σ and the orientation in 3D is not affected by this uncertainty. Furthermore, the latter issue could be solved by removing largely scatted points from the dataset or increasing the initial number of live points for the Ultranest algorithm to a higher value, e.g., 10^5. As for the eccentricities, we find that the new orbits are also highly elliptical and have a signature of high inclination (see Figure 21), which both are considered features of the S-cluster based on the known 32 orbits (see Ali et al. (2020)). 76
This finding supports the uniqueness of the newly derived orbits and proves that the algorithm is efficient in the orbital fitting problem. Concerning the longitude

of ascending node, one has two possible values for each of the 20 orbits with both representing the same three-dimensional plane.

Concerning the results of HDBSCAN, we find that the optimal clustering was for a minimum samples of 3 and a minimum cluster size of 6. More precisely, the DBCV score is 0.478 out of 0.614 after taking into account the noisy points (22). In other words, since the DBCV is a weighted average and considered noise, the range alters, for instance, if half the points are classified as noise, from [-1,+1] to [-0.5,+0.5]. Furthermore, the individual scores of each cluster are 0.86 for the black, 0.75 for the red, and 0.78 for the green, where 1 represents perfect clustering. We also list the probabilities and outlier score with the corresponding classification in Tables 4 and3. Our analysis show that the majority of the 57 stars are organized in three highly inclined disks that agrees with some of the classification in Ali et al. (2020). In greater detail, we find that the green disk (6 stars - along the Galactic plane) and the black disk (7 stars) are separated in azimuth by 45 degrees, which both being almost perpendicular to the red disk (22 stars) (see Figure 20). Furthermore, we find that the red disk is significantly thicker than the other two and might possibly be connected to the CRD. Concerning their three-dimensional orientation, we find that the green disk is seen edge-on at elevation = 0 °and azimuth = -20 °, while the black at elevation = 0 °and azimuth = +20 °, and the red at elevation = 0 °and azimuth = -90°.

4. DISCUSSION AND DYNAMICAL CONSIDERATIONS

In the previous section, it was shown that the S cluster is organized in a system of three disks using machine-learning clustering algorithms. This underlines the overall non-isotropic distribution of the S cluster that was first presented in Ali et al. (2020) for a smaller number of stars. Here we outline and propose dynamical processes that could have led to the observed configurations.

The occurrence of inclined disks and streamer structures is relatively frequent in different environments. In Impellizzeri et al. (2019), authors find evidence for counter-rotating and misaligned disks in NGC1068 on parsec scales. In the Galactic center, the orbital plane of the Western Arc and the Northern Arm of the minispiral is nearly perpendicular to the orbital plane of the Eastern Arm (Vollmer & Duschl 2000; Zhao et al. 2009, 2010). Furthermore, the molecular circumnuclear disk located between 1.5 and 7 pc (Christopher et al. 2005) is nearly perpendicular to the inner part of the clockwise rotating stellar disk (Šubr et al. 2009; Kocsis & Tremaine 2011). This shows that the gas and dust can be channeled to the Galactic center on mutually highly inclined orbits from larger scales. In addition to the existence of at least one previously studied stellar disk within 0.5 pc, the spatial distribution of 16 black-hole low-mass X-ray binaries within the inner parsec is also disk-like at the 87% confidence level (Mori et al. 2021). In the broader context, planets could form on stable polar orbits with respect to the orbital plane of an eccentric binary-star system (Childs & Martin 2021).

The stars deep inside the sphere of influence of the SMBH can be subject to different dynamical processes. Several dedicated studies were aimed to explain the existence of young stars in the innermost region of the Galaxy (see Mapelli & Gualandris 2016, for a review). Regarding the O/WR stars between 0.04 and 0.5 pc, Levin & Beloborodov (2003) find that these stars were most likely formed in situ in a massive self-gravitating gaseous disk(s) around Sgr A*. Their ages have been derived to be between 2.5 and 5.8 Myr (Lu et al. 2013). Slightly more than half of these stars were initially considered to be members of the well-distinguished clockwise disk (Bartko et al. 2009, 2010), nevertheless, Yelda et al. (2014) found that the true disk fraction is only around 20%, which could also be biased by binaries (Naoz et al. 2018). Furthermore, Bartko et al. (2009, 2010) reported that it seemed very probable that around 25% of the remaining are in a second counter-clockwise disk or a streamer structure that is orthogonal to the former, while Lu et al. (2009) and Yelda et al. (2014) concluded their studies with no detection of any anti-clockwise feature. Almost 20% of the O/WR stars seem to have random orientations according to Lu et al. (2009). The latter fraction is certainly much higher according to Yelda et al. (2014), where the authors state that what we observe today could have been a much denser stellar disk, which may have been subjected to dynamical processes that caused a large fraction of these stars to deviate from the original orientation. In fact, the CRD exhibits a noticeable warp of $\sim$ 60 degress between the inner and the outer parts, which could be attributed to the vector resonant relaxation within the spherical cluster of late-type stars (Kocsis & Tremaine 2011). The distant molecular circumnuclear ring could also have induced a warp in the stellar disk due to a differential precession (Nayakshin 2005; Šubr et al. 2009). A larger fraction of OB/Wolf-Rayet stars on randomized orbits, not belonging to any coherent structure, was also confirmed by the analysis of near-infrared stellar bow-shocks (Sanchez-Bermudez et al. 2014). In this context, the S cluster four-disk structure could be a kinematic

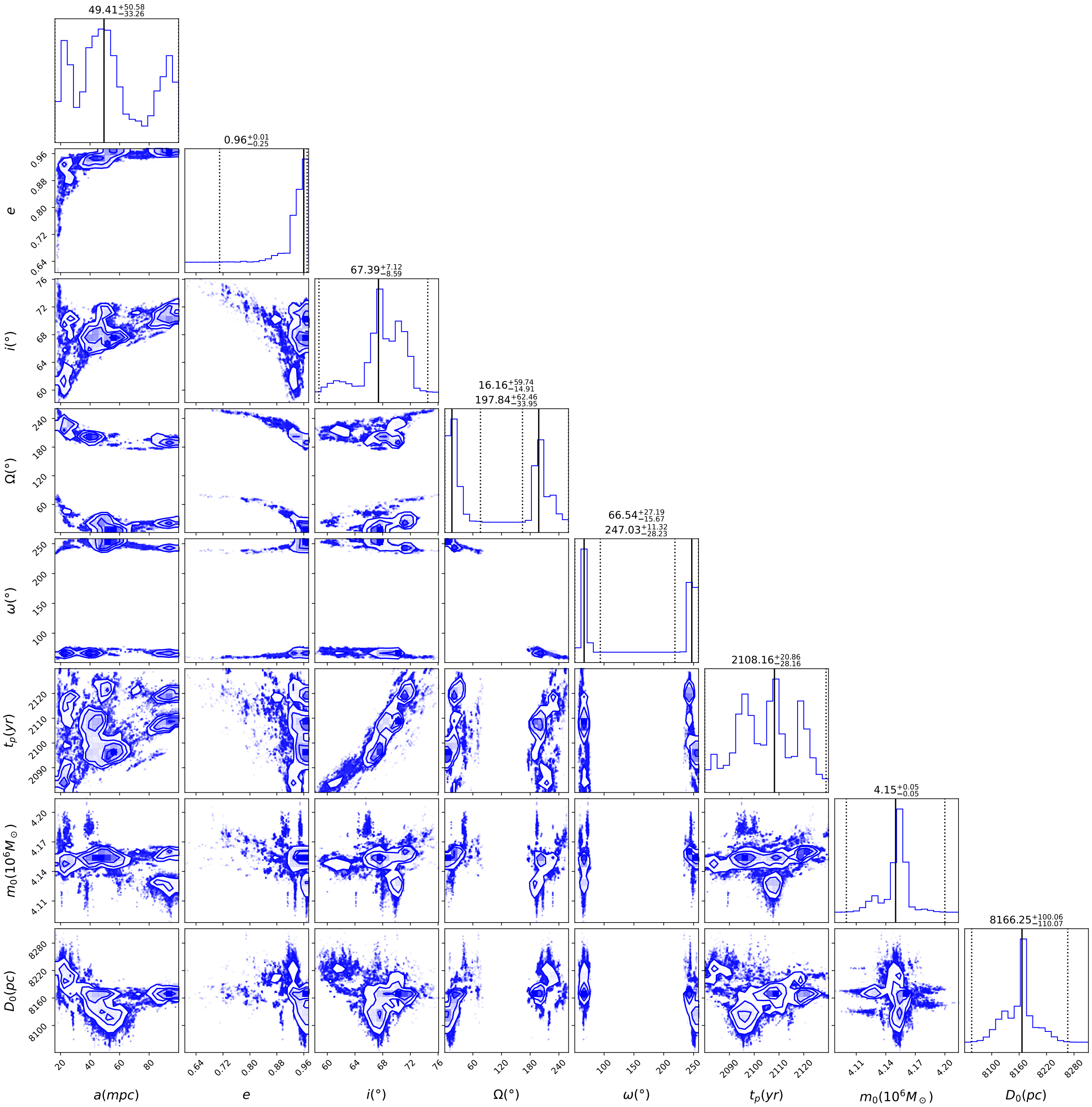

Figure 1. A customized corner plot of the orbit of S7 using Ultranest algorithm. The eight parameters are the semi-major axis (a), eccentricity (e), inclination (i), longitude of ascending node (Ω), argument at the pericenter (ω), time of closest approach (t_p), mass of the SMBH (m_0) and distance to the GC (D_0). The uncertainties represent the 95% confidence interval.

manifestation of the formation and/or the evolution of the youngest generation of stars in the Galactic center. At larger scales, the perturbative external forces could have just started to obliterate the coherent kinematic structure resulting from this recent star-formation event.

Hobbs & Nayakshin (2009) conclude that in order to form the clockwise rotating disk with a significant population of anti-clockwise stars, the collision of two separate gas clouds is required. Concerning the focus of this work, the S-stars located at $\lesssim 0.04\,$pc, our findings hint to a local origin similar to the formation of the OB/WR-type stars. First, their ages seem to agree, in particular

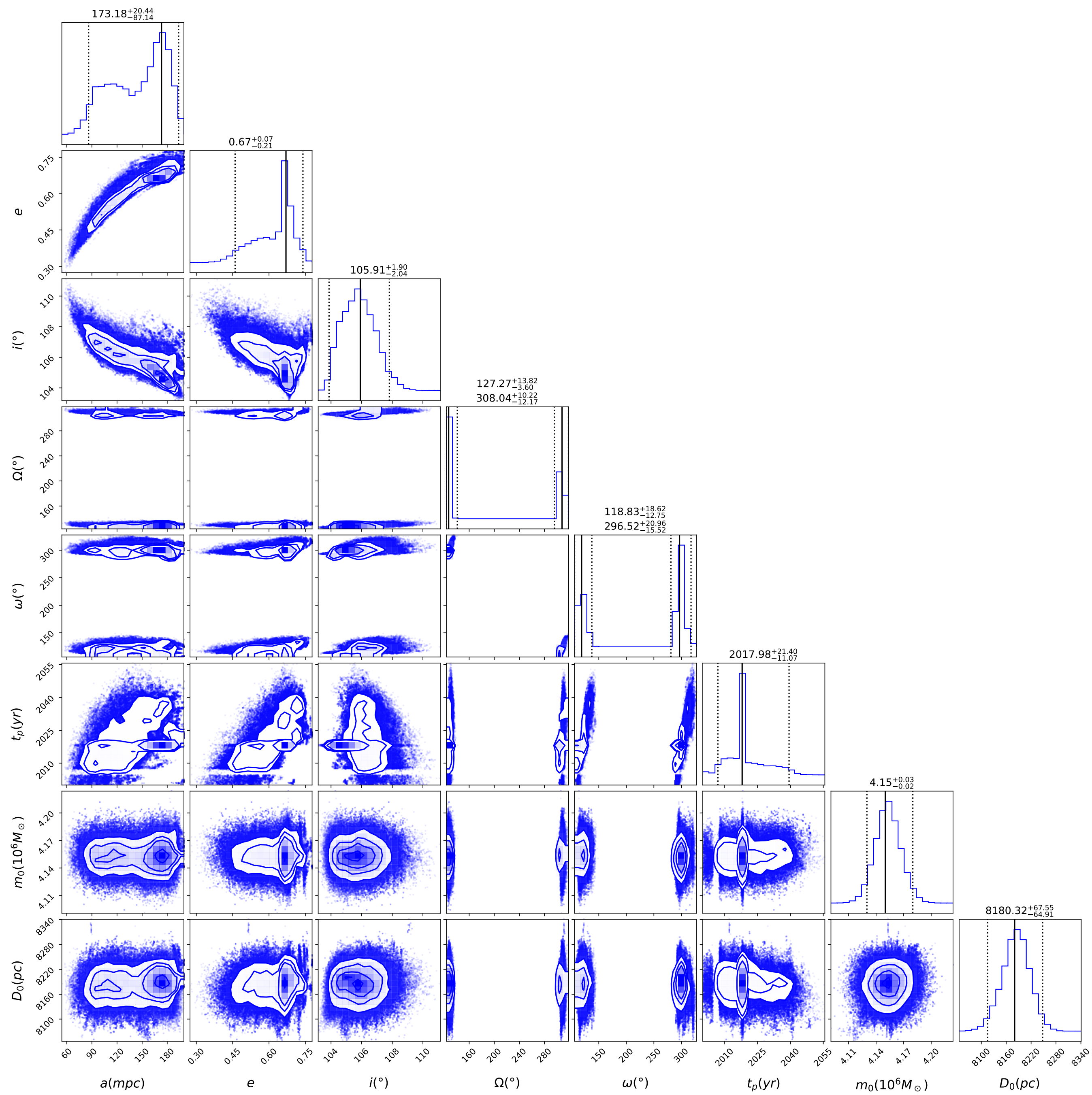

Figure 2. A customized corner plot of the orbit of S11 using Ultranest algorithm. The eight parameters are the semi-major axis (a), eccentricity (e), inclination (i), longitude of ascending node (Ω), argument at the pericenter (ω), time of closest approach (t_p), mass of the SMBH (m_0) and distance to the GC (D_0). The uncertainties represent the 95% confidence interval.

$6.6^{+3.4}_{-4.7}$ Myr for S2 (Habibi et al. 2017) and 2.5 - 5.8 Myr (Lu et al. 2013) for the CRD. Second, the S-stars are also organized in a system of disks. Hobbs & Nayakshin (2009) investigate the situation of the collision of two molecular clouds. They place two clouds of different masses around $R = 1\,\mathrm{pc}$ at large angles with respect to each other with slightly elliptical orbits. Following the collision, the low angular momentum gas settles at $R \approx 0.04$pc and forms a dense small disk that forms many high-mass stars. The radius, at which their disk settles, is in agreement with the mean values of the semi-major axes of the detected disks of the S-stars.

Furthermore, Wardle & Yusef-Zadeh (2008) propose the scenario that a small gaseous disk could form by

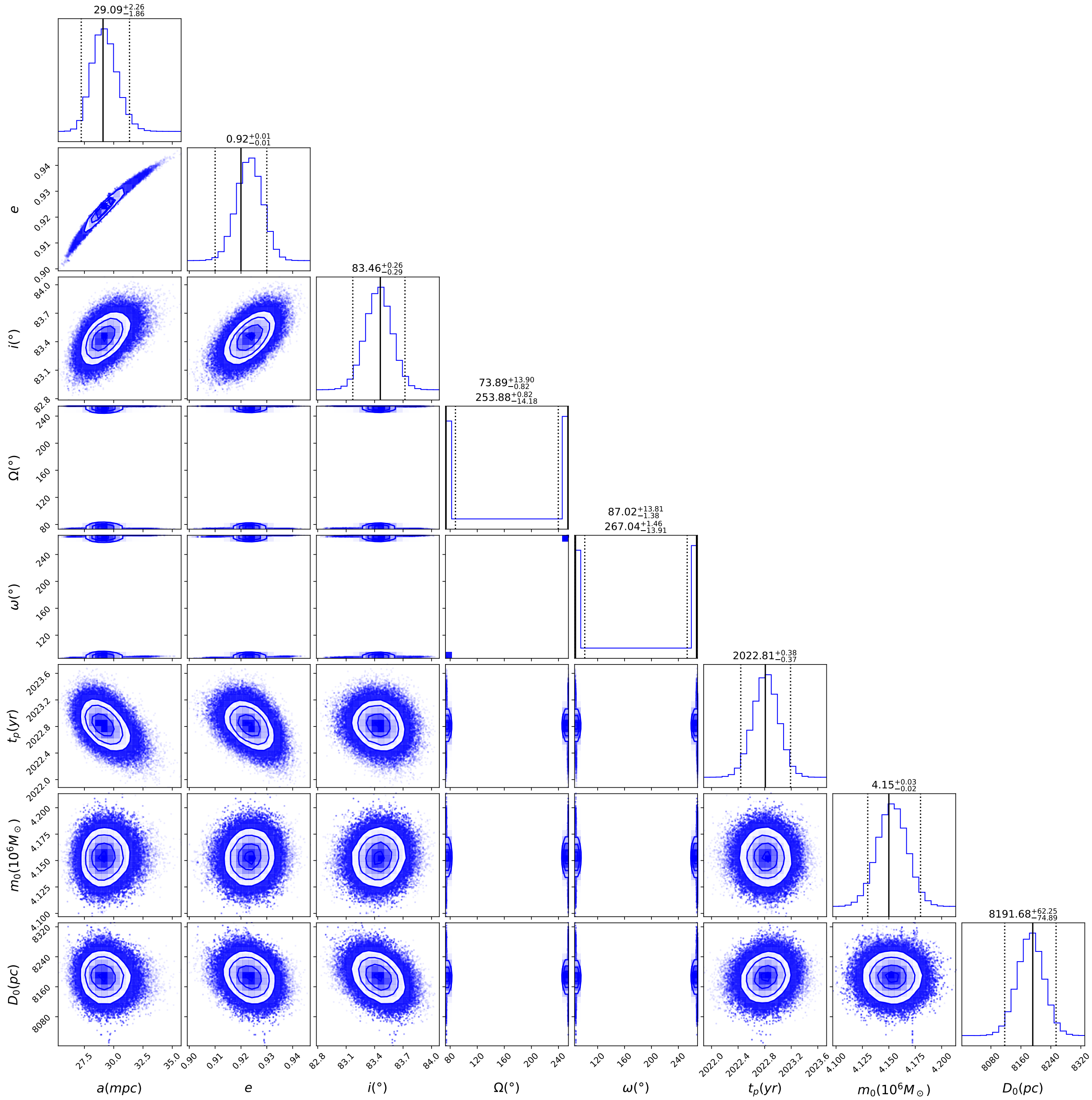

Figure 3. A customized corner plot of the orbit of S20 using Ultranest algorithm. The eight parameters are the semi-major axis (a), eccentricity (e), inclination (i), longitude of ascending node (Ω), argument at the pericenter (ω), time of closest approach (t_p), mass of the SMBH (m_0) and distance to the GC (D_0). The uncertainties represent the 95% confidence interval.

a partial capture of a large massive molecular cloud, such as the ± 50 km/s cloud. As the cloud engulfs the region at a certain impact parameter, the low angular momentum gas could be created by the cancellation of the angular momenta of either side of Sgr A*. Such a cloud may also be able to form stars with opposite angular momenta. This can serve as a valid justification of having two angular momentum directions for each of the S-disks.

In addition, the presence of massive perturbers (giant molecular clouds and stellar clusters) can also shorten the relaxation timescale by orders of magnitude (Perets et al. 2007). It appears that the effect of massive perturbers is more relevant for larger distances, neverthe-

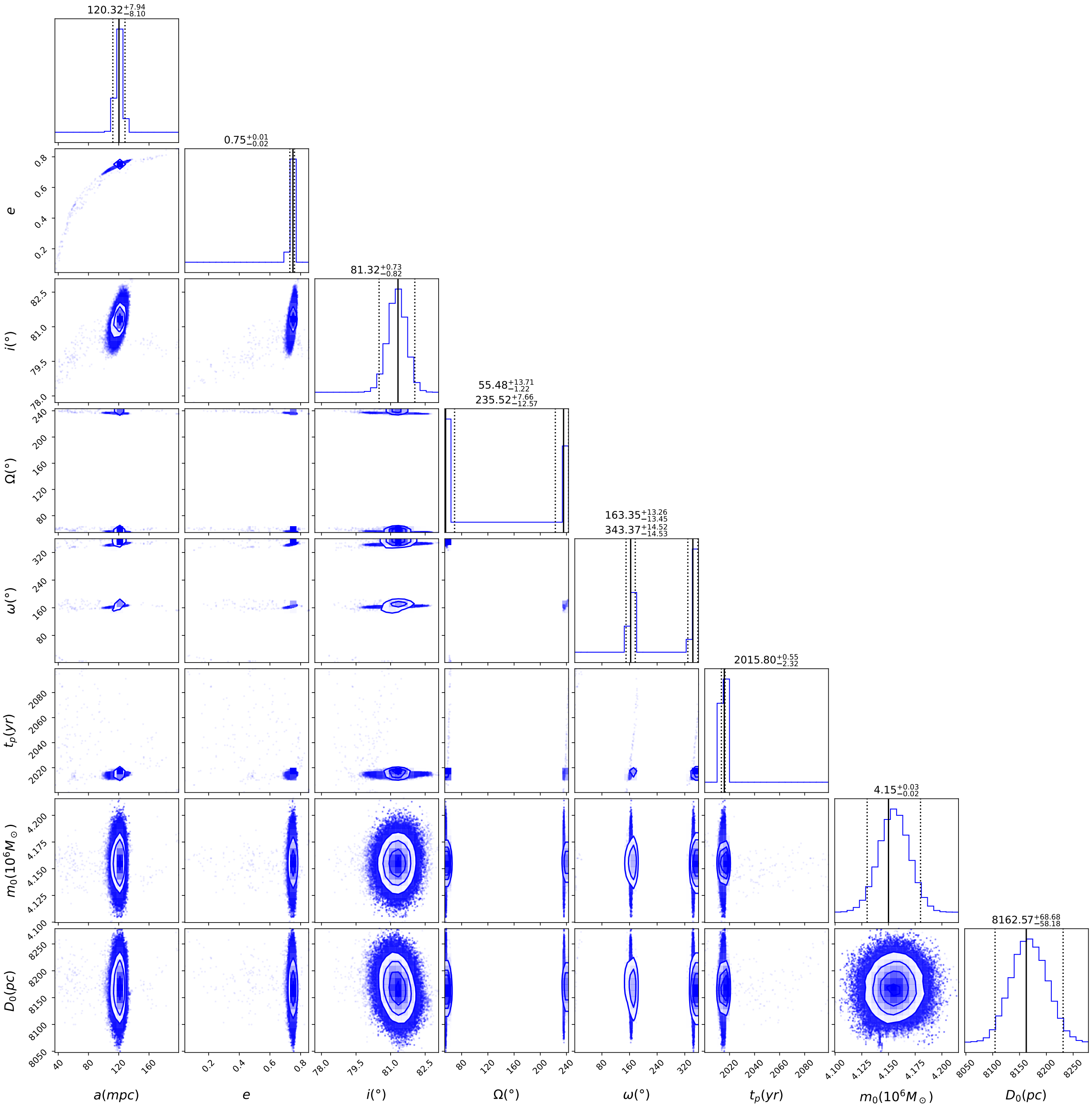

Figure 4. A customized corner plot of the orbit of S26 using Ultranest algorithm. The eight parameters are the semi-major axis (a), eccentricity (e), inclination (i), longitude of ascending node (Ω), argument at the pericenter (ω), time of closest approach (t_p), mass of the SMBH (m_0) and distance to the GC (D_0). The uncertainties represent the 95% confidence interval.

less, in the past or during the formation of the S cluster, such massive perturbers could have been present closer to Sgr A*, such as the remnants of molecular clouds, infalling star clusters and associated IMBHs, hence the mechanism proposed by Perets et al. (2007) is an additional effect that could have contributed to the reduction of the two-body relaxation timescale due to the larger effective mass. We also refer to Moser et al. (2017), where the authors reported molecular clouds near Sgr A* within the inner parsec that are traced using the CS(5-4) transition and these can increase the effective mass of the perturbers above the typical stellar mass. The latter findings were also reported by Tsuboi et al. (2021). In addition, the hypothetical presence of

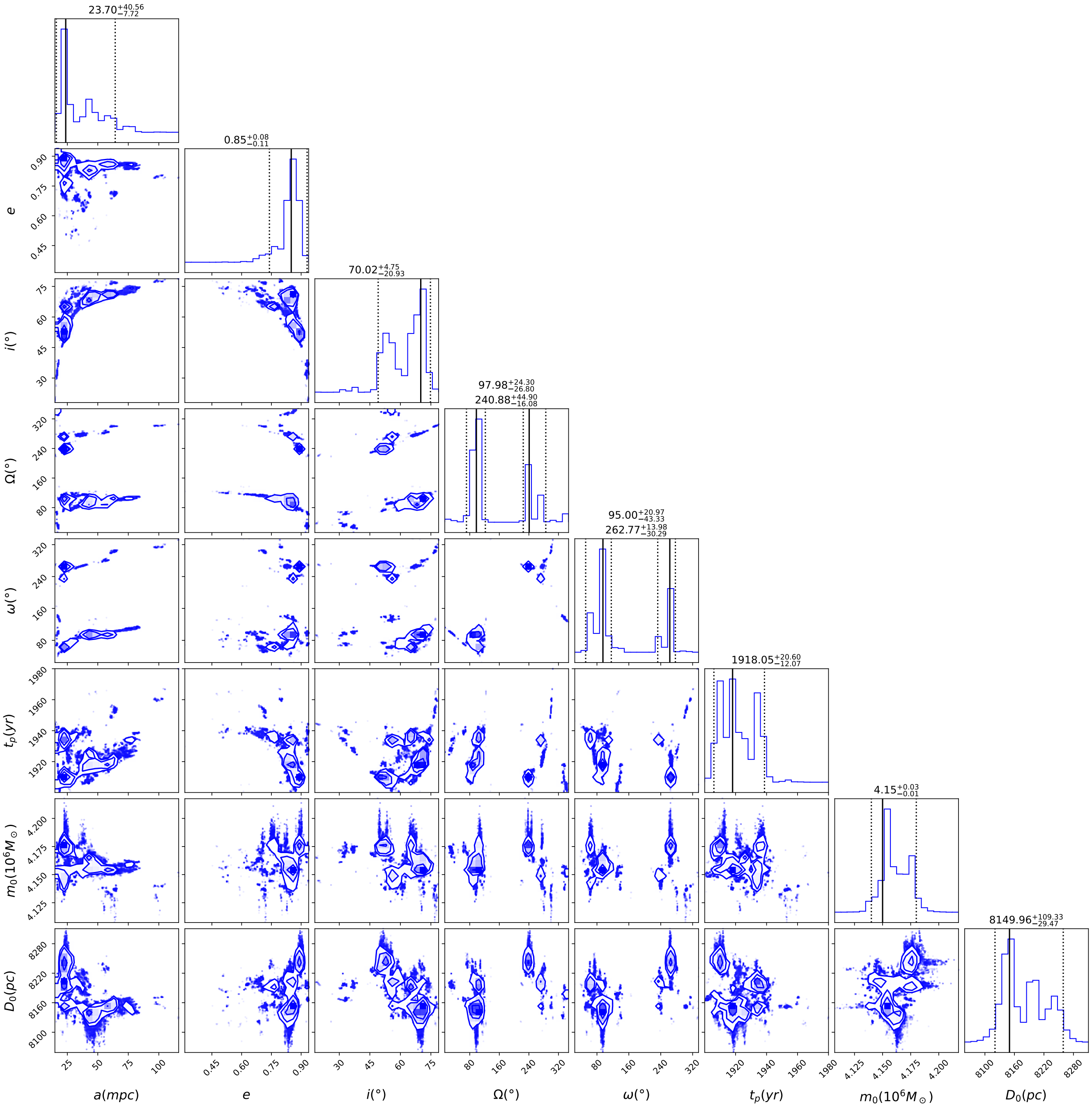

Figure 5. A customized corner plot of the orbit of S30 using Ultranest algorithm. The eight parameters are the semi-major axis (a), eccentricity (e), inclination (i), longitude of ascending node (Ω), argument at the pericenter (ω), time of closest approach (t_p), mass of the SMBH (m_0) and distance to the GC (D_0). The uncertainties represent the 95% confidence interval.

IMBHs (e.g. inside clusters such as IRS13E Fritz et al. 2010) and a cusp of stellar black holes due to a dynamical friction (O'Leary et al. 2009) could increase the effective mass and this would also lead to its radial dependency. Furthermore, massive perturbers could have induced the infall of binaries from a larger scale on parabolic/hyperbolic orbits due to dynamical scattering, and the components of these binaries were captured by Sgr A* via the Hills mechanism. In addition, the past presence of a massive gaseous disk could have triggered the inward disk migration due to the mutual torques between the stars and the disk, see Subsection 4.5.

The inward migration of stars was accompanied by the Hills mechanism, which disrupted the inward migrating

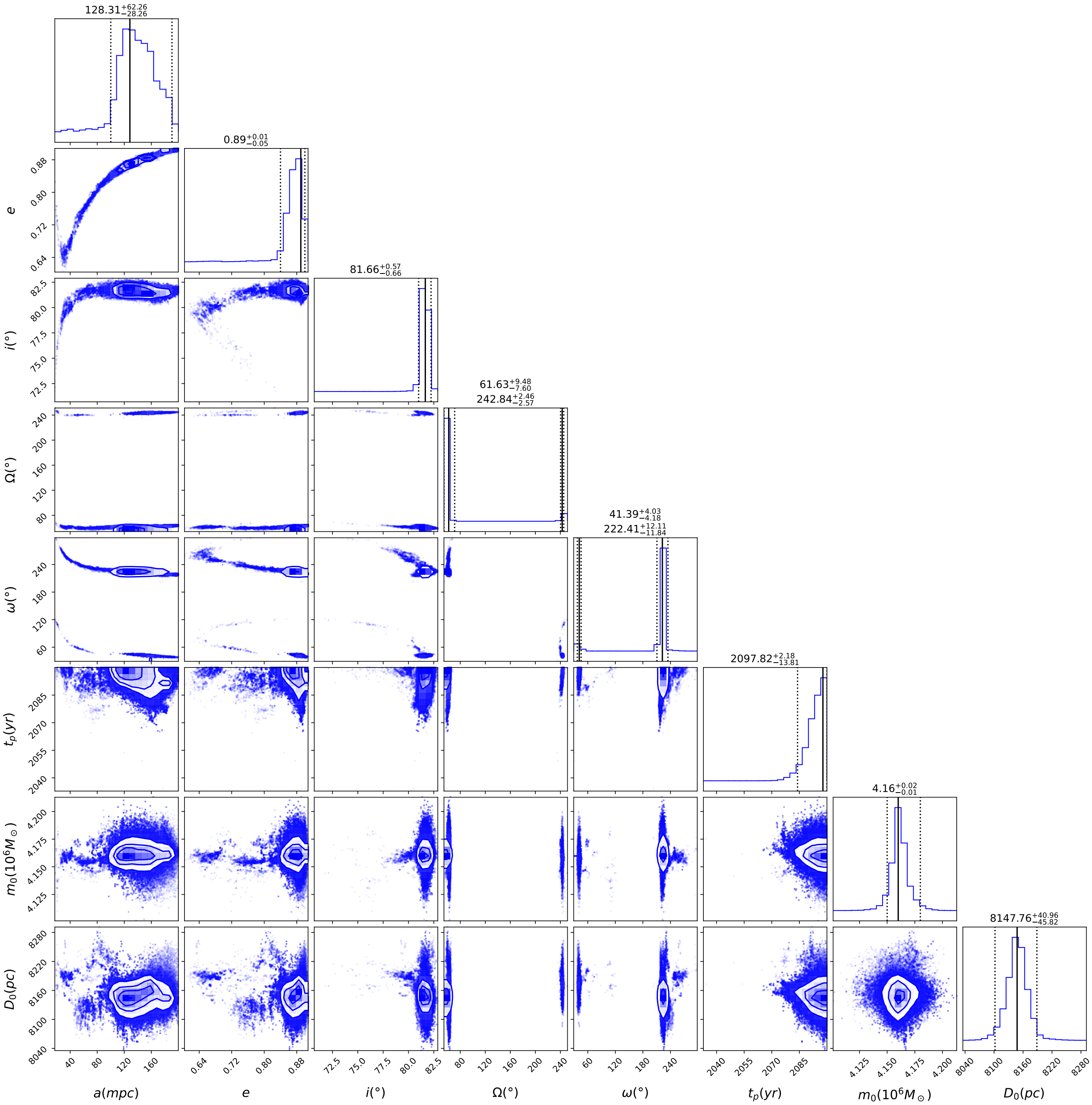

Figure 6. A customized corner plot of the orbit of S32 using Ultranest algorithm. The eight parameters are the semi-major axis (a), eccentricity (e), inclination (i), longitude of ascending node (Ω), argument at the pericenter (ω), time of closest approach (t_p), mass of the SMBH (m_0) and distance to the GC (D_0). The uncertainties represent the 95% confidence interval.

binary and triple systems (Hills 1988; Perets et al. 2007; Löckmann et al. 2009; Madigan et al. 2009; Dremova et al. 2019; Zajaček et al. 2014; Generozov & Madigan 2020). The thermalized eccentricity distribution that we inferred for all disks could have been induced by the already discussed two-body relaxation within the disk (Šubr & Haas 2014) in combination with the Hills mechanism, especially if the formed disk was rather circular with $< e^2 >^{1/2} \sim 0.1$, which significantly shortens the disk relaxation time in comparison with more eccentric orbits. The vector and scalar resonant relaxation have also been ongoing since the formation of the S cluster. The granularity of the distributed mass can be probed by investigating the effects of the orbital torques on the

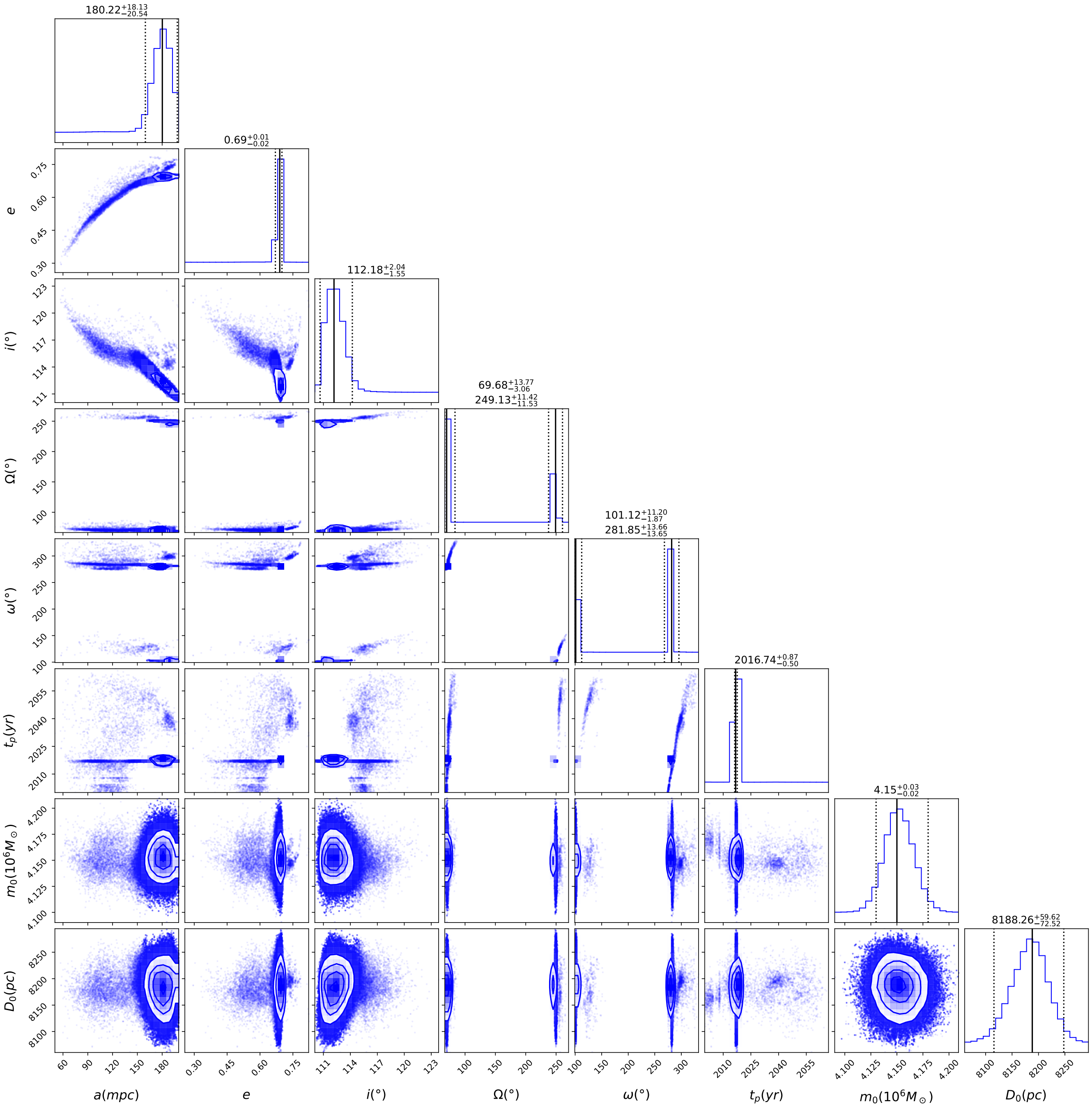

Figure 7. A customized corner plot of the orbit of S34 using Ultranest algorithm. The eight parameters are the semi-major axis (a), eccentricity (e), inclination (i), longitude of ascending node (Ω), argument at the pericenter (ω), time of closest approach (t_p), mass of the SMBH (m_0) and distance to the GC (D_0). The uncertainties represent the 95% confidence interval.

orbits of the closest s-stars (e.g. S2) due to resonant relaxation Sabha et al. (2012). The authors find that if a significant population of stellar black holes is present near Sgr A* then the contributions from the scattering will be important for the trajectory of S2. In principle, the scalar resonant relaxation could have thermalized the S cluster distribution in case a cusp of compact remnants is present, see e.g. (O'Leary et al. 2009), Fouvry et al. (2019), Generozov & Madigan (2020), and Tep et al. (2021).

Detailed numerical models, including hydrodynamical models of in-situ star-formation within the previously formed gaseous disks accompanied by N-body dynamics of young stars, are necessary to test the importance

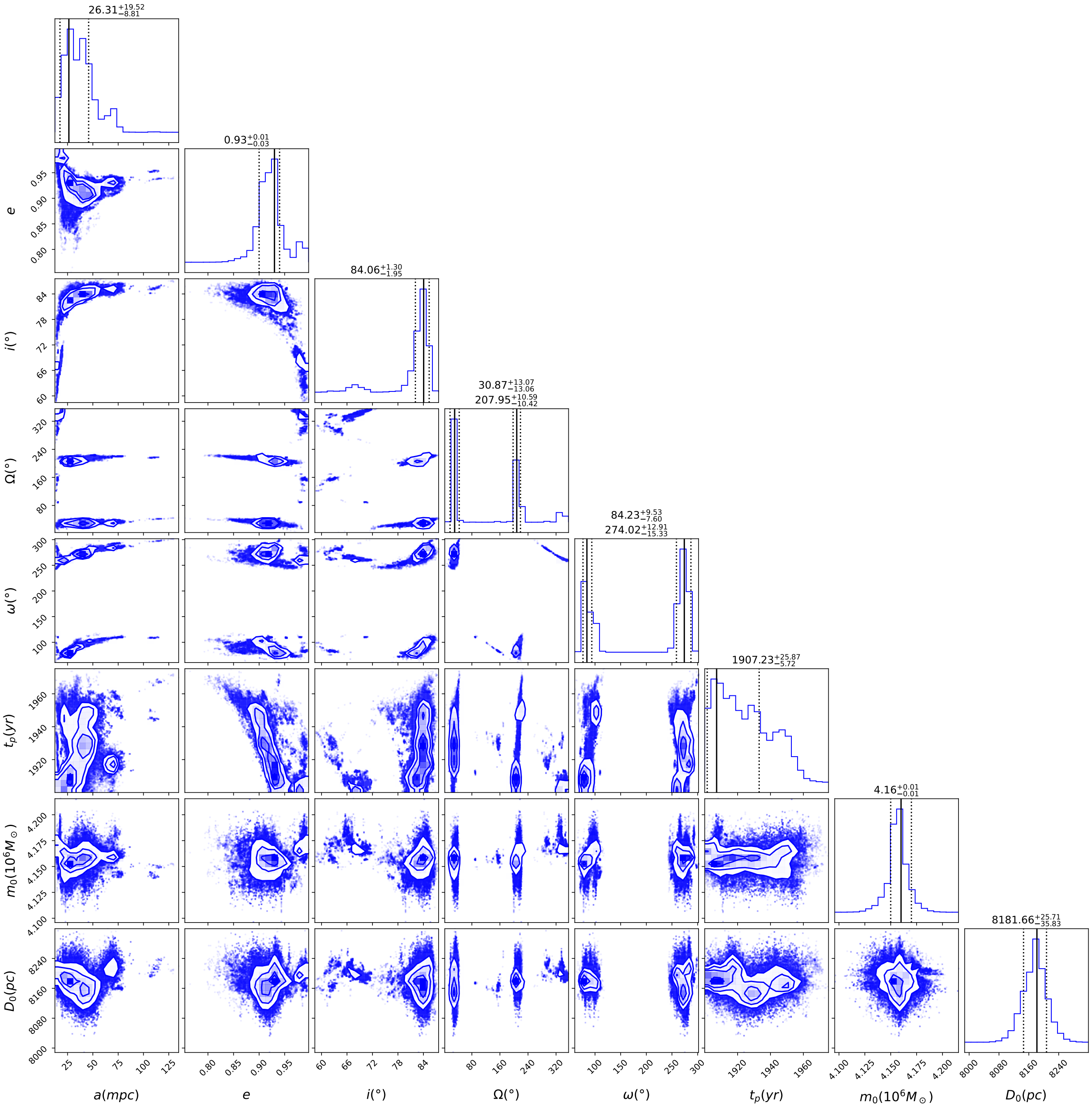

Figure 8. A customized corner plot of the orbit of S36 using Ultranest algorithm. The eight parameters are the semi-major axis (a), eccentricity (e), inclination (i), longitude of ascending node (Ω), argument at the pericenter (ω), time of closest approach (t_p), mass of the SMBH (m_0) and distance to the GC (D_0). The uncertainties represent the 95% confidence interval.

of proposed mechanisms. The analysis should also address the potential connection between S cluster disks on smaller scales and the orthogonal orientation of the minispiral arms and the circumnuclear disk on larger scales. These simulations are outside the scope of the current observational study of S-cluster kinematics.

In the following, we make an outline and discuss in more detail the relevant dynamical processes that could have contributed to the eccentricity distribution as well as the overall distribution of S star orbits in three dimensions. These include the Hills mechanism (Section 4.1), the Loss-cone dynamics (Section 4.2), Kozai-Lidov oscillations due to an intermediate-mass black hole (IMBH)

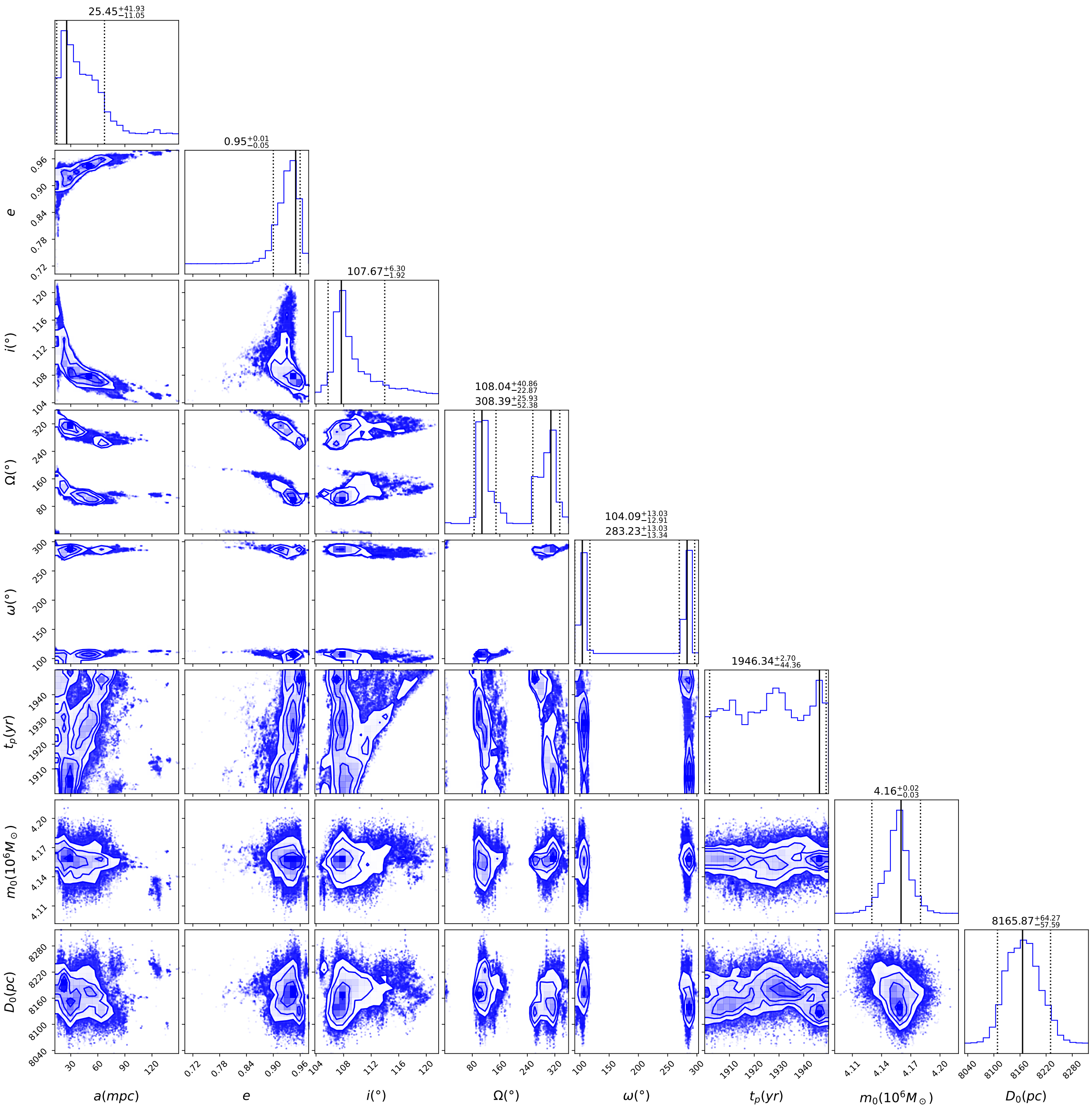

Figure 9. A customized corner plot of the orbit of S41 using Ultranest algorithm. The eight parameters are the semi-major axis (a), eccentricity (e), inclination (i), longitude of ascending node (Ω), argument at the pericenter (ω), time of closest approach (t_p), mass of the SMBH (m_0) and distance to the GC (D_0). The uncertainties represent the 95% confidence interval.

or a gaseous or a stellar disk (Section 4.3), resonant relaxation (Section 4.4), as well as other dynamical processes (Section 4.5) including a fast two-body relaxation within a disk, a disk migration, and the effect of the IMBH.

4.1. *Hills Mechanism*

The Hills mechanism describes the tidal disruption of binaries by SMBHs that ejects one of them with high velocity while keeping the other bound to the SMBH on a highly eccentric orbit. In case of parabolic disruptions, the primary and the secondary have equal chances of orbiting the central SMBH (Hills 1988). Based on the remarkable findings of Generozov & Madigan (2020),

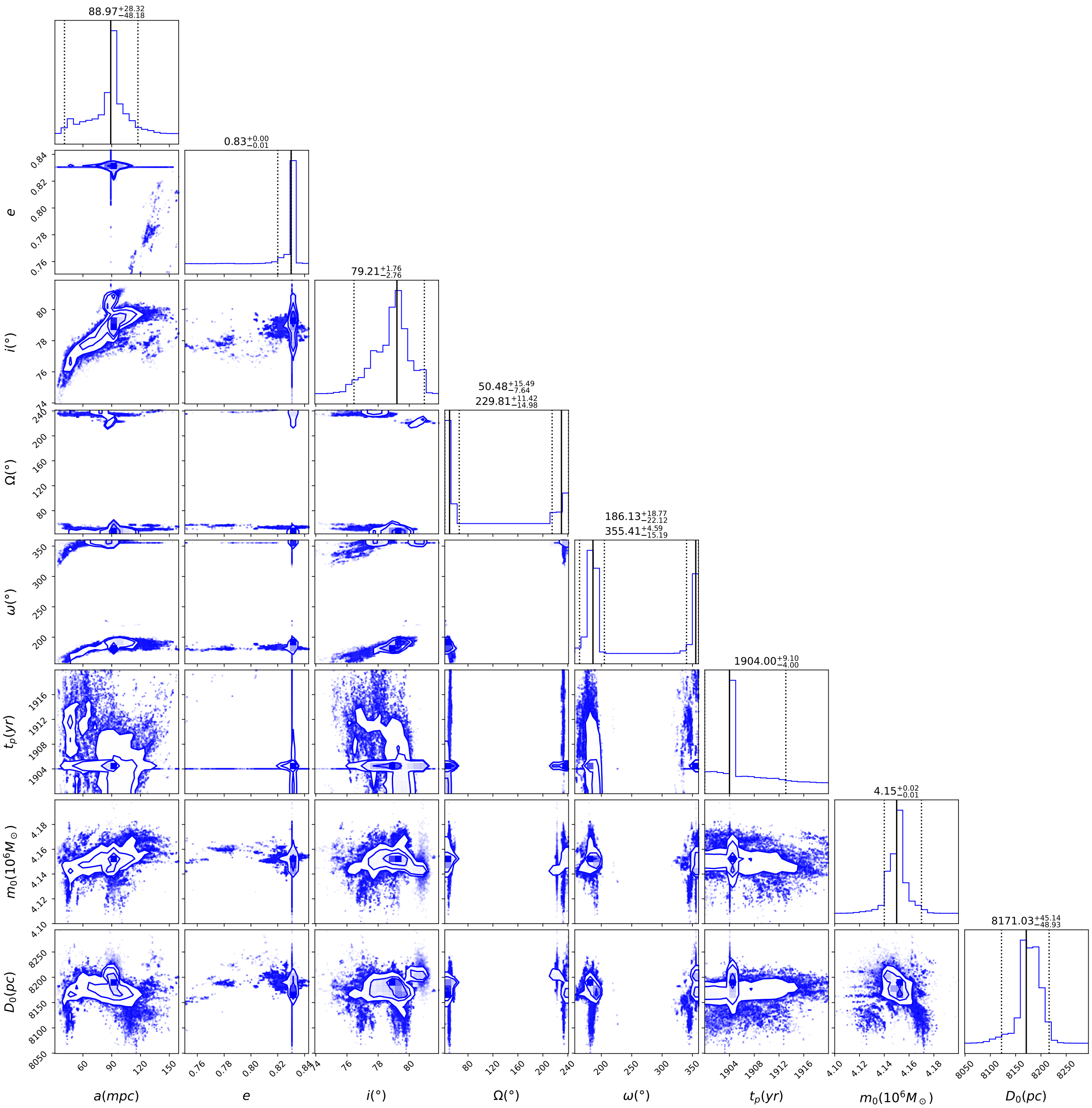

Figure 10. A customized corner plot of the orbit of S43 using Ultranest algorithm. The eight parameters are the semi-major axis (a), eccentricity (e), inclination (i), longitude of ascending node (Ω), argument at the pericenter (ω), time of closest approach (t_p), mass of the SMBH (m_0) and distance to the GC (D_0). The uncertainties represent the 95% confidence interval.

the primary star from an unequal-mass binary would be deposited at larger semimajor axes relative to the secondary, shedding light on the issue of scarcity of O-type stars among the S-population. They also find that the bound stars are on highly eccentric orbits ($e \geqslant 0.96$) with semimajor axes between 10^{-3} - 1 pc. In the further support of the Hills argument, Koposov et al. (2019) recently discovered a hyper-velocity star with a 3D velocity in the Galactic frame of 1755 ± 50 km/s. The authors conclude that this star was probably ejected by Sgr A* 4.8 Myr ago, which is in agreement with the ages of the O- and B-type stars. Moreover, Gautam et al. (2019) find no signs of eclipsing binary systems within the inner arcsecond, nor among the CRD. This suggests

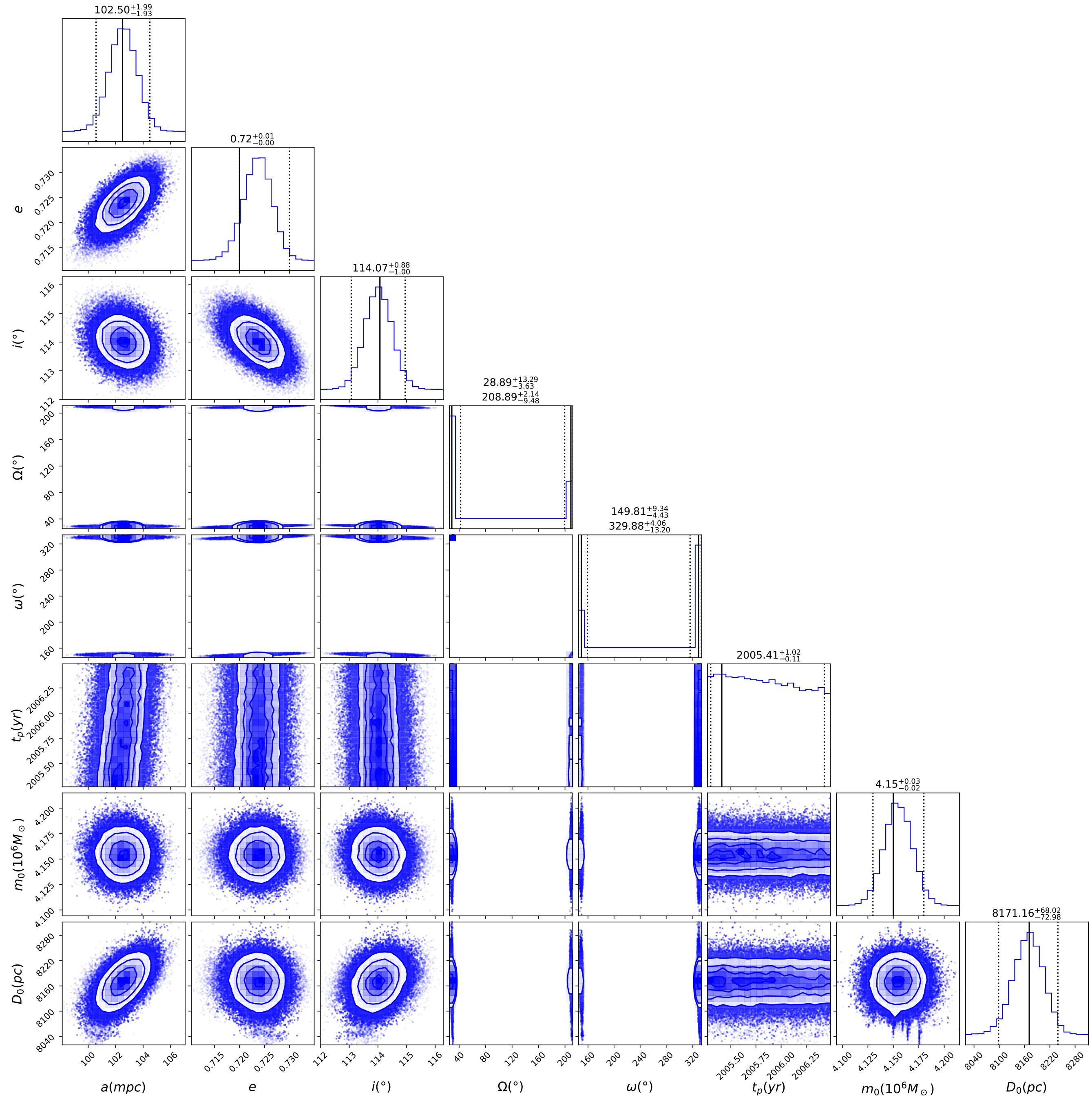

Figure 11. A customized corner plot of the orbit of S48 using Ultranest algorithm. The eight parameters are the semi-major axis (a), eccentricity (e), inclination (i), longitude of ascending node (Ω), argument at the pericenter (ω), time of closest approach (t_p), mass of the SMBH (m_0) and distance to the GC (D_0). The uncertainties represent the 95% confidence interval.

that both populations were most likely subjected to the Hills disruptions after their formation.

The Hills disruption alone, however, cannot explain the thermalized distribution of the S-stars. We focus, therefore, in the following on the other dynamical processes that might have contributed to the current observational findings.

4.2. *Loss-cone Dynamics*

Merritt (2013a) proposes a plausible explanation for a thermalized eccentricity distribution. Assuming that the initial eccentricity distribution of the disks is highly eccentric, i.e., the resulting distribution of the Hills mechanism, then this would place the stars below the so-called Schwarzschild barrier (SB) in the $e-a$ diagram.

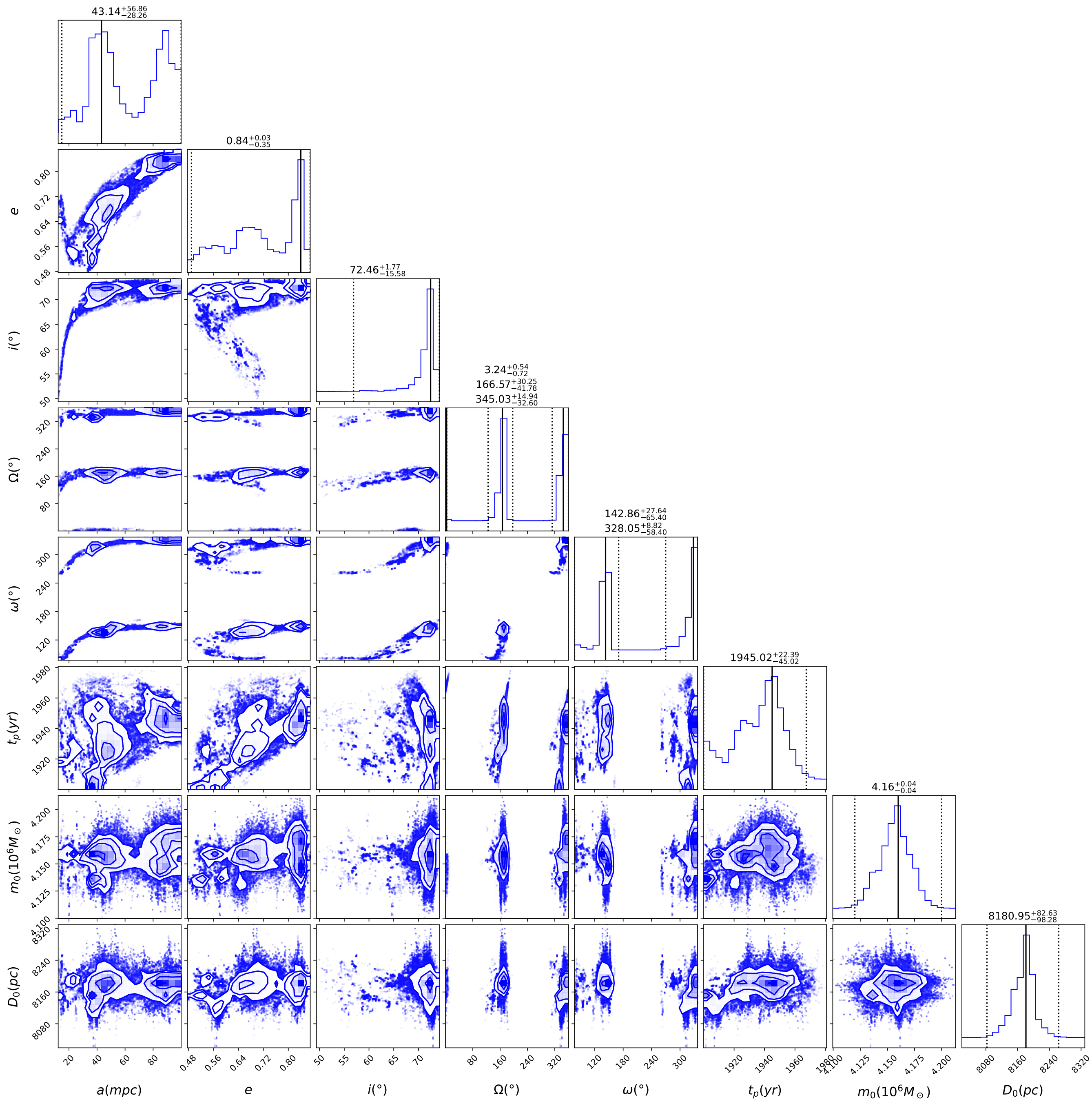

Figure 12. A customized corner plot of the orbit of S52 using Ultranest algorithm. The eight parameters are the semi-major axis (a), eccentricity (e), inclination (i), longitude of ascending node (Ω), argument at the pericenter (ω), time of closest approach (t_p), mass of the SMBH (m_0) and distance to the GC (D_0). The uncertainties represent the 95% confidence interval.

This barrier marks a location at which the relativistic precession timescale becomes smaller than the timescale for changes in the angular momentum due to coherent torques from an enclosed distribution of stars (see Brem et al. (2014) for further details). The star could evolve after some time and cross the SB. As soon as this is achieved, scalar resonant relaxation (SRR; Rauch & Tremaine 1996; Hopman & Alexander 2006) is then triggered, allowing the star to gain angular momentum and thus lowering its orbital eccentricity. Furthermore, the timescale of the SRR is reduced if there is a dense stellar black hole cusp at the center (Morris 1993; Miralda-Escudé & Gould 2000; Perets et al. 2009; Hailey et al. 2018; Mori et al. 2021). This allows us to conclude that

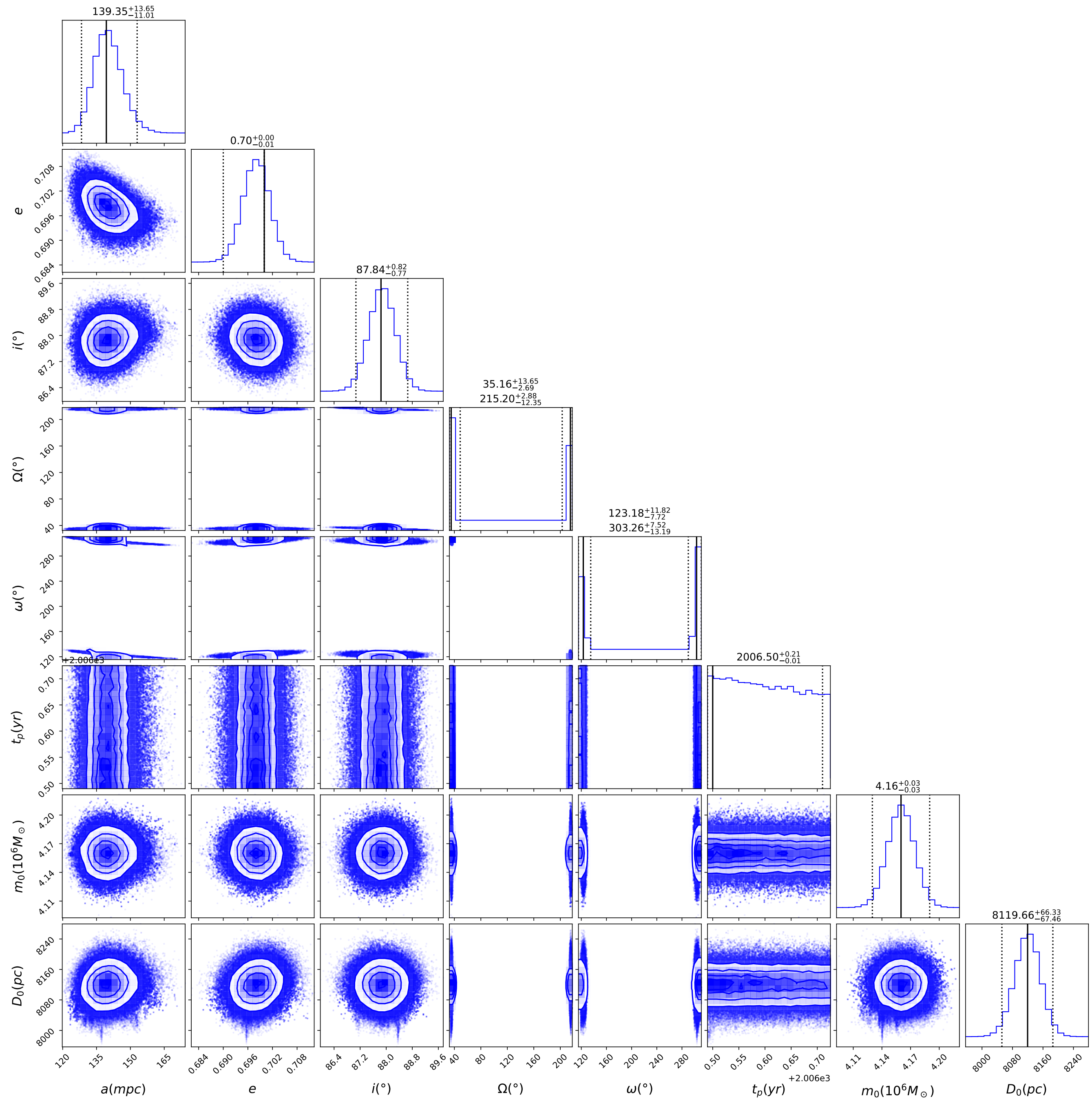

Figure 13. A customized corner plot of the orbit of S53 using Ultranest algorithm. The eight parameters are the semi-major axis (a), eccentricity (e), inclination (i), longitude of ascending node (Ω), argument at the pericenter (ω), time of closest approach (t_p), mass of the SMBH (m_0) and distance to the GC (D_0). The uncertainties represent the 95% confidence interval.

the combination of a dense stellar black hole cusp and SRR could thermalize an initial highly elliptical distribution. Keeping in mind that the cluster has not yet completely relaxed, and the observed distribution may be the result of an ongoing resonant relaxation in combination with other processes, namely the Kozai-Lidov resonance that we discuss in the following section.

4.3. *Kozai-Lidov Oscillations*

Another process that contributes to the distributions of the orbital elements is the Kozai-Lidov mechanism (Kozai 1962; Lidov 1962), which describes the eccentricity-inclination oscillations that are triggered by a third massive perturber. The triple forms a hierarchical system, i.e. it can be considered that the third

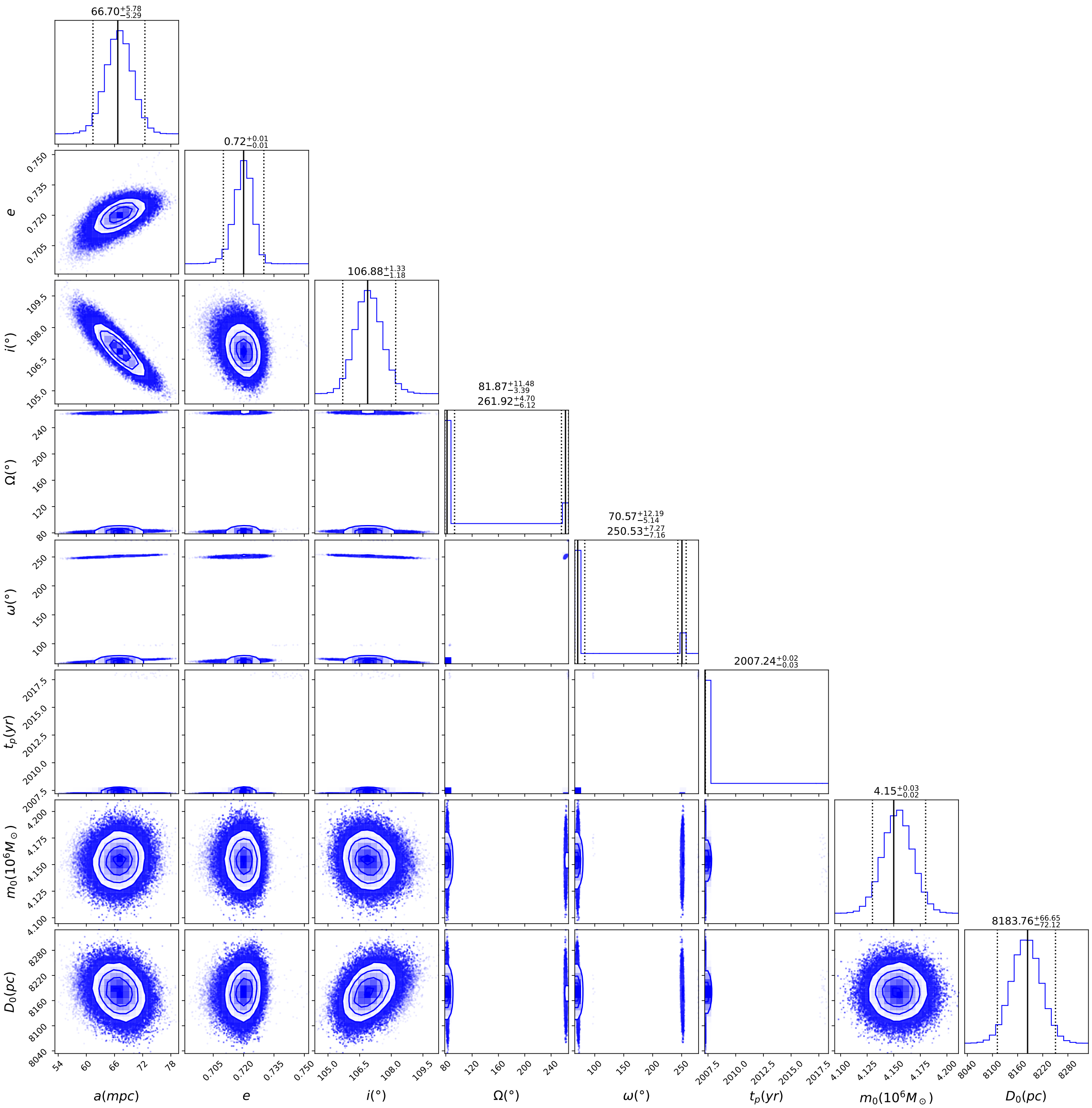

Figure 14. A customized corner plot of the orbit of S56 using Ultranest algorithm. The eight parameters are the semi-major axis (a), eccentricity (e), inclination (i), longitude of ascending node (Ω), argument at the pericenter (ω), time of closest approach (t_p), mass of the SMBH (m_0) and distance to the GC (D_0). The uncertainties represent the 95% confidence interval.

body orbits the inner binary on a much larger distance. The oscillations could in principle drive a highly eccentric face-on orbit to circular edge-on orbit or vice versa according to the conservation of the z-component of the angular momentum vector $L_z = \sqrt{(1-e^2)}\cos i =$ const.

In our case, the inner binary consists of the SMBH and an S-star and the third body could be a massive stellar or gaseous disk (Šubr & Karas 2005) or an intermediate-mass black hole (IMBH). A massive stellar and/or a gaseous disk could be represented by the current clockwise disk with the remnant gas from the early star-formation episode within the disk (Levin &

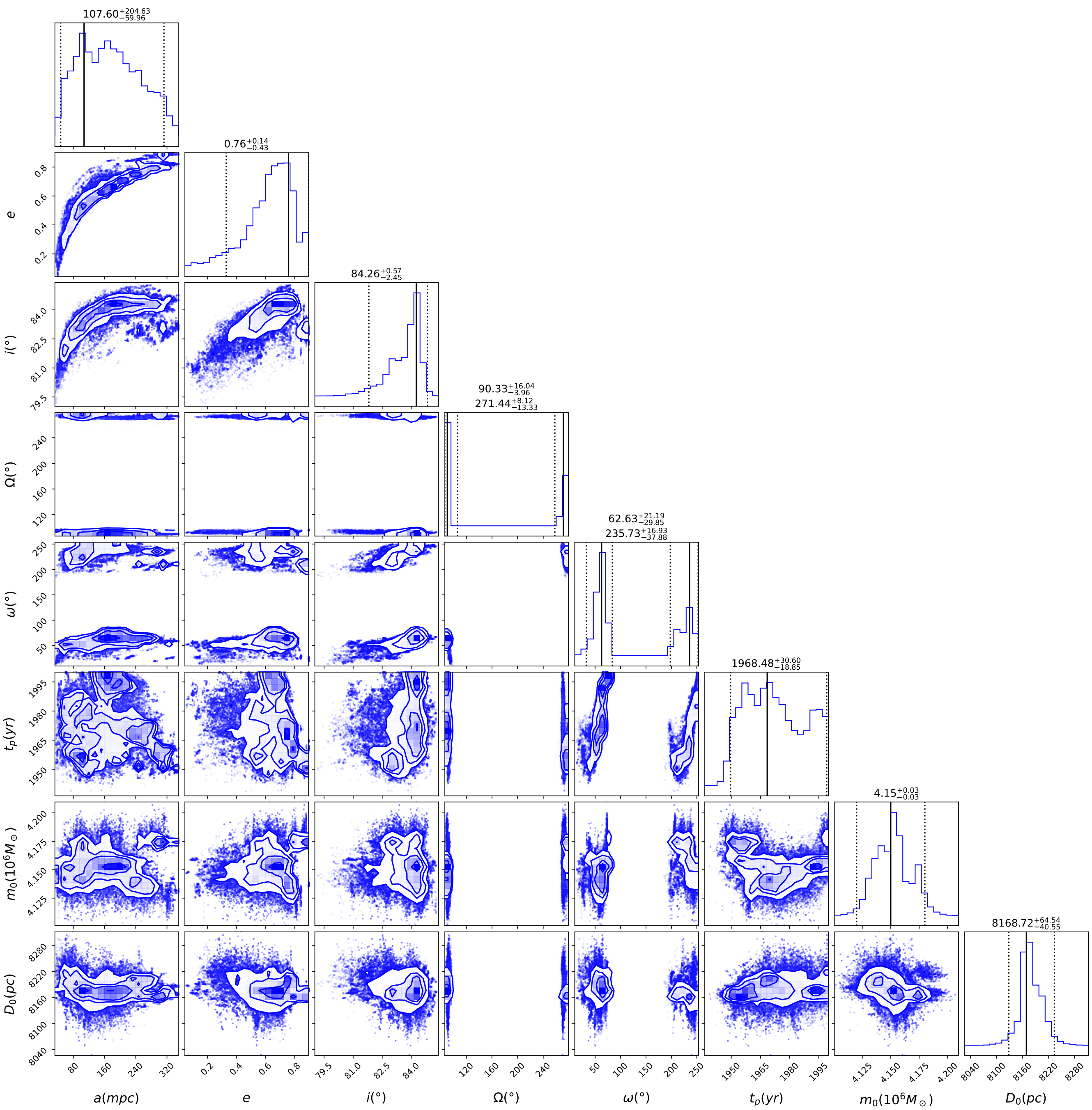

Figure 15. A customized corner plot of the orbit of S57 using Ultranest algorithm. The eight parameters are the semi-major axis (a), eccentricity (e), inclination (i), longitude of ascending node (Ω), argument at the pericenter (ω), time of closest approach (t_p), mass of the SMBH (m_0) and distance to the GC (D_0). The uncertainties represent the 95% confidence interval.

Beloborodov 2003; Milosavljević & Loeb 2004; Nayakshin et al. 2007; Chen & Amaro-Seoane 2014). The total mass during this phase could have been as much as $(3-10) \times 10^4\,M_\odot$ (Nayakshin et al. 2007; Bonnell & Rice 2008; Hobbs & Nayakshin 2009; Mapelli et al. 2012; Chen & Amaro-Seoane 2014). There are several channels for the formation of IMBHs, out of which two are the most relevant for the Galactic center – successive mergers of stellar black holes (Fragione et al. 2021) or repeated black hole-star mergers (Rose et al. 2021), and the dynamical inspiral of an IMBH within a globular cluster (Hansen & Milosavljević 2003; Kim et al. 2004). In both cases, the IMBH masses of the order of 10^3-$10^4\,M_\odot$ are expected. Observationally, the IMBH has

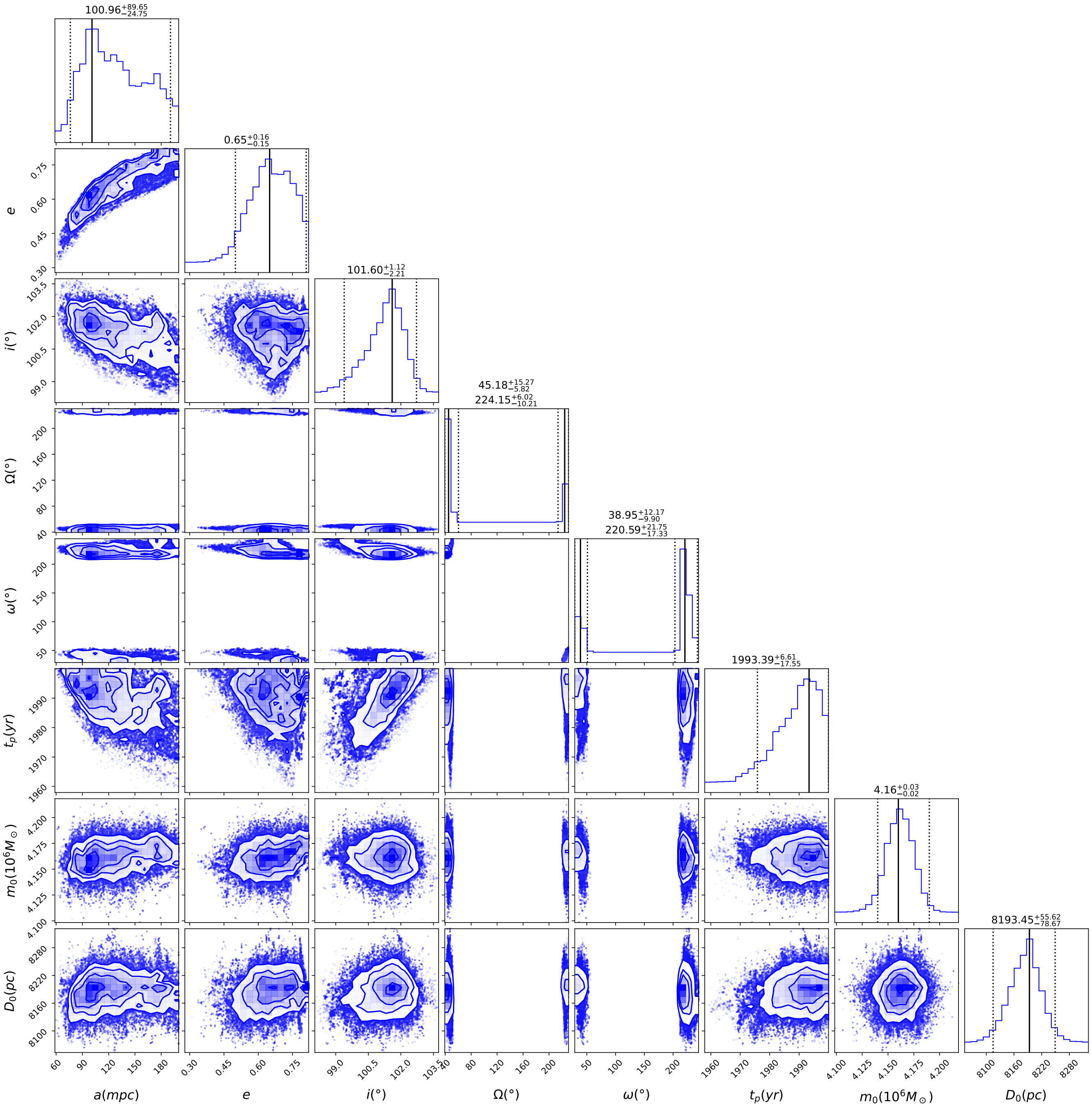

Figure 16. A customized corner plot of the orbit of S58 using Ultranest algorithm. The eight parameters are the semi-major axis (a), eccentricity (e), inclination (i), longitude of ascending node (Ω), argument at the pericenter (ω), time of closest approach (t_p), mass of the SMBH (m_0) and distance to the GC (D_0). The uncertainties represent the 95% confidence interval.

not yet been detected in the Galactic center, however, it has been speculated that compact clusters of massive young stars, such as IRS13E, could host one (Maillard et al. 2004).

To observe the effects of the Kozai-Lidov oscillations, we implement a non-relativistic three-body Hamiltonian, which consists of the Hamiltonian of two isolated binaries and a perturbative term. We use Delaunay orbital elements, since they remain well defined and non-singular when e and i are close to zero. To simplify the Hamiltonian, one could fix the longitude of ascending node and eliminate them, which can be justified by the assumption that one component of the inner binary is a test particle. We are then left with four orbital elements,

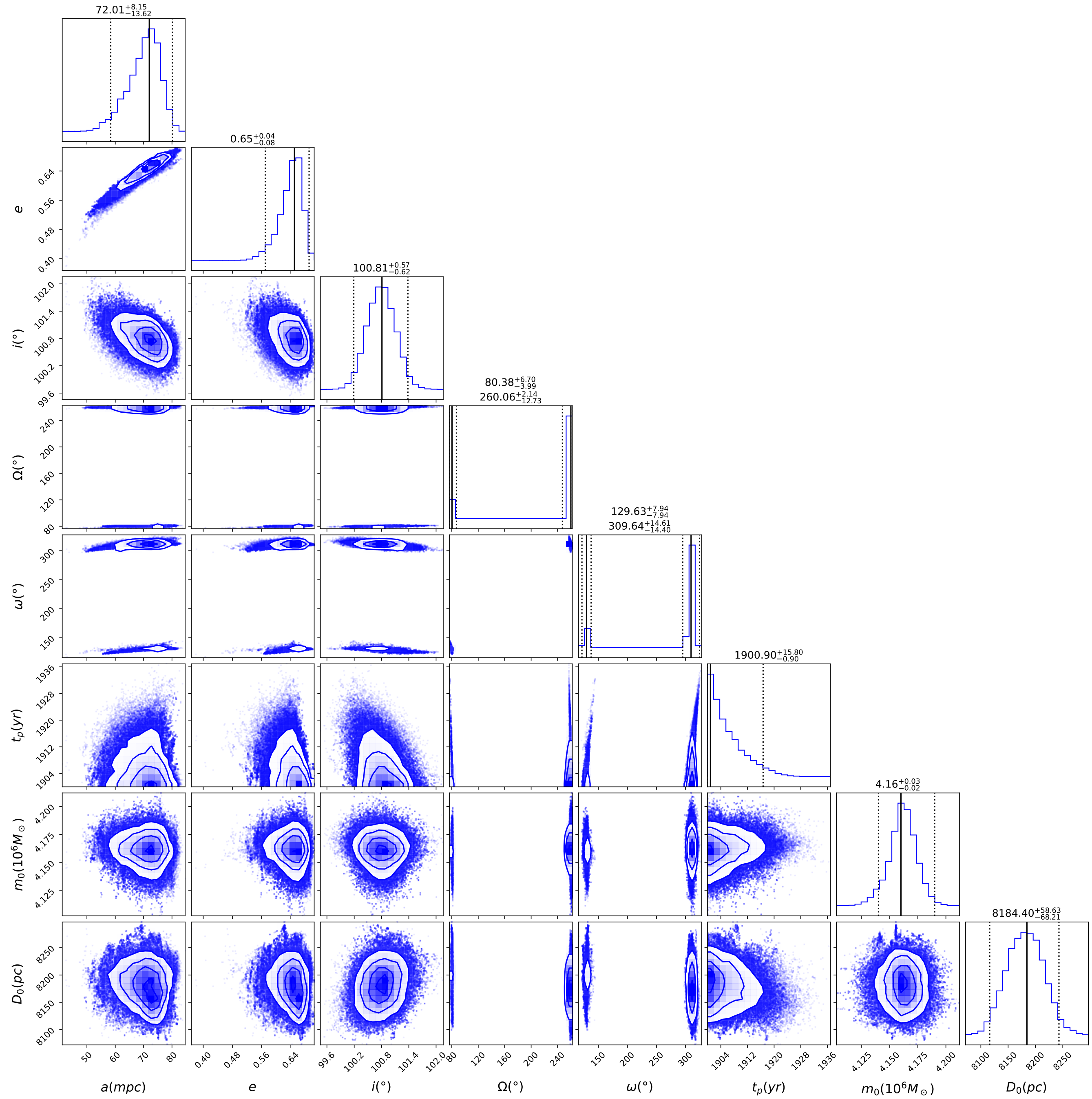

Figure 17. A customized corner plot of the orbit of S65 using Ultranest algorithm. The eight parameters are the semi-major axis (a), eccentricity (e), inclination (i), longitude of ascending node (Ω), argument at the pericenter (ω), time of closest approach (t_p), mass of the SMBH (m_0) and distance to the GC (D_0). The uncertainties represent the 95% confidence interval.

the semimajor axes (a_1, a_2), the eccentricities (e_1, e_2), the arguments of the pericenter (g_1, g_2) and the mutual inclination $i_{\rm mutual}$. Here, 1 refers to the elements of an S-star and 2 to the elements of a massive disturber. We also included General Relativity (GR) pericenter precession as well as the quadrupole and octupole oscillations based on Blaes et al. (2002). Using the numerical integrator ode in Scipy PYTHON, we evolve the triple in time and inspect the outcome. We consider the following three cases:

94

- An IMBH with the mass of $m_3 = 10^3\, M_\odot$ located at $a_2 = 0.15\,\mathrm{pc}$, orbiting the SMBH with an eccentricity of $e_2 = 0.1$.

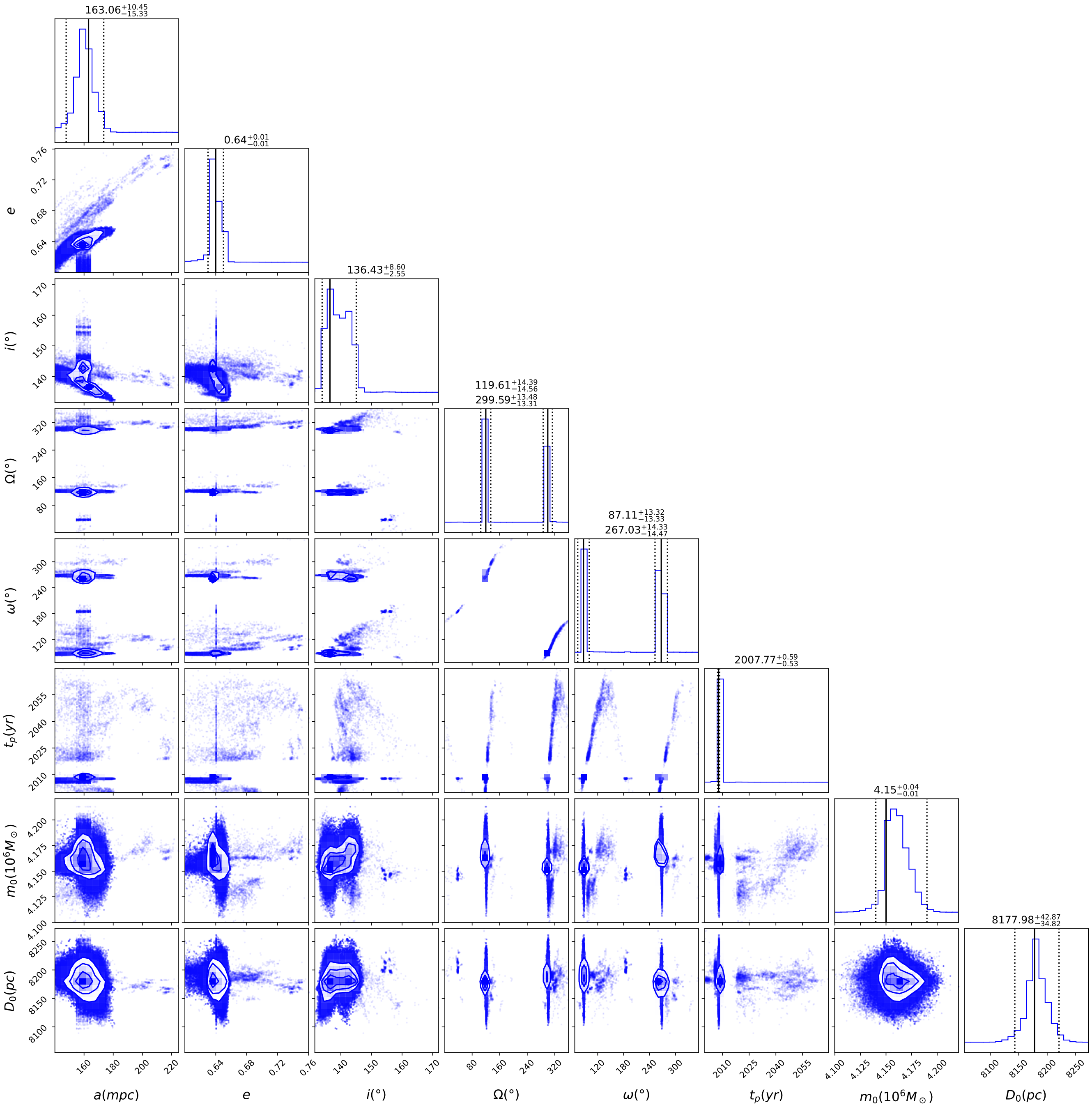

Figure 18. A customized corner plot of the orbit of S72 using Ultranest algorithm. The eight parameters are the semi-major axis (a), eccentricity (e), inclination (i), longitude of ascending node (Ω), argument at the pericenter (ω), time of closest approach (t_p), mass of the SMBH (m_0) and distance to the GC (D_0). The uncertainties represent the 95% confidence interval.

- An IMBH with mass of $m_3 = 10^4\,M_\odot$ located at $a_2 = 0.15\,\mathrm{pc}$, orbiting the SMBH with an eccentricity of $e_2 = 0.1$.

- A gaseous or a stellar disk with the mass of $m_3 = 10^5\,M_\odot$ located at $a_2 = 0.25\,\mathrm{pc}$, orbiting the SMBH with an eccentricity of $e_2 = 0.1$.

In addition, we choose two different mutual inclinations, namely, $i_{\mathrm{mutual}} = 40°$ and $80°$, two different inner binary eccentricities, these are $e_1 = 0.1$ and 0.6, and a fixed inner binary semi-major axis of $a_1 = 0.04$ pc. We then integrate the system for 10 Myr. The resulting evolutions of the eccentricity and the inclination are summarized in Figures 22, 23 and 24. Starting with

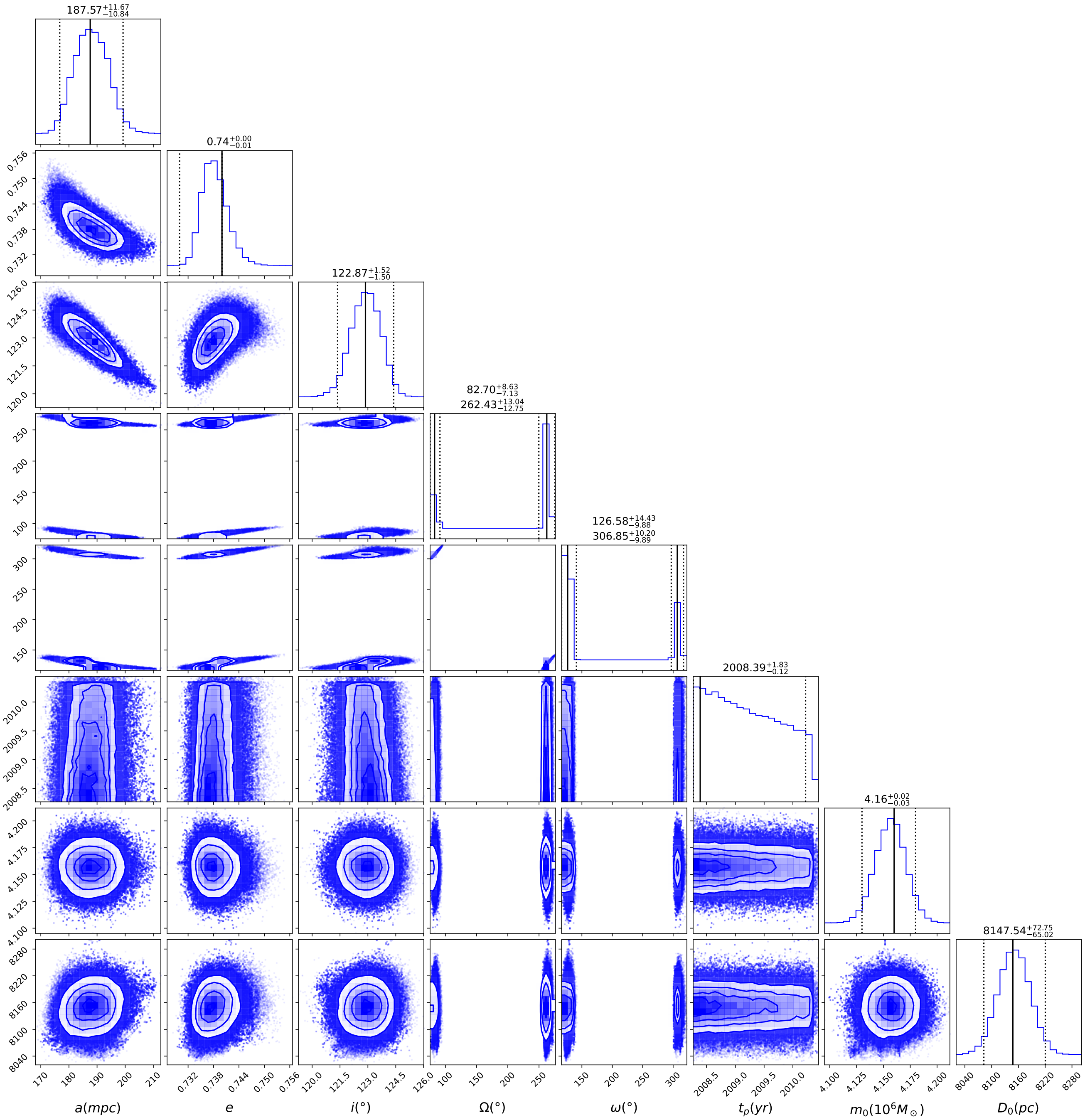

Figure 19. A customized corner plot of the orbit of S81 using Ultranest algorithm. The eight parameters are the semi-major axis (a), eccentricity (e), inclination (i), longitude of ascending node (Ω), argument at the pericenter (ω), time of closest approach (t_p), mass of the SMBH (m_0) and distance to the GC (D_0). The uncertainties represent the 95% confidence interval.

Figure 22, which represents the case of an IMBH of 10^3 $M_\odot$, we detect rather slow and low-amplitude oscillations whose amplitudes and frequencies increase with increasing e_1. Furthermore, the amplitude increases and the frequency decreases with increasing $i_{\rm mutual}$. As for the case of an IMBH of 10^4 $M_\odot$ in Figure 23, we notice that the cycles are faster compared to the former case. In particular, the amplitudes and the frequencies of the cycles are increasing with increasing e_1 and $i_{\rm mutual}$. In the condition of $i_{\rm mutual} = 80°$, we see that the eccentricity (e_1) reaches a maximum value after each cycle with an almost 25° amplitude for the mutual inclination. In the last consideration of a disk of 10^5 $M_\odot$, we find that both the amplitudes and the frequencies

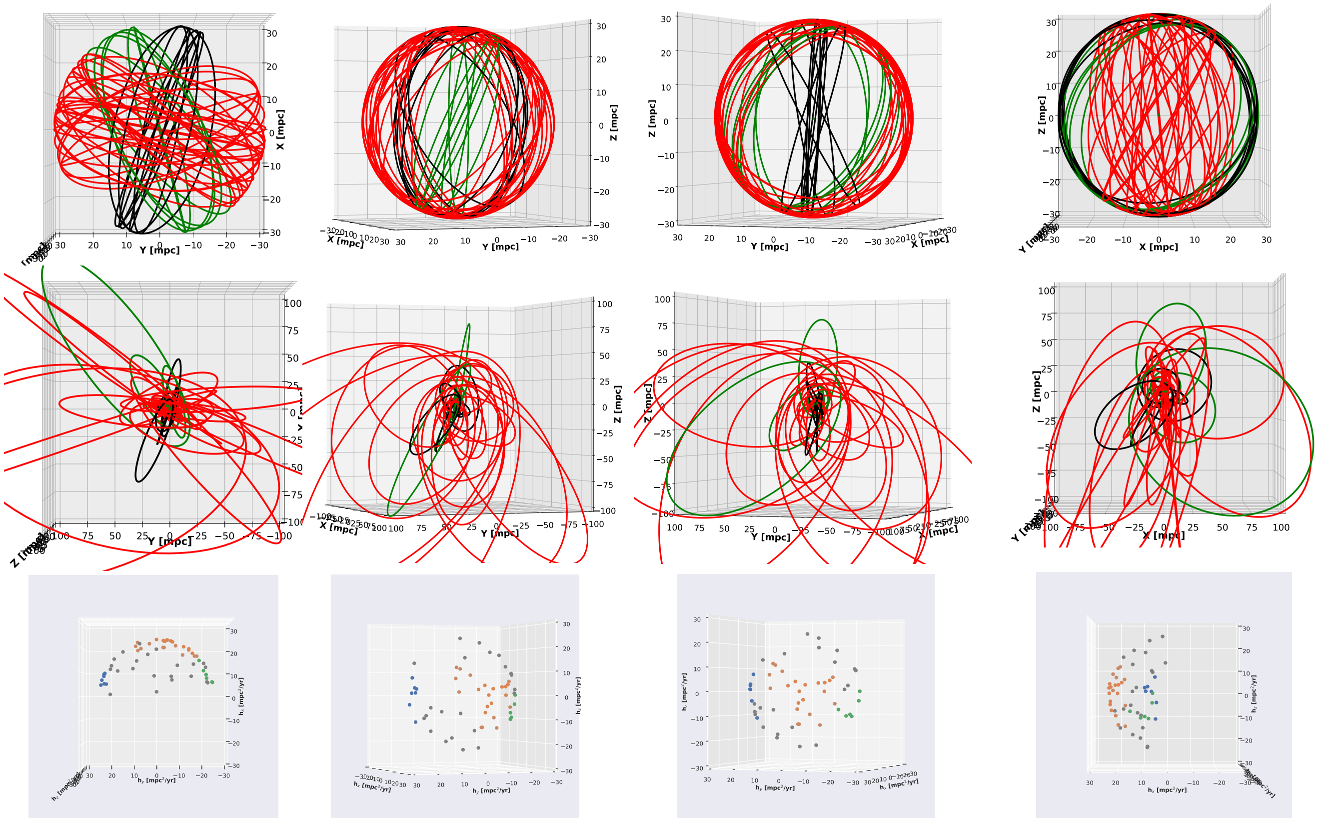

Figure 20. The results of HDBSCAN clustering on the specific angular momentum vectors (botthom row), the corresponding orbital representation in 3D (second row), and the orbits after setting the semi-major axis to a constant value and the eccentricity to zero. The viewing angles are from left to right: line of sight, green disk edge-on (el. = 0°, az. =-20°), black disk edge-on (el. = 0°, az. =+20°)and red disk edge-on (el. = 0°, az. =-90°).

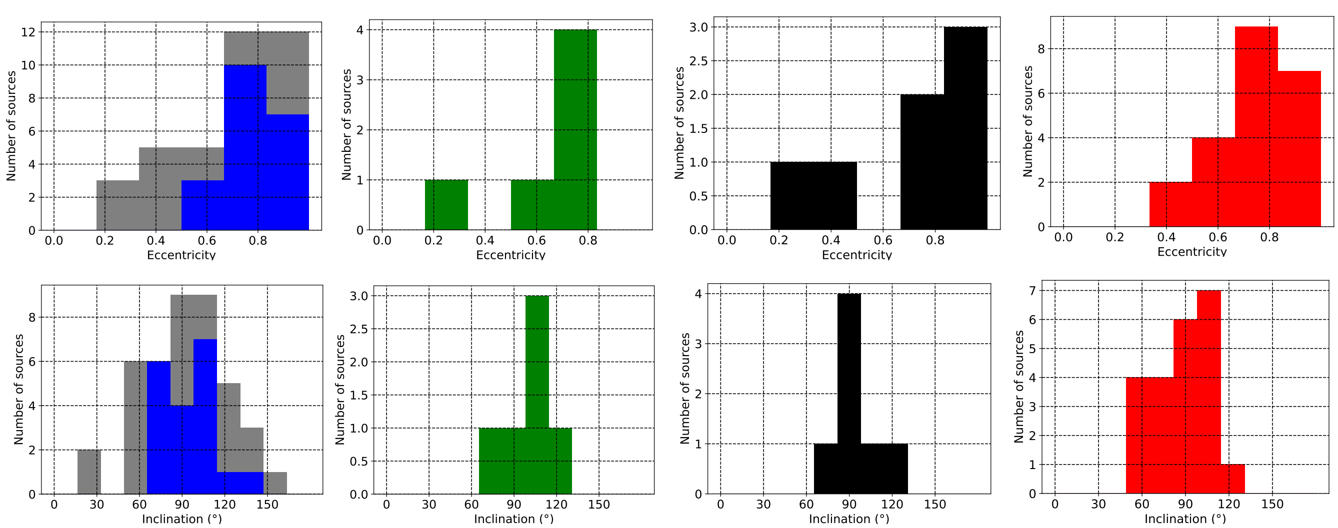

97

Figure 21. Histograms of both of the eccentricities and the inclinations in the following order: starting from left, blue represents the new 20 orbits and gray the 37 orbits, followed by the distribution of each of the disks.

Updated Orbital Elements of the 32 Stars from Ali et al. (2020)

1.	2.	3.	4.	5.	6.	7.	8.
Star	a ± Δa [mpc]	e ± Δe	i ± Δi [rad]	ω ±Δω [rad]	Ω ± ΔΩ [rad]	t_p ± Δt_p [yr]	$\sqrt{\chi^2_\nu}$
S1	$22.606^{+0.320}_{-0.320}$	$0.698^{+0.005}_{-0.005}$	$2.160^{+0.006}_{-0.006}$	$1.884^{+0.004}_{-0.004}$	$6.241^{+0.010}_{-0.010}$	$1999.749^{+0.004}_{-0.004}$	1.115
S2	$4.990^{+0.003}_{-0.003}$	$0.885^{+0.002}_{-0.002}$	$2.408^{+0.004}_{-0.004}$	$1.264^{+0.009}_{-0.009}$	$4.128^{+0.012}_{-0.012}$	$2{,}002.383^{+0.017}_{-0.017}$	1.876
S4	$14.339^{+0.041}_{-0.041}$	$0.348^{+0.008}_{-0.008}$	$1.437^{+0.003}_{-0.003}$	$5.005^{+0.004}_{-0.004}$	$4.466^{+0.008}_{-0.008}$	$1954.676^{+0.015}_{-0.015}$	0.814
S6	$24.664^{+0.416}_{-0.416}$	$0.892^{+0.018}_{-0.018}$	$1.565^{+0.023}_{-0.023}$	$2.088^{+0.009}_{-0.009}$	$1.385^{+0.071}_{-0.071}$	$1933.119^{+4.956}_{-4.956}$	1.810
S8	$21.336^{+0.092}_{-0.092}$	$0.853^{+0.018}_{-0.018}$	$1.361^{+0.007}_{-0.007}$	$5.751^{+0.028}_{-0.028}$	$5.564^{+0.014}_{-0.014}$	$1976.668^{+0.055}_{-0.055}$	0.900
S9	$11.169^{+0.018}_{-0.018}$	$0.673^{+0.021}_{-0.021}$	$1.461^{+0.012}_{-0.012}$	$2.465^{+0.010}_{-0.010}$	$2.725^{+0.009}_{-0.009}$	$1972.495^{+0.033}_{-0.033}$	1.278
S12	$10.753^{+0.298}_{-0.298}$	$0.915^{+0.004}_{-0.004}$	$0.426^{+0.007}_{-0.007}$	$5.462^{+0.011}_{-0.011}$	$4.087^{+0.012}_{-0.012}$	$1996.722^{+0.019}_{-0.019}$	0.855
S13	$9.668^{+2.356}_{-2.356}$	$0.421^{+0.049}_{-0.049}$	$0.417^{+0.183}_{-0.183}$	$4.477^{+0.218}_{-0.218}$	$0.828^{+0.267}_{-0.267}$	$2004.121^{+0.554}_{-0.554}$	7.113
S14	$6.806^{+3.123}_{-3.123}$	$0.851^{+0.299}_{-0.299}$	$1.813^{+0.301}_{-0.301}$	$5.911^{+0.296}_{-0.296}$	$3.961^{+0.420}_{-0.420}$	$2049.157^{+3.546}_{-3.546}$	4.221
S17	$14.607^{+0.915}_{-0.915}$	$0.308^{+0.034}_{-0.034}$	$1.578^{+0.009}_{-0.009}$	$5.070^{+0.042}_{-0.042}$	$3.388^{+0.018}_{-0.018}$	$1993.543^{+0.054}_{-0.054}$	3.659
S18	$10.284^{+0.613}_{-0.613}$	$0.707^{+0.012}_{-0.012}$	$1.874^{+0.066}_{-0.066}$	$5.513^{+0.024}_{-0.024}$	$0.704^{+0.031}_{-0.031}$	$1990.211^{+0.047}_{-0.047}$	4.402
S19	$9.697^{+2.866}_{-2.866}$	$0.685^{+0.073}_{-0.073}$	$1.614^{+0.055}_{-0.055}$	$2.409^{+0.097}_{-0.097}$	$5.889^{+0.082}_{-0.082}$	$2003.741^{+0.011}_{-0.011}$	2.822
S21	$8.743^{+0.244}_{-0.244}$	$0.818^{+0.018}_{-0.018}$	$0.930^{+0.039}_{-0.039}$	$2.651^{+0.056}_{-0.056}$	$4.721^{+0.017}_{-0.017}$	$2027.529^{+0.021}_{-0.021}$	1.901
S22	$52.373^{+3.005}_{-3.005}$	$0.517^{+0.074}_{-0.074}$	$1.860^{+0.014}_{-0.014}$	$1.657^{+0.255}_{-0.255}$	$5.112^{+0.077}_{-0.077}$	$1996.949^{+6.112}_{-6.112}$	2.799
S23	$13.709^{+2.048}_{-2.048}$	$0.524^{+0.213}_{-0.213}$	$0.979^{+0.072}_{-0.072}$	$0.642^{+0.221}_{-0.221}$	$4.155^{+0.416}_{-0.416}$	$2028.653^{+8.643}_{-8.643}$	2.628
S24	$47.170^{+3.128}_{-3.128}$	$0.735^{+0.049}_{-0.049}$	$1.725^{+0.081}_{-0.081}$	$4.558^{+0.037}_{-0.037}$	$0.256^{+0.025}_{-0.025}$	$2023.823^{+0.108}_{-0.108}$	1.403
S29	$34.509^{+4.122}_{-4.122}$	$0.330^{+0.084}_{-0.084}$	$1.732^{+0.009}_{-0.009}$	$5.745^{+0.285}_{-0.285}$	$2.942^{+0.019}_{-0.019}$	$2054.452^{+4.211}_{-4.211}$	2.103
S31	$16.793^{+6.667}_{-6.667}$	$0.534^{+0.159}_{-0.159}$	$1.922^{+0.201}_{-0.201}$	$5.635^{+0.788}_{-0.788}$	$2.548^{+0.327}_{-0.327}$	$2019.194^{+2.992}_{-2.992}$	3.924
S33	$30.650^{+3.825}_{-3.825}$	$0.671^{+0.064}_{-0.064}$	$1.107^{+0.029}_{-0.029}$	$5.281^{+0.048}_{-0.048}$	$1.892^{+0.074}_{-0.074}$	$1923.291^{+9.414}_{-9.414}$	1.553
S38	$5.716^{+0.187}_{-0.187}$	$0.814^{+0.052}_{-0.052}$	$2.788^{+0.320}_{-0.320}$	$0.268^{+0.196}_{-0.196}$	$1.701^{+0.140}_{-0.140}$	$2003.389^{+0.384}_{-0.384}$	4.287
S39	$12.741^{+3.199}_{-3.199}$	$0.918^{+0.038}_{-0.038}$	$1.442^{+0.392}_{-0.392}$	$0.395^{+0.255}_{-0.255}$	$2.779^{+0.034}_{-0.034}$	$1999.921^{+0.430}_{-0.430}$	4.791
S42	$38.498^{+4.546}_{-4.546}$	$0.630^{+0.019}_{-0.019}$	$1.177^{+0.017}_{-0.017}$	$0.696^{+0.031}_{-0.031}$	$3.558^{+0.022}_{-0.022}$	$2011.511^{+0.589}_{-0.589}$	1.430
S54	$48.343^{+12.150}_{-12.150}$	$0.899^{+0.014}_{-0.014}$	$0.997^{+0.042}_{-0.042}$	$2.625^{+0.077}_{-0.077}$	$4.564^{+0.085}_{-0.085}$	$2002.921^{+0.050}_{-0.050}$	4.520
S55	$4.409^{+0.016}_{-0.016}$	$0.752^{+0.009}_{-0.009}$	$2.477^{+0.033}_{-0.033}$	$2.237^{+0.054}_{-0.054}$	$2.281^{+0.050}_{-0.050}$	$2009.315^{+0.039}_{-0.039}$	2.966
S60	$20.079^{+2.028}_{-2.028}$	$0.857^{+0.016}_{-0.016}$	$2.344^{+0.042}_{-0.042}$	$0.970^{+0.271}_{-0.271}$	$3.671^{+0.283}_{-0.283}$	$2020.657^{+1.899}_{-1.899}$	0.978
S62	$3.603^{+0.002}_{-0.002}$	$0.980^{+0.001}_{-0.001}$	$1.078^{+0.001}_{-0.001}$	$0.786^{+0.001}_{-0.001}$	$1.962^{+0.001}_{-0.001}$	$2003.441^{+0.009}_{-0.009}$	1.298
S64	$25.695^{+0.568}_{-0.568}$	$0.607^{+0.014}_{-0.014}$	$1.972^{+0.006}_{-0.006}$	$3.589^{+0.073}_{-0.073}$	$2.613^{+0.025}_{-0.025}$	$2{,}016.284^{+2.399}_{-2.399}$	0.430
S71	$40.095^{+2.008}_{-2.008}$	$0.971^{+0.020}_{-0.020}$	$1.052^{+0.072}_{-0.072}$	$5.847^{+0.044}_{-0.044}$	$0.722^{+0.048}_{-0.048}$	$1667.731^{+13.657}_{-13.657}$	2.156
S85	$181.988^{+4.166}_{-4.166}$	$0.790^{+0.008}_{-0.008}$	$1.514^{+0.022}_{-0.022}$	$2.631^{+0.054}_{-0.054}$	$1.913^{+0.015}_{-0.015}$	$1928.259^{+7.998}_{-7.998}$	1.343
S89	$39.306^{+4.673}_{-4.673}$	$0.725^{+0.202}_{-0.202}$	$1.575^{+0.027}_{-0.027}$	$2.317^{+0.020}_{-0.020}$	$4.119^{+0.014}_{-0.014}$	$1829.259^{+12.730}_{-12.730}$	1.630
S145	$44.272^{+0.399}_{-0.399}$	$0.486^{+0.021}_{-0.021}$	$1.741^{+0.112}_{-0.112}$	$3.180^{+0.044}_{-0.044}$	$4.596^{+0.007}_{-0.007}$	$1808.878^{+2.462}_{-2.462}$	0.536
S175	$29.059^{+0.001}_{-0.001}$	$0.982^{+0.001}_{-0.001}$	$1.609^{+0.001}_{-0.001}$	$1.006^{+0.001}_{-0.001}$	$5.996^{+0.001}_{-0.001}$	$2009.727^{+0.001}_{-0.001}$	0.986

Table 1. A list of the orbital elements and their corresponding uncertainties for the stars mentioned in column (1). The Keplerian elements start with the semi-major axis (a), eccentricity (e), inclination (i), argument at the pericenter (ω), longitude of ascending node (Ω) and time of closest approach (t_p). The last column contains the square root of the reduced chi-square ($\sqrt{\chi^2_\nu}$), which is used to scale the errors such that χ^2_ν approaches unity.

Orbital Elements of the Newly Fitted Stars

1.	2.	3.	4.	5.	6.	7.	8.	9.
Star	a ± Δa [mpc]	e ± Δe	i ± Δi [deg]	Ω ±ΔΩ [deg]	ω ± Δω [deg]	t_p ± Δt_p [yr]	m_0 ± Δm_0 [$M_\odot$x10^6]	D_0 ± ΔD [pc]
S7	$49.41^{+50.58}_{-33.26}$	$0.96^{+0.01}_{-0.25}$	$67.39^{+7.12}_{-8.59}$	$16.16^{+59.74}_{-14.91}$	$66.54^{+27.19}_{-15.67}$	$2108.16^{+20.86}_{-28.16}$	$4.15^{+0.05}_{-0.05}$	$8166.25^{+100.06}_{-110.07}$
				$197.84^{+62.46}_{-33.95}$	$247.03^{+11.32}_{-28.23}$			
S11	$173.18^{+20.44}_{-87.14}$	$0.67^{+0.07}_{-0.21}$	$105.91^{+1.90}_{-2.04}$	$127.27^{+13.82}_{-3.60}$	$118.83^{+18.62}_{-12.75}$	$2017.98^{+21.40}_{-11.07}$	$4.15^{+0.03}_{-0.02}$	$8180.32^{+67.55}_{-64.91}$
				$308.04^{+10.22}_{-12.17}$	$296.52^{+20.96}_{-15.52}$			
S20	$29.09^{+2.26}_{-1.86}$	$0.92^{+0.01}_{-0.01}$	$83.46^{+0.26}_{-0.29}$	$73.89^{+13.90}_{-0.82}$	$87.02^{+13.81}_{-1.38}$	$2022.81^{+0.38}_{-0.37}$	$4.15^{+0.03}_{-0.02}$	$8191.68^{+62.25}_{-74.89}$
				$253.88^{+0.82}_{-14.18}$	$267.04^{+1.46}_{-13.91}$			
S26	$120.32^{+7.94}_{-8.10}$	$0.75^{+0.01}_{-0.02}$	$81.32^{+0.73}_{-0.82}$	$55.48^{+13.71}_{-1.22}$	$163.35^{+13.26}_{-13.45}$	$2015.80^{+0.55}_{-2.32}$	$4.15^{+0.03}_{-0.02}$	$8162.57^{+68.68}_{-58.18}$
				$235.52^{+7.66}_{-12.57}$	$343.37^{+14.52}_{-14.53}$			
S30	$23.70^{+40.56}_{-7.72}$	$0.85^{+0.08}_{-0.11}$	$70.02^{+4.75}_{-20.93}$	$97.98^{+24.30}_{-26.80}$	$95.00^{+20.97}_{-43.33}$	$1918.05^{+20.60}_{-12.07}$	$4.15^{+0.03}_{-0.01}$	$8149.96^{+109.33}_{-29.47}$
				$240.88^{+44.90}_{-16.08}$	$262.77^{+13.98}_{-30.29}$			
S32	$128.31^{+62.26}_{-28.26}$	$0.89^{+0.01}_{-0.05}$	$81.66^{+0.57}_{-0.66}$	$61.63^{+9.48}_{-7.60}$	$41.39^{+4.03}_{-4.18}$	$2097.82^{+2.18}_{-13.81}$	$4.16^{+0.02}_{-0.01}$	$8147.76^{+40.96}_{-45.82}$
				$242.84^{+2.46}_{-2.57}$	$222.41^{+12.11}_{-11.84}$			
S34	$180.22^{+18.13}_{-20.54}$	$0.69^{+0.01}_{-0.02}$	$112.18^{+2.04}_{-1.55}$	$69.68^{+13.77}_{-3.06}$	$101.12^{+11.20}_{-1.87}$	$2016.74^{+0.87}_{-0.50}$	$4.15^{+0.03}_{-0.02}$	$8188.26^{+59.62}_{-72.52}$
				$249.13^{+11.42}_{-11.53}$	$281.85^{+13.65}_{-13.65}$			
S36	$26.31^{+19.52}_{-8.81}$	$0.93^{+0.01}_{-0.03}$	$84.06^{+1.30}_{-1.95}$	$30.87^{+13.07}_{-13.06}$	$84.23^{+9.53}_{-7.60}$	$1907.23^{+25.87}_{-5.72}$	$4.16^{+0.01}_{-0.01}$	$8181.66^{+25.71}_{-35.83}$
				$207.95^{+10.59}_{-10.42}$	$274.02^{+12.91}_{-15.33}$			
S41	$25.45^{+41.93}_{-11.05}$	$0.95^{+0.01}_{-0.05}$	$107.67^{+6.30}_{-1.92}$	$108.04^{+40.86}_{-22.87}$	$104.09^{+13.03}_{-13.34}$	$1946.34^{+2.70}_{-44.36}$	$4.16^{+0.02}_{-0.03}$	$8165.87^{+64.27}_{-57.59}$
				$308.39^{+25.93}_{-52.38}$	$283.23^{+13.03}_{-13.34}$			
S43	$88.97^{+28.32}_{-48.18}$	$0.83^{+0.00}_{-0.01}$	$79.21^{+1.76}_{-2.76}$	$50.48^{+15.49}_{-7.64}$	$186.13^{+18.77}_{-22.12}$	$1904.00^{+9.10}_{-4.00}$	$4.15^{+0.02}_{-0.01}$	$8171.03^{+45.14}_{-48.93}$
				$229.81^{+11.42}_{-14.98}$	$335.41^{+4.59}_{-15.19}$			
S48	$102.50^{+1.99}_{-1.93}$	$0.72^{+0.01}_{-0.00}$	$114.07^{+0.88}_{-1.00}$	$28.89^{+13.29}_{-3.63}$	$149.81^{+9.34}_{-4.43}$	$2005.41^{+1.02}_{-0.11}$	$4.15^{+0.03}_{-0.02}$	$8171.16^{+68.02}_{-72.98}$
				$208.89^{+2.14}_{-9.48}$	$329.88^{+4.06}_{-13.20}$			
S52	$43.14^{+56.86}_{-28.26}$	$0.84^{+0.03}_{-0.35}$	$72.46^{+1.77}_{-15.58}$	$166.57^{+30.25}_{-41.78}$	$142.86^{+27.64}_{-65.40}$	$1645.02^{+22.39}_{-45.02}$	$4.16^{+0.04}_{-0.04}$	$8180.95^{+82.63}_{-98.28}$
				$345.03^{+14.94}_{-32.60}$	$328.05^{+8.82}_{-58.40}$			
S53	$139.35^{+13.65}_{-11.01}$	$0.70^{+0.00}_{-0.01}$	$87.84^{+0.82}_{-0.77}$	$35.16^{+13.65}_{-2.69}$	$123.18^{+11.82}_{-7.72}$	$2006.50^{+0.21}_{-0.01}$	$4.16^{+0.03}_{-0.03}$	$8119.66^{+66.33}_{-67.46}$
				$215.20^{+2.88}_{-12.35}$	$303.26^{+7.52}_{-13.19}$			
S56	$66.70^{+5.78}_{-5.29}$	$0.72^{+0.01}_{-0.01}$	$106.88^{+1.33}_{-1.18}$	$81.87^{+11.48}_{-3.39}$	$70.57^{+12.19}_{-5.14}$	$2007.24^{+0.02}_{-0.03}$	$4.15^{+0.03}_{-0.02}$	$8183.76^{+66.65}_{-72.12}$
				$261.92^{+4.70}_{-6.12}$	$250.53^{+7.27}_{-7.16}$			
S57	$107.06^{+204.63}_{-59.96}$	$0.76^{+0.14}_{-0.43}$	$84.26^{+0.57}_{-2.45}$	$90.33^{+16.04}_{-3.96}$	$62.63^{+21.19}_{-29.85}$	$1968.48^{+30.60}_{-18.85}$	$4.15^{+0.03}_{-0.03}$	$8168.72^{+64.54}_{-40.55}$
				$271.44^{+8.12}_{-13.33}$	$235.73^{+16.93}_{-37.88}$			
S58	$100.96^{+89.65}_{-24.75}$	$0.65^{+0.16}_{-0.15}$	$101.60^{+1.12}_{-2.21}$	$45.18^{+15.27}_{-5.82}$	$38.95^{+12.17}_{-9.90}$	$1993.39^{+6.61}_{-17.55}$	$4.16^{+0.03}_{-0.02}$	$8193.45^{+55.62}_{-78.67}$
				$224.15^{+6.02}_{-10.21}$	$220.59^{+21.75}_{-17.33}$			
S65	$72.01^{+8.15}_{-13.62}$	$0.65^{+0.04}_{-0.08}$	$100.81^{+0.57}_{-0.62}$	$80.38^{+6.70}_{-3.99}$	$129.63^{+7.94}_{-7.94}$	$1900.90^{+15.80}_{-0.90}$	$4.16^{+0.03}_{-0.02}$	$8184.40^{+58.63}_{-68.21}$
				$260.06^{+2.14}_{-12.73}$	$309.64^{+14.61}_{-14.40}$			
S72	$163.06^{+10.45}_{-15.33}$	$0.64^{+0.01}_{-0.01}$	$136.43^{+8.60}_{-2.55}$	$119.61^{+14.39}_{-14.56}$	$87.11^{+13.32}_{-13.33}$	$2007.77^{+0.59}_{-0.53}$	$4.15^{+0.04}_{-0.01}$	$8177.98^{+42.87}_{-34.82}$
				$299.59^{+13.48}_{-13.31}$	$267.03^{+14.33}_{-14.47}$			
S78	$120.46^{+2.96}_{-2.76}$	$0.75^{+0.01}_{-0.00}$	$4.76^{+5.92}_{-4.31}$	$93.00^{+65.37}_{-27.43}$	$70.54^{+27.21}_{-64.74}$	$2018.39^{+0.01}_{-0.28}$	$4.19^{+0.02}_{-0.02}$	$7926.88^{+41.35}_{-50.80}$
				$272.18^{+30.11}_{-19.05}$	$251.38^{+18.68}_{-29.31}$			
S81	$187.57^{+11.67}_{-10.84}$	$0.74^{+0.00}_{-0.01}$	$122.87^{+1.52}_{-1.50}$	$82.70^{+8.63}_{-7.13}$	$126.58^{+14.43}_{-9.88}$	$2008.39^{+1.83}_{-0.12}$	$4.16^{+0.02}_{-0.03}$	$8147.54^{+72.75}_{-65.02}$
				$262.43^{+13.04}_{-12.75}$	$306.85^{+10.20}_{-9.89}$			

Table 2. The results of Ultranest for the newly fitted orbits. These are their orbital elements, estimated mass of Sgr A*, distance to the Galactic center and their corresponding 2σ uncertainties for the stars mentioned in column (1). The Keplerian elements start with the semi-major axis (a), eccentricity (e), inclination (i), longitude of ascending node (Ω), argument at the pericenter (ω) and time of closest approach (t_p). The mass of Sgr A* is listed as m_0 and the distance to the Galactic center as D_0. 99

of the oscillations have remarkably intensified compared to the two former cases. The pattern of the oscillation,

Results of the clustering algorithm HDBSCAN

1.	2.	3.	4.
Star	Cluster	Probability	Outlier-score
S1	outlier	0	0.423
S2	outlier	0	0.056
S4	red	1	0
S6	red	1	0
S8	outlier	0	0.044
S9	black	1	0
S12	outlier	0	0.440
S13	outlier	0	0.174
S14	red	0.768	0.231
S17	green	1	0
S18	green	1	0
S19	black	1	0
S21	outlier	0	0.118
S22	red	0.718	0.281
S23	red	0.649	0.350
S24	green	1	0
S29	black	1	0
S31	outlier	0	0.044
S33	red	0.718	0.281
S38	outlier	0	0.327
S39	black	1	0
S42	green	1	0
S54	red	0.813	0.186
S55	outlier	0	0.186
S60	outlier	0	0.174
S62	red	0.718	0.281
S64	outlier	0	0.044
S71	outlier	0	0.009
S85	red	0.711	0.288
S89	red	0.966	0.033
S145	red	1	0
S175	black	1	0
S4711	green	1	0
S4712	black	0.849	0.150
S4713	outlier	0	0.100
S4714	outlier	0	0.044
S4715	outlier	0	0.049

Table 3. Results of the HDBSCAN algorithm for the 37 orbits with cluster status at second column, followed by the cluster probability (1 close to cluster center - 0 no membership) and outlier-scores at the last column.

Results of the clustering algorithm HDBSCAN

1.	2.	3.	4.
Star	Cluster	Probability	Outlier-score
S7	outlier	0	0.093
S11	outlier	0	0.044
S20	red	1	0
S26	red	1	0
S30	red	0.718	0.281
S32	red	1	0
S34	red	0.745	0.254
S36	outlier	0	0.023
S41	outlier	0	0.003
S43	red	0.998	0.001
S48	green	1	0
S52	black	1	0
S53	outlier	0	0.002
S56	red	0.878	0.121
S57	red	0.921	0.078
S58	red	0.640	0.359
S65	red	1	0
S72	outlier	0	0.224
S78	outlier	0	0.565
S81	red	0.783	0.216

Table 4. Results of the HDBSCAN algorithm for the 20 new orbits with cluster status at second column, followed by the cluster probability (1 close to cluster center - 0 no membership) and outlier-scores at the last column.

however, is similar to the one triggered by an IMBH of $10^4\,M_\odot$. In such a situation, the eccentricity could also reach a maximum value, while the mutual inclination cycles start with around 30° amplitude that decreases with time. Overall, we conclude that for all the three cases, KL oscillations may indeed play a crucial role in the observed eccentricity-inclination distributions.

Things become very interesting when $i_{\rm mutual}$ approaches 90° and e_1 is around 0.8. In this case, the inclination oscillation is heavily diminished and we observe a flip in the orientation of the orbit. The flips could also occur for $i_{\rm mutual}$ of 80° or 100°, for which the evolution of the argument of the pericenter is similar. By inspecting Figure 25, which corresponds to the first condition, i.e. an IMBH of $10^3\,M_\odot$, we find that the eccentricity cycles peak at 0.88. On the other hand, the amplitude of the mutual inclination does not exceed 0.04°. This shows that in this limit ($i_{\rm mutual} \approx 90°$), one observes a very slight change in the inclination. In contrast, the argument of the pericenter of the inner binary increases gradually till reaching a value of 360° after approximately 7 Myr and then drops again to zero and so on. The timescale of the flip is similar to the cases of $i_{\rm mutual} = 80°$ or 100°. However, when one lowers e_1 to 0.7, the timescale of the flip increases from 7 Myr to 10 Myr (see Figures 28 and 29). Since the line of the pericenter is somewhat fixed, this means that the ascending node and the descending node are switching places. Accordingly, if the longitude of the ascending node had an initial value of 90°, here we assume that the direction of the north is perpendicular to the line of nodes, then one would need to add 180° to reach the new position of the ascending node. This results in $\Omega = 270°$, implying that the star is now orbiting anti-clockwise. Concerning Figure 26, we find that by increasing the mass of the IMBH, the eccentricity amplitude could initially reach a maximum value, while the amplitude of the mutual inclination has decreased to 0.012°. Similarly, the argument of the pericenter flips from 0° to around 300°, then it keeps oscillating in that range with a decreasing amplitude. In contrast, for the cases of $i_{\rm mutual} = 80°$ or 100°, we observe two flips after around 3 Myr and 7 Myr. Here also, the timescale of the flip increases slightly when one lowers e_1. In the last consideration of a disk of $10^5\,M_\odot$ (Figure 27), we notice that the frequency of the cycles considerably increases. In such a scenario, the eccentricity oscillates between 0.65 and 0.99, while the amplitude of the mutual inclination has a maximum value of 0.05°. As for the argument of the pericenter, we detect a change from 0° to 120°, followed by frequent 60°-amplitude cycles. On the other hand, the flip occurs after around 2.5 Myr for the cases when the mutual inclination is 80° or 100°, followed by an oscillation in the range between 50° and 100° . By decreasing e_1 to 0.7, the timescale of the flip decreases to about 2 Myr, followed by an oscillation in the range between 250° and 300°. In conclusion, we find that the KL-mechanism could indeed produce counter-orbiting stars and has a vital role in the observed distributions of both the inclination and the eccentricity. In addition, since the disks are highly inclined, the orbit of the pertuber should be observed face-on or close to this configuration, in order for such a mechanism to be triggered. As mentioned earlier, the counter-orbiting stars may also be related to the formation process, in particular a partial capture of a large massive cloud as it engulfs Sgr A* during its orbit (Wardle & Yusef-Zadeh 2008).

4.4. *Resonant Relaxation*

Besides the previously discussed dynamical processes, specifically the non-resonant two-body collisional relaxation, there is also a coherent resonant relaxation due to correlated encounters, namely scalar and vector resonant relaxation (SRR and VRR), which is typical of the nearly symmetrical potential deeply inside the sphere of influence of the SMBH where both the test and the field stars move on closed quasi-Keplerian ellipses (Alexander 2017). Especially the VRR can significantly contribute to the fast change of the angular momentum vector of S stars (Rauch & Tremaine 1996). The VRR proceeds faster than the SRR and changes only the direction of the orbital angular momentum, effectively randomizing the stellar cluster on the timescale of millions of years and potentially less (Hopman & Alexander 2006). In this regard, Ali et al. (2020) conclude that the S-cluster should have exhibited dynamical effects of VRR by now. If in the past all members of each disk had a common inclination angle, then one would interpret the current observed distribution as an imprint from an ongoing VRR. Nevertheless and since the S-stars are still rather well organized, and significantly deviating from a randomized inclination distribution, it is doubtful that VRR has had a strong effect on all the orbits of the cluster. To quantify the VRR timescale, we estimate the total number of S stars within $r \sim 0.04\,$pc to be $N_\star \sim 108$. Furthermore, we define the ratio $Q = M_\bullet/m_\star$ between the SMBH mass and the mean S star mass, which we set to $m_\star = 10\,M_\odot$. Then we can calculate the VRR timescale using (Merritt 2013b; Alexander 2017),

$$\mathrm{T}_{\rm VRR} \simeq \frac{1}{2}\frac{P_{\rm orb}(r)Q}{\sqrt{N_\star}}$$

$$\simeq 7.2\times10^6 \left(\frac{N_\star}{108}\right)^{-1/2}\left(\frac{r}{0.04\,\mathrm{pc}}\right)^{3/2} \times$$

$$\times\left(\frac{M_\bullet}{4\times10^6\,M_\odot}\right)^{-1/2}\left(\frac{Q}{4\times10^5}\right)\mathrm{Myr}\,,$$ which is essentially the self-coherence timescale of the background cluster, during which its orbits are expected to be randomized.

Hence inner stars could already show signs of orbital randomization due to the VRR according to Eq.4.4. The timescale of SRR, which can change the magnitude of the angular momentum and hence the eccentricity, is essentially longer than the VRR timescale by a factor of $\sqrt{N_\star} \sim 10$ (Alexander 2017), i.e. at least 10 if we count only the S stars. Therefore the SRR has not yet significantly contributed much to the eccentricity distribution of S stars, except for the region $r \lesssim 10\,$mpc, where the SRR timescale is comparable to the age of S stars. In addition to the orbital precession caused by the resonant relaxation, there is another, faster effect that causes the orbital orientation to change, namely the Newtonian (retrograde) mass precession on the timescale $t_{\rm mass} \approx QP_{\rm orb}/N_\star$, which expresses the time by which ω changes by π. The mass precession timescale is shorter than the VRR timescale by $\sqrt{N_\star}$, i.e. at least a factor of 10 (Merritt 2013b). Sufficiently close to the SMBH, the relativistic Schwarzschild precession that is prograde takes place on the timescale that can be shorter than the Newtonian mass precession timescale. The prograde relativistic precession can be expressed as (Merritt 2013b),

$$t_{\rm Schw} \approx \frac{1}{12}\frac{a}{r_{\rm g}}P_{\rm orb}\,, \quad (1)$$

where r_g is the gravitational radius. By putting $t_{\rm Schw} < t_{\rm mass}$, we obtain $a/r_g \sim 48\,000$, at which $t_{\rm Schw} \approx 165\,000\,(a/48\,000\,r_g)^{5/2}$ years.

The dependence of the timescales of both the non-resonant and the resonant relaxation processes on the distance from Sgr A* within the cluster is expected to be in the following way. When we assume the power-law density distribution of stars, i.e. a relaxed cusp of late-type stars within the S cluster (Schödel et al. 2020) with $n_\star(r) \propto r^{-\gamma}$ with $\gamma \sim 3/2$ for simplicity, then the number of stars within a certain radius is $N_\star(r) = N_0(r/r_0)^{3-\gamma}$. For the non-resonant collisional timescale, it implies $T_{\rm NR} \propto \sigma_\star^3/n_\star \propto r^{-3/2+\gamma} \sim$ const, i.e. only the weak dependence on the radius. For the VRR, we obtain $T_{\rm VRR} \propto QP_{\rm orb}/\sqrt{N_\star} \propto r^{3/2}/r^{3/2-\gamma/2} \sim r^{\gamma/2} \sim r^{3/4}$. The steepest dependence on the radius is for the SRR, for which we obtain $T_{\rm SRR} \sim QP_{\rm orb} \propto r^{3/2}$. Hence, the resonant relaxation proceeds faster closer to the SMBH, while the non-resonant relaxation could proceed faster for a larger radius, although the dependence is rather weak, see also Ali et al. (2020). The mass precession depends only weakly on the distance as $t_{\rm mass} \propto P_{\rm orb}/N_\star \propto r^{-3/2+\gamma} \approx$ const, while the relativistic prograde precession has a steep dependence $t_{\rm Schw} \propto r^{5/2}$. In case of the Kozai-Lidov oscillations induced by a more massive perturber located further away from the S cluster, the characteristic timescale depends on the distance of the star from Sgr A* as $t_{\rm KL} \propto r^{-3/2}$, i.e. for a larger distance from Sgr A*, the KL timescale becomes shorter unlike the radial dependence for the resonant relaxation. It is also possible that KL-cycles are suppressing VRR, specially in the case of a face-on massive disturber. The latter situation would essentially keep the inclination confined to a very narrow range, remaining almost constant. However, this cannot be certainly generalized to the cluster as a whole until the detection of a suitable perturber.

A further related relaxation process that we briefly discuss is resonant dynamical friction (RDF), which is a result of the existence of a massive perturber such as an IMBH. RDF can be estimated from the ordinary dynamical friction in a sense that it is triggered by stars that orbit the SMBH in near-resonance with a massive perturber. In more detail, Ákos Szölgyén et al. (2021) consider the case of an IMBH of $1000\,M_\odot$ and a disk of $1M_\odot$ stars, orbiting a $10^6M_\odot$ SMBH. In their Figure 1, which represents the case of a mutual inclination of 45°, they find that after 1.8 - 4.5 Myr the stellar disk is warped by the IMBH leading to an increase in its thickness. The warping starts with the inner region of the disk, then increases as the IMBH aligns with the disk, i.e. the mutual inclination becomes zero. This effect is especially profound for stars with semi-major axes within the range of the semi-major axis of the IMBH. If we now consider an IMBH of $1000\,M_\odot$ just outside the inner arcsecond, then it could be the reason behind any observed thickness.

4.5. *Further Dynamical Considerations*

There are additional dynamical processes currently occurring within the S-cluster such as non-resonant relaxation (NRR), which is dominated by two-body interactions that allow for energy exchange. In this regard, Šubr & Haas (2014) conclude that two-body interactions may in principle cause the S-stars to migrate radially towards the center within their estimated ages. This is due to the fact that the stellar velocity dispersion is effectively much smaller within the stellar disk than the one assumed for an isotropic spherical cluster, which leads to a shorter NRR timescale. Accordingly, NRR may have assisted the Hills mechanism in bringing the S-stars to where we observe them today. An additional activity that we may consider is the so-called disk-migration (Papaloizou & Terquem 2006). In such a scenario, the star exchanges torques with the surrounding gas causing alterations in the stellar angular momentum. These variations then affect the semi-major axis and other orbital elements. Nevertheless, we do not find any evidence supporting a strong influence of this process such as a non-thermal peak of the eccentricity distribution or a newly formed gaseous disk around the S-stars that would trigger this mechanism. Furthermore, the current organized state of the cluster, i.e. the non-randomized orbital distribution, excludes the possibility of an interaction with an IMBH with the mass of $M_{\rm IMBH} > 1000M_\odot$ orbiting within the central arcsecond. Such a situation would randomize the S-orbits in a few million years, as was analyzed by Merritt et al. (2009). Our conclusion is also in agreement with GRAVITY Collaboration et al. (2020), where they find, based on the Schwarzschild precession of the orbit of S2, that any third compact mass within the central arcsecond must be less massive than about $1000M_\odot$. In relation to this topic, Zheng et al. (2021) demonstrate how secular perturbation from an IMBH could serve as an alternative to the Hills mechanism. Such a process would trigger rapid eccentricity excitation near the SMBH. They refer to IRS 13E as a possible location for the perturber, which could either be a compact cluster or an IMBH with the mass of around $10^4M_\odot$. A distinguishing factor between this process and the Hills mechanism is the observation of binary hypervelocity stars that could be generated as a consequence of the secular perturbation.

5. SUMMARY AND CONCLUSION

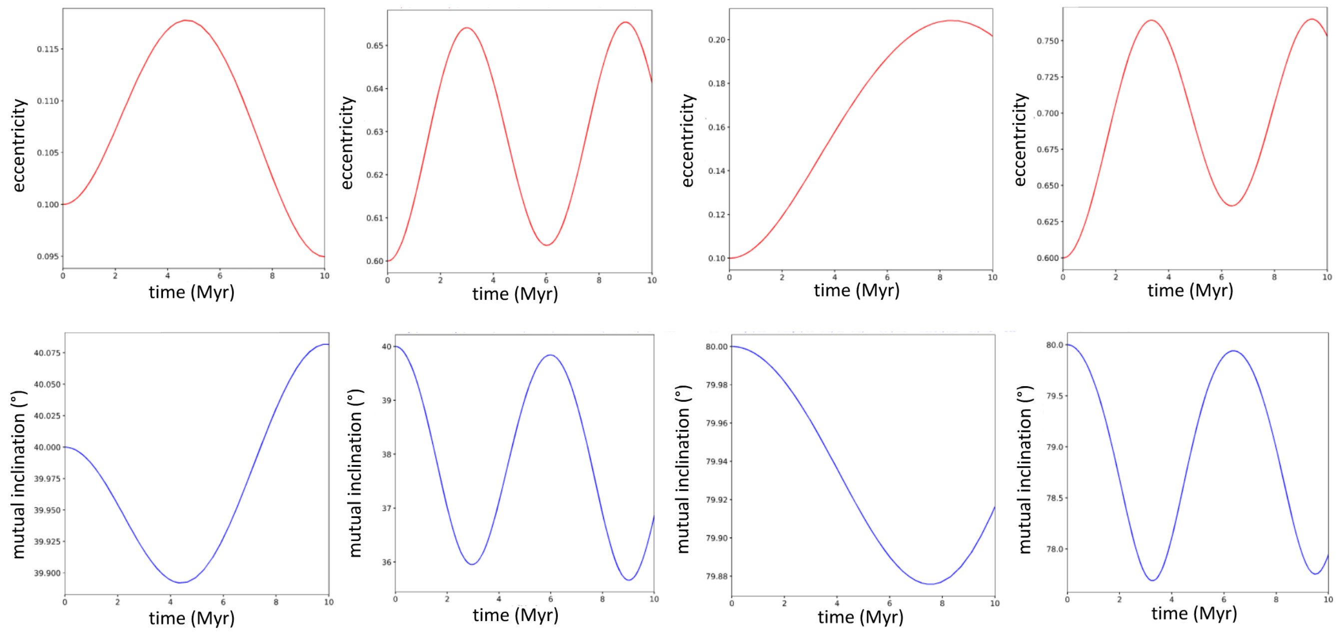

Figure 22. Eccentricity (e_1)- mutual inclination evolution in case of an IMBH of $10^3 M_\odot$, $e_2 = 0.1$ and $a_2 = 0.15$ pc. The first two figures represent $i_{\rm mutual} = 40^\circ$, $e_1 = 0.1$ and $i_{\rm mutual} = 40^\circ$, $e_1 = 0.6$, while the second two figures represent $i_{\rm mutual} = 80^\circ$, $e_1 = 0.1$ and $i_{\rm mutual} = 80^\circ$, $e_1 = 0.6$ with a fixed $a_1 = 0.04$ pc.

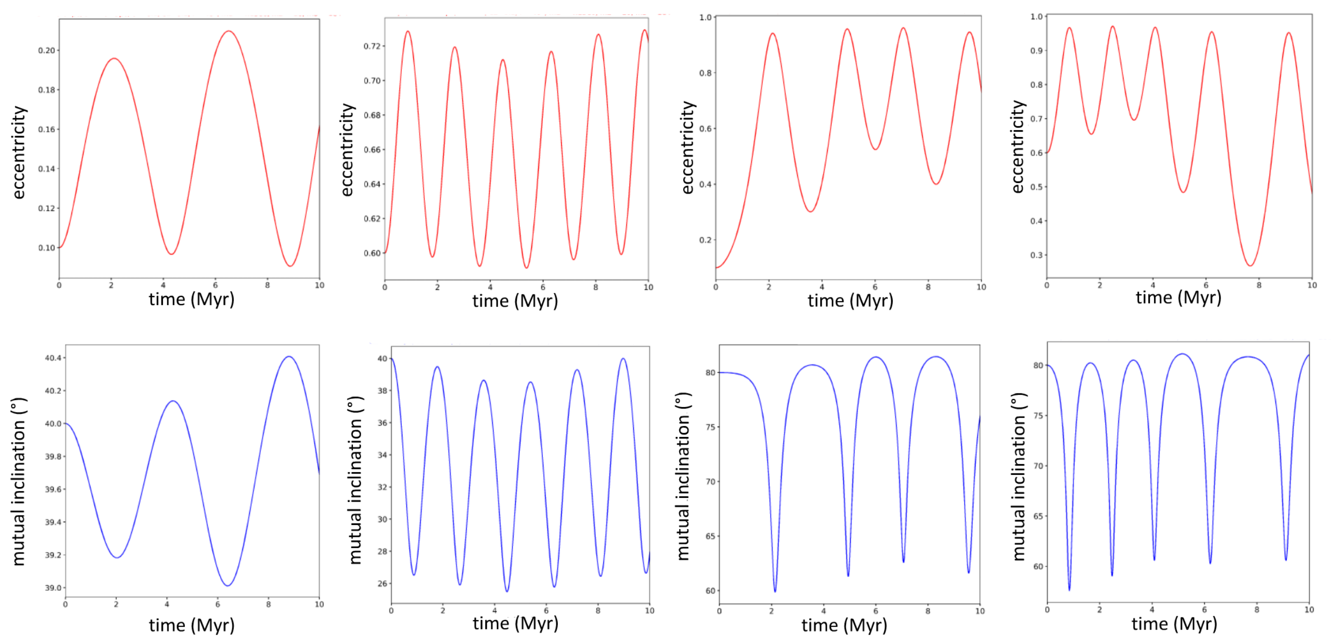

Figure 23. Eccentricity (e_1)- mutual inclination evolution in case of an IMBH of $10^4 M_\odot$, $e_2 = 0.1$ and $a_2 = 0.15$ pc. The first two figures represent $i_{\rm mutual} = 40^\circ$, $e_1 = 0.1$ and $i_{\rm mutual} = 40^\circ$, $e_1 = 0.6$, while the second two figures represent $i_{\rm mutual} = 80^\circ$, $e_1 = 0.1$ and $i_{\rm mutual} = 80^\circ$, $e_1 = 0.6$ with a fixed $a_1 = 0.04$ pc. 103

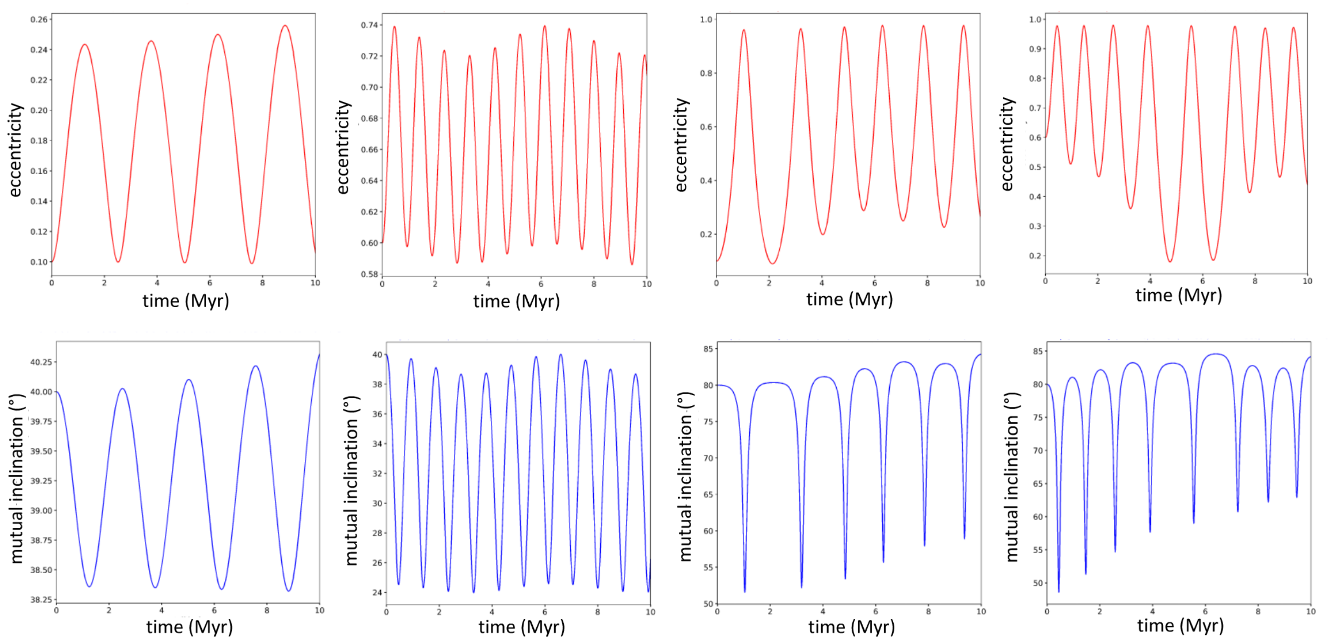

Figure 24. Eccentricity (e_1)- mutual inclination evolution in case of a stellar or gaseous disk of $10^5 M_\odot$, $e_2 = 0.1$ and $a_2 = 0.25$ pc. The first two figures represent $i_{\rm mutual} = 40°$, $e_1 = 0.1$ and $i_{\rm mutual} = 40°$, $e_1 = 0.6$, while the second two figures represent $i_{\rm mutual} = 80°$, $e_1 = 0.1$ and $i_{\rm mutual} = 80°$, $e_1 = 0.6$ with a fixed $a_1 = 0.04$ pc.

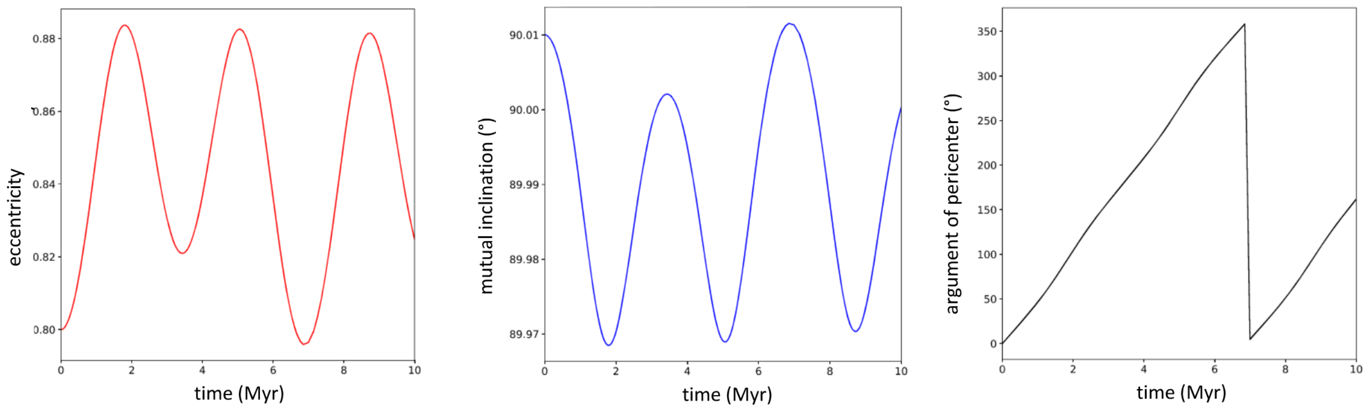

Figure 25. The resulting KL-cycles of the eccentricity (e_1), the mutual inclination and the argument of the pericenter (g_1) for the case of an IMBH of $10^3 M_\odot$, $e_2 = 0.1$, $a_2 = 0.15$ pc and in the limit $i_{\rm mutual} = 90.01°$, $e_1 = 0.8$.

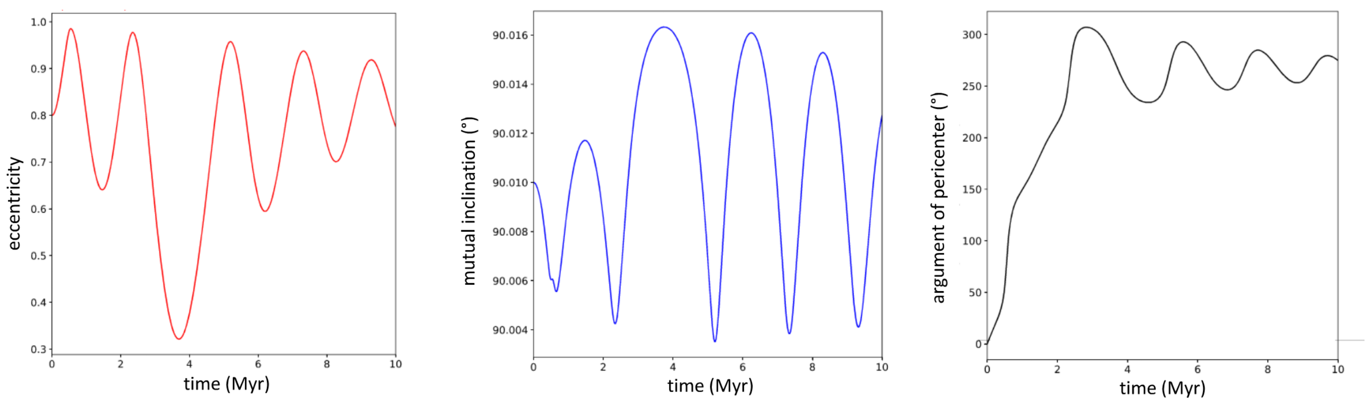

Figure 26. The resulting KL-cycles of the eccentricity (e_1), the mutual inclination and the argument of the pericenter (g_1) for the case of an IMBH of $10^4 M_\odot$, $e_2 = 0.1$, $a_2 = 0.15$ pc and in the limit $i_{\rm mutual} = 90.01°$, $e_1 = 0.8$.

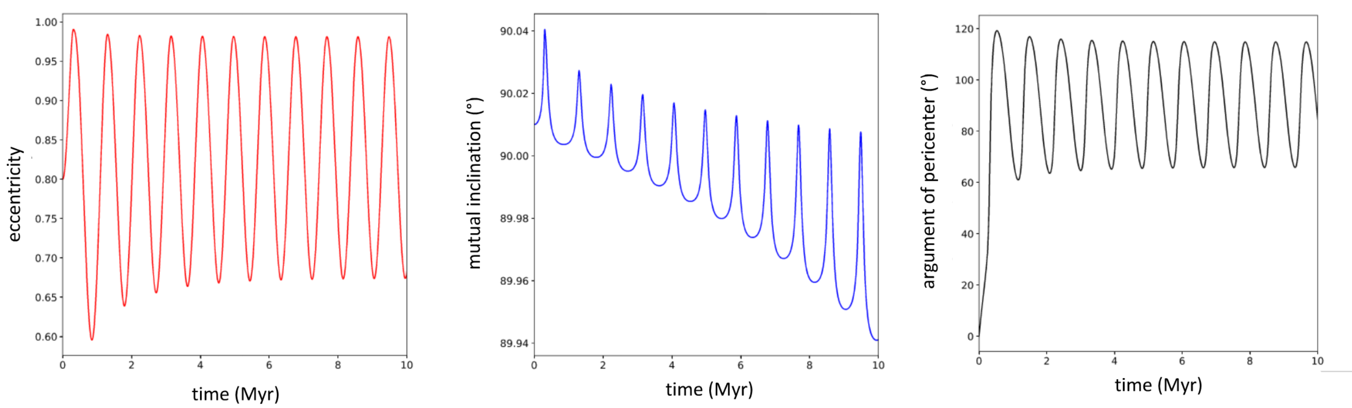

Figure 27. The resulting KL-cycles of the eccentricity (e_1), the mutual inclination and the argument of the pericenter (g_1) for the case of a stellar or gaseous disk of $10^5 M_\odot$, $e_2 = 0.1$, $a_2 = 0.25$ pc and in the limit $i_{\rm mutual} = 90.01°$, $e_1 = 0.8$.

We provide an update on the dynamics of the Galactic center S cluster by presenting new orbital solution for 20 stars. The orbits were determined using a nested sampling approach called Ultranest, which is able to detect multimodal posteriors that arise with the lack of radial velocity measurement. The first finding is that almost of these orbits exhibit high inclination and are highly elliptical, which is in agreement with the features of the known orbits of the cluster. Furthermore, we apply machine-learning clustering algorithm HDBSCAN on the specific angular momentum vectors of the 37 known orbits and of the 20 new orbits. The outcome shows that the majority of the 57 stars are arranged 105 in a system of three highly inclined disks, two of which are separated by 45 degrees (black 7 stars and green 6 stars) and third is almost perpendicular to the two

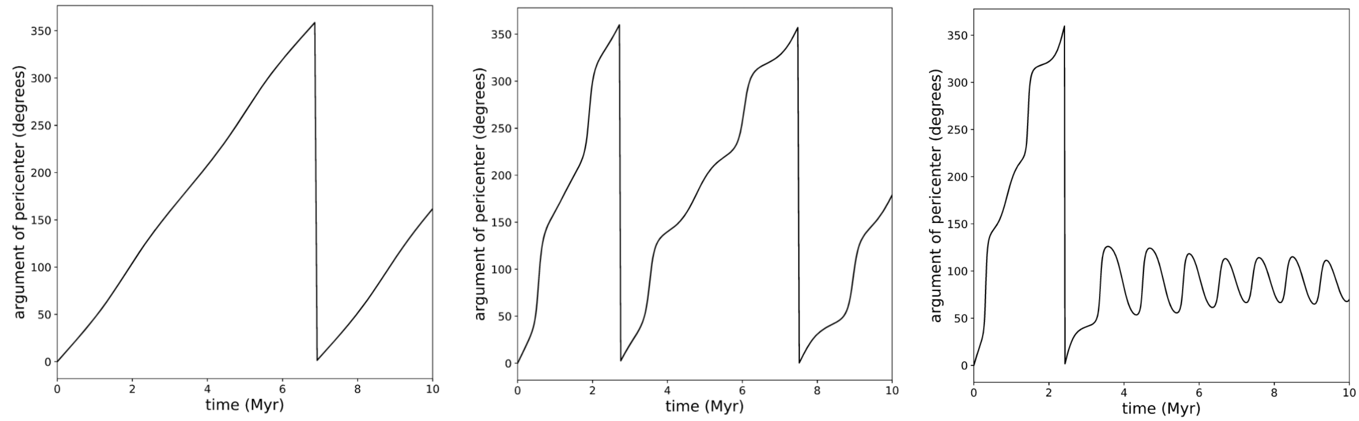

Figure 28. The evolution of the argument of the pericenter (g_1) for $i_{\rm mutual} = 80°$ or $i_{\rm mutual} = 100°$ for the cases of an IMBH of $10^3 M_\odot$ (left), an IMBH of $10^4 M_\odot$ (middle) and stellar of gaseous disk of $10^5 M_\odot$ (right). With $e_2 = 0.1$, $e_1 = 0.8$, $a_2 = 0.15$ pc for the first two cases and $a_2 = 0.25$ pc for the stellar or gaseous disk.

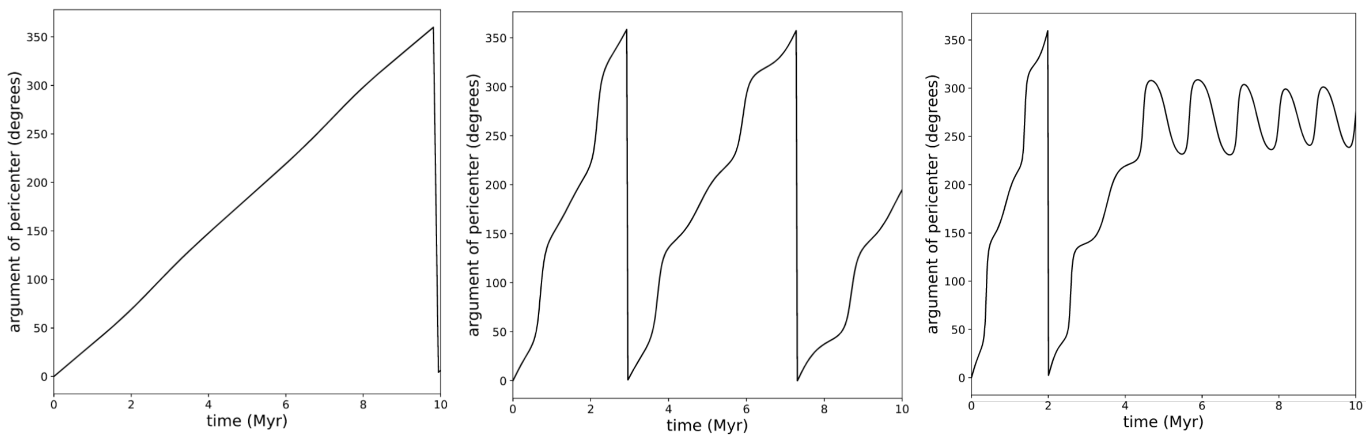

Figure 29. The evolution of the argument of the pericenter (g_1) for $i_{\rm mutual} = 80°$ or $i_{\rm mutual} = 100°$ for the cases of an IMBH of $10^3 M_\odot$ (left), an IMBH of $10^4 M_\odot$ (middle) and stellar of gaseous disk of $10^5 M_\odot$ (right). With $e_2 = 0.1$, $e_1 = 0.7$, $a_2 = 0.15$ pc for the first two cases and $a_2 = 0.25$ pc for the stellar or gaseous disk.

(red 22 stars). The eccentricity distributions of each disk is found to be thermalized, while the inclination peaks around 90 degrees. Since each disk contains clockwise and anti-clockwise moving stars, we attempt to explain this by presenting three-body simulations of Kozai-Lidov cycles that could have probably caused the orbits in some cases to flip their direction of motion and stay in the same plane in 3D. Nevertheless, detailed N-body simulations are needed to give a certain interpretation of the origin of structure.

Acknowledgments:
We received funding from the European Union Seventh Framework Program (FP7/2007-2013) under grant agreement No. 312789—Strong gravity: Probing Strong Gravity by Black Holes Across the Range of Masses. This work was supported in part by the Deutsche Forschungsgemeinschaft (DFG) via the Cologne Bonn Graduate School (BCGS), the Max Planck Society through the International Max Planck Research School (IMPRS) for Astronomy and Astrophysics, as well as special funds through the University of Cologne and CRC956— Conditions and Impact of Star Formation under project A2. M. Z. acknowledges the financial support by the National Science Centre, Poland, grant No. 2017/26/A/ST9/00756 (Maestro 9) as well as by the GAČR EXPRO grant No. 21-13491X "Exploring the Hot Universe and Understanding Cosmic Feedback". We thank the German Academic Exchange Service (DAAD) for support under COPRAG2015 (No.57147386) and the the Czech Science Foundation—DFG collaboration (EC 137/10-1).

REFERENCES

Alexander, T. 2005, PhR, 419, 65, doi: 10.1016/j.physrep.2005.08.002

—. 2017, ARA&A, 55, 17, doi: 10.1146/annurev-astro-091916-055306

Ali, B., Paul, D., Eckart, A., et al. 2020, The Astrophysical Journal, 896, 100, doi: 10.3847/1538-4357/ab93ae

Bartko, H., Martins, F., Fritz, T. K., et al. 2009, ApJ, 697, 1741, doi: 10.1088/0004-637X/697/2/1741

Bartko, H., Martins, F., Trippe, S., et al. 2010, ApJ, 708, 834, doi: 10.1088/0004-637X/708/1/834

Blaes, O., Lee, M. H., & Socrates, A. 2002, The Astrophysical Journal, 578, 775, doi: 10.1086/342655

Blum, R. D., Depoy, D. L., & Sellgren, K. 1995, ApJ, 441, 603, doi: 10.1086/175386

Bonnell, I. A., & Rice, W. K. M. 2008, Science, 321, 1060, doi: 10.1126/science.1160653

Borkar, A., Eckart, A., Straubmeier, C., et al. 2020, in Multifrequency Behaviour of High Energy Cosmic Sources - XIII. 3-8 June 2019. Palermo, 33. https://arxiv.org/abs/1909.13753

Brem, P., Amaro-Seoane, P., & Sopuerta, C. F. 2014, Monthly Notices of the Royal Astronomical Society, 437, 1259

Buchner, J. 2016, Statistics and Computing, 26, 383, doi: 10.1007/s11222-014-9512-y

—. 2019, PASP, 131, 108005, doi: 10.1088/1538-3873/aae7fc

—. 2021, The Journal of Open Source Software, 6, 3001, doi: 10.21105/joss.03001

Campello, R. J. G. B., Moulavi, D., & Sander, J. 2013, in Advances in Knowledge Discovery and Data Mining, ed. J. Pei, V. S. Tseng, L. Cao, H. Motoda, & G. Xu (Berlin, Heidelberg: Springer Berlin Heidelberg), 160–172

Campello, R. J. G. B., Moulavi, D., Zimek, A., & Sander, J. 2015, ACM Trans. Knowl. Discov. Data, 10, doi: 10.1145/2733381

Chen, X., & Amaro-Seoane, P. 2014, ApJL, 786, L14, doi: 10.1088/2041-8205/786/2/L14

Childs, A. C., & Martin, R. G. 2021, ApJL, 920, L8, doi: 10.3847/2041-8213/ac2957

Christopher, M. H., Scoville, N. Z., Stolovy, S. R., & Yun, M. S. 2005, ApJ, 622, 346, doi: 10.1086/427911

Ciurlo, A., Campbell, R. D., Morris, M. R., et al. 2020, Nature, 577, 337, doi: 10.1038/s41586-019-1883-y

Collin, S., & Zahn, J.-P. 1999, A&A, 344, 433

Do, T., Hees, A., Ghez, A., et al. 2019, Science, 365, 664, doi: 10.1126/science.aav8137

Dremova, G., Dremov, V., & Tutukov, A. 2019, Astronomy Reports, 63, 862, doi: 10.1134/S1063772919100032

Eckart, A., Moultaka, J., Viehmann, T., Straubmeier, C., & Mouawad, N. 2004, ApJ, 602, 760, doi: 10.1086/381178

Eckart, A., Mužić, K., Yazici, S., et al. 2013, A&A, 551, A18, doi: 10.1051/0004-6361/201219994

Eckart, A., Hüttemann, A., Kiefer, C., et al. 2017, Foundations of Physics, 47, 553, doi: 10.1007/s10701-017-0079-2

Fouvry, J.-B., Bar-Or, B., & Chavanis, P.-H. 2019, ApJ, 883, 161, doi: 10.3847/1538-4357/ab2f78

Fragione, G., Kocsis, B., Rasio, F. A., & Silk, J. 2021, arXiv e-prints, arXiv:2107.04639. https://arxiv.org/abs/2107.04639

Fritz, T. K., Gillessen, S., Dodds-Eden, K., et al. 2010, ApJ, 721, 395, doi: 10.1088/0004-637X/721/1/395

Gautam, A. K., Do, T., Ghez, A. M., et al. 2019, The Astrophysical Journal, 871, 103, doi: 10.3847/1538-4357/aaf103

Generozov, A., & Madigan, A.-M. 2020, ApJ, 896, 137, doi: 10.3847/1538-4357/ab94bc

Genzel, R., Eisenhauer, F., & Gillessen, S. 2010, Reviews of Modern Physics, 82, 3121, doi: 10.1103/RevModPhys.82.3121

Ghez, A. M., Duchêne, G., Matthews, K., et al. 2003, ApJL, 586, L127, doi: 10.1086/374804

Gillessen, S., Plewa, P. M., Eisenhauer, F., et al. 2017, ApJ, 837, 30, doi: 10.3847/1538-4357/aa5c41

Gravity Collaboration, Abuter, R., Amorim, A., et al. 2018, A&A, 615, L15, doi: 10.1051/0004-6361/201833718

GRAVITY Collaboration, Abuter, R., Amorim, A., et al. 2020, A&A, 636, L5, doi: 10.1051/0004-6361/202037813

Habibi, M., Gillessen, S., Martins, F., et al. 2017, ApJ, 847, doi: 10.3847/1538-4357/aa876f

Hailey, C. J., Mori, K., Bauer, F. E., et al. 2018, Nature, 556, 70, doi: 10.1038/nature25029

Hansen, B. M. S., & Milosavljević, M. 2003, ApJL, 593, L77, doi: 10.1086/378182

Hills, J. G. 1988, Nature, 331, 687, doi: 10.1038/331687a0

Hobbs, A., & Nayakshin, S. 2009, Monthly Notices of the Royal Astronomical Society, 394, 191–206, doi: 10.1111/j.1365-2966.2008.14359.x

Hopman, C., & Alexander, T. 2006, ApJ, 645, 1152, doi: 10.1086/504400

Impellizzeri, C. M. V., Gallimore, J. F., Baum, S. A., et al. 2019, ApJL, 884, L28, doi: 10.3847/2041-8213/ab3c64

Karas, V., Svoboda, J., & Zajaček, M. 2021, in RAGtime: Workshops on black holes and netron stars, E1. https://arxiv.org/abs/1901.06507

Kim, S. S., Figer, D. F., & Morris, M. 2004, ApJL, 607, L123, doi: 10.1086/422032

Kocsis, B., & Tremaine, S. 2011, MNRAS, 412, 187, doi: 10.1111/j.1365-2966.2010.17897.x

Koposov, S. E., Boubert, D., Li, T. S., et al. 2019, Monthly Notices of the Royal Astronomical Society, doi: 10.1093/mnras/stz3081

Kozai, Y. 1962, AJ, 67, 591, doi: 10.1086/108790

Krabbe, A., Genzel, R., Eckart, A., et al. 1995, ApJL, 447, L95, doi: 10.1086/309579

Levin, Y., & Beloborodov, A. M. 2003, ApJL, 590, L33, doi: 10.1086/376675

Lidov, M. 1962, Planetary and Space Science, 9, 719, doi: https://doi.org/10.1016/0032-0633(62)90129-0

Löckmann, U., Baumgardt, H., & Kroupa, P. 2009, MNRAS, 398, 429, doi: 10.1111/j.1365-2966.2009.15157.x

Lu, J. R., Do, T., Ghez, A. M., et al. 2013, The Astrophysical Journal, 764, 155, doi: 10.1088/0004-637x/764/2/155

Lu, J. R., Ghez, A. M., Hornstein, S. D., et al. 2009, The Astrophysical Journal, 690, 1463–1487, doi: 10.1088/0004-637x/690/2/1463

Madigan, A.-M., Levin, Y., & Hopman, C. 2009, The Astrophysical Journal, 697, L44–L48, doi: 10.1088/0004-637x/697/1/l44

Maillard, J. P., Paumard, T., Stolovy, S. R., & Rigaut, F. 2004, A&A, 423, 155, doi: 10.1051/0004-6361:20034147

Mapelli, M., & Gualandris, A. 2016, in Lecture Notes in Physics, Berlin Springer Verlag, Vol. 905, Lecture Notes in Physics, Berlin Springer Verlag, ed. F. Haardt, V. Gorini, U. Moschella, A. Treves, & M. Colpi, 205, doi: 10.1007/978-3-319-19416-5_6

Mapelli, M., Hayfield, T., Mayer, L., & Wadsley, J. 2012, ApJ, 749, 168, doi: 10.1088/0004-637X/749/2/168

Martins, F., Gillessen, S., Eisenhauer, F., et al. 2008, ApJL, 672, L119, doi: 10.1086/526768

McInnes, L., Healy, J., & Astels, S. 2017, The Journal of Open Source Software, 2, doi: 10.21105/joss.00205

Menten, K. M., Reid, M. J., Eckart, A., & Genzel, R. 1997, ApJL, 475, L111, doi: 10.1086/310472

Merritt, D. 2013a, Dynamics and Evolution of Galactic Nuclei; Princeton Series in Astrophysics. https://arxiv.org/abs/ASIN:B00SLW59L4

—. 2013b, Dynamics and Evolution of Galactic Nuclei (Princeton: Princeton University Press)

Merritt, D., Gualandris, A., & Mikkola, S. 2009, The Astrophysical Journal, 693, L35–L38, doi: 10.1088/0004-637x/693/1/l35

Milosavljević, M., & Loeb, A. 2004, ApJL, 604, L45, doi: 10.1086/383467

Miralda-Escudé, J., & Gould, A. 2000, ApJ, 545, 847, doi: 10.1086/317837

Mori, K., Hailey, C. J., Schutt, T. Y. E., et al. 2021, ApJ, 921, 148, doi: 10.3847/1538-4357/ac1da5

Morris, M. 1989, in The Center of the Galaxy, ed. M. Morris, Vol. 136, 171

Morris, M. 1993, ApJ, 408, 496, doi: 10.1086/172607

Moser, L., Sánchez-Monge, Á., Eckart, A., et al. 2017, A&A, 603, A68, doi: 10.1051/0004-6361/201628385

Moulavi, D., Andretta Jaskowiak, P., Campello, R., Zimek, A., & Sander, J. 2014, doi: 10.1137/1.9781611973440.96

Mužić, K., Schödel, R., Eckart, A., Meyer, L., & Zensus, A. 2008, A&A, 482, 173, doi: 10.1051/0004-6361:20078352

Najarro, F., Krabbe, A., Genzel, R., et al. 1997, A&A, 325, 700

Naoz, S., Ghez, A. M., Hees, A., et al. 2018, ApJL, 853, L24, doi: 10.3847/2041-8213/aaa6bf

Nayakshin, S. 2005, MNRAS, 359, 545, doi: 10.1111/j.1365-2966.2005.08913.x

—. 2006, MNRAS, 372, 143, doi: 10.1111/j.1365-2966.2006.10772.x

Nayakshin, S., & Cuadra, J. 2005, A&A, 437, 437, doi: 10.1051/0004-6361:20042052

Nayakshin, S., Cuadra, J., & Springel, V. 2007, MNRAS, 379, 21, doi: 10.1111/j.1365-2966.2007.11938.x

O'Leary, R. M., Kocsis, B., & Loeb, A. 2009, MNRAS, 395, 2127, doi: 10.1111/j.1365-2966.2009.14653.x

Paczynski, B. 1978, AcA, 28, 91

Papaloizou, J. C. B., & Terquem, C. 2006, Reports on Progress in Physics, 69, 119, doi: 10.1088/0034-4885/69/1/R03

Parsa, M., Eckart, A., Shahzamanian, B., et al. 2017, ApJ, 845, 22, doi: 10.3847/1538-4357/aa7bf0

Paumard, T., Genzel, R., Martins, F., et al. 2006, ApJ, 643, 1011, doi: 10.1086/503273

Peißker, F., Eckart, A., & Ali, B. 2021b, ApJ, 918, 25, doi: 10.3847/1538-4357/ac0efc

Peißker, F., Eckart, A., & Parsa, M. 2020a, The Astrophysical Journal, 889, 61, doi: 10.3847/1538-4357/ab5afd

Peißker, F., Hosseini, S. E., Zajaček, M., et al. 2020, A&A, 634, A35, doi: 10.1051/0004-6361/201935953

Peißker, F., Zajaček, M., Eckart, A., et al. 2019, A&A, 624, A97, doi: 10.1051/0004-6361/201834947

—. 2021a, ApJ, 923, 69, doi: 10.3847/1538-4357/ac23df

Peißker, F., Ali, B., Zajaček, M., et al. 2021b, ApJ, 909, 62, doi: 10.3847/1538-4357/abd9c6

Peißker, F., Eckart, A., Zajaček, M., Ali, B., & Parsa, M. 2020d, The Astrophysical Journal, 899, 50, doi: 10.3847/1538-4357/ab9c1c

Perets, H. B., Gualandris, A., Kupi, G., Merritt, D., & Alexander, T. 2009, ApJ, 702, 884, doi: 10.1088/0004-637X/702/2/884

Perets, H. B., Hopman, C., & Alexander, T. 2007, ApJ, 656, 709, doi: 10.1086/510377

Rauch, K. P., & Tremaine, S. 1996, New Astronomy, 1, 149–170, doi: 10.1016/s1384-1076(96)00012-7

Reid, M. J., Menten, K. M., Genzel, R., et al. 2003, ApJ, 587, 208, doi: 10.1086/368074

Reid, M. J., Menten, K. M., Trippe, S., Ott, T., & Genzel, R. 2007, ApJ, 659, 378, doi: 10.1086/511744

Rose, S. C., Naoz, S., Sari, R., & Linial, I. 2021, arXiv e-prints, arXiv:2201.00022. https://arxiv.org/abs/2201.00022

Sabha, N., Eckart, A., Merritt, D., et al. 2012, A&A, 545, A70, doi: 10.1051/0004-6361/201219203

Sanchez-Bermudez, J., Schödel, R., Alberdi, A., et al. 2014, A&A, 567, A21, doi: 10.1051/0004-6361/201423657

Schödel, R., Feldmeier, A., Neumayer, N., Meyer, L., & Yelda, S. 2014, Classical and Quantum Gravity, 31, 244007, doi: 10.1088/0264-9381/31/24/244007

Schödel, R., Nogueras-Lara, F., Gallego-Cano, E., et al. 2020, A&A, 641, A102, doi: 10.1051/0004-6361/201936688

Shahzamanian, B., Eckart, A., Valencia-S., M., et al. 2015, A&A, 576, A20, doi: 10.1051/0004-6361/201425239

Shlosman, I., & Begelman, M. C. 1987, Nature, 329, 810, doi: 10.1038/329810a0

Su, M., Slatyer, T. R., & Finkbeiner, D. P. 2010, ApJ, 724, 1044, doi: 10.1088/0004-637X/724/2/1044

Tep, K., Fouvry, J.-B., Pichon, C., et al. 2021, MNRAS, 506, 4289, doi: 10.1093/mnras/stab1945

Tsuboi, M., Kitamura, Y., Uehara, K., et al. 2021, Publications of the Astronomical Society of Japan, 73, S91, doi: 10.1093/pasj/psaa095

Šubr, L., & Karas, V. 2005, A&A, 433, 405, doi: 10.1051/0004-6361:20042089

Vollmer, B., & Duschl, W. J. 2000, NewA, 4, 581, doi: 10.1016/S1384-1076(99)00043-3

Šubr, L. ., Schovancová, J., & Kroupa, P. 2009, A&A, 496, 695, doi: 10.1051/0004-6361:200811075

Wardle, M., & Yusef-Zadeh, F. 2008, The Astrophysical Journal, 683, L37–L40, doi: 10.1086/591471

Witzel, G., Eckart, A., Bremer, M., et al. 2012, ApJS, 203, 18, doi: 10.1088/0067-0049/203/2/18

Yelda, S., Ghez, A. M., Lu, J. R., et al. 2014, ApJ, 783, 131, doi: 10.1088/0004-637X/783/2/131

Yusef-Zadeh, F., Roberts, D. A., Wardle, M., et al. 2015a, ApJL, 801, L26, doi: 10.1088/2041-8205/801/2/L26

Yusef-Zadeh, F., Wardle, M., Kunneriath, D., et al. 2017, ApJL, 850, L30, doi: 10.3847/2041-8213/aa96a2

Yusef-Zadeh, F., Wardle, M., Sewilo, M., et al. 2015b, ApJ, 808, 97, doi: 10.1088/0004-637X/808/1/97

Zajaček, M., Karas, V., & Eckart, A. 2014, A&A, 565, A17, doi: 10.1051/0004-6361/201322713

Zajaček, M., Britzen, S., Eckart, A., et al. 2017, A&A, 602, A121, doi: 10.1051/0004-6361/201730532

Zhao, J.-H., Blundell, R., Moran, J. M., et al. 2010, ApJ, 723, 1097, doi: 10.1088/0004-637X/723/2/1097

Zhao, J.-H., Morris, M. R., Goss, W. M., & An, T. 2009, ApJ, 699, 186, doi: 10.1088/0004-637X/699/1/186

Zheng, X., Lin, D. N. C., & Mao, S. 2021, The influence of the secular perturbation of an intermediate-mass companion: II. Ejection of hypervelocity stars from the Galactic Center. https://arxiv.org/abs/2104.02989

Ákos Szölgyén, Máthé, G., & Kocsis, B. 2021, Resonant Dynamical Friction in Nuclear Star Clusters: Rapid Alignment of an Intermediate Mass Black Hole with a Stellar Disk. https://arxiv.org/abs/2103.14042

Šubr, L., & Haas, J. 2014, The Astrophysical Journal, 786, 121, doi: 10.1088/0004-637x/786/2/121

Chapter 6

Summary, Conclusions and Outlook

In this thesis, I investigate the orbital and dynamical features of the Galactic center S-cluster by using data from the Very Large Telescope in Chile. The thesis contains three papers with the first paper being summarized as follows:

1. Based on an iterative visual inspection of the orbits, I find that 32 of these orbits are arranged in two almost edge-on disks that contain clockwise and anti-clockwise moving stars.

2. As for the eccentricity distribution, we find that one of the disks shows thermalized distribution and the second peaks at lower eccentricities.

3. The structure is located at $\pm$ 45 degrees w.r.t Galactic plane, and can be recovered in the distributions of the position angle of the projected semi-major axis and the longitude of ascending node.

4. Several dynamical processes could be behind the structure, which are summarized in the paper, however, a separate theoretical research that includes N-body simulations is needed for a well-thought conclusion of the origin of the structure.

The motivation behind the second paper, is to attempt to find orbits for the 71 stars that have no orbital solutions. As these stars have no radial velocity measurements, multimodal posteriors emerge as a consequence. Therefore, I compare different Bayesian methods that belong to MCMCA, ABC and NS in deriving multimodal posteriors by application on the orbital fitting problem. In total, I use 8 different approaches and reach the following conclusions:

1. All MCMCA appraoches fail in determining the correct parameters and in clearly detecting the expected modes, which can be attributed to the walkers getting stuck in local minima.

2. As for ABC, I find that it able to give good results, however, the long computation time is considered a drawback for this approach.

3. Remarkably, I find that NS outperforms both MCMCA and ABC in terms of detecting modes, computational features and uncertainty estimation approach.

4. Finally, I choose the optimal approach (Ultranest) for application on the data of S2 and find that the algorithm is able to give reliable outcome that is in very good agreement with the literature.

5. In conclusion, I consider Ultranest to be suitable for application on the 71 S-stars.

In the third paper, I proceed using Ultranest and attempt to derive orbits for these stars. Due to the large number of objects and the time limit for this thesis submission, I present 20 orbits that were acquired till the current time. The main findings of the analysis are summarized as follows:

1. The algorithm Ultranest is able to clearly detect the two solutions for each orbit and is considered to be efficient in exploring the parameter space and in the orbital fitting problem.

2. The newly determined orbits are highly elliptical and are mostly seen edge-on, which is in agreement with the previously determined orbits.

3. Using machine learning clustering algorithm on a total of 57 orbits, I find that more than half of these stars are organized in a system of three highly inclined disks.
4. Two of the disks are separated by 45 °(black - green), while the red disk is almost perpendicular to both and shows a greater thickness.
5. Furthermore, I use three-body simulations to show that Kozai-Lidov cycles could be the reason behind having two directions in each of the disks.
6. In conclusion, the findings hint to a rather local origin of the S-stars. Nevertheless, to affirm these interpretations, a comprehensive theoretical research of N-body simulations is required.

Last but not least, as the third project is on-going with 51 sources still needing further treatment, the summarized findings may naturally be altered or emphasized with more new orbital solutions.

Acknowledgments

I would like to express my deepest gratitude to my supervisor Prof. Dr. Andreas Eckart for giving me the opportunity to work on such an exciting and interesting topic. I also thank him for his support and advice that have led me to grow and develop personally and scientifically. It has been of great pleasure to discuss history, politics, literature, languages and so many other topics with him. In addition, I thank him for the laughter that made these difficult times easily digestible.

I would like to also give a warm thank you to Prof. Dr. Peter Schilke for agreeing to be the second reviewer, It is greatly appreciated. I thank also Prof. Dr. Yaping Shao for kindly agreeing to act as a chair of the defense committee.

I thank all members of the AE-group, specially Dr. Matthias Subroweit for his plentiful advice. Many thanks to Dr. Harshitha Bhat and Dr. Persis Misquita for proofreading my thesis on such short notice, I'm thankful to have met such great minds. I'm grateful to every fruitful discussion with everyone in the group, in which I truly felt as a member of a family. I also thank Dr. Christian Straubmeier and Dr. Florian Peißker for their support throughout the years. I would like to also thank the administrative staff for their kindness and making bureaucracy as smooth as possible: Dr. Petra Neubauer, Stefanie Simon, Huyen Nguyen and Bettina Krause.

Finally, I thank my family and friends for being there for me when I most needed them.

This thesis is dedicated to my mother and late grandmother.

List of Figures

Bibliography

Ali, B., Paul, D., Eckart, A., et al. 2020, The Astrophysical Journal, 896, 100, doi: 10.3847/1538-4357/ab93ae

Ashton, G., & Talbot, C. 2021, Monthly Notices of the Royal Astronomical Society, 507, 2037, doi: 10.1093/mnras/stab2236

Bartko, H., Martins, F., Trippe, S., et al. 2010, , 708, 834, doi: 10.1088/0004-637X/708/1/834

Beaumont, M. A. 2010, Annual Review of Ecology, Evolution, and Systematics, 41, 379, doi: 10.1146/annurev-ecolsys-102209-144621

Bertorelle, G., BENAZZO, A., & MONA, S. 2010, Molecular Ecology, 19, 2609, doi: https://doi.org/10.1111/j.1365-294X.2010.04690.x

Binnendijk, L. 1960, Properties of Double Stars: A Survey of Parallaxes and Orbits (University of Pennsylvania Press). http://www.jstor.org/stable/j.ctv4t7zpt

Boehle, A., Ghez, A. M., Schödel, R., et al. 2016, , 830, 17, doi: 10.3847/0004-637X/830/1/17

Buchner, J. 2016, Statistics and Computing, 26, 383, doi: 10.1007/s11222-014-9512-y

—. 2019, , 131, 108005, doi: 10.1088/1538-3873/aae7fc

—. 2021, The Journal of Open Source Software, 6, 3001, doi: 10.21105/joss.03001

Campello, R. J. G. B., Moulavi, D., & Sander, J. 2013, in Advances in Knowledge Discovery and Data Mining, ed. J. Pei, V. S. Tseng, L. Cao, H. Motoda, & G. Xu (Berlin, Heidelberg: Springer Berlin Heidelberg), 160–172

Campello, R. J. G. B., Moulavi, D., Zimek, A., & Sander, J. 2015, ACM Trans. Knowl. Discov. Data, 10, doi: 10.1145/2733381

Diolaiti, E., Bendinelli, O., Bonaccini, D., et al. 2000, , 147, 335, doi: 10.1051/aas:2000305

Do, T., Hees, A., Ghez, A., et al. 2019, Science, 365, 664, doi: 10.1126/science.aav8137

Eckart, A., Genzel, R., Ott, T., & Schödel, R. 2002, , 331, 917, doi: 10.1046/j.1365-8711.2002.05237.x

Eckart, A., Schödel, R., & Straubmeier, C. 2005, The black hole at the center of the Milky Way, ed. Eckart, A., Schödel, R., & Straubmeier, C. (London:Imperial College Press ; Hackensack, NJ : Distributed by World Scientific Pub. Co., c2005.)

Eckart, A., Mužić, K., Yazici, S., et al. 2013, , 551, A18, doi: 10.1051/0004-6361/201219994

Eckart, A., Hüttemann, A., Kiefer, C., et al. 2017, Foundations of Physics, 47, 553, doi: 10.1007/s10701-017-0079-2

Eisenhauer, F., Genzel, R., Alexander, T., et al. 2005, , 628, 246, doi: 10.1086/430667

Farr, B., & Farr, W. M. 2015

Figer, D. F. 2004, 322

Genzel, R., Eisenhauer, F., & Gillessen, S. 2010, Reviews of Modern Physics, 82, 3121, doi: 10.1103/RevModPhys.82.3121

Genzel, R., Pichon, C., Eckart, A., Gerhard, O. E., & Ott, T. 2000, , 317, 348, doi: 10.1046/j.1365-8711.2000.03582.x

Ghez, A. M., Salim, S., Hornstein, S. D., et al. 2005, , 620, 744, doi: 10.1086/427175

Ghez, A. M., Duchêne, G., Matthews, K., et al. 2003, , 586, L127, doi: 10.1086/374804

Gillessen, S., Eisenhauer, F., Trippe, S., et al. 2009, , 692, 1075, doi: 10.1088/0004-637X/692/2/1075

Gillessen, S., Plewa, P. M., Eisenhauer, F., et al. 2017, , 837, 30, doi: 10.3847/1538-4357/aa5c41

Goodman, J., & Weare, J. 2010, Communications in Applied Mathematics and Computational Science, 5, 65, doi: 10.2140/camcos.2010.5.65

Gravity Collaboration, Abuter, R., Amorim, A., et al. 2018, , 615, L15, doi: 10.1051/0004-6361/201833718

Guesten, R., Genzel, R., Wright, M. C. H., et al. 1987, , 318, 124, doi: 10.1086/165355

Habibi, M., Gillessen, S., Martins, F., et al. 2017, , 847, doi: 10.3847/1538-4357/aa876f

Heintz, W. D. 1978, Double stars / Wulff D. Heintz (D. Reidel Pub., Co Dordrecht, Holland ; Boston), ix, 174 p. :

Higson, E., Handley, W., Hobson, M., & Lasenby, A. 2018, Statistics and Computing, 29, 891, doi: 10.1007/s11222-018-9844-0

Jarník, V. 1930, Práce Moravské Přírodovědecké Společnosti, 6, 57

Karas, V., Svoboda, J., & Zajaček, M. 2021, in RAGtime: Workshops on black holes and netron stars, E1. https://arxiv.org/abs/1901.06507

Krabbe, A., Genzel, R., Eckart, A., et al. 1995, , 447, L95, doi: 10.1086/309579

Lenzen, R., Hartung, M., Brandner, W., et al. 2003

Lucy, L. B. 1974, Astronomical Journal, 79, 745, doi: 10.1086/111605

MacQueen, J. 1967, in 5th Berkeley Symp. Math. Statist. Probability, University of California Los Angeles LA USA, 281–297

Martins, F., Gillessen, S., Eisenhauer, F., et al. 2008, , 672, L119, doi: 10.1086/526768

McInnes, L., Healy, J., & Astels, S. 2017, The Journal of Open Source Software, 2, doi: 10.21105/joss.00205

Menten, K. M., Reid, M. J., Eckart, A., & Genzel, R. 1997, , 475, L111, doi: 10.1086/310472

Metropolis, N., Rosenbluth, A. W., Rosenbluth, M. N., Teller, A. H., & Teller, E. 1953, The Journal of Chemical Physics, 21, 1087, doi: 10.1063/1.1699114

Mezger, P. G., Zylka, R., Salter, C. J., et al. 1989, , 209, 337

Mikkola, S. 1987, Celestial Mechanics and Dynamical Astronomy, 40, 329, doi: 10.1007/BF01235850

Morris, M. 1989, in The Center of the Galaxy, ed. M. Morris, Vol. 136, 171

Morris, M. 1993, , 408, 496, doi: 10.1086/172607

Moulavi, D., Andretta Jaskowiak, P., Campello, R., Zimek, A., & Sander, J. 2014, doi: 10.1137/1.9781611973440.96

Mukherjee, P., Parkinson, D., & Liddle, A. R. 2006, , 638, L51, doi: 10.1086/501068

Nelson, B., Ford, E. B., & Payne, M. J. 2013, The Astrophysical Journal Supplement Series, 210, 11, doi: 10.1088/0067-0049/210/1/11

Parsa, M., Eckart, A., Shahzamanian, B., et al. 2017, , 845, 22, doi: 10.3847/1538-4357/aa7bf0

Peißker, F., Eckart, A., & Parsa, M. 2020a, The Astrophysical Journal, 889, 61, doi: 10.3847/1538-4357/ab5afd

Peißker, F., Eckart, A., Zajaček, M., Ali, B., & Parsa, M. 2020d, The Astrophysical Journal, 899, 50, doi: 10.3847/1538-4357/ab9c1c

Perets, H. B., Hopman, C., & Alexander, T. 2007, , 656, 709, doi: 10.1086/510377

Plewa, P. M., Gillessen, S., Eisenhauer, F., et al. 2015, , 453, 3234, doi: 10.1093/mnras/stv1910

Prangle, D. 2017, Bayesian Analysis, 12, 289 , doi: 10.1214/16-BA1002

Reid, M. J., Menten, K. M., Genzel, R., et al. 2003, , 587, 208, doi: 10.1086/368074

Reid, M. J., Menten, K. M., Trippe, S., Ott, T., & Genzel, R. 2007, , 659, 378, doi: 10.1086/511744

Richardson, R. 1972, JOSA, 62, 55

Rousset, G., Lacombe, F., Puget, P., et al. 2003, in Society of Photo-Optical Instrumentation Engineers (SPIE) Conference Series, Vol. 4839, Adaptive Optical System Technologies II, ed. P. L. Wizinowich & D. Bonaccini, 140–149, doi: 10.1117/12.459332

Satopaa, V., Albrecht, J., Irwin, D., & Raghavan, B. 2011, in 2011 31st International Conference on Distributed Computing Systems Workshops, 166–171, doi: 10.1109/ICDCSW.2011.20

Schödel, R., Ott, T., Genzel, R., et al. 2002, , 419, 694, doi: 10.1038/nature01121

Shahzamanian, B., Eckart, A., Valencia-S., M., et al. 2015, The Messenger, 159, 41

Shaw, J. R., Bridges, M., & Hobson, M. P. 2007, Monthly Notices of the Royal Astronomical Society, 378, 1365, doi: 10.1111/j.1365-2966.2007.11871.x

Skilling, J. 2004, in American Institute of Physics Conference Series, Vol. 735, Bayesian Inference and Maximum Entropy Methods in Science and Engineering: 24th International Workshop on Bayesian Inference and Maximum Entropy Methods in Science and Engineering, ed. R. Fischer, R. Preuss, & U. V. Toussaint, 395–405, doi: 10.1063/1.1835238

Toni, T., & Stumpf, M. P. H. 2009, Bioinformatics, 26, 104, doi: 10.1093/bioinformatics/btp619

Viehmann, T., Eckart, A., Schödel, R., et al. 2005, A&A, 433, 117, doi: 10.1051/0004-6361:20041748

Witzel, G., Eckart, A., Bremer, M., et al. 2012, , 203, 18, doi: 10.1088/0067-0049/203/2/18

Selbständigkeitserklärung

„Hiermit versichere ich an Eides statt, dass ich die vorliegende Dissertation selbstständig und ohne die Benutzung anderer als der angegebenen Hilfsmittel und Literatur angefertigt habe. Alle Stellen, die wörtlich oder sinngemäß aus veröffentlichten und nicht veröffentlichten Werken dem Wortlaut oder dem Sinn nach entnommen wurden, sind als solche kenntlich gemacht. Ich versichere an Eides statt, dass diese Dissertation noch keiner anderen Fakultät oder Universität zur Prüfung vorgelegen hat; dass sie - abgesehen von unten angegebenen Teilpublikationen und eingebundenen Artikeln und Manuskripten - noch nicht veröffentlicht worden ist sowie, dass ich eine Veröffentlichung der Dissertation vor Abschluss der Promotion nicht ohne Genehmigung des Promotionsausschusses vornehmen werde. Die Bestimmungen dieser Ordnung sind mir bekannt. Darüber hinaus erkläre ich hiermit, dass ich die Ordnung zur Sicherung guter wissenschaftlicher Praxis und zum Umgang mit wissenschaftlichem Fehlverhalten der Universität zu Köln gelesen und sie bei der Durchführung der Dissertation zugrundeliegenden Arbeiten und der schriftlich verfassten Dissertation beachtet habe und verpflichte mich hiermit, die dort genannten Vorgaben bei allen wissenschaftlichen Tätigkeiten zu beachten und umzusetzen. Ich versichere, dass die eingereichte elektronische Fassung der eingereichten Druckfassung vollständig entspricht."

Teilpublikationen und Manuskripte:

- Kinematic Structure of the Galactic Center S Cluster (Ali et al. (2020)).
- Comparing Different Bayesian Methods in Deriving Multimodal Posteriors - Application on Orbital Fitting in the Absence of Radial Velocity Measurements (Ali et al, in prep.)
- An update on the Dynamics of the Galactic Center S Cluster (Ali et al, in prep.)

26.04.2023, Basel Ali

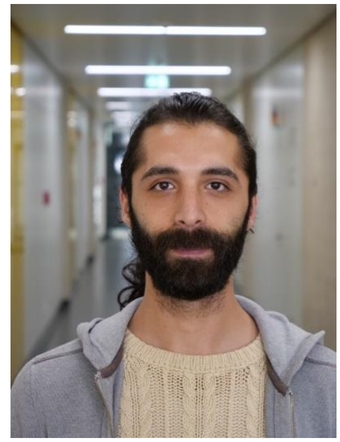

Lebenslauf

Persönliche Daten

Name	**Basel Ali**
Geburtsdaten	**01.01.1992 Aleppo, Syrien**
Adresse	**Piusstr. 22b Ehrenfeld Köln 50823**
Telefon	**015773745234**
Email	**baselali1992@gmail.com**

Ausbildung

04.2020 - Gegenwart	**Universität zu Köln - Promotion in Experimentalphysik**
04.2018 – 04.2020	**Universität zu Köln - Master in Experimentalphysik**
02.2010 – 09.2014	**University of Aleppo – Bachelor in Physik**
09.2006 – 07.2009	**Al-Maary High School in Aleppo – Abitur in Wissenschaften**

Kenntnisse und Interessen

Fremdsprachen	**Arabisch [Muttersprache] – Englisch [fließend]**
	Deutsch [fließend] – Türkisch [mittleres Niveau] –
	Französisch [Grundkenntnisse]
IT- Kenntnisse	**MS- Office : sehr gut**
	Python : sehr gut
Hobbys	**Lesen – Musik – Wandern – Psychologie – Astronomie**

Berufserfahrung

04.2020 - Gegenwart	**Universität zu Köln - wissenschaftlicher Mitarbeiter**
	(Teilzeit) - 1. Physikalisches Institut - Zülpicher Str. 77, 50937